UNIVERSITEIT VAN PRETORIA
UNIVERSITY OF PRETORIA
YUNIBESITHI YA PRETORIA

# Electrochemical and electrocatalytic properties of iron(II) and cobalt(II) phthalocyanine complexes integrated with multi-walled carbon nanotubes

by

SOLOMON ALMANTO MAMURU

A dissertation submitted in fulfilment of the

requirements for the degree

of

**DOCTOR OF PHILOSOPHY**

in the Faculty of Natural and Agricultural Science

**University of Pretoria**

October, 2010

**Supervisor:** Dr KI Ozoemena

# DEDICATION

This dissertation is dedicated to my wife Fidelia and two children, Sheni Adrian and Bonoshi Benedicta for their patience and understanding.

## DECLARATION

I declare that the thesis hereby submitted to the University of Pretoria for the degree of Doctor of Philosophy has not been previously submitted by me for a degree at any other University, that it is my own work in design and execution, and that all material contained therein has been duly acknowledged.

*Solomon Almanto Mamuru*.....

## ACKNOWLEDGEMENTS

I wish to express my sincere and profound gratitude to the Almighty father for His guidance, blessing and protection throughout the duration of my study in South Africa. To Prof. Jacob K. Kwaga and the management of Adamawa State University, Mubi for the opportunity given me to study outside the shores of Nigeria, I say thank you. Sincere appreciation to my supervisor, Dr (Prof.) Kenneth I. Ozoemena, who out of his valuable time read through and made necessary corrections, also not forgetting his moral, financial support and harsh criticism; you have made a diamond out of coal. To the staff and members of Chemistry Department, University of Pretoria and the National Research Foundation (NRF) for the prestigious nanoflagship bursary, I am grateful. To my family, especially my mother Catherine Abubakar, my sister Celina Kanmodi, and my brothers Henry and Tunde, for their moral support and encouragement; to all the members of our research group, we had a wonderful time, despite all inconveniences. I am ever grateful to my very good South African friends, Tebogo Mogosoana and Refilwe Mokate; you made my stay in South Africa worthwhile. I will miss you guys. Finally, to all the friends I made while in South Africa, who have in one way or another impacted positively to my stay in South Africa; especially Pius Chin, Esme, Essien, Sello Segoa, and all the staff of the international student division.

## ABSTRACT

For the first time, new metallophthalocyanine (MPc) complexes: (i) nanostructured MPc (nanoMPc, where M = iron or cobalt); (ii) octabutylsulphonylphthalocyanine (MOBSPc, where M = iron or cobalt); and (iii) iron (II) tetrakis(diaquaplatinum)octacarboxyphthalocyanine (PtFeOCPc) were synthesized and characterized using advanced microscopic and spectroscopic techniques such as MS, AFM, HRTEM, FESEM, and EDX. Electrochemical techniques such as cyclic voltammetry, square wave voltammetry, chronoamperometry, rotating disk electrode, and electrochemical impedance spectroscopy, were used to explore the redox chemistry, heterogeneous electron transfer kinetics (HET), and electrocatalytic properties of these MPc complexes towards oxygen reduction reaction (ORR), oxidation of formic acid, thiocyanate and nitrite on a edge plane pyrolytic graphite electrode (EPPGE) platform pre-modified with or without acid functionalized multi-walled carbon nanotubes (MWCNTs). The MWCNT-MPc platforms exhibit enhanced electrochemical response in terms of (i) HET towards an outer-sphere redox probe ($[Fe(CN)_6]^{3-}/[Fe(CN)_6]^{4-}$), and (ii) catalytic activities towards the investigated analytes. The MWCNT-nanoMPc electrode exhibits faster HET constant ($k_{app}$ ≈ 30 – 56 x $10^{-2}$ $cms^{-1}$ compared to their bulk MPc counterparts (≈ 4 – 25 x $10^{-2}$ $cms^{-1}$). The MWCNT-nanoMPc exhibited enhanced electrocatalytic properties (in terms of sensitivity and limit of detection, LoD) towards the detection of thiocyanate and nitrite in aqueous solutions. ORR was a 4-

electron process with very low onset potential (-5 mV vs. Ag|AgCl saturated KCl). HET and ORR at MOBSPc complexes supported on MWCNTs showed that the MWCNT–MOBSPc exhibited larger Faradaic current responses than the electrodes without MWCNTs. The rate constant at the MWCNT-MOBSPc electrodes ($k_{app}$ ≈ (22 – 37) x $10^{-2}$ $cms^{-1}$) is about a magnitude higher than the electrodes without MWCNT ($k_{app}$ ≈ (0.2 – 93) x $10^{-3}$ $cms^{-1}$). The MWCNT–FeOBSPc electrode gave the best ORR activity involving a direct 4-electron mechanism with low onset potential (0.0 mV vs. Ag|AgCl saturated KCl). The onset potential is comparable and even much lower than recent reports. The HET and electrocatalytic properties of PtFeOCPc supported on a MWCNT platform (MWCNT-PtFeOCPc) gave enhanced electrochemical response in terms of (i) HET ($k_{app}$ ≈ 78 x $10^{-2}$ $cms^{-1}$), (ii) catalytic rate constant ($k_{cat}$ ≈ 41 $cm^3mol^{-1}s^{-1}$) and (iii) tolerance towards CO poisoning during formic acid oxidation. The ORR activity is a direct 4-electron transfer process at a rate constant of 2.78 x $10^{-2}$ $cms^{-1}$; with a very low onset potential approximately 0.0 mV vs. Ag|AgCl saturated KCl. The electro-oxidation of formic acid at MWCNT-PtFeOCPc follows the preferred 'direct pathway'. This work clearly proves that the MWCNT-MPcs hybrid exhibit enhanced electrochemical and electrocatalytic activities towards the selected analytes compared to the MPcs alone. Considering the ease of fabrication of these electrodes (drop-dry method), these nanocomposite materials are promising platform for potential application in sensing and cataly

# Table of Contents

**SECTION A**

**CHAPTER 2**

## Abbreviations

| | |
|---|---|
| A | Electrode surface area ($cm^2$) |
| AFM | Atomic force microscopy |
| Ag | Silver wire pseudo-reference electrode |
| AglAgCl | Silver/silver chloride reference electrode |
| CME | Chemically modified electrode |
| C.E. | Counter electrode |
| CTAB | Hexadecyltrimethylammonium bromide |
| CV | Cyclic voltammetry |
| CV | Cyclic voltammogram |
| D | Diffusion coefficient ($cm^2s^{-1}$) |
| DBU | 1,8-diazacyclo[5.4.0]undec-7-ene |
| DMF | Dimethylformamide |
| EDX | Energy dispersive x-ray |
| EIS | Electrochemical impedance spectroscopy |
| EPPGE | Edge plane pyrolytic graphite electrode |
| FeOBSPc | Iron(II) octabutylsulphonylphthalocyanine |
| $Fe(CN)_6^{4-}$ | Hexacyanoferrate(II) |
| $Fe(CN)_6^{3-}$ | Hexacyanoferrate(III) |
| LoD | Limit of detection |
| MPc | Metallophthalocyanine |
| Pc | Phthalocyanine |

| | |
|---|---|
| PtFeOCPc | Iron(II) tetrakis(diaquaplatinum)octacarboxy phthalocyanine |
| R.E. | Reference electrode |
| SEM | Scanning electron microscope |
| SWV | Square wave voltammetry |
| T | Temperature (K) |
| t | Time(s) |
| TBAP | Tetrabutyl ammonium perchlorate |
| TEM | Transmission electron microscope |
| UV-vis. | Ultra violet visible spectrophotometer |
| W.E. | Working electrode |
| XRD | X-ray diffraction spectroscopy |

# List of Symbols

| | |
|---|---|
| $\alpha$ | Transfer coefficient |
| $\omega$ | Angular velocity |
| $\Gamma$ | Surface concentration |
| $\pi$ | Pi bonding |
| $\lambda$ | Wavelength |
| $\gamma$ | kinematic viscosity |
| c | Molar concentration of analyte |
| C | Capacitance |
| $C_{dl}$ | Double-layer capacitance |
| CPE | Constant phase element |
| D | Diffusion coefficient |
| $E_{pa}$ | Anodic peak potential |
| $E_{pc}$ | Cathodic peak potential |
| $E$ | Potential |
| $E^o$ | Standard potential |
| $E_{1/2}$ | Half-wave potential |
| $\Delta E$ | Potential 'width' |
| $\Delta E_p$ | Anodic-to-cathodic peak potential separation |
| $\Delta E_s$ | Step height |
| $\Delta E_{sw}$ | Pulse height |
| $f$ | Frequency |
| F | Faraday constant |

| | |
|---|---|
| $H_z$ | Hertz |
| $i_{pa}$ | Anodic peak current |
| $i_{pc}$ | Cathodic peak current |
| $j_{pa}$ | Anodic peak current density |
| $j_{pc}$ | Cathodic peak current density |
| K | Kelvin |
| $k_{app}$ | Apparent electron transfer rate constant |
| $k_{cat}$ | Catalytic rate constant |
| n | Number of electron |
| Q | Electrical charge (C) |
| R | Universal gas constant |
| $R_{ct}$ | Charge transfer resistance |
| $R_s$ | Resistance of electrolyte |
| ν | Scan rate |
| V | Volts |
| $-Z''$ | Imaginary impedance |
| $Z'$ | Real impedance |
| $Z_w$ | Warburg impedance |

## List of Schemes

## List of Tables

## List of Figures

# CHAPTER 1

## General Overview of Dissertation

## 1.1 Background of Project

### 1.1.1 *Introduction*

Metallophthalocyanines have continued to be one of the most studied classes of macrocyclic organometallic functional materials. They exhibit remarkable redox[1-4] and physico-chemical properties that are of interests in fundamental and applied research fields such as electrocatalysis and sensing,[1,5-7] electrochromic and electroluminescent display devices,[8] liquid crystal display devices,[9] photodynamic therapy[10] and other photosensitisation processes,[11,12] and in the development of energy storage and conversion systems such as fuel cells,[13] oxygen reduction reaction,[14] lithium ion battery,[15,16] and supercapacitor development.[17,18,19] The importance of MPc complexes in these technologically important applications has remained the major motivation for the intense search for novel MPc complexes. Thus, in this work, a report is given for the synthesis of nanostructured iron(II) and cobalt(II) phthalocyanine (nanoMPc); iron(II) and cobalt(II) octabutylsulphonyl phthalocyanine (MOBSPc) and novel iron phthalocyanine complex peripherally substituted with platinum, iron(II) tetrakis(diaquaplatinum) octa-carboxyphthalocyanine (PtFeOCPc).

In the area of electrocatalysis and energy storage and conversion systems, the use of transition metal phthalocyanine complexes is crucial. A simple approach is to place a monolayer or a few layers of MPc onto an

electrode, for instance a bare edge plane pyrolytic graphite electrode, and measure the response to disturbance by a redox active target, for example molecular oxygen or thiocyanate ion etc.

Considering that many potential applications of the transition MPc complexes, for example in energy systems and heterogeneous catalysis, involve the use of their thin solid films and exchange of electrons between the solid/electrolyte interface, some understanding of the heterogeneous electron transfer kinetics (HET) is important. Thus, the HET of the MPc complexes when supported onto MWCNT-based electrode is also explored. The choice for MWCNT-based electrode is motivated by literature precedents on the ability of carbon nanotubes to enhance the electrochemical performance of the MPc complexes.[17,18,19,20]

### 1.1.2 *Aim*

This thesis is geared towards the search for potential application of iron(II) and cobalt(II) phthalocyanine complexes immobilised on multi-walled carbon nanotubes modified edge plane pyrolytic graphite electrode in the fields of

- **Electrocatalysis:** Development of electrodes modified with thin films of iron(II) and cobalt(II) phthalocyanine complexes for energy conversion devices such as fuel cell (cathodic oxygen reduction reaction and formic acid oxidation).

- **Electroanalysis:** development of sensors for the detection of biologically and environmentally important molecules such as thiocyanate ion ($SCN^-$) and nitrite ($NO_2$).

### 1.1.3 *Objectives*

- To synthesise nanostructured iron(II) and cobalt(II) phthalocyanine; peripherally substituted iron(II) and cobalt(II) phthalocyanine complexes.
- To interrogate the heterogeneous electron transfer behaviour of the iron(II) and cobalt(II) phthalocyanine complexes in an outer-sphere redox probe ($[Fe(CN)_6]^{3-}/[Fe(CN)_6]^{4-}$), using cyclic voltammetry and electrochemical impedance spectroscopy technique.
- To investigate the electrocatalytic oxidation of thiocyanate and nitrite in phosphate buffer solution pH 5 and pH 7.4 respectively, employing cyclic voltammetry and amperometry analysis.
- To study the cathodic reduction of molecular oxygen in 0.1 M NaOH using cyclic voltammetry, linear sweep voltammetry and rotating disk electrode.
- To study the oxidation and stability of formic acid in 0.5 M $H_2SO_4$ solution, using cyclic voltammetry and amperometry technique.

### 1.1.4 *Scientific novelty of the work*

- For the first time, iron(II) and cobalt(II) octabutylsulphonyl phthalocyanine (MOBSPc); and iron(II) tetrakis(diaquaplatinum)

octacarboxyphthalocyanine (PtFeOCPc) complexes were synthesised and a detailed study of their electrochemical properties provided.

- For the first time, a detailed study of the electrocatalytic reduction of molecular oxygen and formic acid on MWCNT-MPc nanocomposite has been provided.

### 1.1.5 *Publication of the work*

Some of the materials presented in this thesis have resulted in 6 papers published in international peer-reviewed scientific journals. The results were also presented at 3 international scientific conferences.

### 1.1.6 *Structure of the thesis*

The thesis consists of 2 sections made up of 6 chapters. Chapter 1 gives a brief summary of the thesis, highlighting the need for carrying out this work and the results obtained. Section A consists of Chapters 2 and 3. Chapter 2 introduces the basics in electrochemistry and a brief review of literature on related works, the experimental procedures and the materials used in this work is presented in chapter 3. Section B is the results and discussion and comprises of chapters 4, 5 and 6. Chapter 4 discusses the results obtained for nanostructured iron(II) and cobalt(II) phthalocyanine, analysis of the result obtained for iron(II) and cobalt(II) octabutyl sulphonyl phthalocyanine is presented in chapter 5, while chapter 6 discusses the result obtained for iron(II) tetrakis(diaquaplatinum)octa-carboxyphthalocyanine.

## References

1. K.I Ozoemena, T. Nyokong, *J. Chem. Soc. Dalton Trans*., (2002),1806
2. Z.X. Zhao, K.I. Ozoemena, D.M. Maree, T. Nyokong, *Dalton Trans*., 2005, 1241.
3. B. Agboola, P. Westbroek, K.I Ozoemena, T. Nyokong, *Electrochem. Commun*., **9** (2007), 310
4. B. Agboola, K.I Ozoemena, P. Westbroek, T. Nyokong, *Electrochim. Acta,* **52** (2007), 2520
5. K.I Ozoemena, T. Nyokong, *Electrochim. Acta,* **51** (2006), 5131
6. K.I Ozoemena, T. Nyokong, *J. Electroanal. Chem.,* **579** (2005), 283
7. B.O. Agboola, K.I. Ozoemena, *Phys. Chem. Chem. Phys*., **10** (2008), 2399
8. M.M Nicholson, in *Phthalocyanine: Properties and Applications*, eds A.B.P. Lever, C.C. Leznof, VCH Publishers, New York, 1993, vol.3
9. J. Simon, P. Bassoul, in *Phthalocyanine: Properties and Applications*, eds A.B.P. Lever, C.C. Leznof, VCH Publishers, New York, 1993, vol.2
10. I. Rosenthal, E. Ben-Hur, in *Phthalocyanine: Properties and Applications*, eds A.B.P. Lever, C.C. Leznof, VCH Publishers, New York, 1993, vol.1
11. K. Ozoemena, N. Kuznetsova, T. Nyokong, *J. Photochem. Photobiol., A: Chem*., **139** (2001), 217

12. K. Ozoemena, N. Kuznetsova, T. Nyokong, *J. Mol. Catalysis, A: Chem.*, **176** (2001), 29
13. Z.P. Li, B.H. Liu, *J. Appl. Electrochem*.,**40** (2010), 475
14. N. Sehlotho, T. Nyokong, *J. Electroanal. Chem*., **595** (2006),161
15. T-l. Che, Q-c. Gao, Y-g. Cai, J-s Zhao, *Dianchi*, **38** (2008), 183
16. A. Shigehara, Y. Asai, M. Onishi, *Jpn. Kokai Tokkyo Koho*, JP 20002216764, 2002.
17. A.T. Chidembo, K.I. Ozoemena, B.O. Agboola, V. Gupta, G.G. Wildgoose, R.G. Compton, *Energy Environ. Sci*., **3** (2010), 228
18. B.O. Agboola, K.I. Ozoemena, *J. Power Sources*, **195** (2010), 3841
19. A.T. Chidembo, K.I. Ozoemena, *Electroanalysis,* 2010 in press
20. J. Zagal, S. Griveau, K.I Ozoemena, T. Nyokong, F. Bedioui, *J. Nanosci. Nanotech.,* **9** (2009), 2201

**SECTION A**

# CHAPTER 2

## Introduction

## 2.1 Electrochemistry: An Overview

### 2.1.1. *Basic concepts*

Electrochemistry, as the name suggests, studies the relationship between electrical and chemical occurrences.[1] It covers mainly two areas: *electrolysis*-conversion of chemical compounds by passage of an electric current and *electrochemical power sources*-energy of chemical reactions transformed into electricity. Electrochemistry is one effective technique to study electron transfer properties. When electron transfer is between a solid substrate and a solution species, it is termed heterogeneous process. Inversely, if electron transfer reaction occurs between two species, both of which are in solution, the reaction is homogeneous. Therefore, electrochemistry can specifically be defined as the science of structures and processes at and through the interface between an electronic (electrode) and an ionic conductor (electrolyte) or between two ionic conductors.[2]

Electrochemistry is an interdisciplinary science that is mainly rooted in chemistry and physics; however, also linked to engineering and biochemistry/biology. Due to its diversity, electrochemistry has found application in various working fields such as: analytical electrochemistry; environmental electrochemistry;[3] electrochemistry of glasses;[4] ionic liquids electrochemistry; microelectrochemistry,

nanoelectrochemistry; photoelectrochemistry;[3] solid state electrochemistry; solution electrochemistry; surface electrochemistry; technical electrochemistry with numerous subtopics such as: Batteries and energy storage[5]; Corrosion and corrosion inhibition; Electrochemical synthesis and reactors (electrosynthesis); Electronic components (capacitors, displays, information storage, rectifiers); Fuel cells and galvanic deposition; Theoretical or quantum electrochemistry.

Electrochemistry also involves the measurement of potential (potentiometry) or current response (voltammetry).[6] The work described in this dissertation involves current measurement, voltammetry and a number of voltammetric techniques, namely, cyclic voltammetry (CV), linear sweep voltammetry (LSV), square wave voltammetry (SWV), chronoamperometry (CA) and chronocoulometry.

#### 2.1.1.1. *The electrode-solution interface*

The interface between a metal (electrode) and an electrolyte solution is considered when trying to gain an impression of the structures and processes that occur in electrochemical systems. Figure 2.1 shows a schematic diagram of the interface structure and the processes. This interface is generally charged; the metal surface carries an excess charge, which is balanced by a charge of equal magnitude and opposite sign on the solution side of the interface. The resulting charge distribution; two narrow regions of equal and opposite

charge, is known as the electric double layer. It can be viewed as a capacitor with an extremely small effective plate separation, and therefore has a very high capacitance.

Reactions involving charge transfer through the interface, and hence the flow of a current, are called electrochemical reactions. Two types of such reactions can occur at the interface. One is an instance of metal deposition. It involves the transfer of a metal ion from the solution onto the metal surface, where it is discharged by taking up electrons. Metal deposition takes place at specific sites. The deposited metal ion may belong to the same species as those on the metal electrode, as in the deposition of a $Ag^+$ ion on a silver electrode, or it can be different as in the deposition of a $Ag^+$ ion on platinum. In any case the reaction is formally written as:

$$Ag^+(solution) + e^- (metal) \rightleftharpoons Ag(metal) \qquad (2.1)$$

Metal deposition is an example of a more general class of electrochemical reactions, ion transfer reactions. In these an ion, e.g. a proton or a halide ion, is transferred from the solution to the electrode surface, where it is subsequently discharged.

Another type of electrochemical reaction, is an electron-transfer reaction, an oxidized species is reduced by taking up an electron from the metal. Since electrons are very light particles, they can tunnel over a distance of 10 Å or more, and the reacting species need not be in contact with the metal surface. The oxidized and the reduced forms of

the reactants can be either ions or uncharged species. A typical example for an electron-transfer reaction is:

$$Fe^{3+}(solution) + e^{-}(metal) \rightleftharpoons Fe^{2+}(metal) \qquad (2.2)$$

Both ion and electron transfer reactions entail the transfer of charge through the interface, which can be measured as the electric current. Based on the definition of the electric double layer, Helmholtz[7] proposed a simple geometric model of the interface. This model gave rise to the concept of the inner and outer Helmholtz planes (layers). The *inner Helmholtz layer* comprises all species that are specifically adsorbed on the electrode surface. If only one type of molecule or ion is adsorbed, and they all sit in equivalent positions, then their centres define the *inner Helmholtz plane* (IHP). The *outer Helmholtz layer* comprises the ions that are closest to the electrode surface, but are not specifically adsorbed. They have kept their solvation spheres intact, and are bound only by electrostatic forces. If all these ions are equivalent, their centres define the *outer Helmholtz plane* (OHP). The layer which extends from the OHP into the bulk solution is a three dimensional region of scattered ions called the diffuse or Gouy layer. The IHP and OHP represent the layer of charges which is strongly held by the electrode and can survive even when the electrode is pulled out of the solution.[8,9]

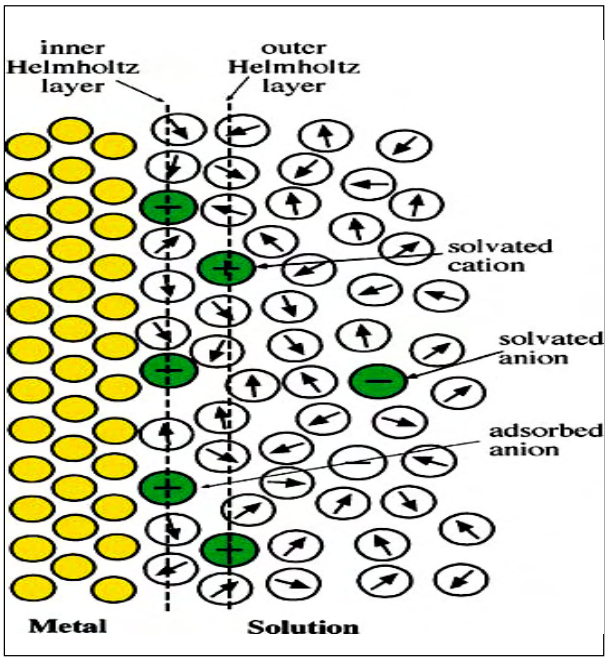


***Figure 2.1:*** *Model of the electrode-solution double layer*[2]

### 2.1.1.2. *Faradaic and non-Faradaic processes*

Faraday's law states that *the number of moles of a substance, produced or consumed during an electrode process, is proportional to the electric charge passed through the electrode*; Redox processes are often governed by this law. Electron transfer reactions proceeding at the charged interface obeying this law are called Faradaic process. Non-Faradaic process arise when an electrode-solution interface shows a range of potentials where no charge-transfer reactions occur. However, processes such as adsorption and desorption can occur, and the structure of the electrode-solution interface can change with changing potential or solution composition. Although charge does not

cross the interface, external currents can flow (at least transiently) when the potential, electrode area, or solution composition changes.

### 2.1.1.3. *Mass transport processes*

The movement of charged or neutral species that allows the flow of electricity through an electrolyte solution in an electrochemical cell is referred to as a mass transport process. **Migration**, **diffusion** and **convection** are the three possible mass transport processes accompanying an electrode reaction.

**Migration:** Migration is the movement of charged particles along an electrical field; this charge is carried through the solution by ions. To limit migrational transport of the ions that are components of the redox system examined in the cell, excess supporting electrolyte is added to the solution; in this work a large concentration of KCl is used. In analytical applications, the presence of a high concentration of supporting electrolyte which is hundred times higher than the concentration of electroactive ions means that the contribution of examined ions to the migrational transport is less than one percent. Then it can be assumed that the transport of the examined species towards the working electrode is by diffusion only. Migration of electroactive species can either enhance or diminish the current flowing at the electrode during reduction or oxidation of cations. It helps reduce the electrical field by increasing the solution conductivity, and

serves to decrease or eliminate sample matrix effects. The supporting electrolyte ensures that the double layer remains thin with respect to the diffusion layer, and it establishes a uniform ionic strength throughout the solution. However, measuring the current under mixed migration-diffusion conditions may be advantageous in particular electrochemical and electroanalytical situations.[1] Uncharged molecules do not migrate.

**Diffusion:** Diffusion is the transport of particles as a result of local difference in the chemical potential.[10] Diffusion is simply the movement of material from a high concentration region of the solution to a low concentration region. Electrochemical reactions are heterogeneous and hence they are frequently controlled by diffusion. If the potential at an electrode oxidizes or reduces the analyte, its concentration at the electrode surface will be lowered, and therefore, more analyte moves to the electrode from the bulk of the solution, which makes it the main current-limiting factor in voltammetric process. Although migration carries the current in the bulk solution during electrolysis, diffusion should also be considered because, as the reagent is consumed or the product is formed at the electrode, concentration gradient between the vicinity of the electrodes and the electroactive species arise. Indeed, under some circumstances, the flux of electroactive species to the electrode is due almost completely to diffusion.

**Convection:** Convection is one of the modes of mass transport which involves the movement of the whole solution carrying the charged

particles. The major driving force for convection is an external mechanical energy associated with stirring or flow of the solution or rotating or vibrating the electrode (forced convection). Convection can also occur naturally as a result of density gradient.[11] In voltammetry, convection is eliminated by maintaining the cell under quiet and stable condition.

### 2.1.2. *Voltammetry*

Voltammetry is the measurement of current as a function of a controlled electrode potential and time. The resultant current–voltage (or current–time or current–voltage–time) display is commonly referred to as the "voltammogram".[1,12] The term "voltammetry" was coined by Laitinen and Kolthoff.[13,14] The objectives of a voltammetric experiment also vary, ranging from analytical measurements designed to determine the concentration of an analyte to measurements designed to elucidate complex mechanisms and the values of the associated thermodynamic and kinetic parameters.[1] The protocol for potential control may vary, leading to a number of different techniques each with their common names. The techniques used in this work are cyclic voltammetry (CV), linear sweep voltammetry (LSV), square wave voltammetry (SWV), chronoamperometry (CA) and chronocoulometry. This section gives the basic theoretical background underlying these techniques.

### 2.1.2.1. *Cyclic voltammetry*

This is a commonly employed type of voltammetry where measurement of the current response of an electrode to a linearly increasing and decreasing potential cycle is performed.[15] Figure 2.2 presents the resulting scan of potential against time, scanning linearly the potential of a stationary working electrode in an unstirred solution, using a triangular potential waveform and the corresponding voltammogram. The experiment is usually started at a potential where no electrode process occurs (0.2 V in the plot) and the potential is scanned with a fixed scan rate to the switching potential (0.7 V in the plot). When an electrochemically active compound is present in the solution phase, an anodic current peak at the potential $E_{pa}$ is detected with the peak current $I_{pa}$. When the potential is swept back during the reverse scan a further current peak at the potential $E_{pc}$ may be observed with a cathodic peak current $I_{pc}$.

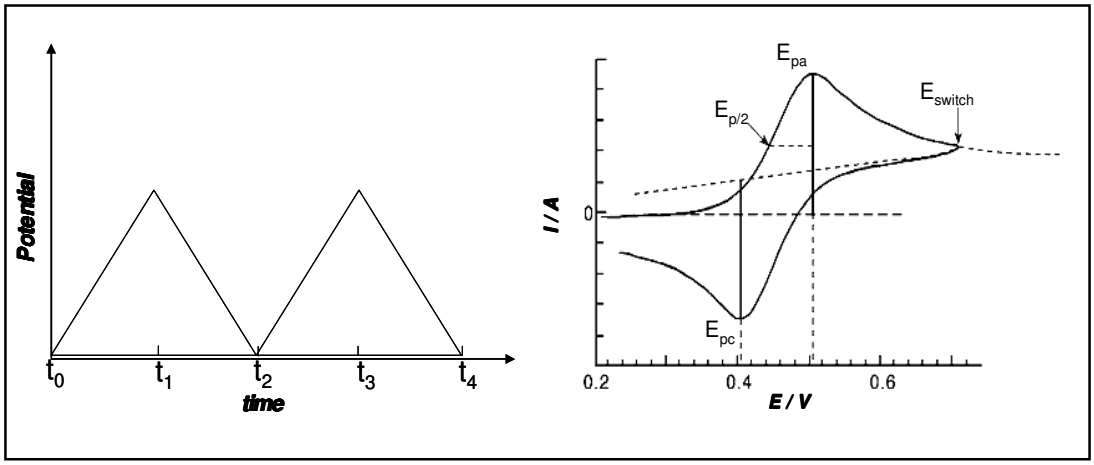


***Figure 2.2:*** *The potential-time waveform and a typical cyclic voltammogram for a reversible redox process*

Cyclic voltammetry is an excellent technique to survey the reactivity of new materials or compounds and can provide information about (i) the potential at which oxidation or reduction processes occur, (ii) the oxidation state of the redox species, (iii) the number of electrons involved, (iv) the rate of electron transfer, (v) possible chemical processes associated with the electron transfer, and (vi) adsorption effects,[1,16,17] etc. Electron transfer processes can be labelled reversible, irreversible or quasi-reversible, and are identified by certain criteria that can be measured by cyclic voltammetry.

#### 1.1.2.1.1. *Reversibility*

Electrochemical reversibility is a practical concept used when the surface concentrations of both species of a redox couple obey the Nernst equation (equation 2.3) at any potential difference applied at the electrode-solution interface. In short, it means that the Nernst equation can be applied also when the actual electrode potential ($E$) is higher (anodic reaction) or lower (cathodic reaction) than the equilibrium potential ($E_e$). Therefore, such a process is called a reversible or Nernstian reaction.

$$E = E^\circ + \frac{RT}{nF}\ln\frac{c_O(x=0)}{c_R(x=0)} \approx E^\circ + \frac{2.303RT}{nF}\log\frac{c_O(x=0)}{c_R(x=0)} \qquad (2.3)$$

where $c_O(x=0)$ and $c_R(x=0)$ are the concentrations of these species at the electrode surface, $E^\circ$ is the formal electrode potential, $n$ is the

number of electrons transferred, F is Faraday's constant, RT have their usual meaning. It follows that the Nernst equation expresses the relationship between the surface concentrations and the electrode potential regardless of the current flow. It should also be mentioned that the appearance of the reversible behaviour depends on the relative value of electron transfer rate ($k_s$) and mass transport, since no equilibrium exists between the surface and bulk concentrations, reactants are continuously transported to the electrode surface by diffusion.

The magnitude of the peak current for a reversible electron transfer is given by the *Randles–Ševčik* equation (2.4)[1]

$$I_p = 0.446nFAc\sqrt{\frac{nF\nu D}{RT}} \approx (2.69\,x10^5)n^{3/2}AD^{1/2}c\nu^{1/2} \qquad (2.4)$$

In this equation the peak current $I_p$ is dependent on $n$, the number of electrons transferred per molecule diffusing to the electrode surface, F, the Faraday constant, A, the electrode area, $c$, the concentration of analyte in solution, R, the gas constant, T, the absolute temperature, $\nu$, the scan rate, and $D$, the diffusion coefficient.

The dependence of current on the scan rate is indicative of electrode reaction controlled by diffusion,[18,19,20] using equation (2.4) a linear plot of $I_p$ vs. $\nu^{1/2}$ is obtained. Deviation from linearity indicates the presence of chemical reaction involving either the oxidized, reduced or both species.

For a reversible process, the half-wave potential, $E_{½}$, is related to the standard potential ($E°$) as in equation (2.5):

$$E_{½} = E^{\circ} + \frac{RT}{2nF} \ln \frac{[O]}{[R]} \qquad (2.5)$$

where R is the gas constant, T the temperature in Kelvin, F the Faraday constant and [O] is the concentration of oxidised species, [R] is the concentration of reduced species in mol $L^{-1}$. The half-wave potential, $E_{1/2}$ can be calculated from equation (2.6):

$$E_{½} = \frac{E_{pa} + E_{pc}}{2} \qquad (2.6)$$

where $E_{pa}$ is the anodic peak potential and $E_{pc}$ is the cathodic peak potential. The number of electrons transferred in a reversible process can be calculated from equation (2.8):

$$\Delta E = E_{pc} - E_{pa} = \frac{RT}{nF} \quad , \quad \text{at } 25^{0}\text{C} \qquad (2.7)$$

$$\Delta E = \frac{0.059\ V}{n} \qquad (2.8)$$

where n is the number of electrons transferred, other symbols have their usual meaning. The peak-to-peak separation is approximately 59 mV at 298 K and is independent of scan rate.

#### 1.1.2.1.2. *Irreversibility*

Irreversibility in electrochemistry is when the charge-transfer step is very sluggish, i.e., the standard rate constant ($k_s$) and exchange current density ($j_o$) are very small.[7] In this case the anodic and cathodic reactions are never simultaneously significant. In order to observe any current, the charge-transfer reaction has to be strongly activated either in cathodic or in anodic direction by application of overpotential. These processes are characterized by a shift of the peak potential with the scan rate and $\Delta E$ can be calculated from equation (2.9).[1,21]

$$\Delta E = E^o - \frac{RT}{\alpha n_a F}\left[0.78 - \ln\frac{k^o}{D^{1/2}} + \ln\left(\frac{\alpha n_a F}{RT}\nu\right)^{1/2}\right] \qquad (2.9)$$

where α is the electron transfer coefficient of the rate determing step and $n_\alpha$ is the number of electrons involved in the charge transfer step and $k^o$ is the standard electrode reaction rate constant in $cms^{-1}$. The other symbols are listed in the list of symbols. At 25°C, the peak potential and the half-peak potential differ by $0.048\ V/\alpha n$. Hence, the voltammogram becomes more drawn-out as $\alpha n$ decreases. In an irreversible process, only forward oxidation or reverse reduction peak is observed, see Figure 2.3. It is common to observe a weak reverse peak at increased scan rates during forward oxidation at times, because of sluggish electron exchange as mentioned above. The Nernst equation is not applicable in the case of irreversible process. This is

due to the rate of electron transfer insufficient to maintain surface equilibrium and thus the oxidized and reduced species are not at equilibrium**.**

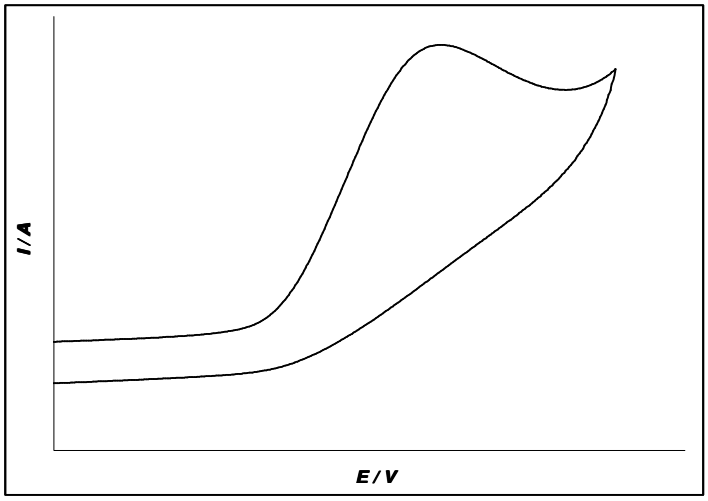


***Figure 2.3****: Typical cyclic voltammogram for an irreversible redox process*

The peak current, $I_p$ for an irreversible process can be calculated from equation (2.10):

$$I_p = \left(2.99x10^5\right)n[(1-\alpha)n]^{1/2} AcD^{1/2}\nu^{1/2} \qquad (2.10)$$

where $\alpha$ denotes the electron transfer coefficient and n the number electrons transferred in the rate determining step.

### 1.1.2.1.3. *Quasi-reversibility*

Mass transport plays a major role in controlling the concentration of the redox couple and the expressions for reversible processes also apply for quasi-reversible processes. The voltammograms of a quasi-reversible process exhibit a large peak-to-peak separation compared to reversible processes. The peak current increase with $\nu^{1/2}$ but is not

linear and Δ*E* is greater than 0.059/n V. In reversible process, current is controlled purely by mass transport but in quasi-reversible process, current is controlled by both the mass transport and charge transfer kinetics.[22,23]

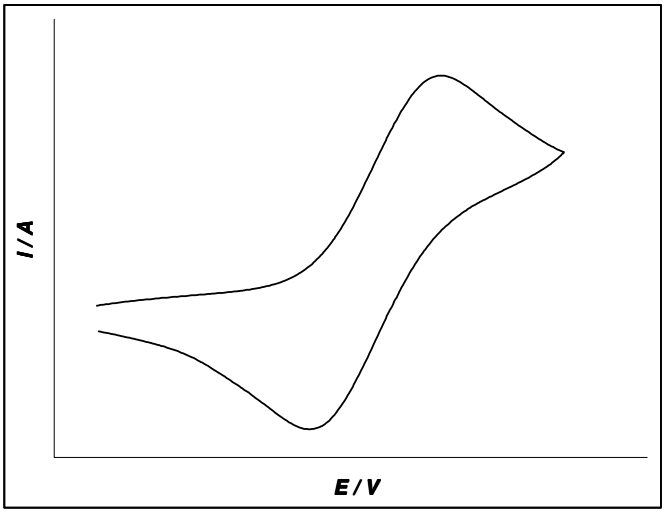


***Figure 2.4**: Typical cyclic voltammogram for a quasi-reversible redox process*

When cyclic voltammetry is applied to immobilised redox systems such as self-assembled monolayer (SAM) at an electrode surface, distinct peak shape and peak currents as depicted in Figure 2.5 may be observed. The peak current now becomes directly proportional to the scan rate.

$$I_p = \frac{n^2 F^2 \Gamma A \nu}{4RT} \qquad (2.11)$$

In this equation the peak current $I_p$ is directly proportional to $\nu$, the scan rate, and $\Gamma$ the surface concentration for the immobilised redox system. A plot of $\log I_p$ vs. $\log \nu$ allows diffusion controlled processes and

processes involving surface immobilised redox systems to be distinguished. When the slope of the plot is 0.5 or 1 it is a diffusion controlled process, or a surface confined (adsorption) process, respectively. The slight differences in cyclic voltammetric processes is summarised in Table 2.1.

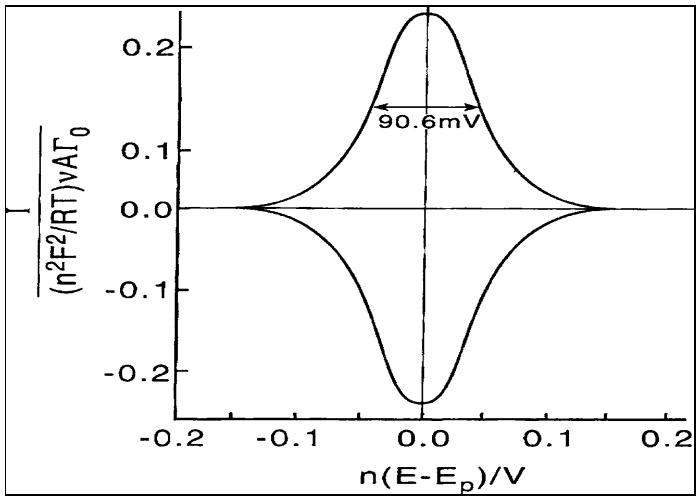


**Figure 2.5**: Symmetric "bell-shaped" cyclic voltammogram for surface confined redox system[7]

***Table 2.1:*** *The diagnostic criteria for reversible, irreversible and quasi-reversible cyclic voltammetric process*

| **Parameter** | **Cyclic Voltammetry Process** | | |
|---|---|---|---|
| | Reversible | Irreversible | Quasi-reversible |
| $E_p$ | Independent of $\nu$ | Shifts cathodically by $30/\alpha n$ mV for 10-fold increase in V | Shifts with $\nu$ |
| $\Delta E_p = E_{pa} - E_{pc}$ | ~ 59/n mV at 25°C and independent of $\nu$ | - | May approach 60/n mV at low $\nu$ but increases as $\nu$ increases |
| $I_p / \nu^{1/2}$ | Constant | Constant | Virtually independent of $\nu$ |
| $I_{pa} / i_{pc}$ | Equals 1 and independent of $\nu$ | For a reduction process, < 1 | Equals 1 only for $\alpha$=0.5 |

### 2.1.2.2. *Linear sweep voltammetry*

Linear sweep voltammetry (LSV) is a method where there is linear variation of the electrode potential with time with the scan rate (ν), ν = dE/dt and current versus potential is recorded. In LSV essentially only the first half-cycle of a cyclic voltammogram is executed. Scanning starts at a potential where no electrochemical reaction occurs. Current can be observed at the potential where the charge transfer begins, which increases with the potential, however, after a maximum value (peak current plateau) it starts to decrease due to the depletion of the reacting species at the interface.

LSV is employed in the rotating disk electrochemistry (RDE). A rotating disk electrode is rotated in the solution under study and the current depends on the solution flow rate. For the rotating disk electrode, the time dependence is in the rotation rate of the disk, which in turn controls the solution velocity near the electrode. The rate of mass transport at the rotating disk electrode is varied by altering the disk rotation speed[24]. The rotating electrode is mounted vertically to a controllable-speed motor and rotated with constant angular velocity. The components of the fluid velocity depends on this angular velocity of the disk, which is given by $\omega = 2\pi f$, where f is the rotation speed in revolutions per minutes (rpm) or rotation frequency in hertz. It depends on other factors such as the radial distance from the centre of the disk (r), the coefficient of kinematic viscosity of the fluid (γ) and on the axial distance from the surface of the disk.[25]

A general equation of the disk current, taking into account both mass transport and electron transfer kinetics can thus be given as the Koutečky-Levich equation[26]:

$$\frac{1}{j} = \frac{1}{j_k} + \frac{1}{j_{\lim}} \qquad (2.12)$$

where $j$ is the measured current density, $j_k$ the disk current density in the absence of diffusion control, for electron transfer controlled process is given by

$$j_k = Fk(E)c \qquad (2.13)$$

with the catalytic rate constant k as a function of the electrode potential E and the concentration c. The diffusion-limited current $j_{\lim}$ at the rotating disk electrode is given by the Levich equation[7] based totally on mass-transfer limited conditions.

$$j_{\lim} = 0.21nFcD^{\frac{2}{3}}\omega^{\frac{1}{2}}\gamma^{\frac{1}{6}} \qquad (2.14)$$

where, $n$ is the number of electrons transferred per molecule, F is the Faraday constant, D is the diffusion coefficient, $\omega$ is the rotation rate in rpm, and $\gamma$ is the kinematic viscosity of the solution.

### 2.1.2.3. *Square wave voltammetry*

Square-wave voltammetry is a large-amplitude differential technique in which a wave form composed of a symmetric square wave, superimposed on a base staircase potential, is applied to the working electrode (Figure 2.6).[27] The current is sampled twice during

each square wave cycle, once at the end of the forward pulse and once at the end of the reverse pulse. The current at the end of the forward pulse, $I_f$, and the current at the end of the reverse pulse $I_b$, are both registered as a function of staircase potential, which is midway between the potentials corresponding to the forward and backward potential steps. The difference between the two measurements is plotted versus the base staircase potential. Since $I_f$ and $I_b$ usually have opposite signs, the difference is larger than each individual component in the region of the peak that is centred on the half-wave potential.

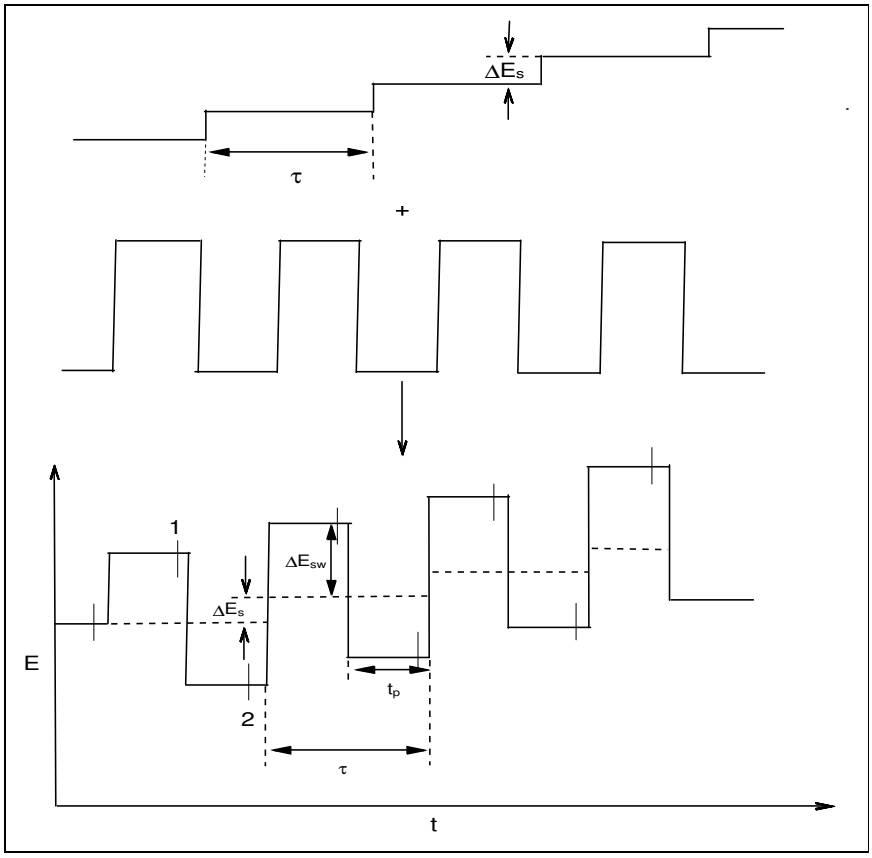


***Figure 2.6**: Square wave voltammetry potential-time waveform: sum of staircase and synchronized square wave*

Square-wave voltammetry is characterised by four parameters: square wave period, $\tau$, pulse width, $t_p = \tau/2$, step height, $\Delta E_s$ and pulse height, $\Delta E_{sw}$. The pulse width is related to the square wave frequency, $f = 1/(2t_p)$ and as the staircase step at the beginning of each cycle is $\Delta E_s$, it means that the effective scan rate is $\nu = \Delta E_s/2t_p = f\,\Delta E_s$. The major advantage of square-wave voltammetry is its speed and excellent sensitivity.[28,29] A complete voltammogram can be recorded within a few seconds. The peak height is directly proportional to the concentration of the electroactive species and direct detection limit as low as $10^{-8}$ mol.L$^{-1}$ is possible. This technique includes the use of faster scan rates compared to conventional differential pulse voltammetry. Applications of square-wave voltammetry include the study of electrode kinetics with regard to catalytic homogeneous chemical reactions, and determination of some species at trace levels. In this research, a computer-controlled square wave voltammetry was employed. Figure 2.7 displays a typical square-wave voltammogram.

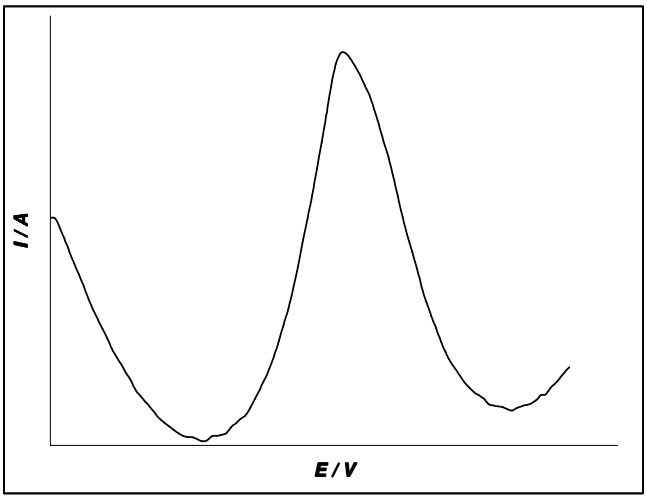


***Figure 2.7**: Typical square wave voltammetric response*

### 2.1.2.4. *Chronoamperometry*

When the potential of a working electrode is stepped from a value at which no Faradaic reaction occurs to a potential at which the surface concentration is effectively zero, is referred to as chronoamperometry. In chronoamperometry the current is measured as a function of time after application of a potential step perturbation. For example, in Figure 2.8a, if the potential is stepped from $E_1$, where no current flows, i.e., where the oxidation or reduction of the electrochemically active species does not take place, to $E_2$ where the current belongs to the electrode reaction. The electrode reaction is diffusion limited. The resulting current-time dependence is monitored. The current-time curve reflects the change in the concentration gradient in the vicinity of the surface. This involves a gradual expansion of the diffusion layer associated with the depletion of the reactant as time progresses, consequently the current decays with time (at a planar electrode) (Figure 2.8b). The current flows at any time after application of the potential step will obey the Cottrell equation.[1]

$$i(t) = \frac{nFAcD^{1/2}}{\pi^{1/2}t^{1/2}} = kt^{-1/2} \qquad (2.15)$$

where $n$, F, A, c, D, and $t$ are the number of electrons, Faradayconstant, the surface area, the concentration, the diffusion coefficient, and time respectively.

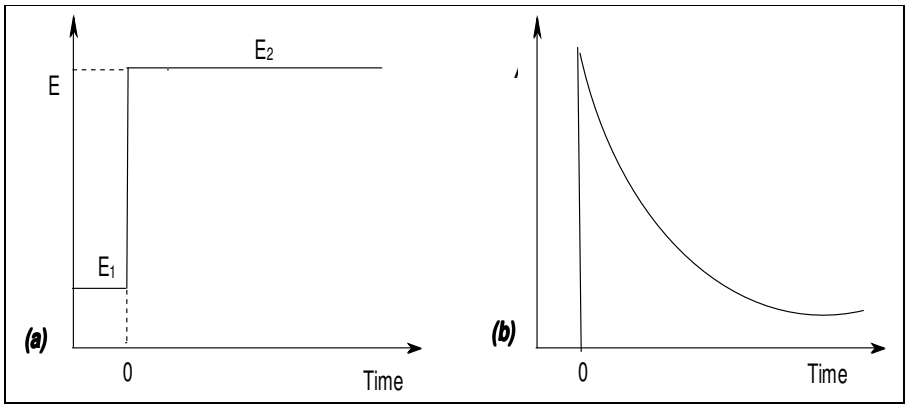


***Figure 2.8**: Potential step chronoamperometry: (a) schematic application of potential step and (b) chronoamperometric response*

Chronoamperometry is often used for measuring the diffusion coefficient of electroactive species or the surface area of the working electrode. It can also be applied to the study of mechanisms of electrode processes.[30,31]

### 2.1.2.5. *Chronocoulometry*

Chronocoulometry belongs to a family of step techniques[31,32] just like chronoamperometry. However, unlike chronoamperometry where current-time dependence is monitored, the charge-time dependence is measured in chronocoulometry. Chronocoulometry gives practically the same information that is provided by chronoamperometry, since it is just based on the integration of the current-time response, and adding corrections for the charge due to the double-layer charging ($Q_{dl}$) and the reaction of the adsorbed species ($Q_i$):

$$Q = \frac{2nFAcD^{1/2}t^{1/2}}{\pi^{1/2}} + Q_{dl} + Q_i \qquad (2.16)$$

Nevertheless, chronocoulometry offers important experimental advantages. First, unlike the current response that quickly decreases, the measured signal usually increases with time, and hence the later parts of the transient can be detected more accurately. Second, a better signal-to-noise ratio can be achieved. Third, contributions of charging/discharging of the electrochemical double layer and any pseudo-capacitance on the surface (charge consumed by the electrode reaction of adsorbed species (adsorption)) to the overall charge passed as a function of time can be distinguished from those due to the diffusing electro-reactants. A plot of the charge (Q) versus $t^{1/2}$, known as Anson plot, yields an intercept at $t$=0 that corresponds to the sum of $Q_{dl}$ and $Q_i$ (Figure 2.9b).

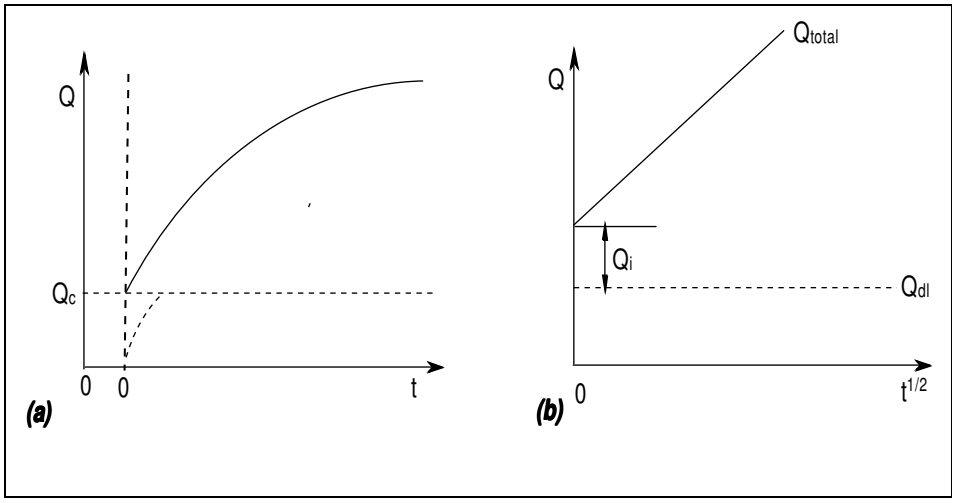


***Figure 2.9**: Chronocoulometric response (a) chronocoulometric charge vs. square root of time plot (b). Dashed curves in (a) displayed for the illustration of the capacitive charge effect, the dashed, horizontal line represents the charge response in the absence of reactant*

### 2.1.3. *Electrocatalysis*

Electrocatalysis is the catalysis of an electrode reaction.[32] The effect of electrocatalysis is an increase of the standard rate constant of the electrode reaction, which results in an increase of the Faradaic current. As the current increase can be masked by other non-electrochemical rate-limiting steps, the most straightforward indication for the electrocatalytic effect is the shift of the electrode reaction to a lower overpotential at a given current density. Electrocatalysis, as chemical catalysis, can be either homogeneous or heterogeneous in character. In homogenous electrocatalysis, both the catalyst and the substrate are in the same phase, commonly dissolved in the bulk solution, and the processes at the interface do not influence the chemical steps that involve it. In heterogeneous electrocatalysis, the catalyst is immobilized on the electrode surface, or the electrode itself plays the role of a catalyst.

MPc complexes exhibit catalytic activity for the electrochemical oxidation and reduction of a variety of target analytes in both homogeneous and heterogeneous phases.[33,34,35,36] These MPc electrodes act by lowering the overpotential of oxidation or reduction of the target analytes, and are known to mediate the redox process at the central metal and/or ring.[37,38] The mechanism for the electrocatalytic oxidation process due to the metal center is given by equation (2.17) and (2.18)

$$M^{(II)}Pc(-2) \longrightarrow M^{(III)}Pc(-2) + e^- \quad (2.17)$$

$$M^{(III)}Pc(-2) + A \longrightarrow M^{(II)}Pc(-2) + A_{ox} \quad (2.18)$$

For the electrocatalytic oxidation process due to the ring, equations (2.19) to (2.21) have been proposed.

$$MPc(-2) \longrightarrow [MPc(-1)]^{+\cdot} + e^- \quad (2.19)$$

$$2[MPc(-1)]^{+\cdot} \longrightarrow ([MPc(-1)]^{+\cdot})_2 \quad (2.20)$$

$$([MPc(-1)]^{+\cdot})_2 + A \longrightarrow MPc(-2) + A_{ox} \quad (2.21)$$

Scheme 2.1 shows an electrocatalytic reduction process promoted by MPc-based electrode. In this process, the MPc complex changes oxidation states upon interacting with the target analyte and it recovers its initial oxidation state by accepting or donating electrons to the electrode. The electrode simply acts as a source of electrons that are exchanged with the surface-confined MPc. Electrocatalytic activities are normally observed at potentials close to the formal potential of the MPc.

In this work, electrocatalytic oxidation of nitrite, thiocyanate, and formic acid and the reduction of oxygen at an edge plane pyrolytic graphite electrode modified with metallophthalocyanine complexes are investigated.

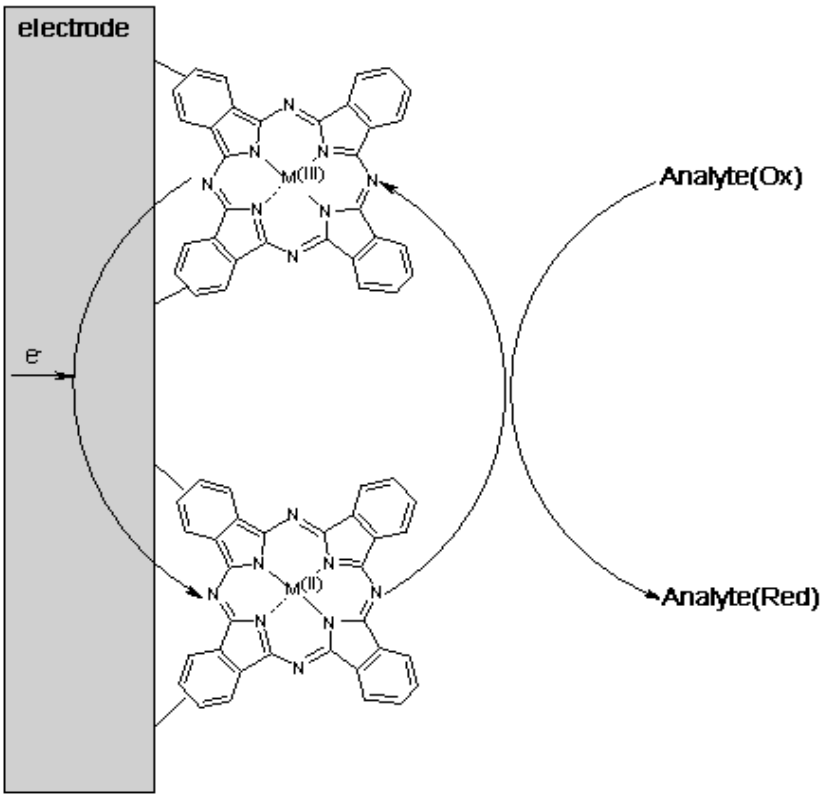


***Scheme 2.1:*** *Schematic presentation of a catalytic process promoted by MPc electrode*[33]

### 2.1.4. *Electrochemical Impedance Spectroscopy*

Impedance spectroscopy is considered a powerful technique for investigating electrochemical systems and processes. Its strength lies in its ability to interrogate relaxation phenomenon, whose time constants range over several orders of magnitude.[39] The impedance technique is based on disturbing an electrochemical cell at equilibrium or steady state with alternating signal of small magnitude and measuring the current response. This disturbance can come from a

wide range of parameters such as applied potential, applied current, the convection rate at hydrodynamic electrodes, or light intensity. The applied disturbance is usually sinusoidal.

If the disturbance due to an applied voltage at a frequency (ω) to the electrochemical cell is considered:

$$V(t) = V_0 \sin \omega t \qquad (2.22)$$

where V ($t$) is voltage at time $t$, $V_0$ is the voltage amplitude, and ω is the radial frequency. The current response will take the form as in equation (2.23) with a phase shift denoted by θ

$$I(t) = I_0 \sin(\omega t + \theta) \qquad (2.23)$$

Where I ($t$) is the current at time $t$, $I_0$ is the current amplitude, and Φ is the phase shift. The impedance of the system is the ratio:

$$Z = \frac{V_t}{I_t} \qquad (2.24)$$

With a magnitude ($Z_0 = V_0/I_0$) and a phase shift (Φ) and thus present itself as a vector quantity. The complex notation for impedance will then be (Figure 2.10b):

$$Z = Z_0(\cos\theta + j\sin\theta) = Z' + jZ'' \qquad (2.25)$$

Where $j = \sqrt{(-1)}$, Z' is the real part and Z" is the imaginary part.

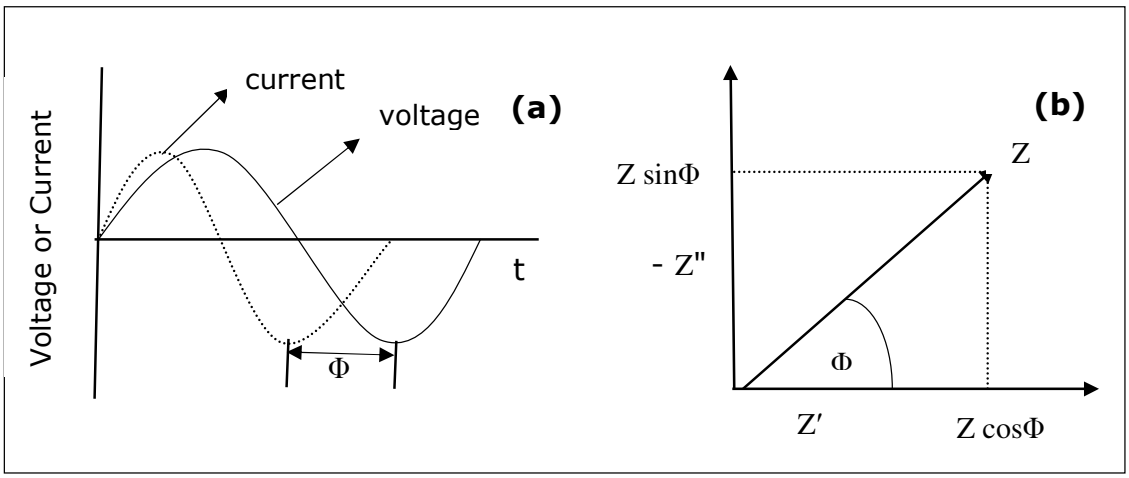


***Figure 2.10**: Sinusoidal voltage perturbation and current response (a), impedance presentation in the complex plane (b)*

### 2.1.4.1. *Data Presentation*

Graphical presentation of the measured impedance data are usually presented as 1) Nyquist or Complex plane plots (Figure 2.11(a)). It consists of plots of the real (Z') and imaginary (-Z") parts of the complex impedance (Z) as x and y axes, which are sometimes referred to as "resistance" and "reactance" respectively. As shown in Figure 2.11(a), the Nyquist plot for a simple charge transfer reaction is made of a semi-circle arc region at high frequencies lying on the x-axis followed by a straight line known as the Warburg impedance at low frequencies. The region of high frequencies is dominated by charge transfer at short times, while at high frequencies; diffusion plays the dominant role over a long time and the phase angle rises towards 45°. At high frequencies, diffusion of the reactants to and from the electrode is not important, because the currents are small and change

sign continuously.[2] Spectra as explained in Figure 2.11(a) can be used to extract information about electron transfer kinetics and diffusional characteristics. For fast electron transfer, the spectra will be completely overwhelmed by the Warburg, while for a sluggish electron transfer, a large semi-circle arc dominates. The diameter of the semi-circle arc equals the electron transfer resistance ($R_{ct}$). 2) Bode plots. This shows a plot of the phase angle and logarithm of the magnitude of impedance versus the logarithm of the frequency (Figure 2.11(b)). When resistive behaviour dominates the impedance behaviour, a horizontal line is observed in the presentation of log Z versus log f and a phase angle close to 0° is measured. When the impedance response is determined by a capacitance, a straight line with a slope of – 1 is observed and a phase angle of 90°, whereas diffusion-controlled phenomena (Warburg Impedance) would give a straight line with a slope of -1/2 and a phase angle of 45°.

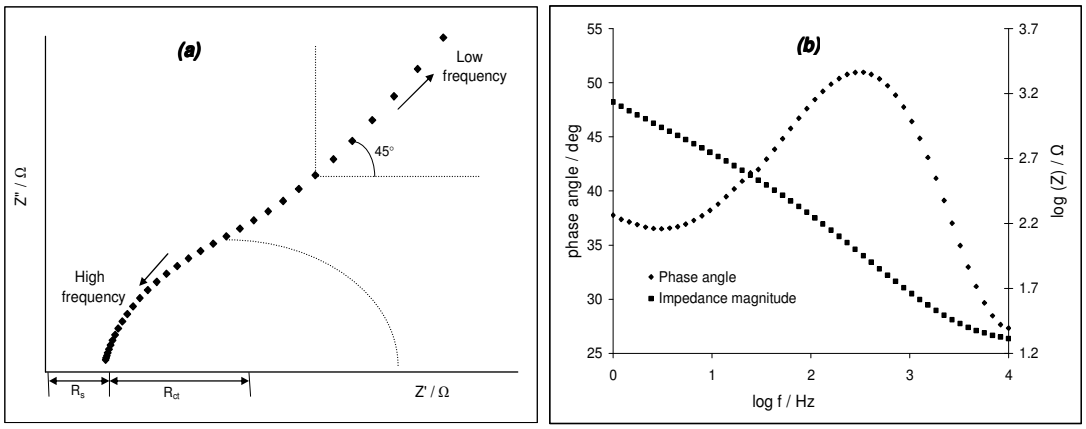


***Figure 2.11**: Nyquist (a) and Bode (b) plots for presentation of impedance data*

### 2.1.4.2. *Data Interpretation*

The measured data interpretation is usually carried out by the use of networks of electrical circuits called equivalent electrical circuits, selected based on the understanding of the electrochemical system. To model a simple three-electrode electrochemical cell in the presence of a diffusion related phenomena in terms of equivalent circuit, the Randles electrical equivalent circuit is employed (Figure 2.12). It consists of the resistance of electrolyte solution between the reference and working electrodes ($R_s$), the electrochemical double layer expressed as double-layer capacitance ($C_{dl}$), the impedance of the charge-transfer process ($R_{ct}$), and the Warburg impedance ($Z_w$) resulting from the semi-infinite diffusion of ions to the electrode surface.

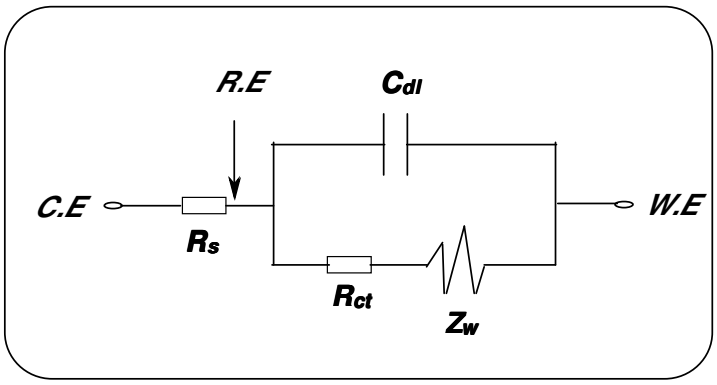


***Figure 2.12**: Classical Randles electrical equivalent circuit for an ideal behaviour*

Figure 2.12 describes a series arrangement of charge-transfer process ($R_{ct}$) and Warburg impedance ($Z_w$) that is in parallel

combination with the double-layer capacitance ($C_{dl}$), with the solution resistance ($R_s$) in series.

Figure 2.12 is made up ideal circuit elements such as resistors and capacitors, however, distributed circuit elements are required in addition to the ideal circuit elements to describe the impedance response of real systems adequately. In all real systems, some deviation from ideal behavior can be observed. If a potential is applied to a macroscopic system, the total current is the sum of a large number of microscopic current filaments, which originate and end at the electrodes.[36] If the electrode surfaces are rough or one or more of the dielectric materials in the system are inhomogeneous, then all these microscopic current filaments would be different. In a response to a small amplitude excitation signal, this would lead to frequency-dependent effects that can often be modeled with simple distributed circuit elements. One of these elements, which have found widespread use in the modeling of impedance spectra, is the so-called constant phase element (CPE). A CPE is defined as

$$Z_{CPE} = \frac{1}{[Q(j\omega)^n]} \tag{2.26}$$

where $Q$ is the frequency-independent constant related to the interface, $j = \sqrt{-1}$, $\omega$ is the radial frequency, the exponent $n$ arises from the slope of log Z versus log f (and has values $-1 \leq n \leq 1$). If $n$ = 0, the CPE behaves as a pure resistor; $n$ = 1, CPE behaves as a pure capacitor, $n$ = –1 CPE behaves as an inductor; while $n$ = 0.5

corresponds to Warburg impedance ($Z_w$) which is associated with the domain of mass transport control arising from the diffusion of ions. In short, CPE arises from several factors such as (i) the nature of the electrode (e.g., roughness and polycrystallinity), (ii) distribution of the relaxation times due to heterogeneities existing at the electrode/electrolyte interface, (iii) porosity and (iv) dynamic disorder associated with diffusion.[40] An electrical equivalent circuit describing the use of the constant phase element is shown in Figure 2.13.

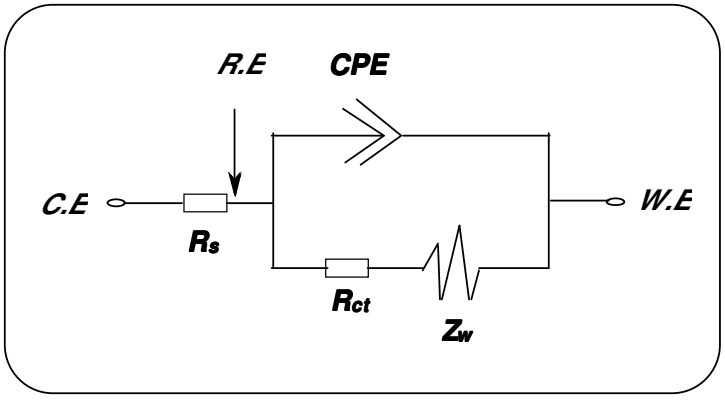


***Figure 2.13:*** *Modified Randles equivalent circuit showing the CPE for non-ideal behaviour*

### 2.1.4.3. *Validation of Measurement*

To properly define an impedance measurement as a transfer function, the system under investigation has to fulfil the conditions of linearity, causality and stability during the measurement.[41] Most electrochemical systems are nonlinear as a result of current voltage at the electrode. Deviation from causality arises when the response is caused by the

concentration, current, or potential relaxation upon departure from equilibrium. Instrument artefacts or noise can also disturb causality. Continually changing corroded electrode does not guarantee stability of an electrochemical system.

To assess whether meaningful data that fulfils the above conditions have been obtained, a range of techniques and diagnostic tools have been developed to validate impedance data. One of the diagnostic tools employed in this work is the Kramer-Kronig test. The K-K tests are a series of integral equations that govern the relationship between the real and imaginary parts of complex quantities for systems fulfilling the conditions of linearity, causality, and stability. To assess whether experimental data fulfill the Kramer–Kronig tests,[36] one part of the impedance is calculated from the other part of the impedance, which has been experimentally determined. For example, the imaginary part can be calculated from the measured real part of the impedance .The calculated imaginary part of the impedance can then be compared with the measured imaginary part of the impedance. Any difference between calculated and measured values would indicate a deviation from one of the conditions of linearity, causality, or stability[36]. This method, however, requires that at least one part of the impedance is known between the frequency limits of zero and infinity. In most cases, the frequency range is not sufficiently large to integrate over the frequency limits zero and infinity. To overcome this problem,

various models for extrapolating the experimental data sets to the frequency limits have been suggested. One model employed is the fit of the impedance data with an equivalent electric circuit. Successful fit of such circuit to a data set is consistent with the Kramer-Kronig test.

## 2.2 Chemically Modified Electrodes

The IUPAC,[42] defined a chemically modified electrode (CME) as an electrode made of a conducting or semiconducting material that is coated with a selected monomolecular, multimolecular, ionic, or polymeric film of a chemical modifier and that by means of Faradaic (charge-transfer) reactions or interfacial potential differences (no net charge transfer) exhibits chemical, electrochemical, and/or optical properties of the film.

### 2.2.1. *General Methods of Modifying Electrode Surfaces*

Chemically modified electrodes are made by using one of the following methods:

#### 2.2.1.1. *Chemisorption*

This is when molecules of modifying species are attached by valence forces. Included in this type of modification are the substrate-coupled self-assembled monolayers (SAMs) in which uncorrelated molecules spontaneously chemisorbed at specific sites on the surface of the electrode to form a superlattice.[43]

#### 2.2.1.2. *Covalent Bonding*

Linking agents are used to covalently attach from one to several monomolecular layers of the chemical modifier to the electrode surface.

#### 2.2.1.3. *Composite*

The chemical modifier is simply mixed with an electrode matrix material, as in the case of an electron-transfer mediator (electrocatalyst) combined with the carbon particles (plus binder) of a carbon paste electrode.

#### 2.2.1.4. *Coating by thin films*

Electron-conductive and nonconductive thin films are held on the electrode surface by some combination of chemisorption and low solubility in the contacting solution or by physical anchoring in a porous electrode. CMEs covered with thin films are the most popular systems, because of their numerous advantages (simplicity of preparation, stability, well-defined or sizeable electrochemical responses). These thin films coated CMEs can be further divided according to the nature of the coating process:[39]

•**Cross-linking**. The chemical components are coupled to an electrode substrate to impart a desired property to the film.

•**Dip coating.** The electrode substrate is immersed in a solution for a given period of time, allowed to form film by adsorption, removed and allowed to dry.

•**Electrochemical deposition (redox deposition).** The electrode substrate is immersed in an electrolyte solution containing one or more dissolved salts or other ions that permit the flow of electricity and subjected to electrochemical treatment. Used in electroplating; by coating a conductive metal with a thin layer of material.

•**Electrochemical polymerization**. The electrode substrate is immersed in an approximately 1 mM concentrated solution of the modifier followed by repetitive voltammetric scanning within a specified potential window. The resulting voltammogram of the first scan is different from the subsequent scans indicative of the formation of the new species on the electrode surface.

•**Solvent evaporation (drop dry).** The droplet of the desired solution of volatile solvent such as dimethylformamide is applied to the electrode substrate and allowed to dry. A major advantage of this approach is that the modifier coverage is immediately known from the original solution concentration and droplet volume. This approach is used in this study.

•**Spin coating (spin casting).** As solvent evaporation, but electrode surface is rotated when excess amount of solution is applied. Rotation is continued while the fluid spins off the edges of the substrate, until the desired thickness of the film is achieved. The solvent used is usually volatile and simultaneously evaporates.

Coating by thin films can be a multi-step process, e.g., to produce multi-layered systems or to further functionalize and to improve

usability. More complex structures of CMEs also exist. They may contain more than one modifying substance, or more than one layer. Such a system can be called a micro- or nano-structured electrode, or integrated chemical system electrode.

## 2.3 Carbon Electrodes

Carbon is selected for many electrochemical applications because of its good electrical and thermal conductivity, low density, adequate corrosion resistance, low thermal expansion, low elasticity, and high purity. In addition, carbon materials can be produced in a variety of structures, such as powders, fibres, large blocks, thin solid and porous sheets, nanotubes, fullerenes, graphite, and diamond. Furthermore, carbon materials are readily available and are generally low-cost materials. There are three common forms of carbon: diamond, graphite, and amorphous carbon. All three are important for electrochemical applications.

### 2.3.1. *Diamond Electrode*

Diamond doped with boron is conductive, and hence can serve as a highly inert and robust electrode material. Indeed, there are many reports on the study of electrochemical reactions with boron-doped diamond electrodes.[44,45] Due to their exceptional chemical inertness and mechanical strength, diamond electrodes have been proposed for applications in extremely aggressive media such as strong acids.

### 2.3.2. *Graphite Electrode*

Graphite is the thermodynamically stable form of carbon under standard conditions.[46] Graphite has a gray metallic appearance, a density of 2.26 g $cm^{-2}$, and an atomic structure composed of graphene sheets, a two-dimensional honey comb structures of carbon atoms

($sp^2$) where each atom has three nearest neighbours in 1.42 Å distance. In graphite, these sheets are stacked with a regular interlayer spacing of 3.35 Å. The structure of graphite allows electrons to move fast within graphene sheets. Graphite is widely employed as electrode material. A range of synthetic graphite materials have been developed such as carbon fibre electrodes, glassy carbon electrodes, carbon paste electrodes and highly oriented pyrolytic graphite electrodes (HOPG).

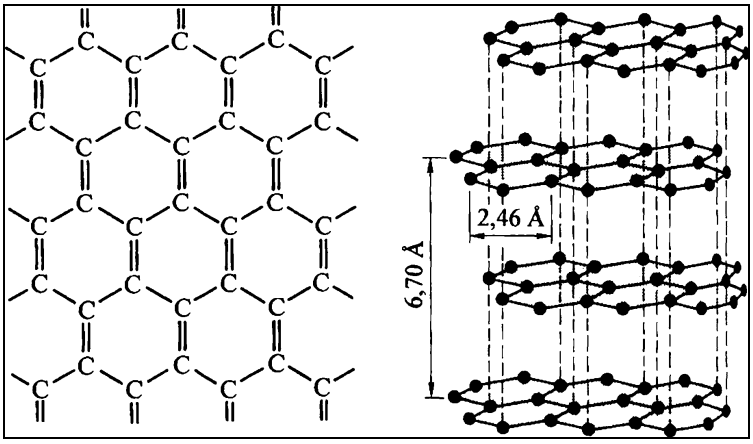


***Figure 2.14**: The structure of graphite electrode*[7]

- ***Carbon fibre electrode*:** Carbon fibre is produced by the carbonization of polyacrylonitrile at 1500 °C – 2500 °C to give highly electrically conducting fibres with 5-10 μm diameter with a carbon content >99%.Carbon fibre-based materials have found many applications due to their exceptionally high tensile strength. In electrochemistry carbon fibre used as microelectrodes are very important in analytical detection[47,48] and for in vivo electrochemical studies.[49,50]

- ***Glassy carbon electrode:*** Glassy carbon (also called vitreous carbon) is an advanced material of pure carbon combining glass-like mechanic characteristics with physical properties of graphite. Its structure comprises of interwoven ribbons of the graphite structure (Figure 2.15) with features of carbon that cannot be transformed into crystalline graphite even at temperatures of 3000°C.

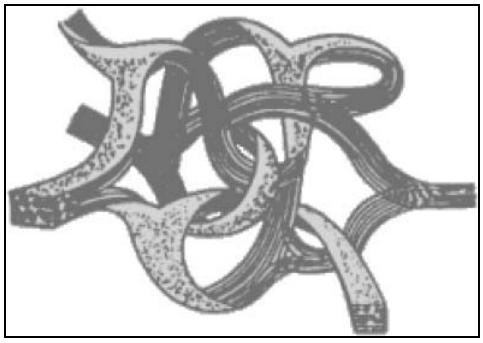

***Figure 2.15****: Interwoven ribbons of graphite structure*[51]

In addition to the above-mentioned resistance to high temperature, it is also extremely resistive to many chemicals, it is impermeable to gases and liquids, has good electric conductivity, low density, high hardness, and high strength. Only strong oxidizing agents like oxygen at elevated temperature, or hot melts, or strong oxidizing acids can attack glassy carbon. But even under such conditions it is probably the most inert carbon material. Glassy carbon can be shaped to produce many forms thus it is widely used as an electrode material in electrochemistry. Surface pre-treatment is usually employed to create active and reproducible glassy carbon electrodes and to enhance

their analytical performance.[52] Such pre-treatment is usually achieved by polishing to a shiny mirror-like appearance with successively smaller alumina particles. The electrode is then rinsed with deionised water before use. The improved electron transfer capability has been attributed to the removal of surface contaminants, exposure of fresh carbon edges, and an increase in the density of surface oxygen groups.[53]

- ***Carbon paste electrode*:** Carbon paste electrodes have been described first by Adams in 1958.[54] He has used graphite powder mixed with a mulling liquid. As such for practical considerations liquids with low volatility, purity, and economy narrowed the choice to a few liquids like bromoform, bromonaphthalene, paraffin oil, silicone grease and Nujol. The paste is housed in a Teflon holder, contacted by a platinum wire, and occasionally a piston is used to renew the surface by extrusion of the used paste. Kuwana and French were the first to modify carbon paste electrodes with electroactive compounds[55] to measure the response of water insoluble compounds in an aqueous electrolyte solution. Later this approach has been expanded to study the electrochemical behaviour of inorganic insoluble compounds that may or may not be electron conductors.[56] Carbon paste electrodes have been developed in the last decades mainly to incorporate reagents and enzymes to prepare specific electrodes for analytical applications.[57,58,59] The long-term stability of the pastes is a problem,

as well as the fact that the binder can affect the electrochemistry of solid embedded particles.

- ***Highly oriented pyrolytic graphite electrode (HOPG)***: Highly oriented pyrolytic graphite (HOPG) is commercially produced by high temperature deposition of carbon at ceramic surfaces and graphitization at 3000°C.[60] Highly oriented pyrolytic graphite is employed as edge plane pyrolytic graphite electrode (EPPGE, graphene sheets perpendicular to the electrode surface) or as basal plane pyrolytic graphite electrode (BPPGE, graphene sheet parallel to the electrode surface) (Figure 2.16). The properties of these electrodes are very different due to the different abilities of electrons to transfer from the graphene edges or perpendicular to the graphite plane.[61] EPPGE is often observed to behave electrocatalytically[62] and has been successfully employed for processes involving immobilized redox proteins.[63] In this work the edge plane pyrolytic graphite electrode is employed.

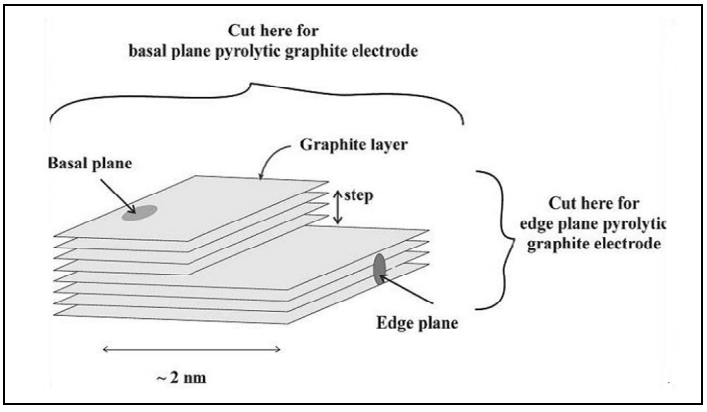


***Figure 2.16****: Schematic representation of a step edge on a HOPG surface*[51]

Between the extremes of graphite and amorphous carbon there is a wide range of carbons with properties that can be tailored, to some extent, for a specific application by controlling the manufacturing conditions and subsequent treatments (heat treatment, chemical oxidation, etc.). Because of the wide variety of carbons that are available, there is a whole range of promising electrochemical applications for these materials, such as fuel cells, batteries, industrial electrochemistry, and electroanalytical chemistry. In fuel cells, carbon (or graphite) is an acceptable material of construction for electrode substrates, electrocatalyst support, bipolar electrode separators, current collectors, and cooling plates. Carbon and graphite are used in batteries as electrodes or as additives in order to enhance the electronic conductivity of the electrodes. As electrodes, graphites and disordered carbons reversibly insert lithium, and hence they may serve as the anode material in lithium batteries. Graphitic carbons intercalate lithium in a reversible multi-stage process up to $LiC_6$ and are used as the main anode material in commercial rechargeable Li ion batteries. As additives, carbon and graphite can be found in most of the composite electrodes of batteries, such as lithium and alkaline batteries. Flow batteries are also batteries where carbon and graphite can be found, both as electrodes and as bipolar separators. For the bipolar separators, nonporous carbon or graphite is required (for example, carbon–polymer composites, dense graphite, or other nonporous carbon such as glassy carbon). Activated carbon and

graphite are used as electrodes in these batteries, where the high surface area of these electrodes is used to store the electroactive species. Highly porous carbons can serve as electrodes in super (EDL = electric double layer) capacitors. Their very wide electrochemical window allows their use in nonaqueous (relative) high energy-high power density super (EDL) capacitors. A wide range of applications of carbon materials can be seen in what is termed industrial electrochemistry. These applications include the use of carbon electrodes in reactions involving inorganic compounds (e.g. chlorine evolution, ozone generation, etc.), the synthesis of organic materials using electrochemical methods, electrochemical treatment of solutions (removal and recovery of charged and uncharged species by electroadsorption and ion exchange in the porous structure of the carbon electrodes), and carbon capacitors, where the high and specific surface area leads to an extremely high double layer capacitance. Last, but not least, is the field of electroanalytical chemistry, in which carbon electrodes can be found. This field includes voltammetry, potentiometry, coulometry, etc., for measuring the concentration and detecting the presence of specific chemical species.

## 2.4 Carbon Nanotubes: General Introduction

Carbon nanotubes are made of $sp^2$-hybridized carbon atoms arranged in graphite type sheets building-up seamless hollow tubes capped by fullerene-type hemispheres. Their length ranges from tens of nanometers to several microns. They can be divided into two classes; single-walled carbon nanotubes (SWCNTs) and multi-walled carbon nanotubes (MWCNTs). SWCNTs consist of single hollow tubes with diameter 0.4 to 2 nm. They can be metallic conductors or semiconductors. The conductivity depends on their chirality, presence of catalytic particles, ion doping, and functionalisation. MWCNTs are composed of concentric tubes. Their diameter ranges from 2 to 100 nm and they can be regarded as metallic conductors. Both classes of carbon nanotubes are already recognized as attractive electrode material.

### 2.4.1. *Historical Perspective*

The history of carbon nanotubes have generated a lot of controversy as to who is/were to be given credit for the discovery of carbon nanotubes. While some authors[64] credited Radushkevich and Lukyanovich[65], others[48] credited Wiles and Abrahamson[66] and more recently Peter Harris in his book[67] credited Iijima[68] for producing better carbon nanotubes than those that have been previously produced catalytically, and differed from them in being all-carbon structures,

closed at both ends, and not 'contaminated' with catalyst particles. The current explosion of interest in carbon nanotubes only came after the rediscovery by Iijima. The uncertainty surrounding the question of who actually discovered nanotubes probably explains why no Nobel Prizes have yet been awarded in this area.

### 2.4.2. *Structure of Carbon Nanotubes*

Carbon nanotubes appear as sheets of graphite cells that have been mended together to look almost like a latticework fence and then rolled up in a tube shape (Figure 2.18). Although this is a simple explanation for the look of the structure of carbon nanotubes, this is not how carbon nanotubes are created, nor does it explain their immense strength or other incredible structural abilities. Carbon nanotubes are typically around two millimeters in length or less but have the capability, if formed correctly, of being more than one hundred times stronger than steel.

Carbon nanotubes are capable of being formed in both single walled structures, also known as Single Walled Carbon Nanotubes (SWCNTs) (Figure 2.17a) and multiple walled structures, also known as Multi-Walled Carbon Nanotubes (MWCNTs) (Figure 2.17b). Each structure of carbon nanotubes has its own set of properties that make it appropriate for different uses across science, architecture, geology,

agriculture and engineering, among the many fields carbon nanotubes have become useful for.

Single walled carbon nanotubes have electric properties that are not present in multi-walled carbon nanotubes due to the makeup of their structure. These single walled structures can be used in large quantities for thermal purposes. Additionally, the electric properties of these macro miniature carbon nanotubes make them perfect for engineering electronics to even smaller than their current "nano" sized status. Although they do not share the same electric properties in the structure of carbon nanotubes as single walled carbon nanotubes, multi walled carbon nanotubes have their place in science and exhibit several properties that are more useful than single walled carbon nanotubes for a variety of applications. For instance, the makeup of multi-walled carbon nanotubes makes them perfect for use in the medical field. The medical field utilizes multi-walled carbon nanotubes in the production of sensors for medical diagnostics. Biosensors are able to detect microscopic amounts of biological or chemical agents, which help to diagnose an illness much quicker. Multi-walled carbon nanotubes are used for these purposes because of their electrochemically advanced properties, which are due in part to their double or multi walled structures.

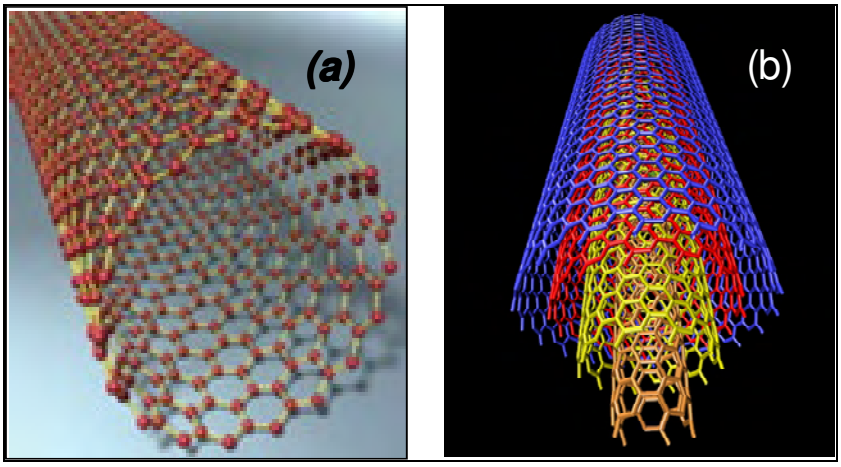


***Figure 2.17:*** *Geometric structures of (a) SWCNT and (b) MWCNT*

In addition to the two different basic structures, there are three different types of carbon nanotubes that are possible. These three types of carbon nanotubes are armchair carbon nanotubes, zigzag carbon nanotubes and chiral carbon nanotubes.

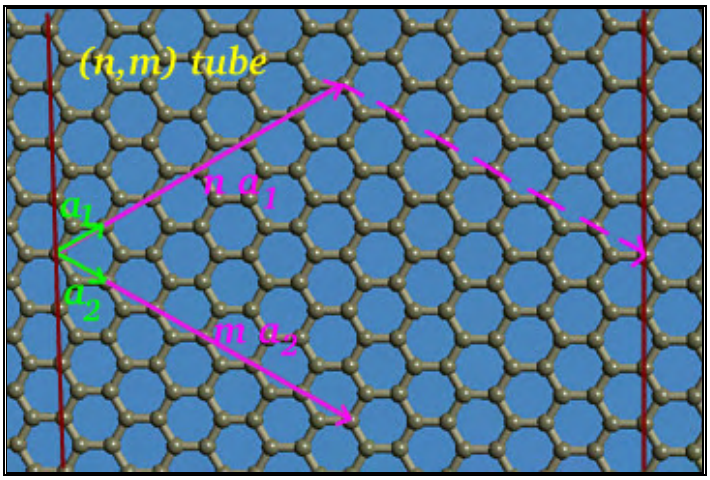


***Figure 2.18****: Unit cells of carbon nanotubes*

The difference in these types of carbon nanotubes are created depending on how the graphite is "rolled up" during its creation process. The structure is expressed in terms of one-dimensional unit

cell, defined by the vector where $a_1$ and $a_2$ are unit vectors, and n and m are integers. A nanotube constructed in this way is called an (n,m) nanotube. Rolling up the sheet along one of the symmetry axis gives either a zig-zag (m=0) tube or an armchair (n=m) tube. It is also possible to roll up the sheet in a direction that differs from a symmetry axis to obtain a chiral nanotube. Each structure of carbon nanotubes in these three varieties is different and has different implications for science.

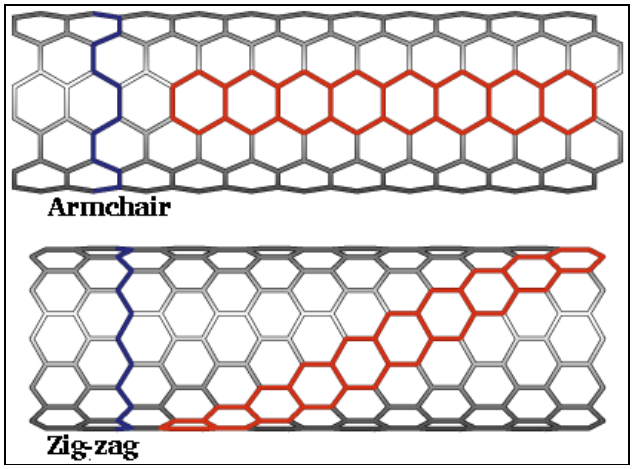


***Figure 2.19**: The types of carbon nanotubes created from how the graphene sheet is rolled*

### 2.4.3. *Synthesis of Carbon Nanotubes*

SWCNTs and MWCNTs are usually made by d.c. electric-arc discharge, high temperature heat treatment, laser vaporisation, or catalytic chemical vapour deposition.[64] The two most popular methods are the arc discharge and the chemical vapour deposition. The arc

discharge method produces carbon nanotubes of the best quality whereas the chemical vapour deposition method can produce more carbon nanotubes. These synthesis methods for carbon nanotubes introduce high concentration of impurities. The carbon-coated metal catalyst contaminates the nanotubes of the HiPco route, and both carbon-coated metal catalyst and, typically, ~60% forms of carbon other than nanotubes are formed in the carbon-arc route.[69,70] Harsh acid treatment is used to remove these impurities, which introduce other impurities, can degrade or shorten nanotube length and perfection, and adds to nanotube cost. Nevertheless, the acid treatment was used in this project to shorten the tubes and introduce the carboxyl groups.[71]

### 2.4.4. *General Applications of Carbon Nanotubes*

Potentially carbon nanotubes have varied applications in fields such as nanotechnology, electronics, optics, materials science and architecture. The superior mechanical properties of CNTs offers structural application ranging from clothes, sport gears and space elevators,[72] while from its electronic properties, nanotube based transistors have been made.[73] As paper battery,[74] produced from a thin sheet of cellulose infused with aligned carbon nanotubes. The nanotubes act as electrodes; allowing the storage devices to conduct electricity. The battery, which functions as both a lithium-ion battery

and a supercapacitor, can provide a long, steady power output comparable to a conventional battery, as well as a supercapacitor's quick burst of high energy.

Currently, the application of carbon nanotubes has been limited to the use of bulk nanotubes. Bulk CNTs have already been used as composite fibres in polymers to improve the mechanical, thermal and electrical properties of the bulk product. In solar cells,[75] ultracapacitors,[76] and nanoelectromechanical systems.[77,78] Nitrogen-doped carbon nanotubes may replace platinum catalysts used to reduce oxygen in fuel cells.[79]

## 2.5 Metallophthalocyanines: General Introduction

### 2.5.1. *Historical Perspective*

According to history, an unidentified blue compound, which we now know as metal-free phthalocyanine, was described in 1907.[80] In 1927, Swiss researchers accidentally synthesized copper phthalocyanine, copper naphthalocyanine, and copper octamethylphthalocyanine in an attempted conversion of *o*-dibromobenzene into phthalonitrile. They remarked on the enormous stability of these complexes but did not further characterize these blue complexes.[81] The same blue product was further investigated at Scottish Dyes, Ltd., Grangemouth, Scotland (later ICI) in 1928.[82] The phthalocyanines are intensely coloured and are used as dyes.[83,84,85]

### 2.5.2. *Structure of Metallophthalocyanines*

Phthalocyanine is a planar, 18 $\pi$-electron, tetradentate dianionic ligand that binds metals through four inwardly projecting nitrogen centres to form metallophthalocyanine complex (Figure 2.20). Metallophthalocyanines are structurally related to other macrocyclic pigments such as porphyrin; both consist of four pyrrole-like subunits linked to form a 16-membered ring. The pyrrole-like rings within the phthalocyanine are closely related to isoindole. Ring-substituted derivatives in the peripheral and non peripheral positions are also possible. The central atoms of MPc can carry additional ligands.

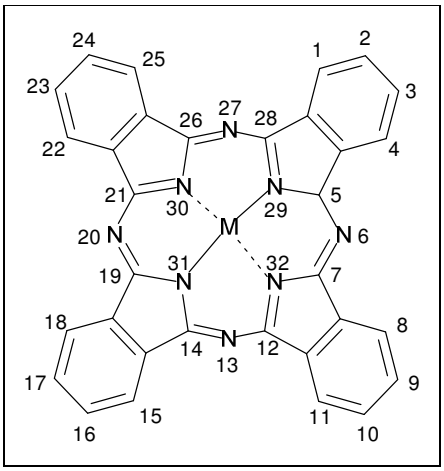


***Figure 2.20:*** *Geometric structure of metallophthalocyanine*

### 2.5.3. *Synthesis of Metallophthalocyanines*

Metallophthalocyanines can be prepared according to the following synthetic routes[86,87] as shown in Scheme 2.2. It generally involves heating a mixture of metal salt (or metal) with a desired precursor, which might be phthalonitrile or diiminoisoindole (which are referred to as the classical precursors; others include phthalic anhydride, o-cyanobenzamide and phthalimide etc), in the presence of various reagents to form the MPc. For high purity MPc, the phthalonitrile route is preferred, while for large volume the phthalic anhydride route is employed.[88] Another synthetic route which is fast and eliminates the use of solvents is the microwave irradiation[89,90]

The strong intermolecular cohesion of unsubstituted MPc makes it a non-melting insoluble solid; introduction of substituents on the phthalocyanine ring drastically changes their basic properties[91,92]

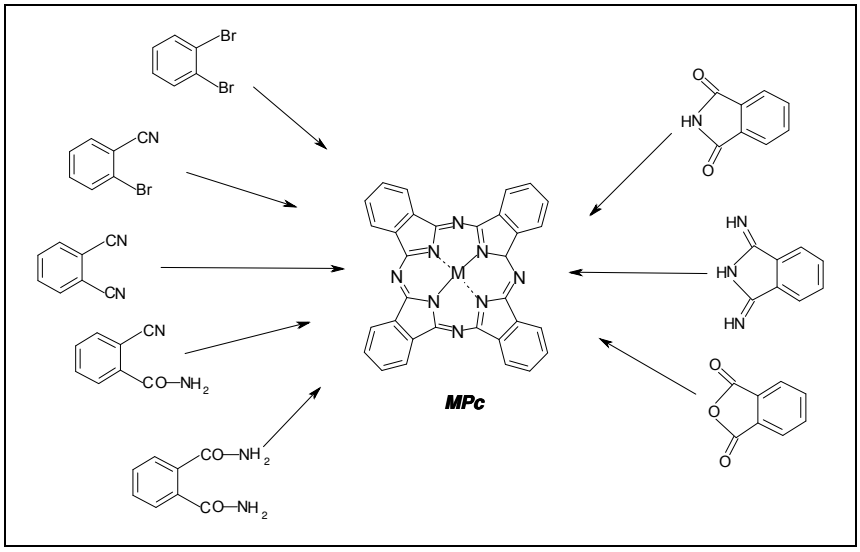


***Scheme 2.2:*** *General synthetic routes for Metallophthalocyanines*

Cyclotetramerisation of the appropriate substituted phthalonitrile derivative is used to obtain a substituted MPc. Synthetic routes for the synthesis of peripherally and non-peripherally octasubstituted MPc derivatives which are usually obtained from the disubstituted phthalonitrile and the metal salt[88,93] is shown in Scheme 2.3. This route was used in the preparation of the peripherally octasubstituted butylsulphonyl derivative (MOBSPc, where M = Co or Fe) described in this thesis. The octacarboxymetallophthalocyanine described in this thesis was obtained from its amide intermediate product, tetra-amidometallophthalocyanine (MTAPc) using pyromellitic anhydride and DBU as a catalyst[94] (Scheme 2.4).

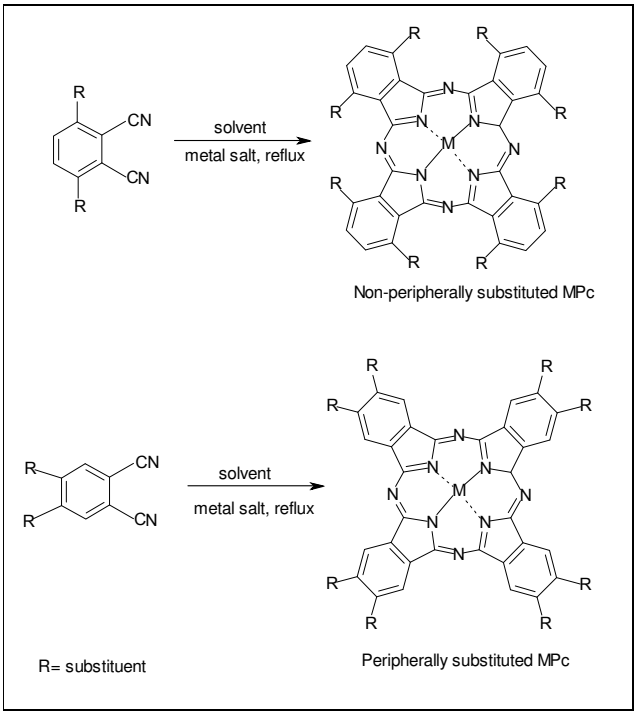


***Scheme 2.3:*** *Synthetic routes for peripherally and non-peripherally substituted MPc*

The introduction of an axial ligand onto an appropriate cation held within the central cavity of the MPc give rise to an axial-ligated MPc. This is obtained by refluxing the uncoordinated MPc in a coordinating solvent or other axial ligands (Scheme 2.5).[95,96]

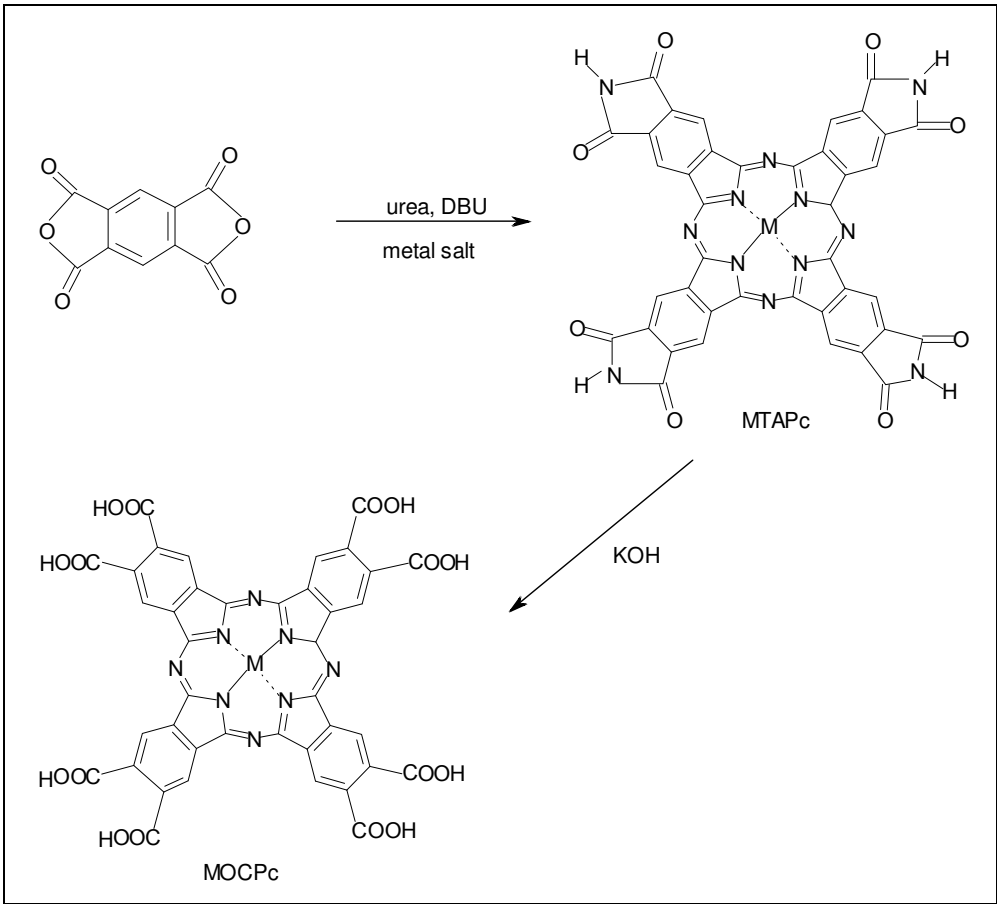


***Scheme 2.4:*** *Synthetic route for octacarboxy-metallophthalocyanine*[91]

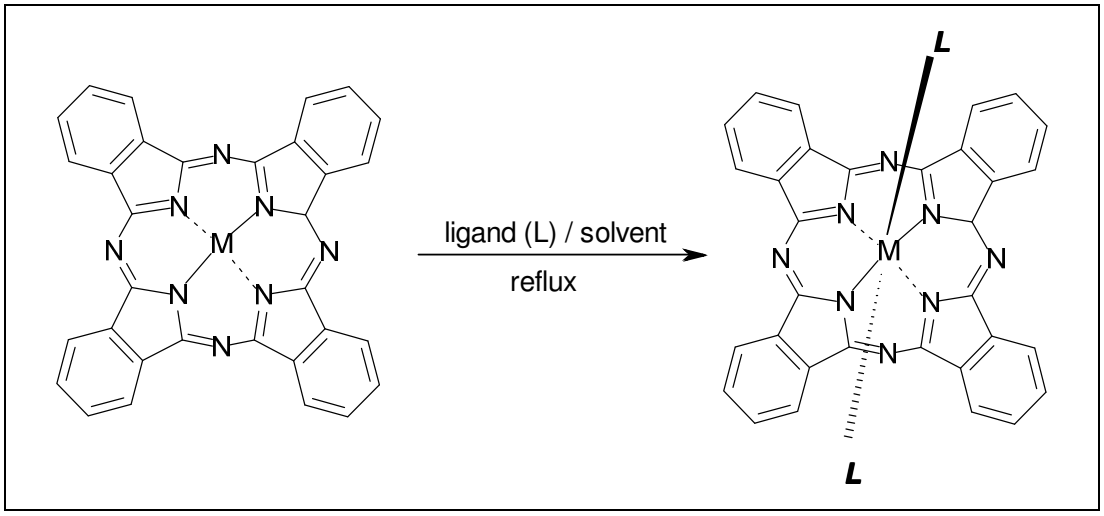


***Scheme 2.5:*** *Synthetic route for axial-ligated MPcs*[92,93]

### 2.5.4. *Electronic Absorption Spectra of Metallophthalocyanines*

The typical absorption spectra of MPc complex are shown in Figure 2.21 (A). It consist of an intense absorption peak appearing at the red end of visible region around 600 – 700 nm known as the Q band and a less intense peak at the blue end around 300 – 400 nm known as the B or Soret band. These peaks are characteristics of MPc complexes, however, MPcs can also show intense absorption peaks at the near infra-red region (700 – 1,300 nm).[97] Both bands are due to π → π* transitions within the delocalized phthalocyanine ring system[98,99,100]

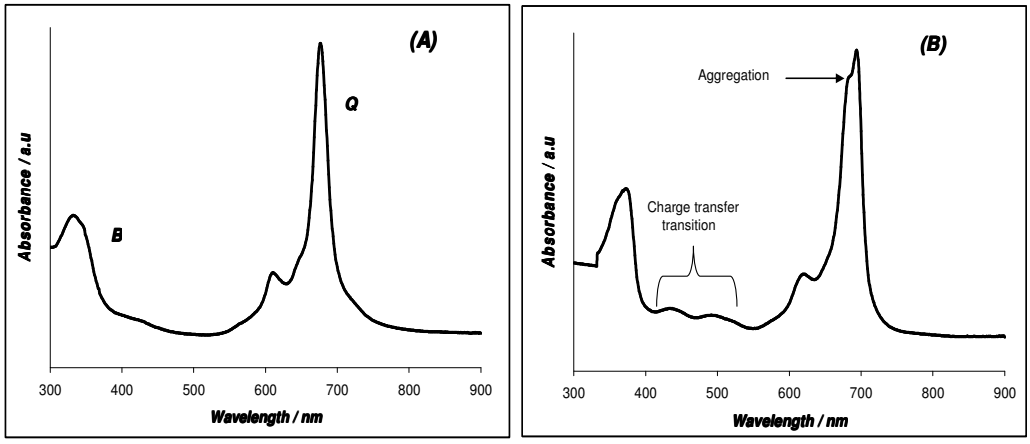


***Figure 2.21:*** *Typical electronic absorption spectra of phthalocyanine showing the B and Q bands (A) and the charge transfer transition (B)*

The Gouterman's four-orbital model[101] depicted in Scheme 2.6 describes the transitions as the transfer of electrons from the highest occupied molecular orbital (HOMO) (π) to the lowest unoccupied molecular orbital (LUMO) (π*). The B band consists of two transitions

arising from the HOMO $a_{2u}$ and $b_{2u}$ to LUMO $e_g$, while the Q band transition arises from HOMO $a_{1u}$ to LUMO $e_g$ orbital[96]

As shown in Figure 2.21(B) other absorption bands might be observed in the spectra of MPc, these bands are known as charge transfer transition (CTT). The d orbital of the transition metal may lie between the HOMO and LUMO of the phthalocyanine ligand (Scheme 2.6), consequently a possible charge transfer transition may take place either by metal to ligand (MLCT) or ligand to metal (LMCT). These bands appear as weak absorption peaks occurring at the near infra-red region or between the B and Q bands in the 300 – 400 nm regions[96,102,103] The following are known to affect the position of the absorption bands in phthalocyanines, especially the Q band: central metal, axial ligation, solvents, peripheral and non-peripheral substituents, aggregation and ring extension.[94]

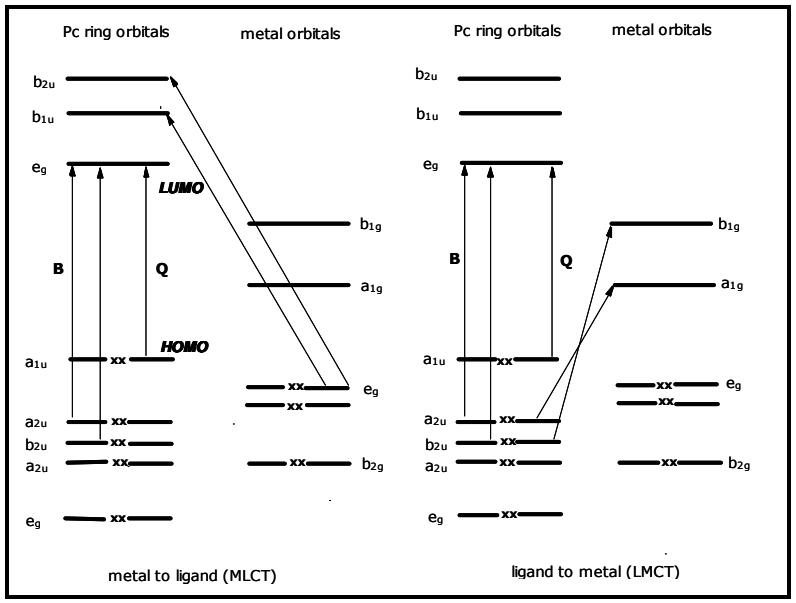


***Scheme 2.6:*** *Gouterman's four – orbital model*[97]

### 2.5.5. *Electrochemical Properties of Metallophthalocyanines*

The functions of metallophthalocyanine complexes are mostly based on their electron transfer reactions because of the π electron conjugated ring system. It is of vital importance that the electron transfer behaviour (redox process) of MPcs is interrogated in solution in order to study further application. This redox process is usually observed using electrochemical or spectro-electrochemical methods.[96,104] Neutral MPc exists as a dianion ($Pc^{-2}$),[105] which may be successively oxidised or reduced at the MPc ring, the metal centre or both.

#### 2.5.5.1. *Ring Process*

$[MPc^{-1}]^{+}$and $[MPc^{0}]^{2+}$ cation radicals are formed when the MPc dianion is oxidised by loss of one or two electrons respectively from the HOMO. As shown in Scheme 2.7, a hole is created in the $a_{1u}$ level which allows for a transition from the low-lying $e_g$ level,[97] leading to the formation of $[MPc^{-1}]^{+}$. Loss in intensity of the Q band, formation of weak bands in the 700 – 825 nm region and a broad band near 500nm characterises the presence of $[MPc^{-1}]^{+}$. $MPc^{-3}$, $MPc^{-4}$, $MPc^{-5}$ and $MPc^{-6}$ species are formed when the phthalocyanine ring is reduced by gaining successively one to four electrons at the LUMO.[102,106]

### 2.5.5.2. *Metal Process*

Redox processes may or may not take place at the central metal ion of the MPc. This redox process is due to the interaction between the phthalocyanine ring and the central metal. It is well known that the first row transition metals of various MPcs differ from those of the main group MPcs due to the fact that the metal d orbitals may be positioned between the HOMO and the LUMO of the neutral Pc ligand.[101,103,107,108] The first oxidation and first reduction processes occur at the metal centre of the MPc only for Mn, Fe and Co derivatives, depending on factors within the environment such as solvent, electrolyte, axial ligands and ring substituents. For Ni, Cu and Zn derivatives, redox processes occur only on the Pc ring. Redox process at the metal centre is characterised by a shift in the Q band without much reduction in intensity.[109]

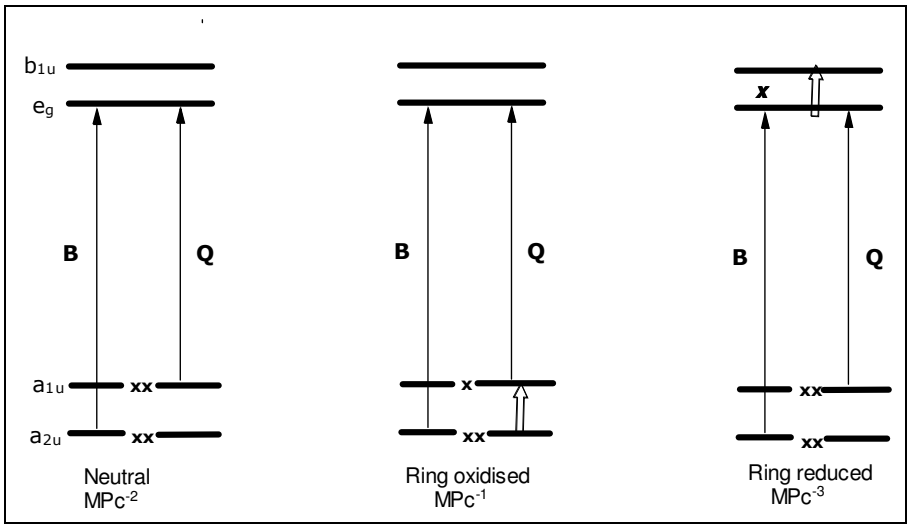


***Scheme 2.7:*** *Energy level diagram of one-electron ring oxidised and one-electron ring reduced MPc complex*[97]

The redox properties of a given MPc complex is determine by the nature of the central metal, axial ligands, solvents and the substituents on the periphery of the ring. Electron-withdrawing substituents such as sulphonyl groups, decreases the electron density of the ring and the central metal, thereby making it easier to reduce and difficult to oxidise MPc complexes, and vice versa for electron donating substituents. Furthermore, redox processes occurring at the central metal or ring results in colour changes, with ring redox processes showing more drastic colour changes. New peaks are formed on oxidation or reduction of the Pc ring because of transitions[97] (Scheme 2.7).

### 2.5.6. *General Applications of Metallophthalocyanines*

The phthalocyanines are a remarkable class of macrocyclic compounds possessing interesting physical and chemical properties, with their areas of application stemming from these properties. Due to their excellent thermal and chemical stability, beautiful bright colours, high tinctorial strength and fastness to light,[85,110] they have mainly found application as dyestuffs for jeans and other clothing, and as pigments in pens, plastics and metal surfaces. More recently, they have found applications in the printing, photocopying and electrophotography industry; thermal writing display, solar cells, fuel

cells, molecular electronics, electronic and chemical sensors, catalysis, photodynamic therapy and optical data storage devices.[85,107,111,112,113] New applications of phthalocyanine complexes are reported on a constant basis.

## 2.6 Overview of Target Analytes

### 2.6.1. *Oxygen Reduction Reaction (ORR)*

Oxygen, with the molecular formula $O_2$, sometimes referred to as dioxygen, is of fundamental importance in biological processes of energy conversion such as breathing and aerobic metabolism.

Oxygen reduction reaction as an electrochemical process has been extensively studied.[114,115,116] The reasons for such interest in this reaction are (i) its fundamental significance with respect to electrode kinetics, (ii) its role in the area of electrochemical energy conversion and corrosion.

In electrochemical energy conversion, oxygen reduction in aqueous solutions is considered to proceed via two overall reaction pathways:

The direct four electron pathway:

$$O_2 + 4H^+ + 4e^- \rightarrow 2H_2O \text{ (acidic)} \qquad 1.23 \text{ V (SHE)} \qquad (2.27)$$

$$O_2 + 2H_2O + 4e^- \rightarrow 4OH^- \text{ (alkaline)} \qquad 0.40 \text{ V (SHE)} \qquad (2.28)$$

The peroxide pathway:

$$O_2 + 2H^+ + 2e^- \rightarrow H_2O_2 \xrightarrow{(2H^+ + 2e^-)} 2H_2O \text{ (acidic)} \qquad 0.70 \text{ V (SHE)} \qquad (2.29)$$

$$O_2 + H_2O + 2e^- \xrightarrow{-OH^-} HO_2^- \xrightarrow{(H_2O + 2e^-)} 3OH^- \text{ (alkaline)} \qquad -0.07 \text{ V (SHE)} \qquad (2.30)$$

The two reaction pathways may also take place in parallel. These pathways are usually determined by the structure of the catalyst used to catalyze the reaction, the reaction conditions and the nature of the electrode upon which the catalyst is adsorbed. Electrodes that promote

the 4$e^-$ reduction of oxygen to water are Ag,[117] Pt[118] and the Pt family metals.[119] Platinum is considered to be the best and most expensive electrocatalyst for oxygen reduction, since the reduction on this electrode is known to occur with the lowest potential.[120] Electrodes that promote the 2$e^-$ reduction of oxygen to water are Au,[121] Hg[122] and various carbon materials.[123]

The mode of adsorption of molecular oxygen on the metal surface also determines the reaction pathway. Three different models for adsorption have been proposed; the Griffiths model,[124] the Pauling's model,[125] and the bridge model.[126,127]

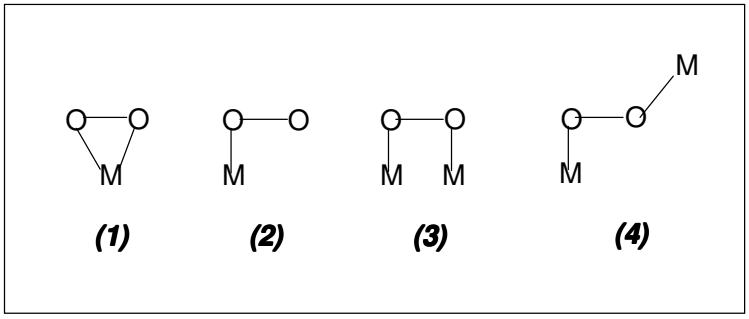


***Scheme 2.8:*** *Possible adsorption mechanism of oxygen on a metal complex*

The Griffiths model **(1)** involves a side-on interaction of oxygen with the metal. The bonding can be viewed as arising from two contributions: a $\sigma$ type bond formed by the overlap between a mainly $\pi$ orbital of oxygen and $dz^2$ (and s) orbital on the metal and a $\pi$ back bond interaction between the metal d$\pi$ orbitals and the partially occupied $\pi^*$ antibonding orbital on oxygen.

The Pauling model **(2),** an end-on interaction of oxygen with the metal forming an angle close to 120° is proposed. In this model, a σ – rich orbital of oxygen donates electron density to an acceptor orbital $dz^2$ on the metal forming a σ – type bond. A π interaction is also produced between the metal dπ (dxz, dyz) orbital's and π* on oxygen, with charge transfer from the metal to the oxygen molecule. This model favours the $2e^-$ reduction of oxygen to peroxide. The principal difference between the Griffiths and Pauling model is the steric factors and the nature of the σ bond formed. They both exhibit strong σ donation of an electron pair from oxygen but with different donor orbital's being considered.

The Bridge model **(3)** was proposed by Yeager[123,124] and is likely to occur on noble metals such as Pt where oxygen is reduced to water with little or no peroxide formed. This type of interaction promotes the rupture of the O-O bond, favouring the direct $4e^-$ reduction of oxygen to water. The Griffith type of interaction could also lead to the rupture of O-O bond. The bridge model can also occur as a *trans* form **(4)**.

The ORR is a multi-electron reaction that may include a number of elementary steps involving different reaction intermediates. Of the various reaction schemes proposed, the simplified version of the scheme given by Wroblowa and co-workers [128](Scheme 2.9) appears to be the most effective one to describe the complicated reaction pathway by which oxygen is reduced at metal surfaces:

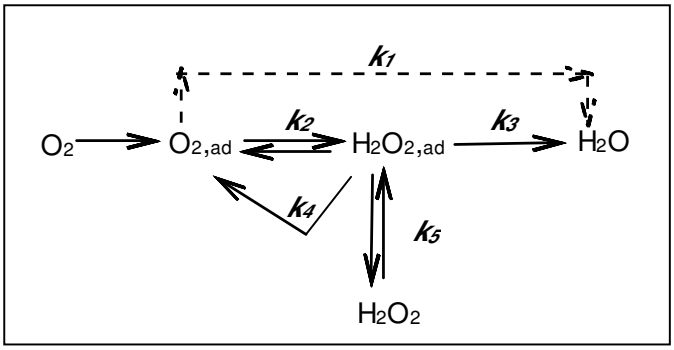


***Scheme 2.9**: Series-parallel reaction scheme for oxygen reduction*[125]

On the basis of this reaction scheme, oxygen can be electrochemically reduced either directly to water with the rate constant $k_1$ (direct 4*e*- reduction) or to $H_2O_{2ad}$ with rate constant $k_2$ (peroxide pathway). The adsorbed peroxide can be electrochemically reduced to water with the rate constant $k_3$, catalytically/chemically decomposed on the electrode surface $k_4$, or decomposed into the bulk of the solution $k_5$.

The main problem in the development of an efficient electrochemical energy conversion device (fuel cell) is in the sluggish ORR kinetics even on the most catalytically active electrode material. Transition metal MPc complexes, notably the iron-centred (FePc) and cobalt-centred (CoPc) phthalocyanine complexes have been intensively reported as possible alternative electrocatalysts for the ORR. FePc complexes are preferred to their CoPc counterparts as their ORR activities occur at low potentials, following the direct 4-electron process that result to water as the main reduction product.[129,130] Several reports have shown that MPc complexes integrated or supported on

carbon nanotubes (CNTs) greatly enhance the electrocatalytic performance of the electrode.[131] However, the use of such MPc for ORR is limited. There are other reports involving metalloporphyrins (MPs) and CNTs.[132,133] It is well established that MPc and MPs are structurally different and, expectedly, exhibit contrasting physico-chemical properties. In this study the impact of co-immobilising MPc complexes with acid functionalized MWCNT for ORR activity is explored.

### 2.6.2. *Formic Acid Oxidation*

Research into formic acid (FA) has received great attention and has been considered as a replacement candidate for methanol as fuel in fuel cells. This is due to its high electrochemical activity arising from its non-toxicity, non-flammability and its ability to facilitate the transport of proton within the anode catalyst.[134,135] Because of its advantages over methanol, a direct formic acid fuel cell (DFAFC) is being gradually recognised as a promising power source.[136]

Platinum is one of the most frequently used catalyst for formic acid oxidation,[137,138] however, previous studies have shown that practical applicability is inadequate because the electro-oxidation process on a platinum catalyst surface could occur through two parallel pathways, the "direct pathway" and the "CO pathway"[139,140]. In the "direct pathway" which is preferred, the formic acid is oxidized directly to $CO_2$:

$$HCOOH + Pt \longrightarrow X \longrightarrow CO_2 + 2H^+ + 2e^- \quad (2.31)$$

where X is an active intermediate with relatively short lifetimes[136]. However, the formic acid is oxidized slowly in the "CO pathway", because a poisoning intermediate $CO_{ad}$ will be formed before the end product $CO_2$ is yielded.

$$HCOOH + Pt \longrightarrow Pt\text{-}CO + H_2O \quad (2.32)$$

$$Pt + H_2O \longrightarrow Pt\text{-}OH + H^+ + e^- \quad (2.33)$$

$$Pt\text{-}CO + Pt\text{-}OH \longrightarrow 2Pt + CO_2 + H^+ + e^- \quad (2.34)$$

$$\text{Overall: } HCOOH \longrightarrow CO_2 + 2H^+ + 2e^- \quad (2.35)$$

The $CO_{ad}$ intermediate formed in the CO pathway can be strongly adsorbed on the surface of the Pt, thereby poisoning the catalyst, hence not desirable. Unfortunately, various studies indicate that the electro-oxidation on common Pt catalysts occurs mainly through the CO pathway[141,142] In order to lead the reaction to the desired "direct pathway", the Pt-based bimetallic catalysts (Pt-M), such as PtSn[134,143,144] PtGe,[134,135,136] PtPb,[134] PtAs,[134] PtBi,[133] and PtRu[145] were redesigned and tested. It was found that bimetallic catalyst performed much better than pure Pt catalyst.[135,136,146]

On the other hand, the use of Pt catalyst integrated with metal macrocyclic compounds (such as MPc) for the oxidation of formic acid is virtually unknown. The only closest work in this area is the work by Zhou *et al.*[147] who carried out the electro-oxidation of formic acid using a bulk Pt disc electrode modified with water-soluble iron(II)

tetrasulphophthalocyanine (FeTSPc) complex. The obvious disadvantages of such system include (i) the high cost of Pt bulk metal support and (ii) the high probability of the immobilised FeTSPc to be easily washed off from the electrode during operation due to its high solubility in aqueous solution. Therefore, it is important to explore low content Pt systems that contain FePc complexes that are not water soluble (hydrophobic system) and supported on a low-cost carbon electrode substrate. In this work, it is shown that hydrophobic PtFeOCPc can serve as potential electrocatalyst for the oxidation of formic acid in acidic medium.

### 2.6.3. *Thiocyanate Oxidation*

Thiocyanate ($SCN^-$) is considered less toxic than cyanide hence is found in many industrial and biological applications, for instance its concentration in mining effluent is not regulated at the present time.[148] However, thiocyanate is known to decompose and form cyanide when exposed to ultraviolet radiation, it is then possible that sunlight may liberate cyanide to levels toxic to aquatic life from effluent rich in thiocyanate and has been known to block the iodine uptake by thyroid gland .In view of this consideration, it is not unlikely that in the future some limit may be imposed on the concentration of thiocyanate in effluents. The presence of thiocyanate in body fluids as a detoxification product of hydrogen cyanide (HCN),[149] has been used to monitor

hydrogen cyanide from tobacco smoke, fire atmospheres, and some vegetables that contain cyanogenic glucosides.[150] Electrodes modified with MPcs have been reported as efficient potential electrochemical sensors for the determination of thiocyanate. Electrochemical detection of thiocyanate with MPc based sensors is best performed in acidic conditions (between pH 4 and 5)[151] and the oxidation of $SCN^-$ catalysed by horseradish peroxidase, an FePc-like molecule, occurs optimally at pH 4.0, hence this study was carried out in pH 5 phosphate buffer conditions.[152,153]

### 2.6.4. *Nitrite Oxidation*

Nitrite ($NO_2^-$), has been known for centuries and is still been used as a preservative[154] due to its anti-microbial activity. It is a color-enhancing agent to cured meat products and also provides indirect beneficial effect on flavour.[155] When ingested it react with haemoglobin, leading to reduction in the blood oxygen-carrying capacity, and with amines converting them into nitrosamines, which are well known carcinogenic substances. The build – up of nitrite concentrations in the environment, owing to their use in agricultural processes (as fertilizers), resulting in contamination of water sources for human consumption, has been of major concern.[156] Hence, it is almost impossible not to encounter nitrite ions or the products of their use in our everyday domestic activities. Various researchers have

suggested strategies to facilitate the detection, determination and monitoring of nitrite.[145,157] Intensive studies have been carried out in the electrocatalytic behaviour and detection of nitrite using MPc complexes.[158,159] The electrochemical detection of nitrite is best performed in neutral pH phosphate buffer solution,(pH 7.4), this is because nitrite exist as nitrite ion ($NO_2^-$) in neutral phosphate buffer solution but disproportionate to produce neutral nitric oxide (NO) in slightly acidic conditions,[160] hence this study was carried out in phosphate buffer pH 7.4.

## 2.7 Microscopic and Spectroscopic Techniques

Wealth of macroscopic information can be obtained about the processes occurring at the electrode-solution interface with the electrochemical methods so far discussed, however, to obtain microscopic information about the structure of an electrode surface requires the use of microscopic methods since the surface of a solid in contact with a liquid phase usually differs substantially from the interior of the solid both in chemical composition and physical properties. Some of the microscope and spectroscopic methods used in this work to characterise an electrode surface are scanning probe microscopy (SPM), which consist of the scanning tunnelling microscope (STM) and atomic force microscope (AFM). For the purpose of this study the AFM technique was employed. Others are scanning electron microscope (SEM), transmission electron microscope (TEM), energy dispersive spectroscopy (EDS), and X-ray diffraction (XRD).

### 2.7.1. *Atomic Force Microscopy (AFM)*

Atomic force microscopy is one of the two techniques of scanning probe microscopy used for imaging of sample surfaces. The AFM was invented in 1986[161], and relies on raster scanning to probe sample properties at or near the surface (typically several nanometers deep) and immediately above the surface (typically up to several tens of nanometers high). Raster scanning is performed with actuators whose

motion can be incremented in small steps and with high precision. These actuators are usually made of piezoelectric materials shaped into the form of a hollow tube, or they are made of a mechanical flexures or a hybrid of both. Raster scanning makes it possible to record the probe-sample interaction point-by-point. For each x, y coordinate pair, the interaction is recorded as one data point. The collection of these data points is then synthesised into the SPM image, a 3-D map. The most common images are the topography images (Figure 2.22). The AFM imaging is made possible when a flexible force-sensing cantilever with a sharp tip at the end is scanned in a raster pattern over the surface of the sample. During a scan, the force on the tip is held constant by the up and down motion of the tip, which then provides the topographic information. Two modes are operational with AFM; the contact mode and the tapping mode.

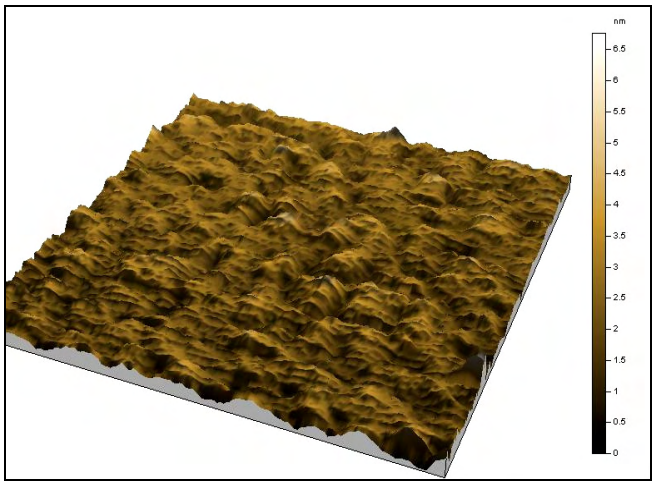


***Figure 2.22:*** *AFM 3-D topographical image of iron(II) pthalocyanine on glassy carbon plate*

### 2.7.2. *Scanning Electron Microscopy (SEM)*

The scanning electron microscope (SEM) produces high resolution images of a sample surface in high vacuum.[162] The samples must be clean, dry, and electrically conductive. Scanning of the sample surface is achieved with a beam of energetic electrons in a raster pattern focused to a spot with a diameter in the range of some nanometer. When the electrons penetrate the sample, they interact with the atoms up to a depth of some micrometer releasing several signals such as backscattered electrons, Auger electrons, elastically scattered electrons, characteristic and bremsstrahlung X-rays, and secondary electrons from the surface. The backscattered and secondary electrons which serve as the basis of SEM originate within a few nm from the surface due to their low energy and are detected by photomultipliers to form a two-dimensional image of the surface with a lateral resolution down to 1 nm. The brightness of the signal depends on the number of secondary electrons. Morphological and topographical information is extracted that is necessary in understanding the behavior of surfaces; hence SEM examination is the first step in the study of surface properties of solids.

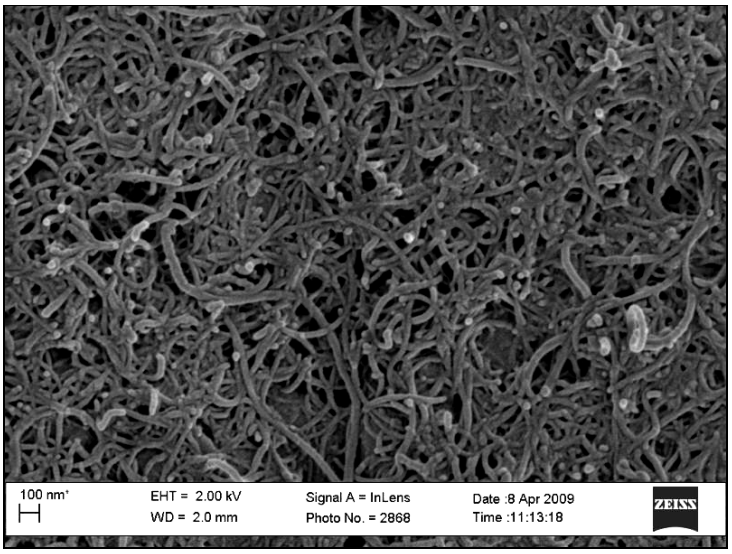


***Figure 2.23:*** *High resolution SEM image of multi-walled carbon nanotubes*

### 2.7.3. *Transmission Electron Microscopy (TEM)*

The transmission electron microscope was first built by Max Knoll and Ernst Ruska in 1931 and was commercially available in 1936 with the microscope having a resolving power greater than that of light. Transmission electron microscopy is a microscopy technique that uses beam of energetic electrons generated by thermionic emission from a filament. The electrons interact with the ultra thin sample as it passes through. An image is formed from this interaction; magnified and focused onto an imaging device.[163] A TEM is composed of several components, which include a vacuum system in which the electrons travel, an electron emission source for generation of the electron stream, a series of electromagnetic lenses, as well as electrostatic plates. Also required is a device to allow the insertion into, motion within, and removal of specimens from the beam path. Imaging

devices are subsequently used to create an image from the electrons that exit the system. TEMs are capable of imaging at a significantly higher resolution due to the small *de Broglie* wavelength of electrons. This allows for examination of single columns of atoms which are in the region of nanometers, hence it has found application in nanoscience and nanotechnology research.[164]

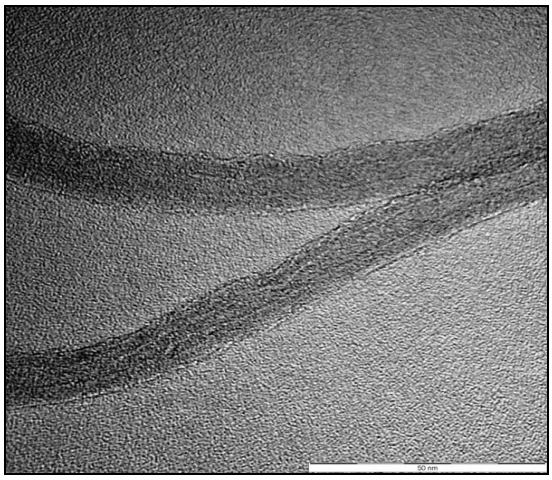

***Figure 2.24:*** *TEM image of multi-walled carbon nanotubes*

### 2.7.4. *Energy Dispersive X- Ray Spectroscopy (EDS)*

EDS is an analytical capability that can be coupled with applications such as SEM and TEM. When beam of electrons interact with a sample surface, variety of emissions including X-rays are produced[165]. An energy-dispersive (EDS) detector is used to separate the characteristic x-rays of different elements into an energy spectrum, and EDS system software is used to analyze the energy spectrum in order to determine the abundance of specific elements. EDS can be used to find the

chemical composition of materials down to a spot size of a few microns, and to create element composition maps over a much broader raster area.

EDS systems include a sensitive x-ray detector, a liquid nitrogen dewar for cooling, and software to collect and analyze energy spectra. The detector is mounted in the sample chamber of the main instrument at the end of a long arm, which is itself cooled by liquid nitrogen. The most common detectors are made of Si (Li) crystals that operate at low voltages to improve sensitivity. The detector contains a crystal that absorbs the energy of incoming x-rays by ionization, yielding free electrons in the crystal that become conductive and produce an electrical charge bias. The x-ray absorption thus converts the energy of individual x-rays into electrical voltages of proportional size; the electrical pulses correspond to the characteristic x-rays of the element. A typical EDS spectrum is portrayed as a plot of x-ray counts vs. energy (in keV). Energy peaks correspond to the various elements in the sample. Generally they are narrow and readily resolved, but many elements yield multiple peaks. For example, iron commonly shows strong $K_{\alpha}$ and $K_{\beta}$ peaks. Elements in low abundance will generate x-ray peaks that may not be resolvable from the background radiation.

### 2.7.5. *X-Ray Diffraction (XRD)*

X-ray diffraction is a unique method for studying the phase composition and atomic structure of crystalline materials. The method is based on the X-ray (neutron or electron) reflection from the atomic planes. The reflection angle $\theta$ depends on the X-ray wave length $\lambda$ and the distance d between the atomic planes (Bragg's Law):

$2d \sin \theta = n\lambda$ ($n$ = integer) (2.36)

The positions (angles) and intensities of the reflections in the diffraction patterns are fingerprint for each compound and can be transformed into the atomic arrangement.

The samples for the crystal structure determinations are usually single crystals, but more complex modern methods allow such an analysis for powder materials. The X-ray powder diffraction patterns are widely used to identify the type of material in any mixture by comparing them with the standard patterns of the International Powder Diffraction File (PDF) database.[166]

## References

1. A.J Bard, L.R Faulkner, *Electrochemical Methods*, 2nd edition, Wiley, New York, (2001)

2. W. Schmickler, *Interfacial Electrochemistry*, Oxford University Press, Inc, New York (1996)

3. J.O'M Bockris, S.U.M Khan, *Surface Electrochemistry*, Plenum, New York, (1993)

4. H Bach, F Baucke, D Krause, *Electrochemistry of Glasses and Glass Melts, Including Glass Electrodes*, Schott Series, Springer, Berlin (2000)

5. T Osaka, M Datta, *Energy Storage for Electronics*, Gordon and Breach Science Publ. (2000)

6. P.M.S. Monk, *Fundamentals of Electroanalytical Chemistry*, John Wiley and Sons Ltd, Chichester, New York (2001)

7. A.J. Bard, G. Inzelt, F. Scholz (Eds), *Electrochemical Dictionary*, Springer, Berlin (2008)

8. J. Wang, Analytical *Electrochemistry*, VCH Publishers Inc. New York (1994)

9. D.B. Hibbert, *Introduction to Electrochemistry*, Macmillan, London (1993)

10. C. Kittel, *Thermal Physics*, 3rd edition, Wiley, New York (1969)

11. G. Inzelt, *Kinetics of Electrochemical Reactions*. In: F. Scholz (ed) *Electroanalytical Methods,* Springer, Berlin (2000)

12. K.B Oldham, J.C Myland, *Fundamentals of Electrochemical Science*, Academic Press, San Diego,(1994)

13. H.A Laitinen, I.M Kolthoff, *J Phys Chem* **45** (1941), 1061

14. H.A Laitinen, I.M Kolthoff, *J Phys Chem* **45** (1941), 1079

15. R.S Nicholson, I Shain, *Anal Chem* **6** (1964), 3706

16. F. Marken, A. Neudeck, A.M Bond, *Cyclic Voltammetry* In: F Scholz (ed) *Electroanalytical Methods*, Springer, Berlin, (2000)

17. D.K Gosser, *Cyclic Voltammetry: Simulation and Analysis of Reaction Mechanisms*, VCH, New York, (1993)

18. J. E. B. Randles, *Trans. Faraday Soc*. **44** (1948) 327

19. R. S. Nicholson, I. Shain, *Anal. Chem*. **36** (1964) 1351

20. A. Sevcik, *Coll. Czech*. *Chem. Comm*. **13** (1958) 349

21. J.A. Harrison, Z.A. Khan, *J. Electroanal. Chem*. **28** (1970) 131

22. J. Wang, *Analytical Electrochemistry*, 3rd ed, Wiley-VCH John Wiley & Sons Publishers Inc., Hoboken, New Jersey (2006).

23. E. R. Brown, R. F. Large, *in Physical Methods of Chemistry, Vol.1-Part IIA:Electrochemical Methods*, eds. A. Weissberger and B. Rossiter, Willey-Interscience, New York (1971).

24. R.G. Compton, C. E. Banks, *Understanding Voltammetry*, World Scientific Publishing Co. Pte. Ltd (2007).

25. J. Ni, H. Ju, H. Chen, D. Leech, *Anal. Chim. Acta* **378** (1999) 151

26. R. D. Rocklin, R. W. Murray, *J. Phys. Chem.* **85** (1981) 2104

27. C.M.A. Brett, A.M.O. Brett, *Step and Pulse Techniques* in A.J. Bard, M. Stratmann, P.R. Unwin (Eds), *Encyclopedia on Electrochemistry*, vol 3, Wiley-VCH, Weinheim, Germany (2008)

28. J. A. Turner, J. H. Christie, M. Vukovic, R. A. Osteryoung, *Anal. Chem*. **49** (1977) 1904

29. G. C. Barker, A. W. Gardner, *J. Electroanal. Chem*. **100** (1979) 641

30. P. H. Rieger, *Electrochemistry*, Prentice Hall, Oxford (1987)

31. A. J. Bard (ed) *Electroanalytical Chemistry*, Marcel Dekker, New York 13 (1994)

32. F.G. Banica, A. Ion, *Electrocatalysis-based Kinetic Determination*. In: R.A Meyers (ed) *Encyclopaedia of Analytical Chemistry*. Wiley, Chichester, 11115, (2000)

33. J.H. Zagal, S. Griveau, J.F. Silva, T. Nyokong, F. Bedioui, *Coord. Chem. Rev.,* (2010) in press

34. T. Mugadza, T. Nyokong, *Electrochim. Acta*, **55** (2010) 2606

35. W. Lu, N. Li, W. Chen, Y. Yao, *Carbon*, **47** (2009) 3337

36. H-s. Yin, Y-l. Zhou, S-y. Ai, *J. Electroanal. Chem*. **626** (2009) 80

37. J. Oni, T. Nyokong, *Anal. Chim. Acta*, **432** (2001) 9

38. J. H. Zagal, *Coord. Chem. Rev.,* **119** (1992) 89

39. S.Krause, *Impedance Method* In: A.J. Bard, M. Stratmann, P.R. Unwin (eds), *Encyclopaedia on Electrochemistry*, vol 3, Wiley-VCH, Weinheim, Germany (2008)

40. M.E. Orazem, B. Tribollet, *Electrochemical Impedance Spectroscopy,* John Wiley & Sons Inc, Hoboken, NJ, (2008)

41. C. M. Brett, A. M. O. Brett, *Electrochemistry: Principle, Methods and Applications*, Oxford University Press, New York, USA (1993).

42. R.A. Durst, A.J. Baumner, R.W. Murray, R.P. Buck, C.P. Andrieux, *Pure & Appl. Chem.*, **69** (1997), 1317

43. D.L. Allara, *Biosens. Bioelectronics* **10** (1995), 771

44. E.R. Sartori, R.A. Medeiros, R.C.Rocha-Filho, O. Fatibello-Filho, *Talanta* **81** (2010) 1418

45. S.C.B. Oliviera, A.M.Oliviera-Brett*, Electrochim. Acta* **55** (2010) 4599

46. A.F Holleman, N Wiberg, *Inorganic Chemistry*, Academic Press, London, (1995)

47. H. Kuramitz, M. Matsushita, S. Tanaka, *J. Watres*., **38** (2004) 2331

48. G. Munteanu, S. Munteanu, D.O. Wipf, *J. Electroanal. Chem*., **632** (2009) 177

49. M-F. Suaud-Chagny, *Methods* **33** (2004), 322

50. L. Xiang-Qin, K. Guang-Feng, C. Ying, *Chin J Anal Chem*, **36** (2008) 157

51. C.E. Banks, R.G. Compton, *Analyst*, **131** (2006), 15

52. R.C. Engstrom, *Anal.Chem*. **56** (1984)

53. R.L. McCreery, *Carbon electrodes: Structural effects on electron transfer kinetics,* in A.J. Bard, (ed), *Electroanalytical Chemistry* , vol. 18, Marcel Dekker, New York, (1991)

54. R.N Adams, *Anal Chem* **30**, (1958), 1576

55 . T. Kuwana, W.G. French, *Anal Chem* **36**, (1964), 241

56. F Scholz, B Meyer, *Voltammetry of Solid Microparticles Immobilized on Electrode Surfaces*. In: A.J. Bard, I Rubinstein (eds) *Electroanalytical Chemistry*, vol. 20. Marcel Dekker, New York, (1998)

57. I. Švancara, K. Vytřas, J. Barek, J. Zima, *Crit Rev Anal Chem* **31** (2001), 311

58 . L. Gorton *Electroanalysis* **7** (1995),23

59. K. Kalcher, J.M. Kauffmann, J. Wang, I. Švancara, K. Vytřas, C. Neuhold, Z. Yang *Electroanalysis* **7** (1995), 5

60. H.O Pierson, *Handbook of carbon, graphite, diamond and fullerenes,* Noyes Publications, New Jersey, (1993)

61. R.L. McCreery, Carbon electrodes: Structural effects on electron transfer kinetics, in A.J. Bard, (ed), *Electroanalytical Chemistry* , vol. 17, Marcel Dekker, New York, (1991)

62. C.E. Banks, R.G. Compton, *Anal Sci* **21** (2005),1263

63. L.S. Conrad, H.A.O. Hill, N.I. Hunt, J. Ulstrup, *J. Electroanal. Chem*. **364** (1994), 17

64. M. Monthioux, V.L. Kuznetsov, *Carbon* **44** (2006) 1621

65. L.V Radushkevich, V.M Lukyanovich, *Zurn Fisic Chim*, **26** (1958) 88

66. P.G. Wiles, J. Abrahamson *Carbon* **6** (1978) 341

67. P.J.F. Harris, *Carbon Nanotube Science*, Cambridge University Press, New York, (2009)

68. S. Iijima, *Nature* **354** (1991) 56

69. S. H. Lai, Y. L. Chen, L. H. Chan, Y. M. Pan, X. W. Liu, H. C. Shih, *Thin Solid Films* **444** (2003) 38

70. S. G. Louie, *Top. Appl. Phys*. **80** (2001) 113

71. J. Liu, A. G. Rinzler, H. Dai, J.H. Hanfer, R.K. Bradley, P.J. Boul, A. Lu, T. Iverson, K. Shelimov, C.B. Huffman, F. R. Macias, Y. S. Shon, T.R. Lee, D.T. Colbert, *Science* **280** (1998) 1253

72. B.C. Edwards, *The Space Elevator*. BC Edwards, ISBN 0974651710, (2003)

73. H.W.C. Postma, T. Teepen, Z. Yao, M. Grifoni, C. Dekker, *Science* **293** (2001) 76

74. "Beyond Batteries: Storing Power in a Sheet of Paper Eurekalert.org. August 13, 2007. http://www.eurekalert.org

75. "New Flexible Plastic Solar Panels Are Inexpensive And Easy To Make". ScienceDaily, July 19, 2007.http://www.sciencedaily.com

76. MIT LEES on Batteries, MIT press release, 2006

77. T. Simmons, D. Hashim, R. Vajtai, P.M. Ajayan, *J. Am. Chem. Soc.* **129** (2007) 10088

78. "Hot nanotube sheets produce music on demand", *New Scientists News*, 31 October 2008

79. Chemical & Engineering News, 9 February 2009, "Nanotube Catalysts", p. 7

80. A. Braun, J. Tcherniac, *Berichte der Deutschen Chemischen Gesellschaft,* **40** (1907), 2709.

81. H. de Diesbach, E. von der Weid, *Helevtica Chimica Acta*, **10** (1927), 886

82. J. M. Robertson, *J. Chem. Soc.* (1936) 1195

83. C. C. Leznoff, A.B.P. Lever (eds), *The Phthalocyanines*, vols 1-4, Wiley, (1986-1993)

84. N. B. McKeown, *Phthalocyanine Materials - Synthesis, Structure and Function*, Cambridge University Press, New York, (1998)

85. K. Kadish, K. M. Smith, R. Guilard (eds), *The Porphyrin Handbook*, Vols. 15-20, Academic Press, (2003)

86. C.C. Leznoff, in *Phthalocyanine: Properties and Applications*, C.C. Leznoff, A.B.P. Lever (eds), Vol 1, VCH Publishers, New York, (1989)

87. R.B. Linstead, A.R. Lowe, *J. Chem. Soc*., (1934), 1022

88. P. Gregory, *J. Porphyrins Phthalocyanines*, **3** (1999), 468

89. D.M. Maree, T. Nyokong, *J. Chem. Res*. (S), (2001), 68

90. E. Ç. Kaya, H. Karadeniz, H. Kantekin, *Dyes and Pigments* **85** (2010), 177

91. D. Wohrle, V. Schmidt, *J. Chem. Soc. Dalton Trans*. (1988), 549

92. D. Schlettwein, N.R. Armstrong, *J. Phys. Chem.*, **98** (1994), 11771

93. M. Hanack, P.Haisch,, H. Lehman, *Synthesis*, (1993), 387

94. K. Sakamoto, E. Ohno, *Prog. Org. Coating*, **31** (1997), 139

95. J. Metz, M. Hanack, *J. Am. Chem. Soc.,* **105** (1983), 829

96. T. Nyokong, *J. Chem. Soc., Dalton Trans*., (1993), 3601

97. T. Nyokong, *Electronic Spectra, and Electrochemical Behaviour of Near Infra-red Absorbing Metallophthalocyanines*. In: J. Jiang (ed), *Functional Phthalocyanine Molecular Materials*, vol 135, (2010)

98. L. Boucher, *Coordination Chemistry of Macrocyclic Compounds*, G.A. Melson (ed) Plenum Press, (1979)

99. T. Nyokong, M.J. Stillman, In: C. C. Leznoff, A.B.P. Lever (eds), *Phthalocyanines: Properties and Applications,* VCH Publishers, New York, Vol 1, (1989)

100. A.B.P. Lever, *Adv. Inorg. Radiochem*., **7** (1965), 28

101. M. Gouterman, In: D. Dolphin (ed), *The Porphyrins, Vol III, Part A, Physical Chemistry,* Academic Press, New York, (1978)

102. A.B.P. Lever, S.R. Pickens, P.C. Minor, L. Licoccia, B.S. Ramaswamy, K. Magnell, *J. Am. Chem. Soc*., **103** (1981), 6800

103. R. Taube, *Pure Appl. Chem*., **38** (1974), 427

104. A. Luoati, M.E.I. Meray, J.J. Andre, J.Simon, K.M. Kadish, M. Gross, A. Giraurdeau, *Inorg. Chem*., **24** (1985), 1175

105. J.F. Meyers, R.G.W. Canham, A.B.P. Lever, *Inorg. Chem*., **14** (1975), 461

106. A.B.P. Lever, E.R. Milaeva, G. Spier, In: A.B.P. Lever, C.C. Leznoff (eds) *Phthalocyanines: Properties and Applications*, VCH Publishers, New York, vol 3, (1993)

107. R.O. Loufty, C. Chang, *J. Chem. Phys*., **73** (1980), 2902

108. A.B.P. Lever, J.P. Wilshire, *Can. J. Chem*., **54** (1976), 2514

109. T. Nyokong, Z. Gasyna, M. Stillman, *ACS, Symp. Ser*., **321** (1986), 309

110. N.B. Mckeown, *Chem. Ind*., (1999), 92

111. P. Gregory, *High Technology Applications of Organic Colorants*, Plenum Press, New York (1991)

112. K. Morishige, S. Tomoyasu, G. Iwano, *Langmuir*, **13** (1997), 5184

113. J.E. Kuder, *J. Imaging Sci*., **32** (1988), 51

114. B. Wang, *J. Power Sources*, **152** (2005), 1

115. J-S. Zheng, X-Z. Wang, J-L. Qiao, D-J. Yang, B. Li, P. Li, H. lv, J-X. Ma, *Electrochem. Commun.* **12** (2010), 27

116. J. Zeng, S. Liao, J. Y. Lee, Z. Liang, *Int. J. Hydrogen Energy* **35** (2010), 942

117. J. J. McMahon, M. Barry, K. J. Breen, A. K. Radziwon, L. D. Brooks, M. R Blair, *J. Phys. Chem. C.* **112** (2008) 1158

118. M-H. Shao, P. Liu, R.R Adzic, *J. Am. Chem. Soc* **128** (2006), 7408

119. I. Morcos, *Electrochim. Acta* **22** (1977), 497

120. J. Zhang, K. Sasaki, E. Sutter, R.R. Adzic*, Science* **315** (2007) 220

121. F. Mirkhalaf, K. Tammeveski, D. J Schriffin, *Phys. Chem. Chem. Phys.* **11** (2009), 3463

122. M. M. Islam, T. Ohsaka, *J. Electroanal. Chem.* **623** (2008), 147

123. H. Liu, L. Zhang, J. Zhang, D. Ghosh, J. Jung, B.W. Downing, E. Whitmore, *J. Power Sources* **161** (2006), 743

124. J.S. Griffith, *Proc. R. Soc. London Ser. A*, **235** (1956) 23

125. L. Pauling, *Nature*, **203** (1964) 182

126. E. Yeager, *J. Electrochem. Soc.*, **128** (1981) 160 C

127. E. Yeager, D. Scherson, B. Simic-Glavaski, in J.D.E. McIntyre, M. Weaver, E.B. Yeager (eds.), *Chemistry and Physics of Electrocatalysis, The Electrochem. Soc. Proc. Ser.*, (1984) 247

128. H.S. Wroblowa, Y.C. Pan, G. Razumney, *J. Electroanal. Chem. Interfacial Electrochem.*, **69** (1978), 195

129. J. Zagal, M. Paez, *J Electroanal. Chem*. **339** (1992) 15

130. J. Zagal, P. Bindra, E. Yeager, *J. Electrochem. Soc*. **127** (1980) 1506

131. J. Zagal, S. Griveau, K.I Ozoemena, T. Nyokong, F. Bedioui, *J. Nanosci. Nanotechnol.* **9** (2009) 2201

132. B. Dembiska, P.J. Kulesza, *Electrochim. Acta* **54** (2009) 4687

133. A. Okunola, B. Kowalewska, M. Bron, P.J. Kulesza, W. Schuhmann, *Electrochim. Acta* **54** (2009) 4687

134. Y.W. Rhee, S. Ha, C. Rice, R.I. Masel, *J. Power Sources* **117** (2003), 35

135. R. Larsen, S. Ha, J. Zakzeski, R.I. Masel, *J. Power Sources* **157** (2006), 78

136. Z. Zhang, Y. Huang, J. Ge, C. Liu, T. Lu, W. Xing, *Electrochem. Commun* **10** (2008), 961

137. C. Rice, S. Ha, R.I. Masel, P. Waszczuk, A. Wieckowki, T. Barnard, *J. Power Sources* **111** (2002), 83

138. S. Wang, N. Kristian, S. Jiang, X. Wang, *Electrochem. Commun* **10** (2008), 961

139. J.D. Lovic, A.V. Tripkovic, S.L. Gojkovic, *J. Electroanal Chem* **581** (2005), 294

140. Z. Zhang, X. Zhou, C. Liu, W. Xing, *Electrochem Commun* **10** (2008), 131

141. R. Parson, T. VanderNoot*, J. Electroanal Chem* **257** (1988), 9

142. N. Markovic, H. Gaseiger, P. Ross, X. Jian, I. Villegas, M. Weaver, *Electrochim Acta* **40** (1995), 91

143. A. Capon, R. Parsons, *Electroanal Chem Interf Electroanal Chem* **45** (1973), 205

144. X. Xia and T.J. Iwasita, *J. Electrochem. Soc*. **140** (1993), 2559

145. M. Watanabe, Y. Futuuchi, S. Motoo, *J. Electroanal Chem* **191** (1985), 367

146. M.D. Macia, E. Herrero, J.M. Feliu, A. Aldaz, *J. Electroanal Chem* **500** (2001), 498

147. X. Zhou, C. Liu, J. Liao, T. Lu, W. Xing, *J. Power Sources* **179** (2008), 481

148. J. Javier, S. Heriban and N. Fabiola, *Regeneration of Cyanide by oxidation of thiocyanate* (1996) US Patent 5482694.

149. K. A. Singh, U. P. Singh, S. Mehtab and V. Aggarwal, *Sens. Actuators* B **125** (2007), 453

150. J. A. Cox and T. Gray, *Anal. Chem.* **60** (1988), 1710

151. M.K. Amini, S. Shahrokhian, S. Tangestaninejad, *Anal. Chim. Acta* **402** (1999) 137

152. S. Adak, A. Mazumdar, R.K. Banerjees, *J. Biol. Chem.* **272** (1997) 11049.

153. K.I. Ozoemena, T. Nyokong, *J. Electroanal. Chem*. **579** (2005) 283

154. M.J. Moorcroft, J. Davies, R.G. Compton, *Talanta* **54** (2000), 785

155. J.F. van Staden, T.A. van der Merwe, *S. Afr. J. Chem*. **51** (1998), 109

156. P. Brimblecombe, D.H. Stedman, *Nature* **298** (1982), 460

157. T. Nyokong, *Curr. Topics Electrochem*. **9** (2003), 197

158. N. Chebotareva, T. Nyokong, *J. App. Electrochem*. **27** (1997), 975

159. Z-H. Wen, T-F. Kang, *Talanta* **62** (2004), 351

160. C. Yang, Q. Lu, S. Hu, *Electroanalysis* **18** (2006) 2188

161. G. Binnig, C. Gerber, C. Quate, *Phys. Rev. Let.* **56** (1986), 930

162. S.L Flegler, J.W Heckman, K.L Klomparens, *Scanning and Transmission Electron Microscopy: An Introduction,* Oxford University Press, Cary, (1993)

163. M. De Graef, *Introduction to Conventional Transmission Electron Microscopy,* Cambridge University Press, UK, (2003)

164. M. A. O'Keefe, L. F. Allard, *Sub-Ångstrom Electron Microscopy for Sub-Ångstrom Nano-Metrology*, National Nanotechnology Initiative Workshop on Instrumentation and Metrology for Nanotechnology**,** Gaithersburg, MD (2004)

165. H.G. Brittain, *X-ray diffraction and X-ray fluorescence*, In: S. Ahuja, N. Jespersen (eds), *Comprehensive Analytical Chemistry* vol 47, Elsevier B.V, (2006)

166. R. Jenkins, R.L. Snyder, *Introduction to X-ray Powder Diffractometry,* Wiley, New York, (1996)

# CHAPTER 3

# Experimental

## 3.1 Introduction

In this chapter, a list is made of the reagent used and their grades. A detailed description is given of the synthesis of nanoMPc, MOBSPc and PtFeOCPc, as well as the process of functionalization of MWCNT. Also described are the equipment, the electrochemical measurements and non-electrochemical characterization techniques such as AFM, SEM, etc, employed in the various experimental procedures reported in this dissertation.

### 3.1.1. Reagents and Materials

Potassium hexacyanoferrate(II) was obtained from B. Jones Ltd., SA, potassium hexacyanoferric(III) was purchased from Bio-Zone Chemicals, SA. Potassium thiocyanate was obtained from Associated Chemicals Enterprises, SA. Hexadecyltrimethylammonium bromide (CTAB), iron(II) and cobalt(II) phthalocyanine, Pristine MWCNTs (>90% purity) were obtained from Sigma–Aldrich. Chloroform, toluene, methanol, ethanol dimethylformamide (DMF) were purchased from SAARCHEM (PTY) Ltd SA. 1,2-Dichloroethane, sodium nitrite, potassium chloride and sulphuric acid were obtained from Merck. Iron pentacarbonyl ($Fe(CO)_5$, Kanto), chloronaphthalene (Nacalai), Potassium tetrachloroplatinate (BDH). Iron(II) octa-carboxy phthalocyanine (FeOCPc), and 1,2-dibutyl-4,5-dicyanobenzene courtesy Professor Nagao Kobayashi, (Tohoku University, Sendai,

Japan). DMF was freshly distilled after drying over alumina before use. Tetrabutylammonium perchlorate (TBAP) was recrystallised from ethanol. Phosphate buffers were prepared using appropriate amounts of $H_3PO_4$, $KH_2PO_4$, $K_2HPO_4$ and $K_3PO_4$ depending on the pH and adjusted with 0.1M NaOH where needed.

### 3.1.2. Synthesis

#### 3.1.2.1. *Synthesis of Nanostructured Iron(II) and Cobalt(II) Phthalocyanines*

The nanostructured iron(II) and cobalt(II) phthalocyanine complexes were prepared using the established method[1,2] as shown in Scheme 3.1. Briefly, 0.06 g iron(II) phthalocyanine or cobalt(II) phthalocyanine was dissolved in 2 mL 98% concentrated sulphuric acid, then the solution was added drop wise into 120 mL aqueous solution containing 0.18 g CTAB in an ultrasonic iced-water bath. The resulting leaf green (for iron(II) phthalocyanine) and blue (for cobalt(II) phthalocyanine) colloid solution was ultra centrifuged until separated. The obtained precipitate was washed repeatedly with water until neutral, and allowed to air-dry at room temperature for 48 h to obtain the nanostructured MPc powder.

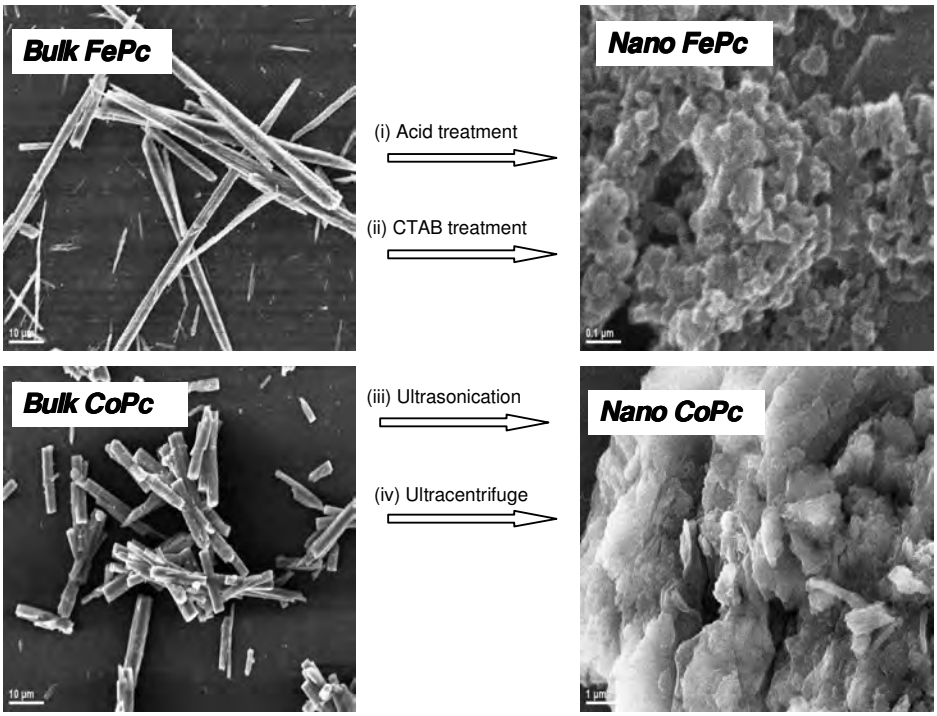


***Scheme 3.1:*** *Schematic representation (SEM images) of the preparation of nanoMPc from the bulk MPc*

### 3.1.2.2. *Synthesis of Iron(II) and Cobalt(II) Octabutylsulphonylphthalocyanines*

1,2-dibutyl-4,5-dicyanobenzene (**1**) was prepared according to the method described in literature[3]. Quinoline was distilled over $CaH_2$ under vacuum prior to use.

*Preparation of iron(II) octabutylsulphonylphthalocyanine (FeOBSPc), 2a*

A mixture of (**1**) (100 mg, 0.13 mmol), and (10 μL) of iron pentacarbonyl ($Fe(CO)_5$,) was suspended in chloronaphthalene and heated at 190 °C for 2 h under argon. *(CAUTION: $Fe(CO)_5$ is suspected to be a neurotoxicant and has been ranked as one of the most*

*hazardous compounds to the ecosystem and human health; so it must be used with caution)*. After cooling to room temperature, the reaction mixture was poured into methanol and the resultant precipitate filtered off. The filtrate was vacuum dried and the residue separated successfully, first by using short column of normal silica gel ($CHCl_3$) and finally with $CHCl_3$/MeOH (200:2 v/v) as eluent to obtain the first green-coloured fraction. Recrystallization from $CHCl_3$/methanol gave pure FeOBSPc, (**2a**). UV–visible ($CHCl_3$, $\lambda_{max}$/nm): 360, 696 MASS (ESI-FTICR) (m/z): 1551.2714, Calcd for $C_{64}H_{80}N_8S_8O_{16}FeNa$:1551.2700.

*Preparation of cobalt(II) octabutylsulphonylphthalocyanine (CoOBSPc) 2b*

A mixture of (**1**) (100 mg, 0.13 mmol), cobalt chloride dihydrate (23 mg, 0.14 mmol), and a catalytic amount of ammonium molybdate (120 mg) was suspended in distilled quinoline (1 mL) and heated at 190 °C for 2 h under argon. After cooling to room temperature, the reaction mixture was poured into methanol and the resultant precipitate filtered off. The filtrate was vacuum-dried and the residue separated successfully, first by using short column of normal silica gel ($CHCl_3$) and finally with $CHCl_3$/MeOH (200:2 v/v) as eluent to obtain the first blue-coloured fraction. Recrystallization from $CHCl_3$/methanol gave pure CoOBSPc, (**2b**). UV– visible ($CHCl_3$, $\lambda_{max}$/nm): 343, 678.

MASS (ESI-FTICR) (m/z): 1554.2702, Calcd for $C_{64}H_{80}N_8S_8O_{16}CoNa$: 1554.2682.

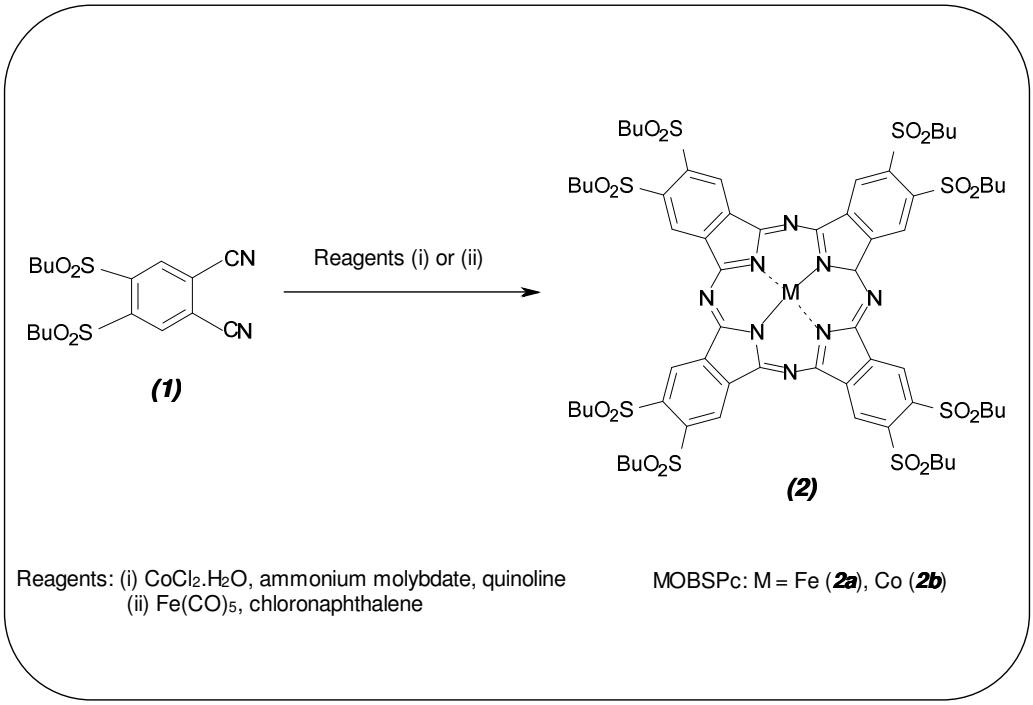


***Scheme 3.2:*** *Synthetic route for MOBSPc*

### 3.1.2.3. *Synthesis of Iron(II) tetrakis(diaquaplatinum) octa-carboxyphthalocyanine ($C_{40}H_{24}N_8FeO_{24}Pt_4$)*

**STEP 1**

The iron(II) tetrakis(diaquaplatinum)octacarboxyphthalocyanine (PtFeOCPc) (**5**) was synthesised by adopting the same strategy reported for the cobalt derivative by Dolotova and Kaliya,[4] (Scheme 3.3). Briefly, the sodium salt of iron(II) octacarboxy phthalocyanine (**4**) (0.10 g) obtained from (**3**), was dissolved in distilled water (12 mL)

and methanol (106 mL), potassium tetrachloroplatinate (0.12g, 0.28 mmol) dissolved in 50% ethanol (190 mL) was added to the solution of (**4**), stirred for 3 h at room temperature. The resultant precipitate was filtered off after 48 h, washed with distilled water and allowed to dry (yield 0.10g, 0.24 mmol).

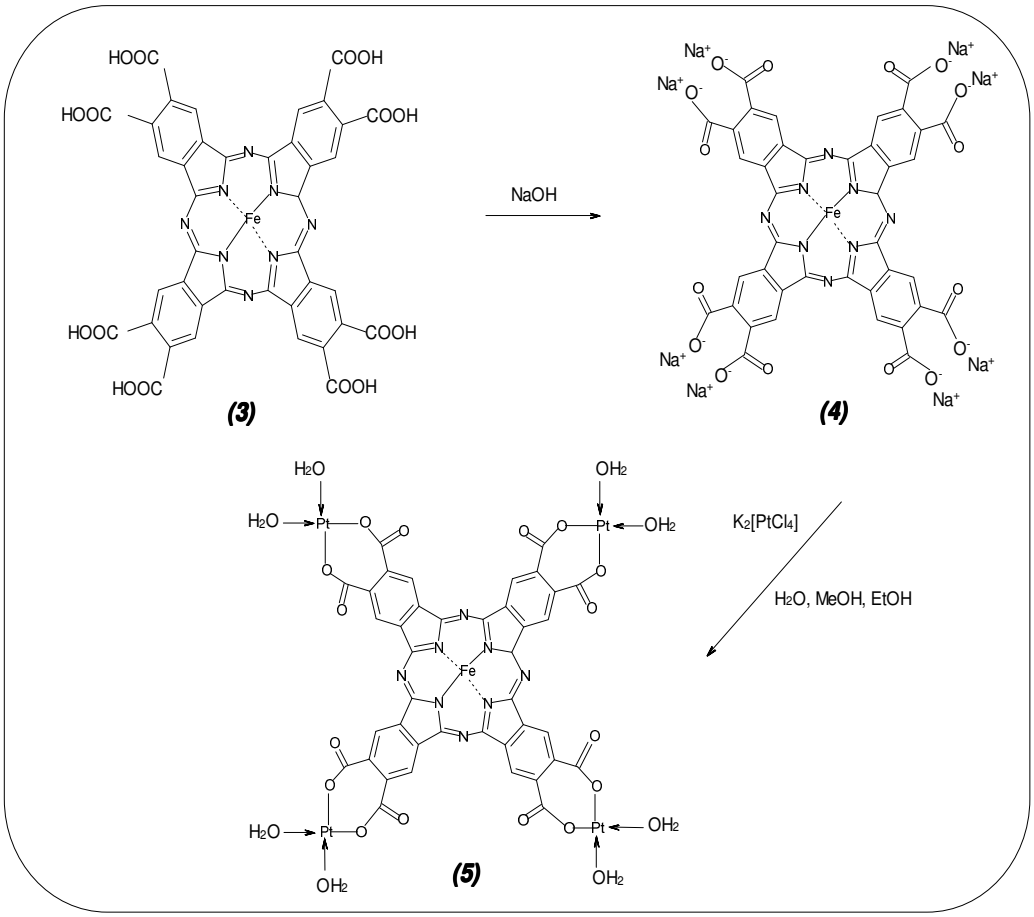


***Scheme 3.3**: Synthetic route for PtFeOCPc*

**STEP 2**

Potassium tetrachloroplatinate (0.10g, 0.24 mmol) dissolved in 50% ethanol (119 mL) was added to the suspension of the product obtained in step 1 which has already been dissolved in a mixture of distilled water (20 mL) with methanol (85 mL), stirred for 3 h at room temperature. The resultant precipitate was filtered off after 48 h, washed with distilled water, ethanol, acetone, and ether and allowed to dry (yield 0.070g). The dried product (**5**) is a dark green-coloured crystalline compound. (UV-visible (DMF, $\lambda_{max}$/nm): 313, 450, 685. FTIR $\nu_{max}/cm^{-1}$: 3400($\nu_{O-H}$), 1605($\nu_{C-O}$), 1550($\nu_{C-O}$), 1200($\nu_{COO^-}$). Elemental analysis: Found C, 25.60; H, 1.39; N, 6.34. $C_{40}H_{24}N_8FeO_{24}Pt_4$ requires C, 26.14; H, 1.31; N, 6.10)

### 3.1.3. *Purification of Multi-Walled Carbon Nanotubes*

Pristine MWCNTs (> 90% purity) were purified and acid-functionalised as described before.[5] Briefly, 1 g of MWCNTs was added to 140 mL of 2.6 M $HNO_3$, and the mixture was refluxed for 48 h. The multi-walled carbon nanotubes sediment was separated by centrifugation, and washed with distilled water. It was then sonicated in a concentrated mixture of $H_2SO_4$ and $HNO_3$ (3:1 ratio) at 40 °C for 24 h. The sediment was thereafter washed with distilled water, stirred for 30 minutes in a 4:1 $H_2SO_4/H_2O_2$ mixture at 70 °C, and washed with

distilled water. The final purified and functionalised MWCNT slurry was then oven-dried at 50 $^{o}$C for 48 h.

### 3.1.4. *Electrode Modification Procedure*

The working electrode used for electrochemical studies in this thesis is bare edge plane pyrolytic graphite electrode herein referred to as EPPGE, fabricated in-house from EPPG plate (Le Carbone, Sussex, UK). Electrical contact with the disk was maintained through an inserted copper wire held in place with conducting silver varnish. The working electrode for the rotating disk electrode experiment was fabricated in-house from an EPPG plate housed in an AUTOLAB–RDE Teflon cover. Prior to modification, the bare EPPGE was first polished with slurries of aluminium oxide nanopowder, mirror finished on a Buehler felt pad and then subjected to ultrasonic stirring in acetone and ultrapure water respectively for 3 min to remove residual alumina particles that might be trapped at the surface. 1 mg MWCNT was dispersed in 1mL DMF with the aid of ultrasonic stirring. 15 µL of the MWCNT solution was cast on the EPPGE surface and allowed to dry at room temperature to prepare the EPPGE-MWCNT electrode. 15 µL of the MPc complexes prepared in the same manner was cast onto the surface of the bare EPPGE to prepare the EPPGE-MPc electrode or cast onto the surface of the EPPGE-MWCNT to prepare the EPPGE-MWCNT-MPc electrode.

### 3.1.5. *Electrochemical Procedure and Instrumentation*

All electrochemical studies were performed with Autolab potentiostat PGSTAT 20, driven by the General Purpose Electrochemical Systems data processing software (GPES 4.9) (Eco-Chemie, Utrecht, The Netherlands), equipped with a conventional three-electrode system (Figure 3.1), were the working electrode is either a bare EPPGE (*d* = 3.0 mm) or modified EPPGE. An Ag|AgCl (saturated 3 M KCl) was used as reference electrode and a platinum rod as a counter electrode. Solution electrochemistry was performed in ~1mM of MPc complexes in dry DMF containing 0.1 M tetrabutylammonium perchlorate (TBAP) as the supporting electrolyte under nitrogen atmosphere. Glassy carbon electrode (0.07 $cm^2$), platinum rod and Ag|AgCl wire were used as the working, counter and reference electrodes, respectively.

Electrochemical impedance spectroscopy (EIS) measurements were performed with Autolab Frequency Response Analyser (FRA) software between 10 kHz and 10 mHz using a 5 mV rms sinusoidal modulation in 0.1M of $K_4Fe(CN)_6$ and 0.1M $K_3Fe(CN)_6$ (1:1) mixture containing 1.0 M KCl at the $E_{1/2}$ of the $[Fe(CN)_6]^{3-/4-}$ (0.30 V vs. Ag|AgCl saturated KCl). Solutions were deoxygenated by a stream of high purity nitrogen for at least 5 min before running the experiment and the solution was protected from air by a blanket of nitrogen during the experiment.

Oxygen reduction was studied using cyclic voltammetry. The rotating disk electrode (RDE) technique was also used in order to eliminate mass transport problems, employing an AUTOLAB–RDE (Eco-Chemie, Utrecht, The Netherlands), For the RDE, 30 mL of 0.1 M NaOH solution was used as the electrolyte to study the reduction of oxygen after bubbling with high purity nitrogen (99.99%) and oxygen, as the case may be, for 15 minute. The voltammograms were recorded using linear sweep potential scan between 0.40 to -0.80 V.

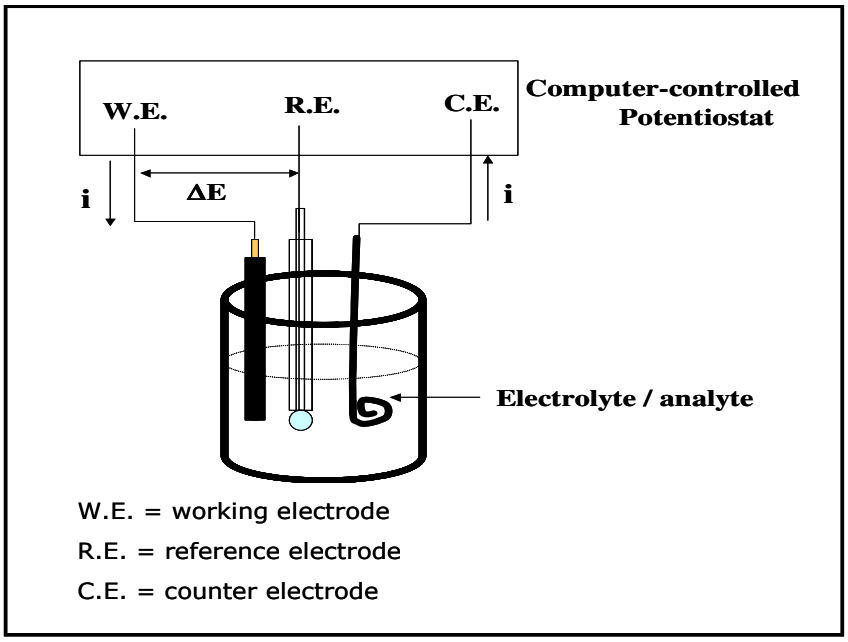


***Figure 3.1:*** *Diagrammatic presentation of a conventional three-electrode system*

A BENCHTOP, 420A (LABOTEC) pH meter was used for pH measurements. Ultra pure water of resistivity 18.2 MΩ.cm was obtained from a Milli-Q Water System (Millipore Corporation, Bedford,

MA, USA) and was used throughout for the preparation of solutions. Ultrasonic bath (INTEGRAL SYSTEMS) was used for ultrasonic stirring.

All the AFM experiments were performed with AFM 5100 System (Agilent Technologies, USA) using a contact mode AFM scanner interfaced with a PicoView 1.4.3 controller (scan range 1.25 μm in *x*–*y* and 2.322 μm in *z*). Silicon type PPP-CONT-20 (Nanosensors®) of thickness 2.0±1.0 μm, length 450±10 μm, width 50±7.5 μm, spring constants 0.02–0.77 $Nm^{-1}$, resonant frequencies of 6–21 kHz and tip height of 10–15 μm were used. All images were taken in air at room temperature in an anti-vibration chamber at scan rates 0.5 – 0.6 lines $s^{-1}$. Field emission scanning electron microscopy (FESEM) images were captured with JEOL JSM 5800 LV (Japan). Morphological analyses of the different MPc complexes were carried out and viewed at an accelerating voltage of 5 k*e*V and using the lowest beam current in order to avoid sample damage. Transmission electron microscopy (TEM), imaging and energy-dispersive X-ray spectroscopy (EDS) analysis were carried out using JEOL JEM– 2100 F/HT TEM, operating at an accelerating voltage of 200 KeV equipped with EDS. Digital processing of the TEM images was carried out using UTHSCSA ImageTool® software version 3.0. The UV – Visible spectra were measured using a Cary 300 UV- Visible Spectrophotometer, driven by Varian software version 3.0 at a scan rate of 600 nm/min. IR spectra were measured using a Perkin Elmer Spectrum RX 1 FT – IR system attached with a MIRacle ATR with diamond / ZnSe crystal plate for

transmission in the 400 – 4000 $cm^{-1}$ range. Elemental analysis was carried out with a Carlo Erba NA 1500 Nitrogen Carbon Sulphur Analyser. Gas Chromatography (GC) was used to separate the gases, i.e. N (in the form of $N_2$), C (in the form of $CO_2$) and S (in the form of $SO_2$), using a He carrier gas and a thermal conductivity detector, driven by PeakNet software (Dionex Corporation, May 1998), with an external A/D interface (UI20 Universal Interface, Dionex). XRD analysis was carried out using a back loading preparation method. It was analyzed with a PANalytical X'Pert Pro powder diffractometer with X'Celerator detector and variable divergence and receiving slits with Fe filtered Co-Kα radiation. The diffraction patterns were collected from 10° to 110°. The phases were identified using X'Pert Highscore plus software.

## References

1. M. Siswana, K.I. Ozoemena, T. Nyokong, *Talanta* **69** (2006) 1136.
2. Y.Wang, K. Deng, L. Gui, Y. Tang, J. Zhou, L. Cai, J. Qui, D. Ren, Yq.Wang, *J. Colloid Interf. Sci*. **213** (1999) 270
3. K.M. Keshavarz, B. Knight, G. Srdanov, F. Wudl, *J. Am. Chem. Soc*. **117** (1995) 11371
4. O.V. Dolotova, O.L. Kaliya, *Russ. J. Coord. Chem.* **33** (2007), 111
5. J. Liu, A.G. Rinzler, H. Dai, J.H. Hafner, R. Kelley Bradley, P.J. Boal, A. Lu, R.E. Smalley, *Science* **280** (1998), 1253

# SECTION B

# RESULTS AND DISCUSSION

# CHAPTER 4

# Microscopic, Spectroscopic, Electrochemical and Electrocatalytic Properties of Nanostructured Iron(II) and Cobalt(II) Phthalocyanine*

* The following publications resulted from part of the research work presented in this chapter and they are not referenced further in this thesis:

1. S.A. Mamuru, K.I. Ozoemena, *Materials Chemistry and Physics*, **114** (2009), 113-119
2. S.A. Mamuru, K.I. Ozoemena, *Electroanalysis*, **22** (2010), 985-994

## 4.1 Microscopic and Spectroscopic Characterisation

Following the synthesis of the nanostructured iron(II) and cobalt(II) phthalocyanine complexes from their bulk counterpart, their surface morphologies were examined to obtain microscopic and spectroscopic information. Atomic force microscopy, scanning electron microscopy and energy dispersive x-ray spectroscopy were employed for this investigation.

### 4.1.1. *Comparative SEM, AFM and EDX*

Scanning electron microscope (SEM) images of the MPc and nanoMPc as depicted in Scheme 3.1 clearly confirm the successful nanostructuring of the bulk (crystallite form) MPc molecules to their amorphous nanoparticles protected by surfactant layer (CTAB particles). The main principle of the synthesis as depicted in Scheme 3.1 is simply the breaking of the intramolecular forces of the MPc and protecting the species in CTAB environments. As observed in the SEM images, these nanoparticles form aggregates which is an indication of the existence of an attractive interaction among nanoparticles. The preservation of their individuality suggests the existence of a stabilisation mechanism resulting from the surfactant layer adsorbed at the nanoparticle surface.[1] Figure 4.1 shows AFM images of the bulk FePc and nanoFePc, it closely resembles that of the SEM.

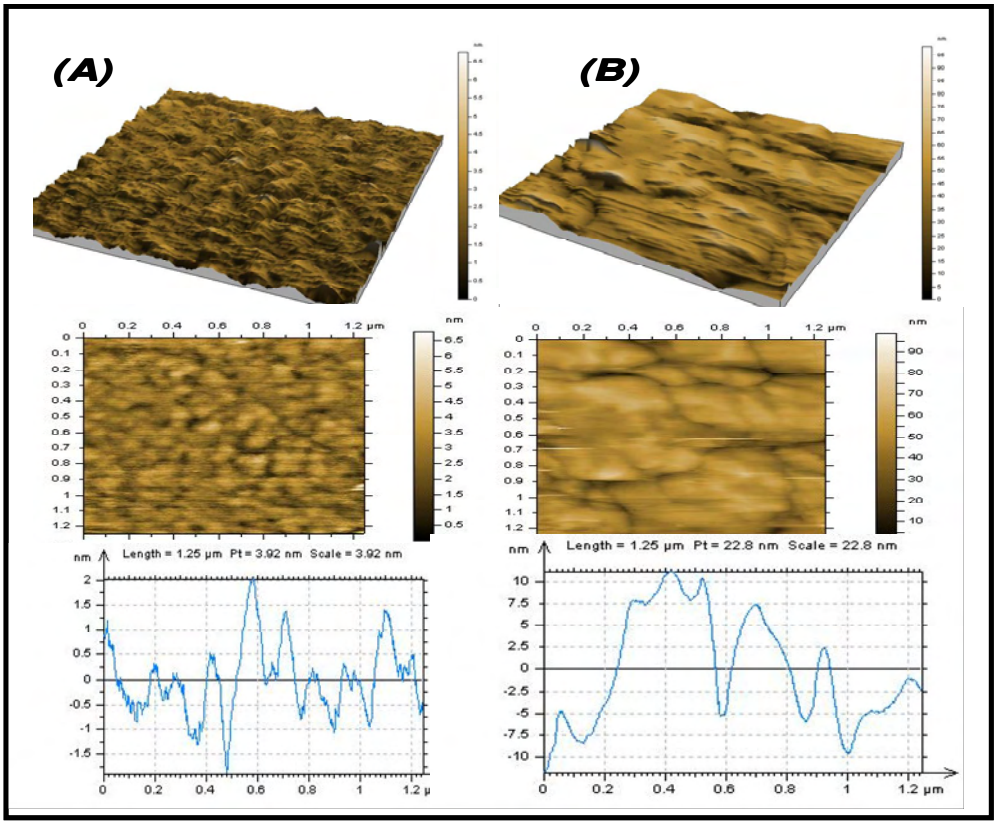


***Figure 4.1:*** *AFM images of bulk FePc (A) and nanostructured FePc (B)*

The energy dispersive x-ray (EDX) profile (Figure. 4.2) clearly shows the analytical details of the elemental composition of the bulk FePc, nanostructured FePc and surfactant (CTAB).The FePc (A) was dominated by carbon and iron. With CTAB (B), carbon and bromine were observed only. Similarly, as expected, with the nanoFePc (C), the presence of these two species (FePc and CTAB) was clearly evident. The sulphur peak at 2.4 *e*V could have arisen from the sulphuric acid solution used in the synthesis. Similar profiles were observed for the cobalt (II) phthalocyanine.

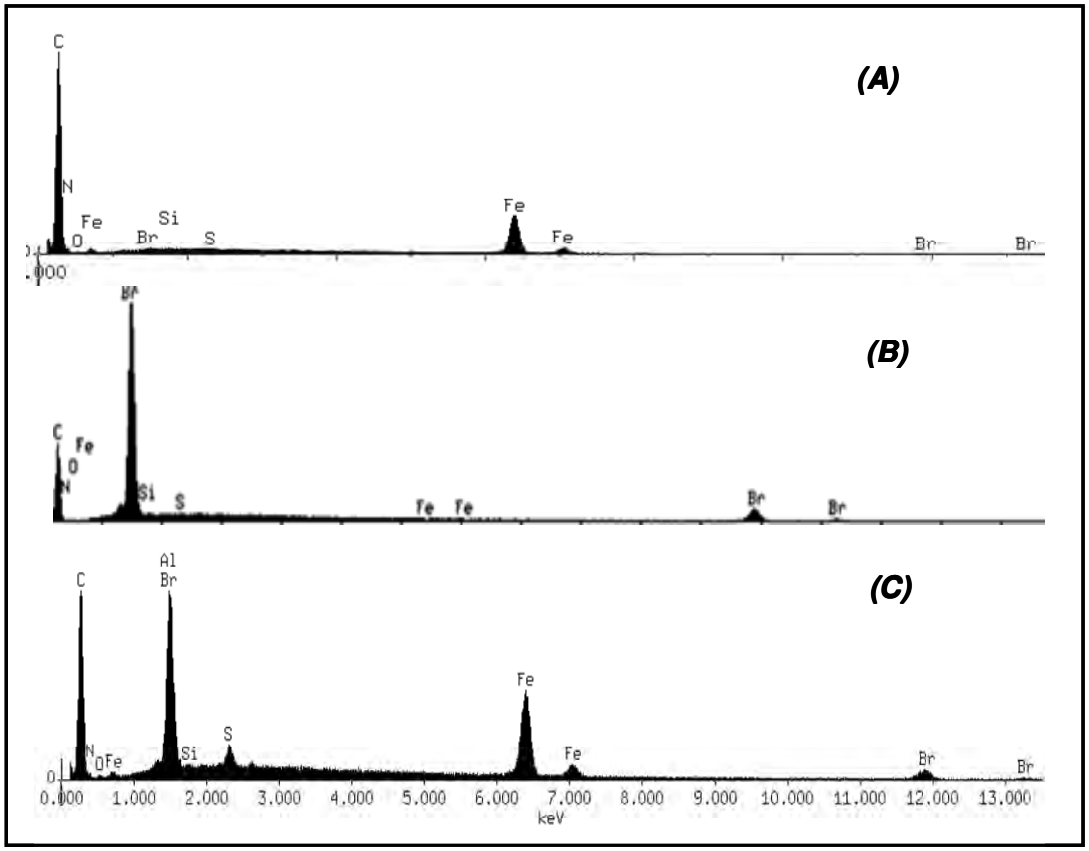


***Figure 4.2:** EDX profile of bulk FePc (A), CTAB (B) and nanoFePc (C)*

## 4.2 Electrochemical Characterisation

### 4.2.1. *Electron transfer behaviour: cyclic voltammetry*

Figure 4.3 compares typical cyclic voltammetric evolutions of the bare EPPGE, EPPGE-FePc, EPPGE-nanoFePc,EPPGE-MWCNT, EPPGE-MWCNT-FePc and EPPGE-MWCNT-nanoFePc and the corresponding CoPc derivatives recorded in 0.1 M $[Fe(CN_6)]^{3-}/[Fe(CN_6)]^{4-}$ solution containing 1.0 M KCl. It should be noted that $[Fe(CN)_6]^{3-}/[Fe(CN)_6]^{4-}$ is an important redox probe known to exhibit 1-electron reversible process. The choice of this redox probe in this work is to answer the question as to what extent can the modifying species permit the electron transfer of the $[Fe(CN)_6]^{3-}/[Fe(CN)_6]^{4-}$ species to the underlying EPPG electrode. In Figure 4.3 (a) the bare EPPGE gave similar voltammogram as those of the EPPGE-FePc and EPPGE-nanoFePc. This cyclic voltammetric result has certain implications. First, the result is in excellent agreement with the reports of Griveau *et al*[2] and Ozoemena and Nyokong.[3] These workers[2,3] had examined the cyclic voltammetric responses of $[Fe(CN)_6]^{3-}/[Fe(CN)_6]^{4-}$ at both bare and MPc-modified electrodes and found that they produced similar voltammetric shapes with no detectable change in the redox potential and with nearly equal peak current intensities. However, there was a huge current difference between the MWCNT-based electrodes and the other electrodes. A similar trend was observed with the EPPGE-CoPc derivatives and the EPPGE-MWCNT-CoPc derivatives. Analysis of the

potential peak-to-peak separation ($\Delta E_p$) of the electrodes are essentially similar (approximately 100 mV), suggesting that no meaningful electron transfer kinetics could be obtained using the $\Delta E_p$ values.

### 4.2.2. *Diffusion Domain Approximation Theory*

The type of diffusion process that could be occurring at these electrodes was interrogated by using the "diffusion domain approximation" theory developed by Davies and Compton for the voltammetric responses at spatially heterogeneous electrodes/partially blocked electrodes,[4,5,6] which can also be applied to a 3-dimensional electrochemically heterogeneous electrode, for example, EPPGE modified with gold and anthraquinone.[4] More information on this theory can be found in the cited references. As shown in Figure 4.3, and according to the theory, radial diffusion plays the dominant role where there is near complete electrolysis of the redox probe to the surface of the electrodes in the bare EPPGE and the EPPGE-MPc electrodes. The questions that then arise should include: (a) what is the origin of the large current response observed at the EPPGE-MWCNT, a negatively-charged surface, that should have been lower considering that a repulsive interactions should have existed between this electrode and the negatively-charged redox probe, ($[Fe(CN)_6]^{3-}$/ $[Fe(CN)_6]^{4-}$)?; (b) why is the current response at the EPPGE-MWCNT-

nanoFePc (a positively-charged surface) the same as that of the EPPGE-MWCNT?, and (c) why is the current response at the EPPGE-MWCNT-nanoFePc larger than that observed at the EPPGE-MWCNT-FePc?

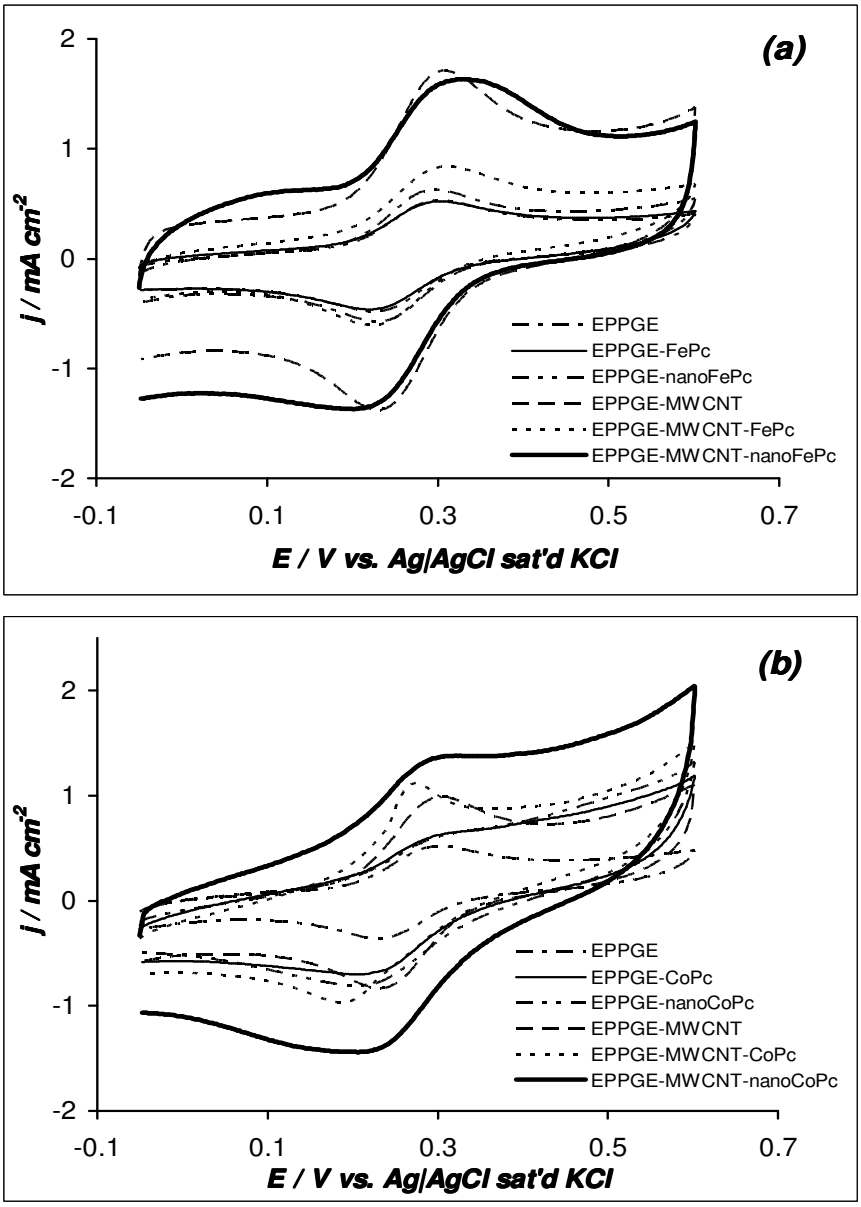


***Figure 4.3:*** *Comparative cyclic voltammograms of the electrodes in 1.0 M KCl containing 0.1 M $[Fe(CN)_6]^{3-}/[Fe(CN)_6]^{4-}$ solution (a) FePc derivatives (b) CoPc derivatives*

The answers to these questions may be found in the work of Compton and co-workers,[7] where the authors cautioned on the interpretation of the current response at CNT-based electrodes where the electrode surface is not truly planar. According to them, such large current response could arise from (i) electrocatalysis, (ii) a change in diffusion regime (i.e., semi-infinite linear diffusion and / or thin layer diffusion processes, the latter process arising from the oxidation of electroactive species/electrolytes trapped in pockets in between the nanotubes), or (iii) a combination of (i) and (ii). Thus, it may suffice to say that in this case, this may be due to the redox processes of the ferrocyanide/ferricyanide species that were trapped within the porous layers of the high surface area MWCNTs or MWCNT-nanoFePc. The slightly lower capacitive current (in the region between +0.1 and -0.1 V) at the MWCNT-nanoFePc compared to the MWCNT alone may be attributed to the enhanced Faradaic response induced by the electrostatic attraction between the nanoFePc and the redox probe.

According to Davies and Compton, the diffusion layer thickness, $\delta$, which helps in categorizing the type of diffusion occurring at the electrodes, can be obtained from the modified Einstein equation for the root mean square displacement of diffusing particles,[4,5,6] equation (4.1):

$$\delta = \sqrt{2D\frac{\Delta E}{v}} \qquad (4.1)$$

where *D* is diffusion coefficient of aqueous ferrocyanide ($6.3x10^{-6}$ $cm^2$ $s^{-1}$)[6], Δ*E* is the potential "width" of the voltammogram (i.e., the distance between the onset potential to where the peak potential or limiting current is attained)[6] and $\upsilon$ is the scan rate (0.05 V $s^{-1}$ in the case of Figure 4.3 (a)). Using ΔE of 0.197 V (for the EPPGE, EPPGE-FePc and EPPGE-nanoFePc), 0.186 V for the EPPGE-MWCNT-FePc, 0.176 V for the EPPGE-MWCNT and 0.170 V for the EPPGE-MWCNT-nanoFePc for the EPPGE-MWCNT-FePc, 0.135 V for EPPGE-CoPc and EPPGE-nanoCoPc, 0.129 V for EPPGE-MWCNT-CoPc and 0.148 V for the EPPGE-MWCNT-nanoCoPc, an approximate value of 51 μm was estimated as the diffusional distance for the FePc derivatives while 59 μm was obtained for the CoPc derivatives. These values correspond to the type 3 behaviour of the voltammetric responses at spatially heterogeneous electrodes,[5] and is associated with an overlap of adjacent diffusion layers resulting from the small size of the inert part of the electrode.

### 4.2.3. *Electron transport behaviour: Impedimetric characterization*

Since the potential peak-to-peak separation ($\Delta E_p$) of the electrodes are essentially similar (approximately 100 mV), suggesting that no meaningful electron transfer kinetics could be obtained using

the $\Delta E_p$ values. This prompted the exploration of the electrochemical impedance spectroscopy route to follow the heterogeneous electron transfer kinetics at these electrodes. EIS is a complementary technique to CV; while the latter represents only part of an electrochemical system, the results of the EIS measurements give fuller description of the electrochemical system,[8] providing vital information about processes occurring at the electrode/electrolyte interface. Figures 4.4 (a) and 4.5 (a) shows examples of the Nyquist plots obtained for the electrodes in the $[Fe(CN)_6]^{3-}/[Fe(CN)_6]^{4-}$ solution. As seen in Figure 4.4 (a) and 4.5 (a) (data summarized in Table 4.1), the impedance spectra of the electrodes were satisfactorily fitted (especially in terms of the low fitting errors and the pseudo-chi square ($\leq 10^{-4}$) from the Kramers-Kronig tests) with the proposed modified Randles equivalent electrical circuits (Fig. 4.4 (d)). The bare EPPGE, EPPGE-FePc and EPPGE-nanoFePc were fitted with circuit (i) while the EPPGE-MWCNT, EPPGE-MWCNT-FePc and EPPGE-MWCNT-nanoFePc were fitted with circuit (ii). In Figure 4.5, the impedance spectra were fitted with the equivalent electrical circuit as proposed in Figure 4.5 (d). The EPPGE-CoPc was fitted with circuit (i), while EPPGE-nanoCoPc, EPPGE-MWCNT-CoPc and EPPGE-MWCNT-nanoCoPc were fitted with circuit (ii). The fitting parameters involve the electrolyte resistance ($R_s$), electron-transfer resistance ($R_{ct}$), constant phase element (CPE), double layer capacitance ($C_{dl}$) and Warburg-type impedance ($Z_w$) which is

associated with the diffusion of the ions of the redox probe. The apparent electron-transfer rate constant ($k_{app}$) values of the electrodes were obtained from the equation (4.2):[9]

$$k_{app} = \frac{RT}{n^2 F^2 A R_{ct} c} \qquad (4.2)$$

where n is the number of electron transferred, A is the area of the electrode, c is the concentration of the $[Fe(CN)_6]^{3-}$ (in mol $cm^{-3}$, the concentration of $[Fe(CN)_6]^{3-}$ and $[Fe(CN)_6]^{4-}$ are equal), R is the ideal gas constant, T is the absolute temperature (K) and F is the Faraday constant. The calculated values are shown in Table 4.1. The $k_{app}$ values decrease as: EPPGE-MWCNT-nanoFePc > EPPGE-MWCNT-FePc > EPPGE-nanoFePc > EPPGE-FePc, for the FePc derivatives while for the CoPc derivatives is as: EPPGE-MWCNT-nanoCoPc > EPPGE-MWCNT-CoPc > EPPGE-nanoCoPc > EPPGE-CoPc indicating that electron transfer processes between the redox probe and the underlying EPPGE surface is much easier at the EPPGE-MWCNT-nanoMPc compared to the other electrodes.

The impedance of the CPE ($Z_{CPE}$) is defined as equation (2.26):

$$Z_{CPE} = \left[Q(j\omega)^n\right]^{-1} \qquad (2.26)$$

where Q is the frequency-independent constant related to the interface, $j = \sqrt{-1}$, $\omega$ is the radial frequency, the exponent n arises from the slope of log Z vs. log f (and has values $-1 \leq n \leq 1$). If n=0, the CPE behaves as a pure resistor; n=1, CPE behaves as a pure capacitor, n=

-1 CPE behaves as an inductor; while n=0.5 corresponds to Warburg impedance ($Z_w$) which is associated with the domain of mass transport control arising from the diffusion of ions. In short, CPE arises from several factors such as (i) the nature of the electrode (e.g., roughness and polycrystallinity), (ii) distribution of the relaxation times due to heterogeneities existing at the electrode/electrolyte interface, (iii) porosity and (iv) dynamic disorder associated with diffusion. In the circuits, notice that the Warburg in the ideal Randles circuit has been replaced by the $CPE_2$, which simply describes the porous nature of the concerned electrodes. From the Bode plots (Figs. 4b and 4c), the slopes of the log Z vs. log f plot at the mid frequency region are less than the ideal -1.0 for pure capacitive behaviour, which is indicative of pseudocapacitive behaviour. It is worthy to mention here that all attempt to replace the $C_{dl}$ in circuit (i) with a CPE (which is a more practical situation) led to huge fitting errors. This should not be interpreted to signify that the $C_{dl}$ is a pure double layer capacitance. According to Orazem and Tribollet,[10] frequency dispersion leading to CPE behaviour takes place through the distribution of time constants along either the area of the electrode surface (involving a 2-dimensional aspect of the electrode, which mimics an ideal RC behaviour) or along the axis normal to the electrode surface (involving a 3-dimensional surface). Thus, suffice to say here that the observed impedimetric behaviour of the modified electrodes is CPE. The data

from the Bode plots (i.e., -phase angle vs. log f) further confirms the absence of ideal capacitive behaviour as the observed phase angles are less than the 90° expected of an ideal capacitive behaviour.

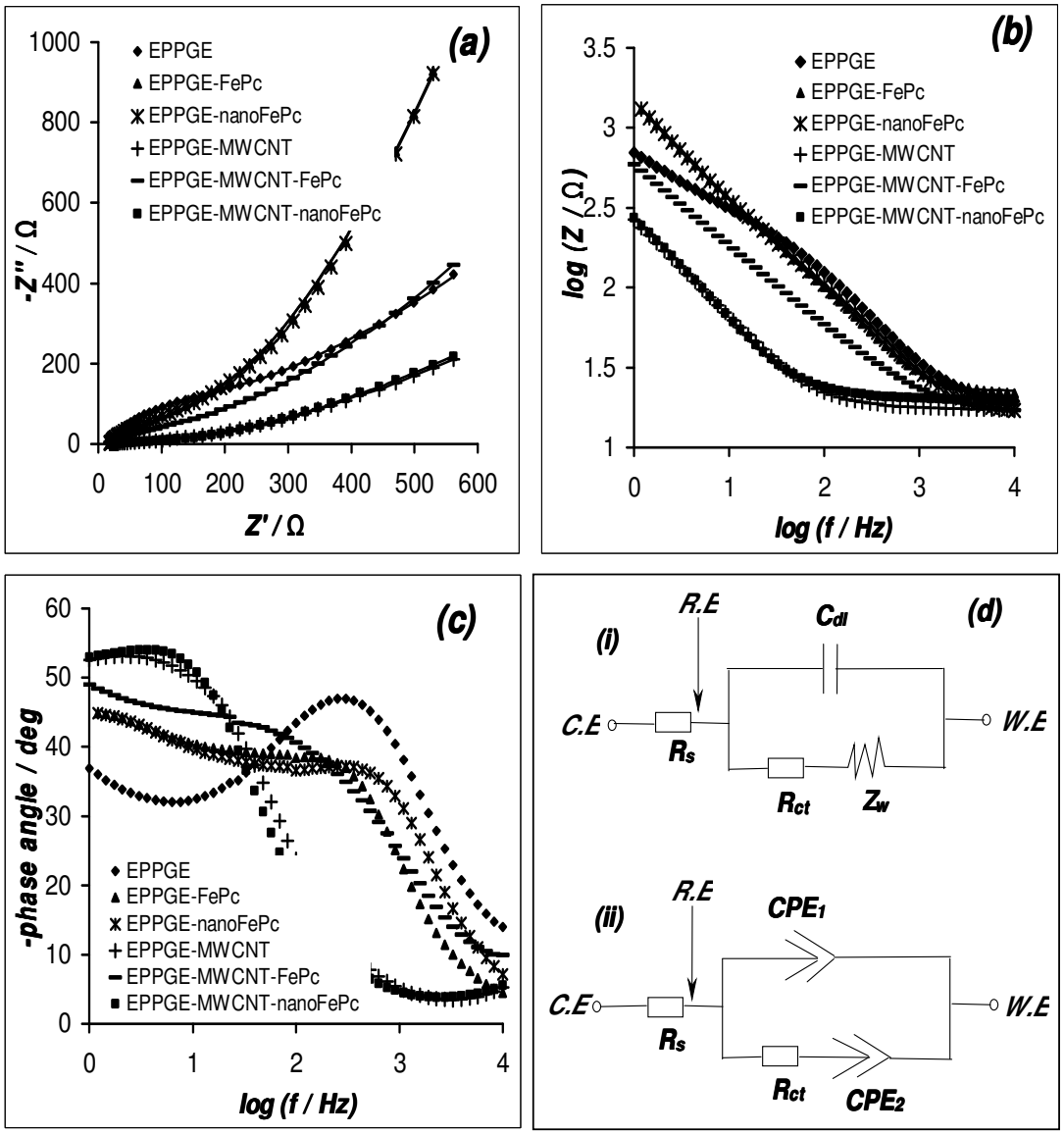


***Figure 4.4:*** *Comparative (FePc derivatives) Nyquist plots (a) and Bode plots (b) and (c) obtained for the various electrodes studied in 1.0 M KCl containing 0.1 M* $[Fe(CN)_6]^{3-}/[Fe(CN)_6]^{4-}$*, equivalent electrical circuit diagrams (d)*

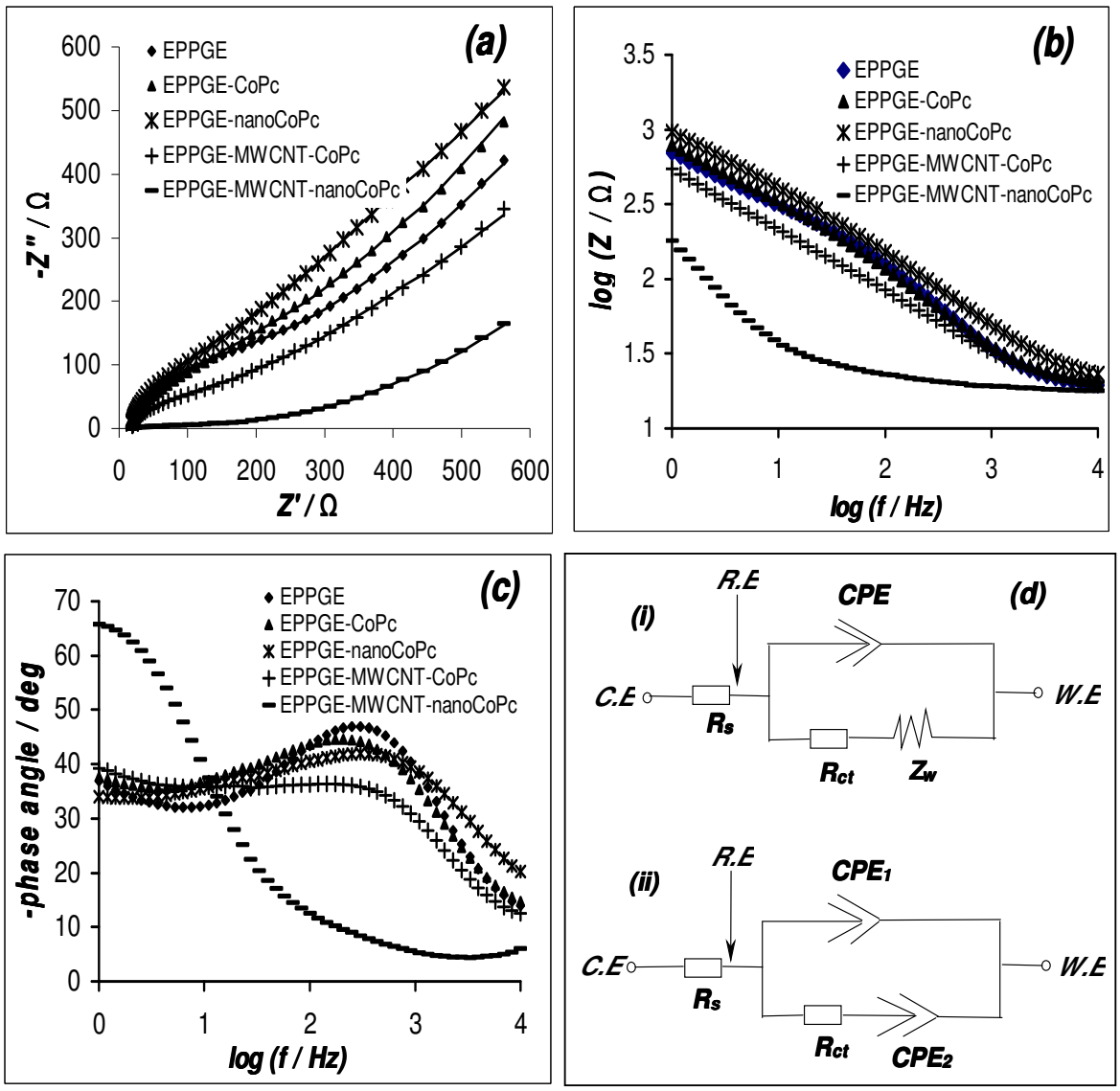


***Figure 4.5:*** *Comparative(CoPc derivatives) Nyquist plots (a) and Bode plots (b) and (c) obtained for the various electrodes studied in 1 M KCl containing 0.1 M $[Fe(CN)_6]^{3-}/[Fe(CN)_6]^{4-}$, equivalent electrical circuit diagrams (d)*

***Table 4.1:** Impedance parameters obtained for the various electrodes studied in 0.1 M $[Fe(CN)_6]^{3-/4-}$ 1.0 M KCl solution*

| EPPGE Modifier | $R_s$ /Ω | $R_{ct}$ /Ω | $CPE_1$/μF | $n_1$ | $CPE_2$ /μF | $n_2$ | $C_{dl}$ /μF | $10^6 Z_w$ | $10^2 k_{app}$/cms$^{-1}$ |
|---|---|---|---|---|---|---|---|---|---|
| FePc | 22.7±0.2 | 30.9±2.0 | - | - | - | - | 20.7±0.7 | 966±9 | 12.0±0.8 |
| NanoFePc | 17.6±0.3 | 29.4±1.5 | - | - | - | - | 12.8±0.4 | 971±10 | 13.0±0.7 |
| CoPc | 17.3±0.2 | 324±9.7 | 78.8±3.0 | 0.71 | - | - | - | 551±6 | 1.2±0.1 |
| nanoCoPc | 17.2±0.2 | 169±31 | 55.7±6.3 | 0.71 | 523±4.9 | 0.36 | - | - | 2.2±0.4 |
| MWCNT | 16.5±0.5 | 4.5±0.4 | 1290±77 | 0.51 | 304±11 | 0.85 | - | - | 84.1± 6.5 |
| MWCNT-FePc | 16.4±0.4 | 15.01±0.8 | 565±16 | 0.60 | 205±3 | 0.93 | - | - | 25.3± 1.3 |
| MWCNT-nanoFePc | 15.3±0.5 | 6.8±0.4 | 1106±19 | 0.44 | 299±9 | 0.90 | - | - | 55.6± 3.3 |
| MWCNT-CoPc | 17.6±0.2 | 105±13 | 95.2±12.1 | 0.71 | 797±17 | 0.45 | - | - | 3.6±0.5 |
| MWCNT-nanoCoPc | 17.5±0.2 | 12.5±1.7 | 819±147 | 0.70 | 544±4 | 0.92 | - | - | 30.3±3.8 |

## 4.3 Electrocatalytic Properties

### 4.3.1. *Electrocatalytic reduction of oxygen*

Transition metal macrocyclic complexes can catalyze the oxygen reduction reaction through a 2-electron or 4-electron transfer pathway to produce either $H_2O_2$ or $H_2O$. They can sometimes catalyze ORR through a mixed pathway of 2- and 4- electron transfer reduction and in rare cases, can also catalyze a 1-electron oxygen reduction, producing superoxide. Hence, comparative studies for oxygen reduction reaction were performed in 0.1 M NaOH solution with a view to establishing the catalytic efficiency of the different electrodes and determine their catalytic pathway. As shown in Figure 4.6(a), the catalytic efficiency of EPPGE-MWCNT-nanoFePc towards oxygen reduction was better (in terms of onset potential, -5 mV, and catalytic current response of approximately -1.7 mA $cm^{-2}$) compared to other electrodes that were observed at negative onset potentials (between -20 and -50 mV) and lower current densities (between -0.6 and -1.05 mA $cm^{-2}$).

In Figure 4.6(b), the EPPGE-MWCNT-nanoCoPc and EPPGE-MWCNT-CoPc showed better electrocatalytic activity towards ORR (with onset potential at approximately -60 mV and current densities of -2.26 and -1.51 mA $cm^{-2}$ respectively) compared to the other electrodes with onset potential at approximately -100 mV and current density of 0.60 mA $cm^{-2}$. Two peaks were observed at -200 mV and -600 mV for the

CoPc derivatives (Fig. 4.6(b)), which is attributed to the two 2-electron reduction of oxygen to peroxide and then to water at high potential. Moreover, mononuclear Co-$N_4$ complexes are known to favour the 2-electron transfer pathway to peroxide,[11] at the standard electrode potential of -264 mV (Ag|AgCl saturated KCl) in alkaline medium.[12]

At the EPPGE-MWCNT-nanoFePc electrode, three peaks were observed at approximately -100, -200 and -500 mV. The origin of these peaks was explored by performing further cyclic voltammetric experiments using the EPPGE-MWCNT and EPPGE-MWCNT-nanoFePc electrodes in 0.1 M NaOH solution saturated with pure nitrogen (Figure. 4.7). Three peaks can be observed in EPPGE-MWCNT-nanoFePc (Fig. 4.7(b)); peaks I and II can be attributed to $Fe^{2+}/Fe^{3+}$ and $Fe^{2+}/Fe^{1+}$ redox couples, respectively,[13] while peak III can be attributed to the surface bound carboxylic or quinone-type group on the MWCNT. This explanation is in agreement with the report by Zagal and co-workers[13] who observed that compounds with $M^{2+}/M^{3+}$ redox couples close to the onset of oxygen reduction promote the 4-electron reduction of oxygen at that potential region. As a consequence, the observed peak at -100 mV might be due to the direct reduction of oxygen to water. X-ray absorption spectroscopy was used by Yang *et al*.[14] to identify the ferrous ion coordinated with 4 nitrogen atoms as the electrocatalytic active sites for oxygen reduction in an aligned carbon nanotubes with built in Fe-$N_4$ molecule. The existence of carboxylic acid and quinone-

type groups on functionalized carbon nanotubes has also been claimed to most likely determine their electrocatalytic properties,[14,15,16] hence the role played by various surface bound quinones in the electrocatalysis of oxygen reduction has been well established.[16,17]

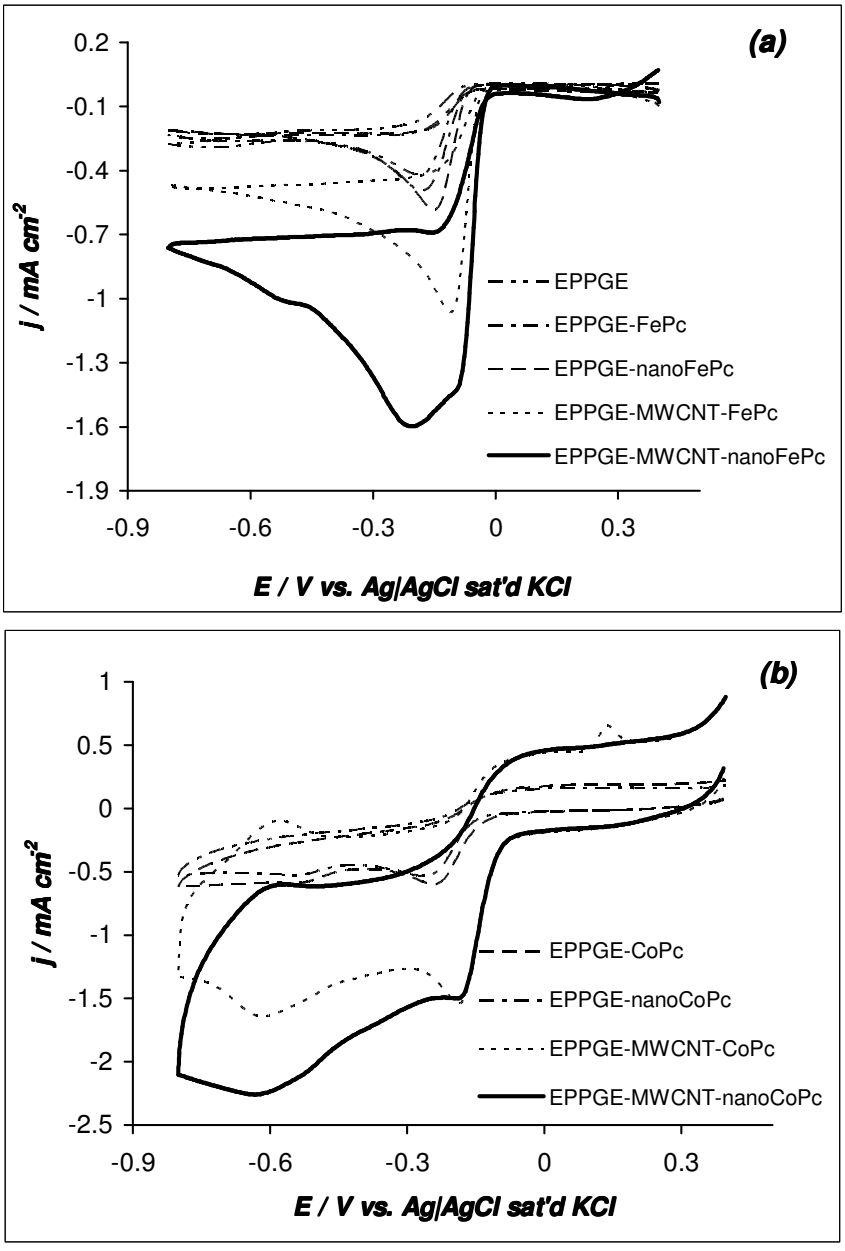


***Figure 4.6:*** *Comparative cyclic voltammograms of the various electrodes in oxygen saturated 0.1 M NaOH solution. FePc derivatives (a), CoPc derivatives (b)*

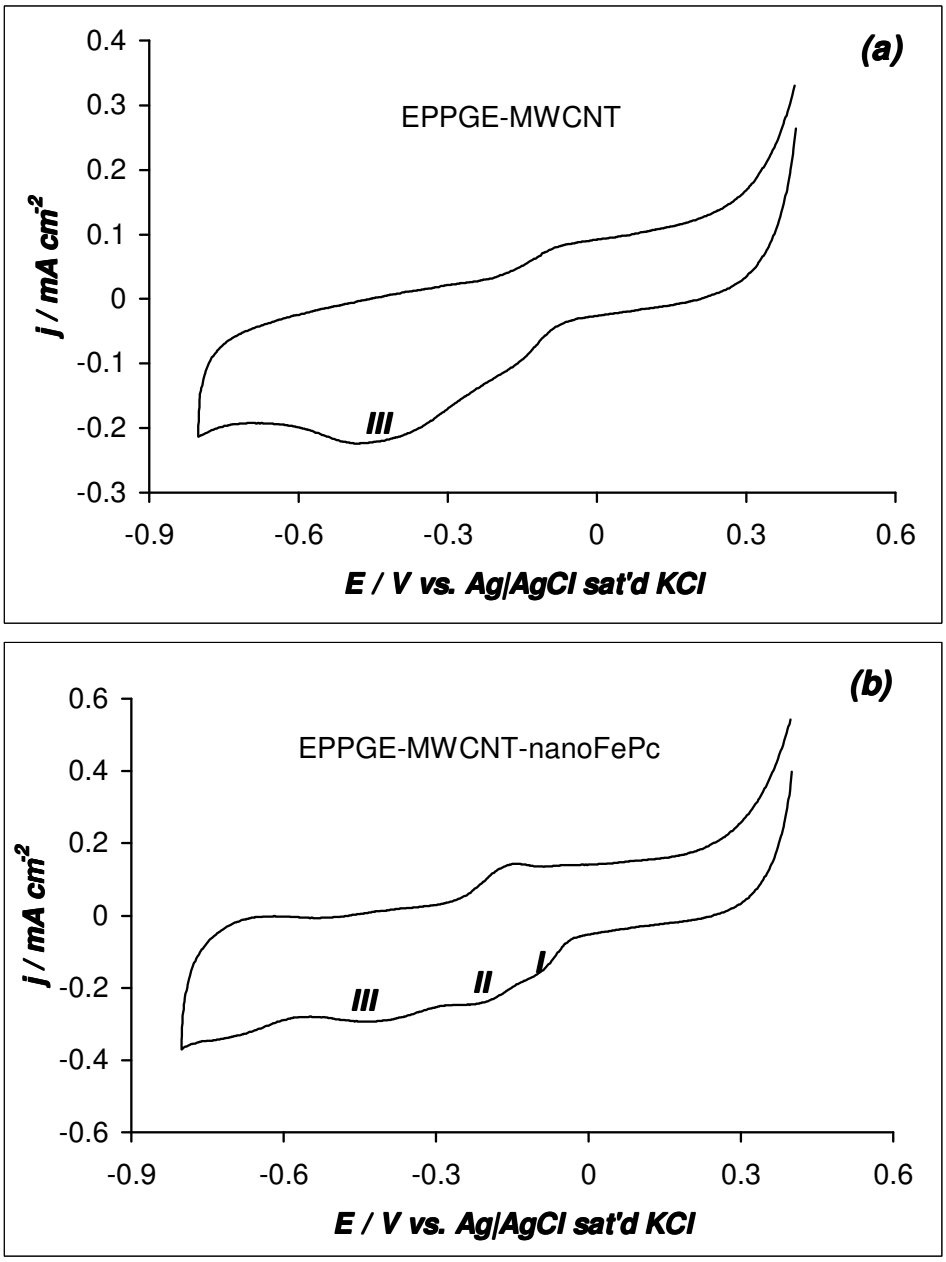


***Figure 4.7:*** *Comparative cyclic voltammograms of the different electrodes in nitrogen saturated 0.1 M NaOH (a) EPPGE-MWCNT, (b) EPPGE-MWCNT-nanoFePc. Scan rate: 25 mV* $s^{-1}$

It is known that these electrodes catalyze the 2-electron reduction of oxygen to peroxide in alkaline solution at more negative potential.[18,19] Therefore, the observed peak at -500 mV might be due

to the 2-electron reduction of oxygen to peroxide and subsequent reduction of the peroxide to water by the quinone group. The enhanced catalytic activity of the MWCNT-nanoFePc nanocomposite may be due to the large surface area of these two electrocatalytic π-electron species which provides more active sites for the adsorption of molecular oxygen. Given the high activity of the EPPGE-MWCNT-nanoFePc, all subsequent studies were performed with the electrode.

Given that multiple peaks were observed for the reduction of oxygen at EPPGE-MWCNT-nanoFePc, further analysis was carried out to establish the peak that is responsible for the 4–electron reduction of oxygen.

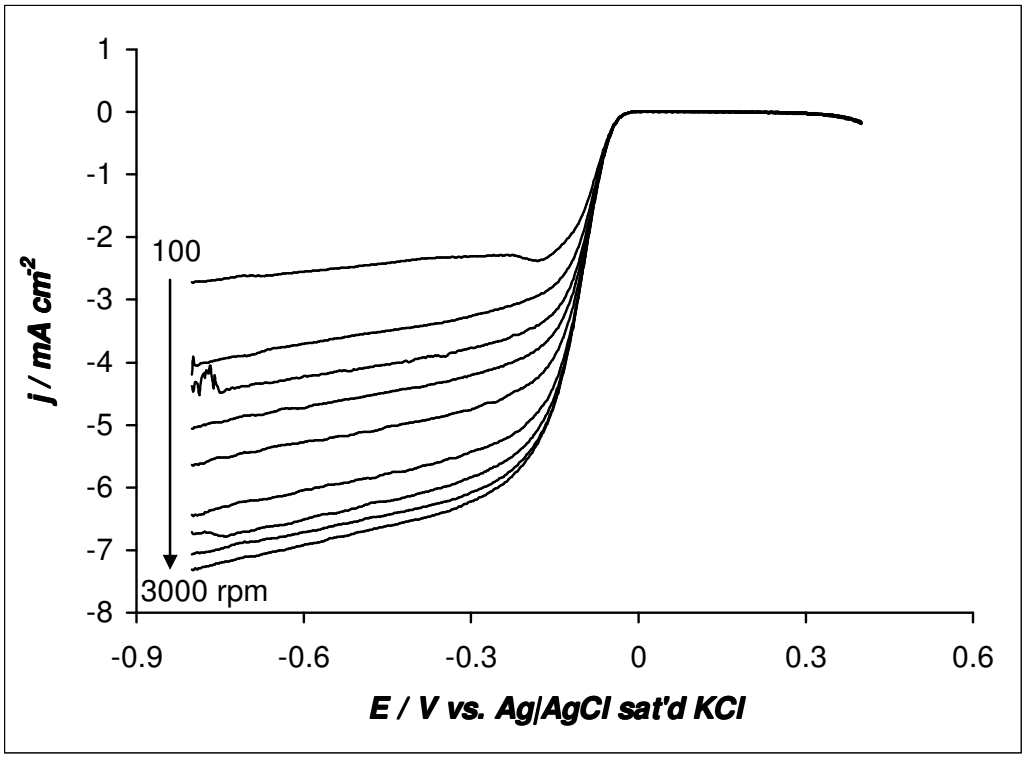


***Figure 4.8:*** *RDE polarization curves of EPPGE-MWCNT-nanoFePc in oxygen saturated 0.1 M NaOH solution*

Figure 4.8 presents the results of the rotating disk electrode (RDE) measurement in oxygen saturated 0.1 M NaOH. It can be seen that the limiting current densities increases with increasing rotation. If we assume an electrode of first order in reactant and negligible contribution from the film diffusion resistance to the measured current density, the voltammetric response of a porous RDE is described by the Koutecky–Levich (K–L) equation (equation 2.12) used to determine the number of electrons (n) involved in the reaction:[20]

$$\frac{1}{j} = \frac{1}{j_{Lev}} + \frac{1}{j_{kin}} \tag{2.12}$$

$$j_{kin} = nFkc_O\Gamma \tag{2.13}$$

$$j_{Lev} = 0.21nFD^{2/3}\gamma^{-1/6}c_{O_2}\omega^{1/2} \tag{2.14}$$

where $j_{kin}$ and $j_{Lev}$ are the kinetic and diffusion limited current densities respectively, F is Faraday constant (96485 C $mol^{-1}$), D is the diffusion coefficient of oxygen ($1.51x10^{-5}$ $cm^2$ $s^{-1}$),[20] $c_{O_2}$ is the concentration of the dissolved oxygen in the electrolyte solution ($0.25x10^{-6}$ mol $cm^{-3}$),[21] $\gamma$ is the kinematic viscosity of the electrolyte solution (0.01 $cm^2$ $s^{-1}$),[20] ω is the rotation rate in rpm, (0.21 is used when ω is expressed in rpm), *k* is the kinetic rate constant for the catalyzed oxygen reduction reaction and $\Gamma$ is the surface concentration of the adsorbed species (~ $1.8 \times 10^{-8}$ mol $cm^{-2}$).

Figure 4.9(a) shows the K–L plots obtained from the RDE data, it can be seen that the K–L lines are approximately linear; indicating that the

reaction order with respect to $O_2$ was unity for the electrode. The number of electrons transferred was estimated as 4.0, indicating that oxygen was reduced to water at approximately -100 mV as observed in Fig. 4.6(a).

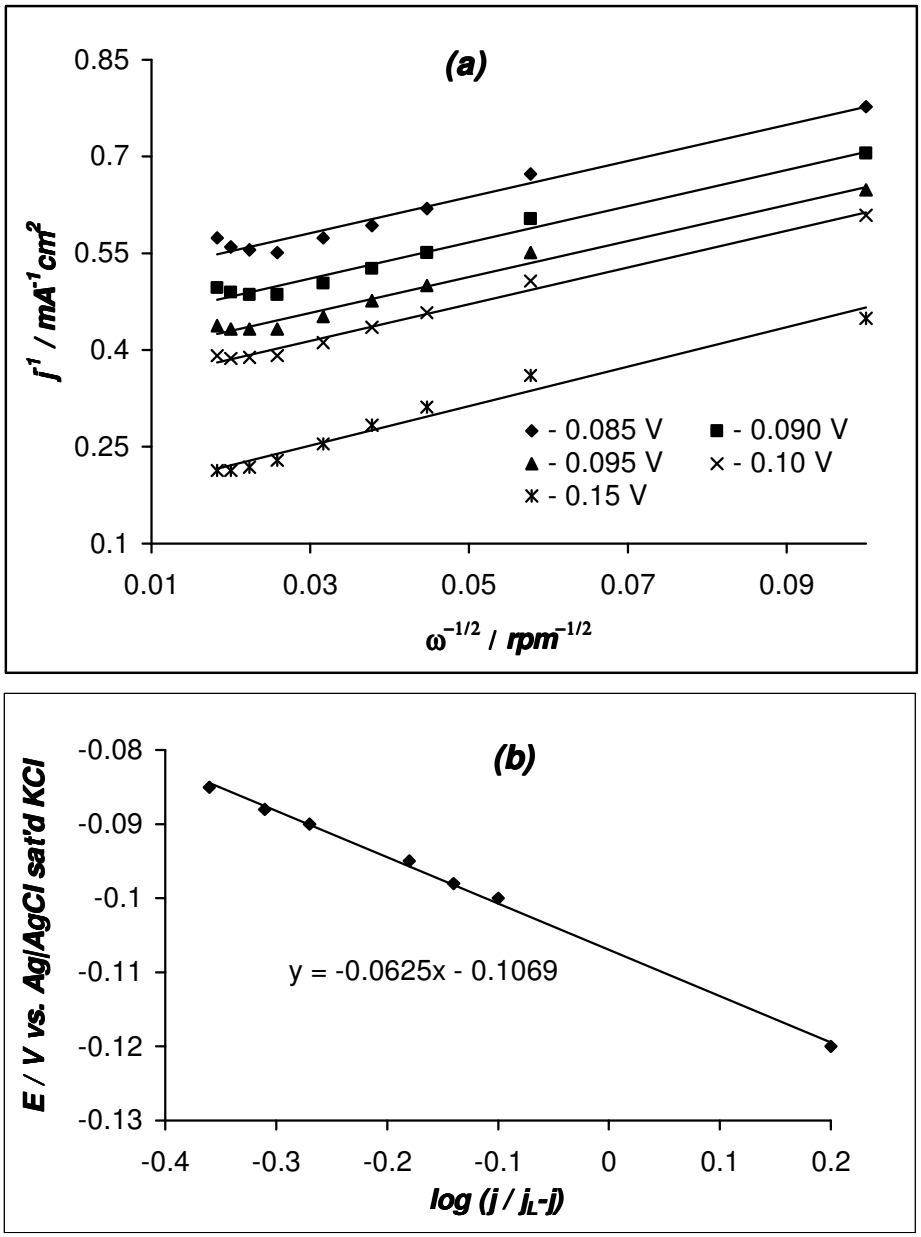


***Figure 4.9:*** *Koutecky-Levich plot (a) and Tafel plot (b) of EPPGE-MWCNT-nanoFePc generated from Figure 4.8*

This is not completely surprising considering that FePc based electrodes are well known to reduce oxygen to water. The kinetic rate constant (k) was estimated from the intercept of the K–L plot as 2.2 x $10^8$ $M^{-1}$ $s^{-1}$, a value in the same range as reported by other workers for ORR.[22,23] On correction of the polarization curve for diffusion effects for first order reaction, one obtains the Tafel equation as equation (4.3):[24]

$$E = E_{eq} - b \log j_k \tag{4.3}$$

$$j_K = \left( \frac{j}{j_L - j} \right) \tag{4.4}$$

where E is the applied potential, $E_{eq}$ is the equilibrium potential, $\alpha n$ is the kinetic parameter for the electrode process, j is the disk current density, $j_L$ is the diffusion limiting current density, b is the Tafel slope described as in equation (4.5):

$$b = \frac{2.3RT}{\alpha nF} \tag{4.5}$$

where the symbols represent their usual meaning. The Tafel slope was from the plot of E vs. log ($j/j_L$-j), Fig. 4.9(b), with j and $j_L$ obtained directly from Figure 4.8. Tafel slope was estimated as -63 mV $dec^{-1}$, resulting to $\alpha n$=0.94. Assuming a transfer coefficient ($\alpha$) of 0.5, the number of electron (n) involved in the rate-determining step would be 2. Although Beck[25] proposed a 2-electron process as the rate determining step in acidic medium, rate determining step involving a 2-electron process is not usually favoured.[20,26] Indeed, several workers have observed FePc complexes to give small Tafel slopes at

low potentials and also promote the 4-electron reduction of oxygen at that potential.[13,26,27] For example, Zagal *et al*.[27] observed a Tafel slope of -60 $mVdec^{-1}$ for oxygen reduction reaction using water-soluble iron(II) phthalocyanine-based electrode and proposed a single-electron rate determining step. The small Tafel slope was associated to such factors as redox potentials and pKa's of the phthalocyanine catalyst as well as the pH of the electrolytes.[27] In this case, it seems reasonable therefore to assume a single-electron rate determining step process, suggesting that $\alpha$ value is 0.94. The $\alpha$ value gives an indication on the conductivity of the electrode; for the most conductive electrodes, $\alpha$ = 0.5, the least conductive ones give $\alpha$ = 0.25, while $\alpha$ > 0.5 is an indication of enhanced electrocatalytic process.[28] Also, from several literature,[29-33] it may be speculated here that the global oxygen reduction reaction leading to water may be due to combined processes involving MWCNTs and nanoFePc; reaction involving nanoFePc leading to direct four-electron pathway[26] and the other due to the quinone (Q) group on the surface of the MWCNTs involving a two-electron pathway.[33] The combined high surface area of the MWCNT-nanoFePc nanocomposites is expected to encourage the adsorption of the oxygen molecule on the surface of the nanocomposites.

### 4.3.2. *Electrocatalytic oxidation of thiocyanate*

Figure 4.10 shows the comparative CV of the FePc derivative (a) and the CoPc derivative electrodes (b), in 1mM $SCN^-$ solution contained in phosphate buffer (pH 5). In both figures the MWCNT-nanoMPc electrodes gave the highest peak current densities, this is mostly likely due to the large surface area provided by the MWCNT and the nanostructured MPc species. The onset potential for the oxidation of thiocyanate is ~ 50 mV less positive at the EPPGE-MWCNT-nanoFePc compared to the EPPGE-MWCNT-nanoCoPc, with a peak current density of 3.62 mA $cm^{-2}$. This means that the electrocatalytic activity of EPPGE-MWCNT-nanoFePc towards thiocyanate oxidation is better than at EPPGE-MWCNT-nanoCoPc. Surface immobilized FePc complexes are known to sometimes show better catalysis compared to their surface immobilized CoPc counterparts.[34]

The effect of varying the scan rate on the response of EPPGE-MWCNT-nanoFePc and EPPGE-MWCNT-nanoCoPc in the thiocyanate solution was also interrogated (Figure 4.11(a) and (b)). Scan rates studies where only possible at scan rate range between 10–150 mV $s^{-1}$. This suggests that the $SCN^-$ is prone to adsorption on the EPPGE-MWCNT-nanoMPc electrodes. All plots of the peak current density against the square root of scan rate shows linearity (Figure 4.11 (c) and (d)), indicating diffusion-controlled electrode reactions.

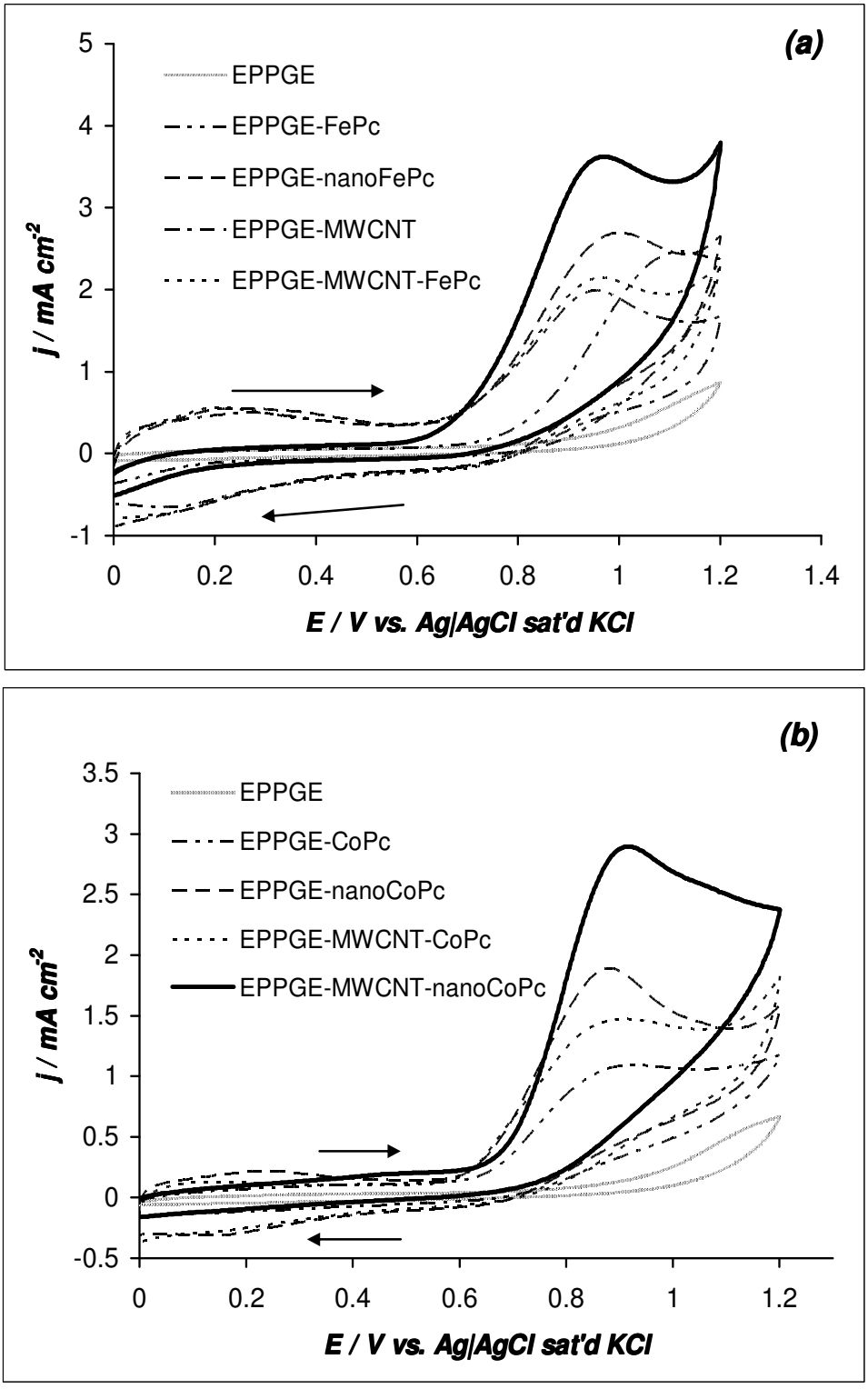


***Figure 4.10:** Comparative cyclic voltammograms of the various electrodes in 1 mM $SCN^-$ solution contained in phosphate buffer (pH 5). FePc derivatives (a), CoPc derivatives (b)*

The current density function ($j_p/v^{1/2}$) decreased with the scan rate for both electrodes (exemplified in Figure 4.12 (a) and (b)) confirming that the electrocatalytic processes observed here are coupled with chemical reaction, $EC_{cat}$ mechanisms.[35]

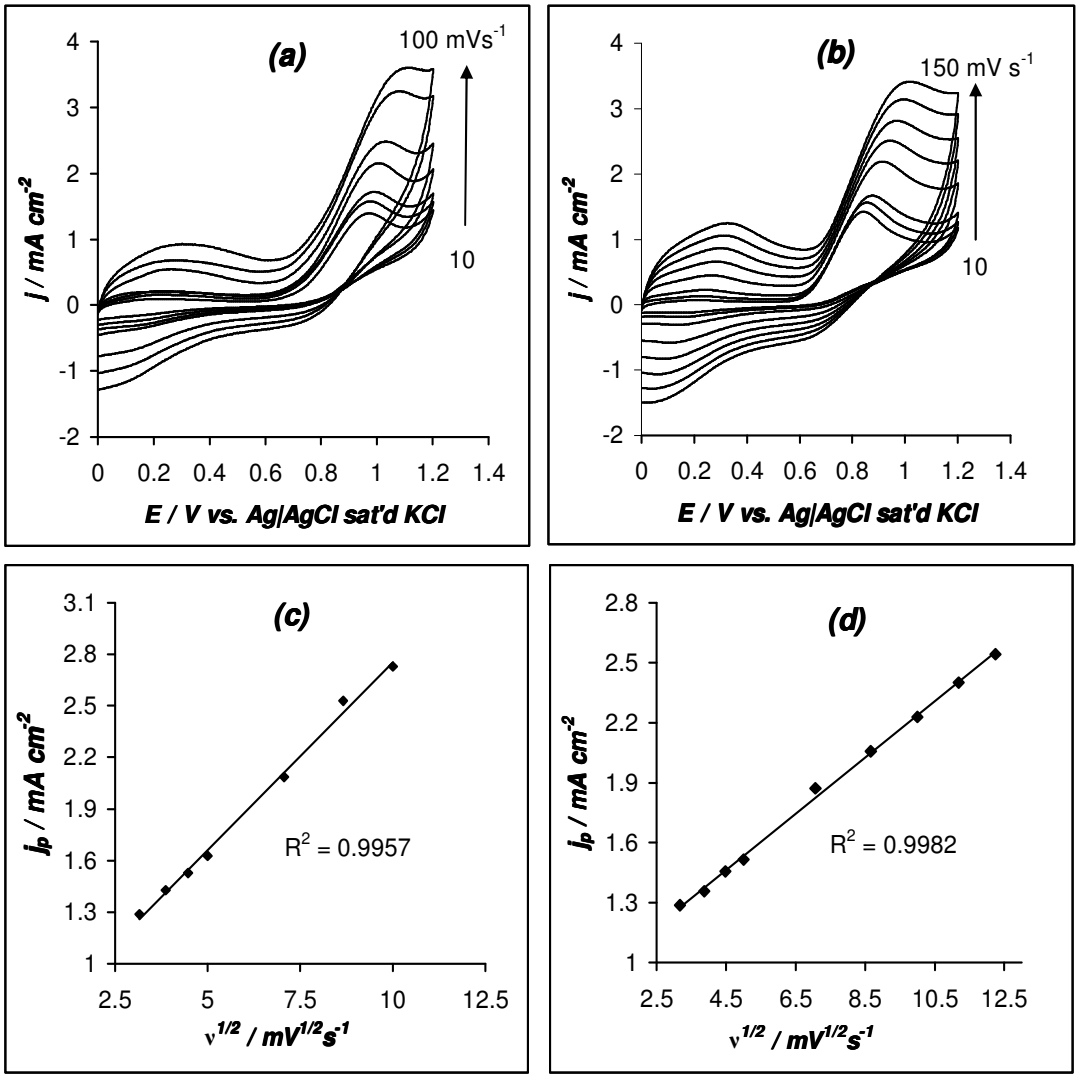


***Figure 4.11:** Cyclic voltammetric evolutions at different scan rates of (a) EPPGE-MWCNT-nanoFePc and (b) of EPPGE-MWCNT-nanoCoPc in 1.0 mM of thiocyanate (pH 5). Plots of peak current density vs. square root of scan rate (c) EPPGE-MWCNT-nanoFePc and (d) of EPPGE-MWCNT-nanoCoPc*

For irreversible reactions where diffusion and charge-transfer control the rate of reaction, the peak potentials should vary with the scan rates according to:

$$E_p = E^o - b'\left[0.78 + \ln\left(\frac{D^{1/2}}{k^o}\right) + \ln(b')^{1/2}\right] - \frac{2.303RT}{2\alpha nF}\log\nu \qquad (2.9)$$

where $k°$ is the standard heterogeneous rate constant at the standard potential ($E°$), and $b'$ is as in equation (4.5). equation (2.9) can be simplified as:

$$E_p = \frac{b}{2}\log\nu + \text{constant} \qquad (4.6)$$

where b = Tafel slope = 2.303$b'$ and all symbols retain their usual meanings. On the basis of the $\delta E_p/\delta\log\nu$ slopes of the plots of $E_p$ vs. log $\nu$, (Figure 4.12 (c) and (d)), the Tafel slopes were obtained as -163 and -181 mV $dec^{-1}$ at EPPGE-MWCNT-nanoFePc and EPPGE-MWCNT-nanoCoPc, respectively in the analyte solution. This result indicates the involvement of a 1-electron transfer electrode process in the rate-determining step (i.e., assuming electron transfer coefficient of $\alpha$= 0.50). The high Tafel slopes is associated with adsorption since it is known that Tafel slope greater than the 120 mV $dec^{-1}$ value expected for a 1- electron process is indicative of adsorption of the analytes onto the electrodes.[36,37]

The following mechanism for the electrocatalytic reactions for the thiocyanate ion is proposed:

$$\text{nano}M^{2+}\text{Pc} \rightarrow \text{nano}M^{3+}\text{Pc} + e^- \qquad (4.7)$$

$$nanoM^{2+}Pc + SCN^{-} \rightarrow [SCN\text{-}nanoM^{3+}Pc]^{-} \quad (4.8)$$

$$[SCN\text{-}nanoM^{3+}Pc]^{-} \rightarrow [SCN\text{-}nanoM^{3+}Pc] + e^{-} \quad \text{rate determining step} \quad (4.9)$$

$$[SCN\text{-}nanoM^{3+}Pc] \rightarrow nanoM^{2+}Pc + {}^{\cdot}SCN \quad (4.10)$$

$${}^{\cdot}SCN + {}^{\cdot}SCN \rightarrow (SCN)_2 \quad \text{fast} \quad (4.11)$$

$$(SCN)_2 + H_2O \rightarrow \text{reaction products} \quad (4.12)$$

(Where M is Fe or Co)

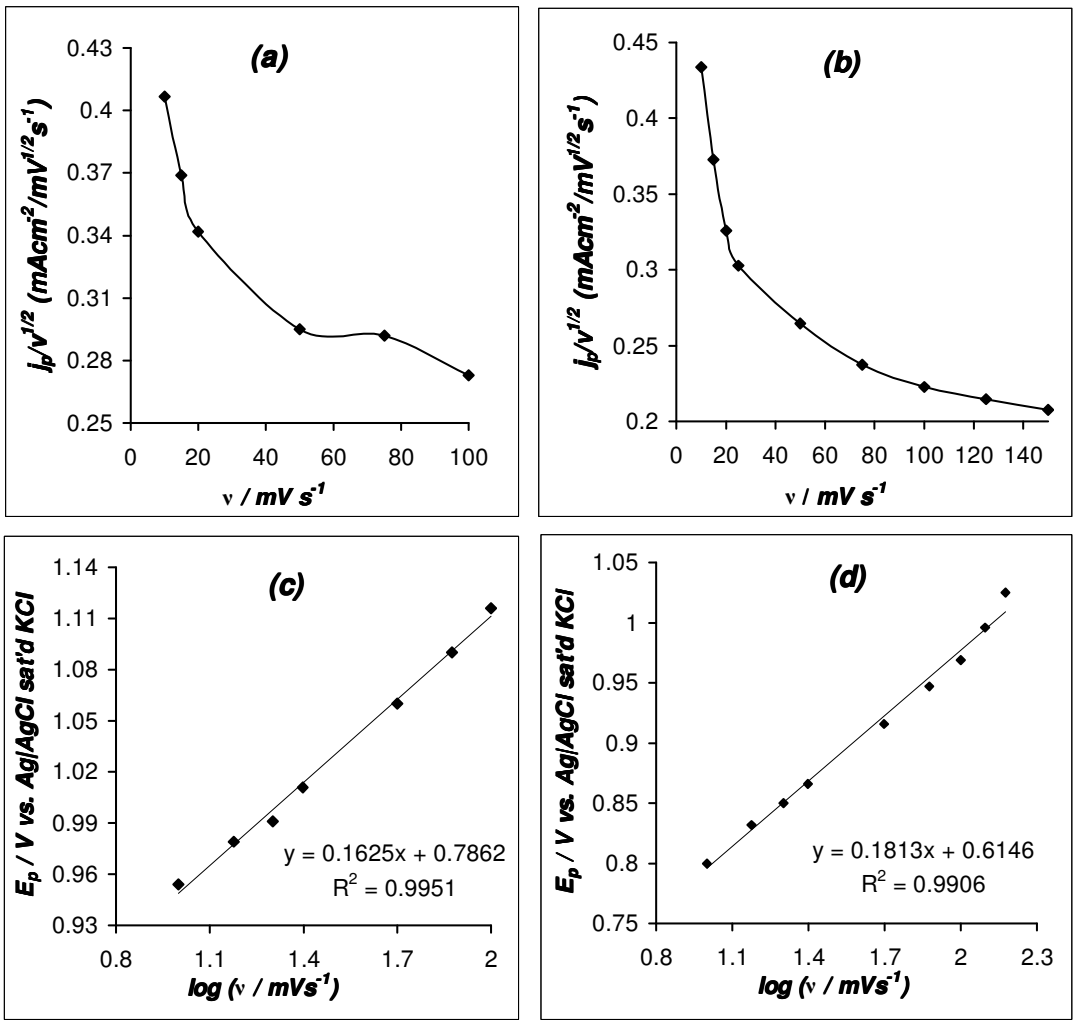


***Figure 4.12:** Current function plots: (a) EPPGE-MWCNT-nanoFePc, (b) EPPGE-MWCNT-nanoCoPc and Tafel plots: (c) EPPGE-MWCNT-nanoFePc, (d) EPPGE-MWCNT-nanoCoPc*

It is also well established that iron porphyrins and phthalocyanine-catalysed reactions of $SCN^-$ occur by initial binding of the $SCN^-$ to the $Fe^{3+}$.[38,39,40] Also, FePc complex is a natural mimic of the Horseradish peroxidase (HRP), and HRP-catalysed oxidation of $SCN^-$ occurs via the formation of the thiocyanate radical as an intermediate product, which readily dimerises to form the unstable thiocyanogen $(SCN)_2$. The $(SCN)_2$ is unstable in aqueous solution and readily hydrolyses to form some stable intermediate products.

As shown in Figure 4.13, well resolved single-step chronoamperometric evolutions were obtained at the EPPGE-MWCNT-nanoFePc (a) and EPPGE-MWCNT-nanoCoPc (b) electrodes in the absence and presence of consecutive addition of 40 µM thiocyanate in phosphate buffer solution (pH 5). The numbers 1 to 8 in Figure 4.13, correspond to 0.0, 40.0, 80.0, 120, 160, 200, 240, and 280 µM, respectively. It shows that at the conditions employed for this work, the $SCN^-$ was irreversible. Inset Figure.4.13 (a) and (b) depicts linearity between $j_p$ vs. $[SCN^-]$. Also, a linear relationship was obtained when log $j_p$ vs. log $[SCN^-]$ was plotted for both electrodes with slope values approximately 0.7143 and 0.6157, respectively which is close to unity, suggesting that one $SCN^-$ species interacts with one molecule of the nanoMPc species. From the slope and the relative standard deviation of the intercept obtained from a plot of $j_p$ vs. $[SCN^-]$, the limit of detection (LoD) were estimated as 26.34 and 21.37 µM for the

EPPGE-MWCNT-nanoFePc and EPPGE-MWCNT-nanoCoPc electrodes, respectively. $LoD = \frac{3.3s}{m}$, where s is the relative standard deviation of the intercept and m the slope.[41]

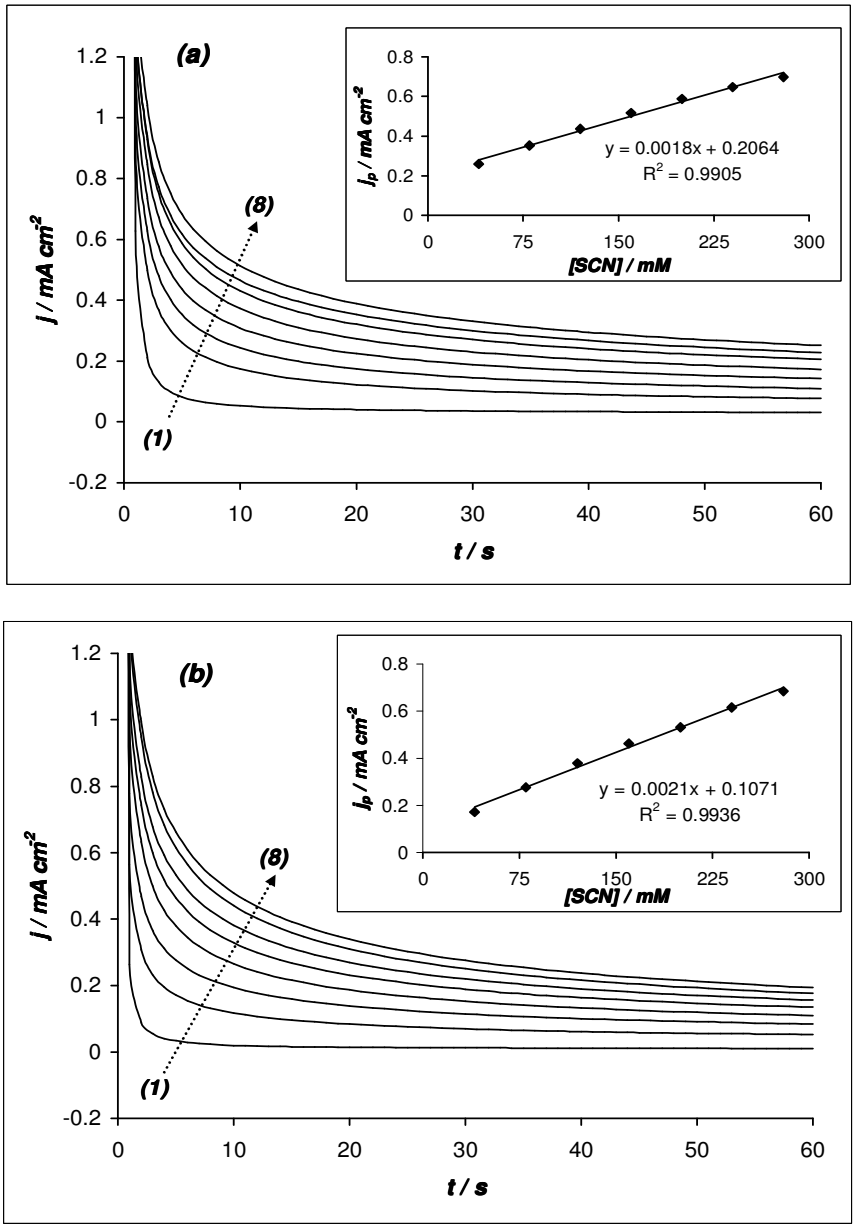


***Figure 4.13:** Chronoamperometric evolutions obtained at the EPPGE-MWCNT-nanoFePc (a) and EPPGE-MWCNT-nanoCoPc (b) electrodes in the absence and presence of consecutive addition of 40 µM thiocyanate in phosphate buffer solution (pH 5). Insets, plot of peak current density vs. concentration of thiocyanate*

### 4.3.3. *Electrocatalytic oxidation of nitrite*

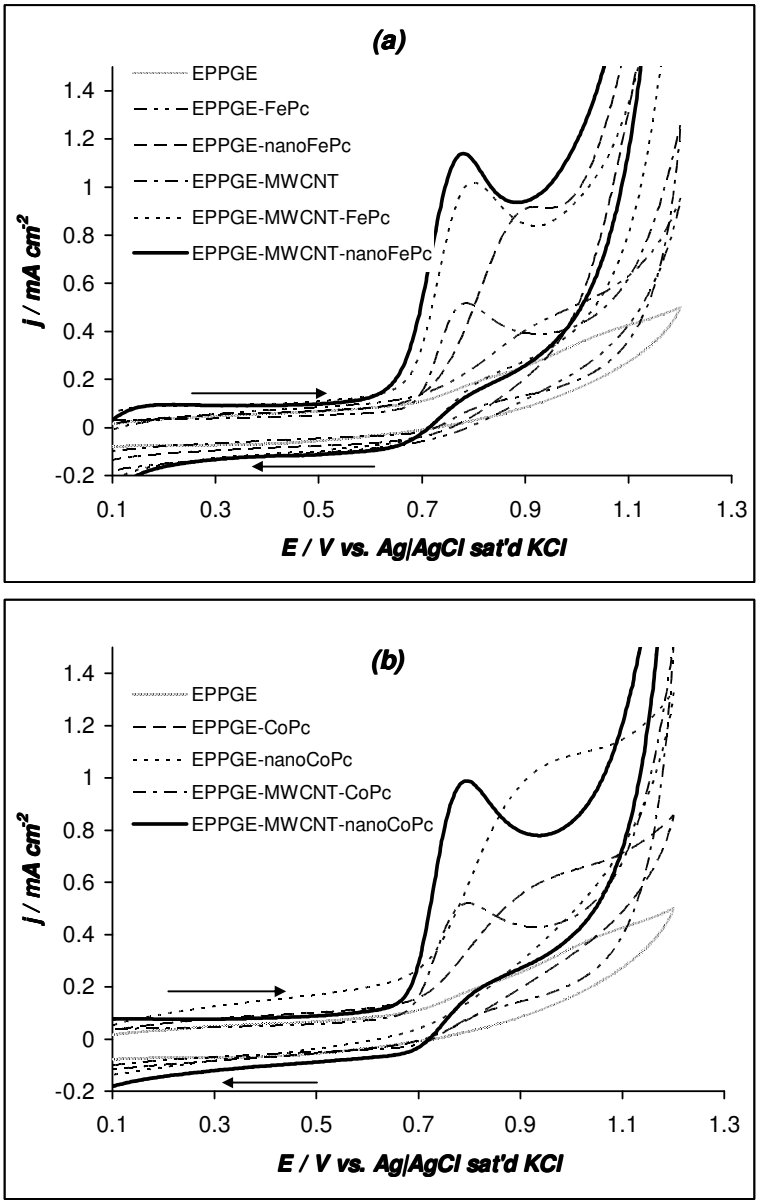


***Figure 4.14:*** *Comparative cyclic voltammograms of the various electrodes in 1mM nitrite solution contained in phosphate buffer (pH 7.4). FePc derivatives (a), CoPc derivatives (b)*

Figure 4.14 shows the cyclic voltammograms of 1mM nitrite in phosphate buffer (pH 7.4) at (a) the FePc derivative and (b) the CoPc

derivative electrodes. As observed in the figures, the EPPGE-MWCNT-nanoMPc electrodes showed better catalytic activity towards nitrite oxidation with peak potential at approximately 0.80 V compared to the other electrodes (peak potentials between 0.83 – 0.97 V) and at increased current densities, (~ 1 mA $cm^{-2}$).

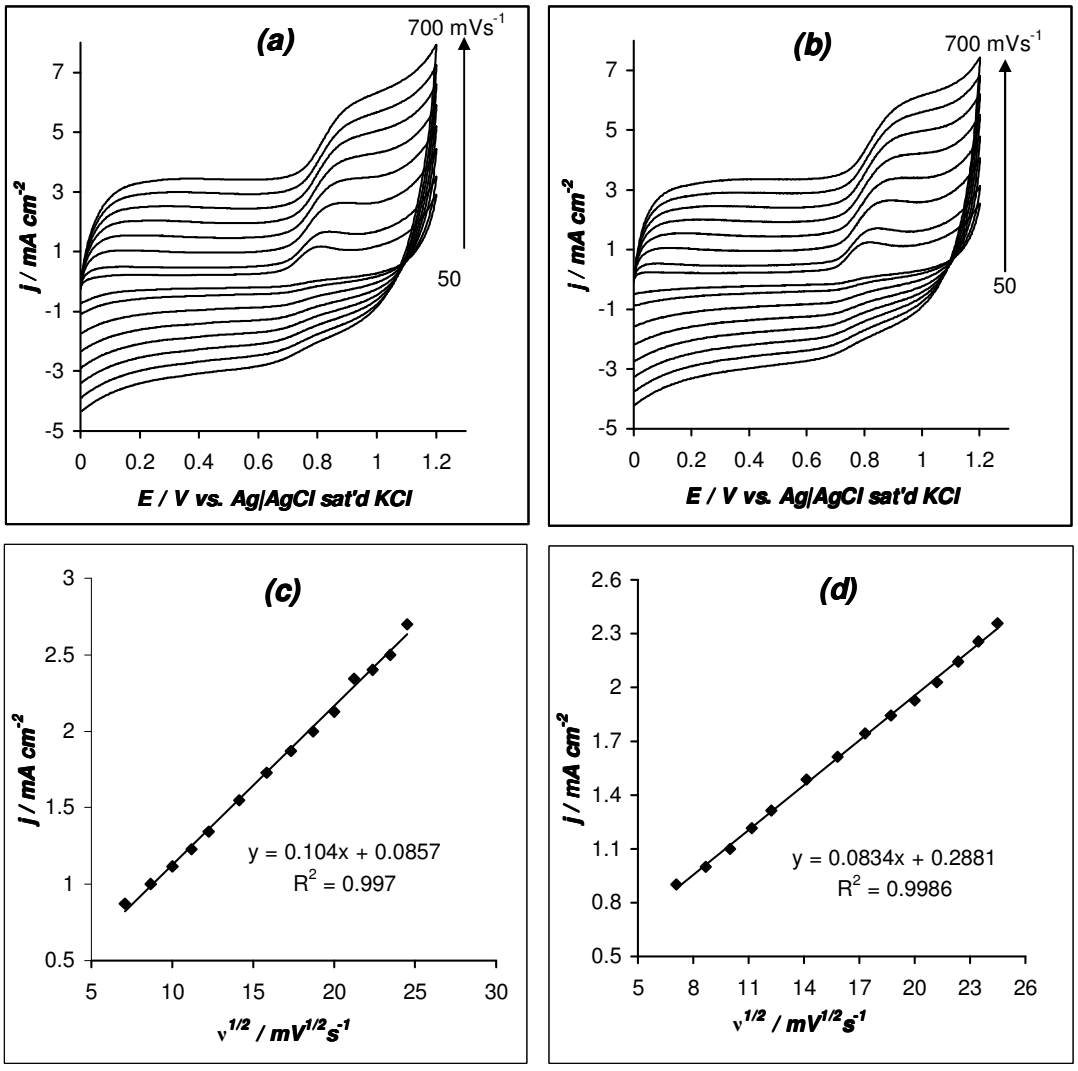


***Figure 4.15:*** *Cyclic voltammetric evolutions at different scan rates of (a) EPPGE-MWCNT-nanoFePc and (b) of EPPGE-MWCNT-nanoCoPc in 1.0 mM of nitrite (pH 7.4). Plots of peak current density vs. square root of scan rate (c) EPPGE-MWCNT-nanoFePc and (d) of EPPGE-MWCNT-nanoCoPc*

Figure 4.15 (a) and (b) shows the effect of varying the scan rate on the response of EPPGE-MWCNT-nanoFePc and EPPGE-MWCNT-nanoCoPc in the nitrite solution. Analysis of the scan rate reveals that the electrocatalytic oxidation of nitrite is a diffusion-controlled process judging from the linearity observed when the peak current density ($j_p$) was plotted against the square root of scan rate (Figure 4.15 (c) and(d)

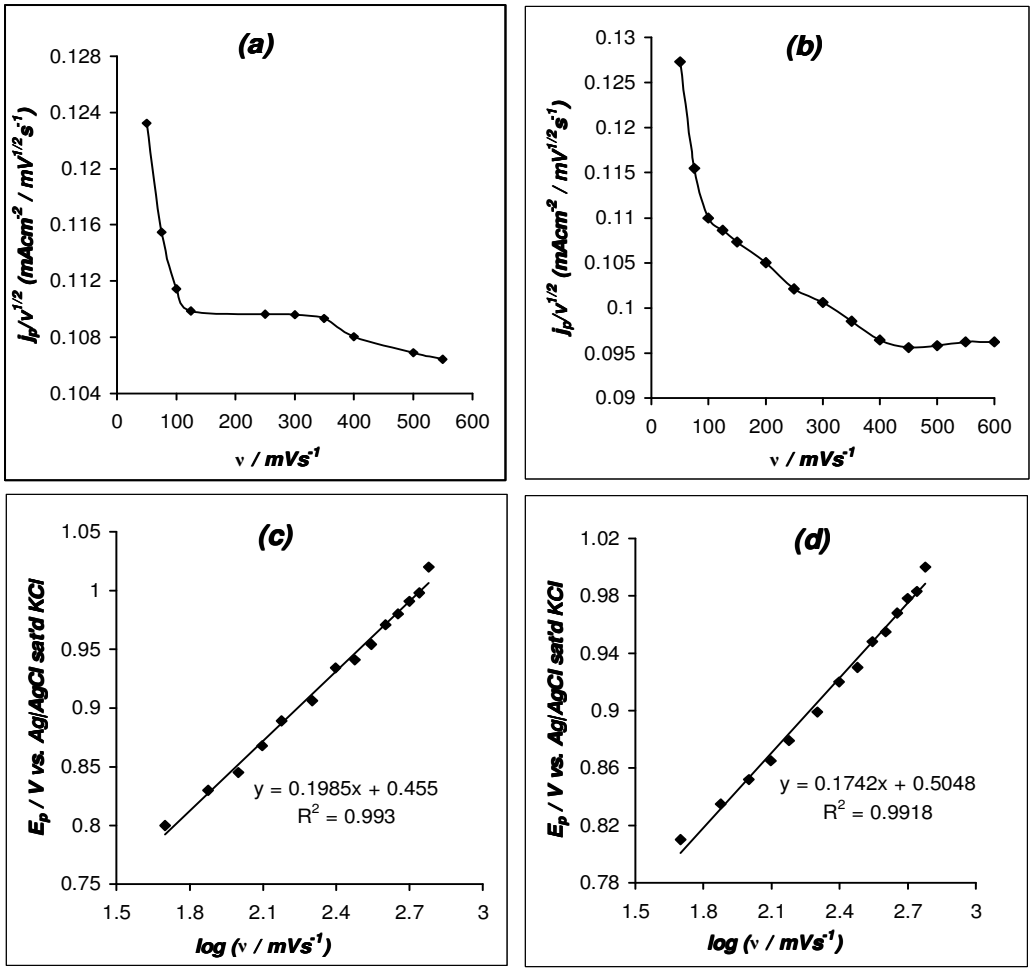


***Figure 4.16:*** *Current function plot (a) EPPGE-MWCNT-nanoFePc, (b) EPPGE-MWCNT-nanoCoPc and Tafel plot (c) EPPGE-MWCNT-nanoFePc, (d) EPPGE-MWCNT-nanoCoPc*

The electrocatalytic oxidation of nitrite by the EPPGE-MWCNT-nanoMPc electrodes was further confirm as a catalytic process judging from the shape of the plot of current density function against scan rate which is typical of a catalytic process [42] (Figure 4.16 (a) and (b)). Catalysis of nitrite oxidation by the electrodes, shows that the peak potentials shifted with the log of scan rate (Figure 4.16 (c) and (d)), this indicates that the electrocatalytic oxidation of nitrite is irreversible.[43] From the plot of $E_p$ vs. log of scan rate, and governed by equation (4.6), Tafel slope values corresponding to 199 and 174 mV $dec^{-1}$ were obtained for EPPGE-MWCNT-nanoFePc and EPPGE-MWCNT-nanoCoPc, respectively.

It is known that nitrite ion form axial ligation with central transition metal of the MPc,[44,44] it can be speculated here that the same mechanism as observed by others occurs in this case, thus the following mechanism:

$$\text{nanoM}^{2+}\text{Pc} + NO_2^- \rightarrow (NO_2^-)\text{nanoM}^{2+}\text{Pc} \quad (4.13)$$

$$(NO_2^-)\text{nanoM}^{2+}\text{Pc} \rightarrow (NO_2^-)\text{nanoM}^{3+}\text{Pc} + e^- \quad \text{rate determining step} \quad (4.14)$$

$$(NO_2^-)\text{nanoM}^{3+}\text{Pc} \rightarrow \text{nanoM}^{2+}\text{Pc} + NO_2 \quad (4.15)$$

$$NO_2 + H_2O \rightarrow NO_2^- + NO_3^- + 2H^+ \quad \text{fast} \quad (4.16)$$

(Where M is Fe or Co)

Chronoamperometric experiments, polarized at 0.80 V was carried out on the two electrodes. Figure 4.17 (a) and (b) shows the chronoamperometric evolutions of the two electrodes after successive additions of 40 μM nitrite solution in phosphate buffer (pH 7.4).

The numbers (1) to (8) corresponds to 0.0, 40.0, 80.0, 120, 160, 200, 240 and 280 μM respectively. Inset Figure.4.16 (a) and (b) depicts linearity between $j_p$ vs. [$NO_2$]. From the slope and the relative standard deviation of the intercept obtained from a plot of $j_p$ vs. [$SCN^-$], the limit of detection (LoD) were estimated as 21.89 and 23.08 μM for the EPPGE-MWCNT-nanoFePc and EPPGE-MWCNT-nanoCoPc electrodes, respectively.

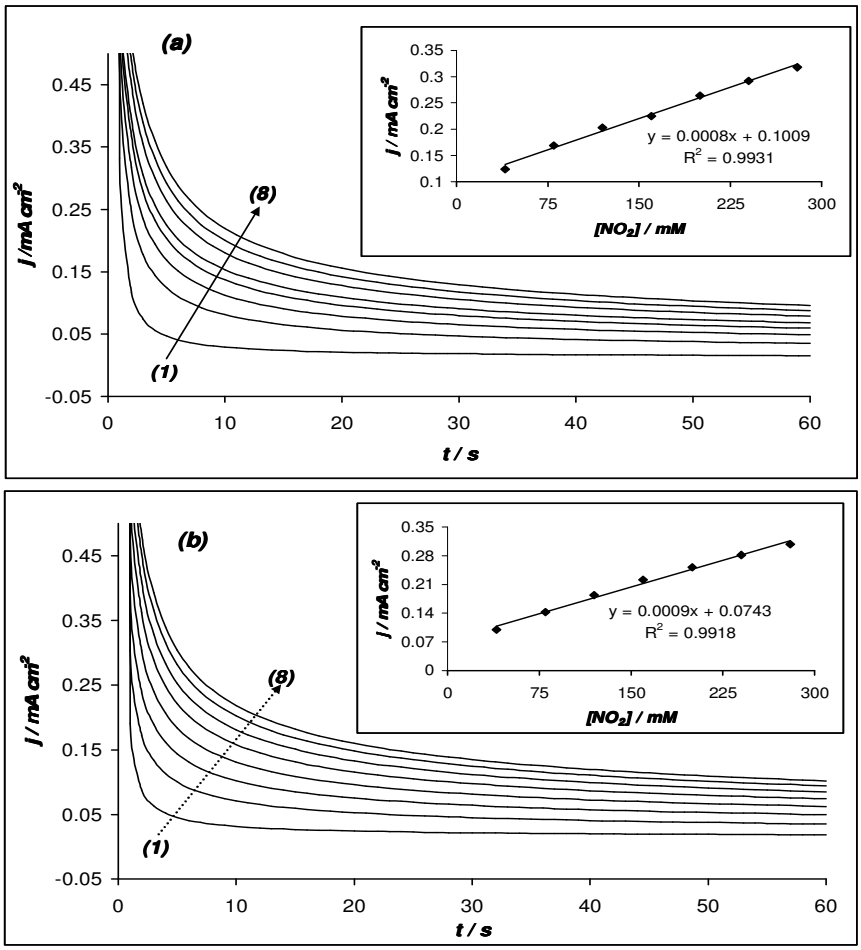


***Figure 4.17:** Chronoamperometric evolutions obtained at the EPPGE-MWCNT-nanoFePc (a) and EPPGE-MWCNT-nanoCoPc (b) electrodes in the absence and presence of consecutive addition of 40 μM nitrite in phosphate buffer solution (pH 7.4).Insets, plot of peak current density vs. concentration of nitrite*

## References

1. V. Arcoleo, V.T. Liveri, *Chem.Phys.Lett*. **258** (1996) 223
2. S. Griveau, J. Pavez, J.H. Zagal, F. Bedioui, *J. Electroanal. Chem*. **497** (2001) 75
3. K.I. Ozoemena, T. Nyokong, *Electrochim. Acta* **42** (2002) 4035
4. T.J. Davies, R.G. Compton, *J. Electroanal. Chem*. **585** (2005) 63
5. T.J. Davies, C.E. Banks, R.G. Compton, *J. Solid State Electrochem.* **9** (2005) 797
6. R.G. Compton, C.E. Banks, *Understanding Voltammetry*, World Scientific Publishing Company, London, 2007
7. I. Streeter, G.G. Wildgoose, L. Shao, R.G. Compton, Sens. Actuators B **133** (2008), 462
8. B-Y. Chang, S-Y. Hong, J-S. Yoo, S-M. Park, *J. Phys. Chem*. *B* **110** (2006) 19385
9. E. Sabatani, I. Rubinstein, *J. Phys. Chem*. **91** (1987),6663
10. M. E. Orazem, B. Tribollet, *Electrochemical Impedance Spectroscopy*, Wiley, Hoboken, NJ 2008
11. J. Zagal, P. Bindra, E. Yeager, *J. Electrochem. Soc.* **127** (1980),1506
12. E. Yeager, *J. Mol. Catal*., **38** (1986) 5
13. J. Zagal, M. Paez, A. A. Tanaka, J. R. dos Santos Jr, C. A. Linkous, *J. Electroanal. Chem.* **339** (1992) 13

14. J. Yang, D-J. Liu, N. N. Kariuki, L. X. Chen, *Chem. Commun*. (2008), 329
15. P. J. Britto, K. S. V. Santhanam, *Adv. Mater.* **11** (1999), 154
16. C. E. Banks, T. J. Davies, G. G. Wildgoose, R. G. Compton, *Chem. Commun*. (2005), 829
17. K. Tammeveski, K. Kontturi, R. J. Nichols, R. J. Potter, D. J. Schiffrin, *J. Electroanal. Chem*. **515** (2001), 101
18. G. Jurmann, K. Tammeveski, *J. Electroanal. Chem.* **597** (2006), 119
19. A. Sarapuu, K. Vaik, D. J. Schiffrin, K. Tammeveski, *J. Electroanal. Chem*. **541** (2003), 23
20. A. J. Bard, L. R. Faulkner, *Electrochemical Methods: Fundamentals and Applications* 2nd ed., Wiley, Hoboken, NJ 2001.
21. D. H. Evans, J. J. Lingane, *J. Electroanal. Chem*. **6** (1963), 283
22. R. Baker, D. P. Wilkinson, J. Zhang, *Electrochim. Acta* **53** (2008), 6906
23. N. Kobayashi, Y. Nishiyama, *J. Phys. Chem*. **89** (1985), 1167
24. I. Koç, M. Camur, M. Bulut, A. R. Özkaya, *Catal. Lett.* **131** (2009), 370
25. F. Beck, *J. Appl. Electrochem*. **7** (1977), 241
26. A. J. Appleby, J. Electroanal. Chem. **357** (1993), 117

27. J. Zagal, P. Bindra, E. Yeager, *J. Electrochem. Soc*. **127** (1980), 1506
28. J. N. Soderberg, A. C. Co, A. H. C. Sirk, V. I. Birss, *J. Phys*. *Chem. B* **110** (2006), 10401
29. C. Ercolani, M. Gardini, F. Monacelli, G. Pennesi, G. Rossi, *Inorg. Chem*. **22** (1983), 2584
30. R. Holtze, *Electrochim. Acta* **33** (1988), 1619
31. F. Monacelli, C. Ercolani, *Inorg. Acta* **346** (2003), 95
32. S. Baranton, C. Coutanceau, E. Garnier, J.-M. Leger, *J. Electroanal. Chem*. **590** (2006), 100
33. I. Kruusenberg, N. Alexeyeva, K. Tammeveski, *Carbon* **47** (2009), 651
34. K.I. Ozoemena, T. Nyokong*, Electrochemical sensors based on phthalocyanines and related complexes:* Encyclopeadia of sensors, (C.A Grimes, E.C Dickey and M.V Pishko Eds) Vol. 3 American Scientific Publishers (2006) 157-199
35. P.M.S. Monk, *Fundamentals of Electroanalytical Chemistry*, Wiley, New York, 2002
36. J-M. Zen; A. Senthil Kumar; M-R. Chang, *Electrochim. Acta* **45** (2000) 1691
37. M.E.G. Lyons, C.A. Fitzgerald, M.R. Smyth, *Analyst* **119** (1994) 855

38. K.I. Ozoemena, T. Nyokong, *J. Electroanal. Chem*. **579** (2005) 283
39. D. Nkosi, K.I. Ozoemena, *J. Electroanal. Chem*. **621** (2008) 304
40. D. Gao, J-Z. Li, R-Q. Yu, *Anal. Chem*. **66** (1994) 2245
41. G. D. Christian, *Analytical Chemistry*, 6th ed. John Wiley and Sons, New York, 2004, p.113
42. C.A. Caro, F. Bedioui, J.H. Zagal, *Electrochim. Acta* **47** (2002) 489
43. T. Malinsky, Z. Taha, *Nature* **358** (1992) 676
44. B. Agboola, T. Nyokong, *Anal. Chim. Acta* **587** (2007) 116
45. F. Matemadombo, T. Nyokong, *Electrochim. Acta* **52** (2007) 6856

# CHAPTER 5

# Microscopic, Spectroscopic, Electrochemical and Electrocatalytic Properties of Iron(II) and Cobalt(II) Octabutylsulphonylphthalocyanine*

* The following publications resulted from part of the research work presented in this chapter and they are not referenced further in this thesis:

3 K.I. Ozoemena, S.A. Mamuru, T. Fukuda, N. Kobayashi, T. Nyokong, *Electrochemistry Communication*, **11** (2009) 1221-1225

4 S.A. Mamuru, K.I. Ozoemena, T. Fukuda, N. Kobayashi, T. Nyokong, *Electrochimica Acta*, **55** (2010) 6367-6375

## 5.1 Microscopic and Spectroscopic Characterisation

Following the synthesis of the iron(II) and cobalt(II) octabutylsulphonylphthalocyanine, their surface morphologies were examined to obtain microscopic and spectroscopic information. Scanning electron microscopy and UV-visible spectroscopy were employed for this investigation.

### 5.1.1. *SEM characterisation*

Fig. 5.1 shows typical comparative SEM images of the MOBSPc (a), MWCNT (b) and MWCNT/MOBSPc (c), showing porous morphology. The images are perhaps not surprising as MWCNT-based electrodes are known to exhibit porous morphology.[1] Also; the drop-cast method used in the fabrication of the electrode mostly gives layers of modifiers rather than just a layer or mono-layer.

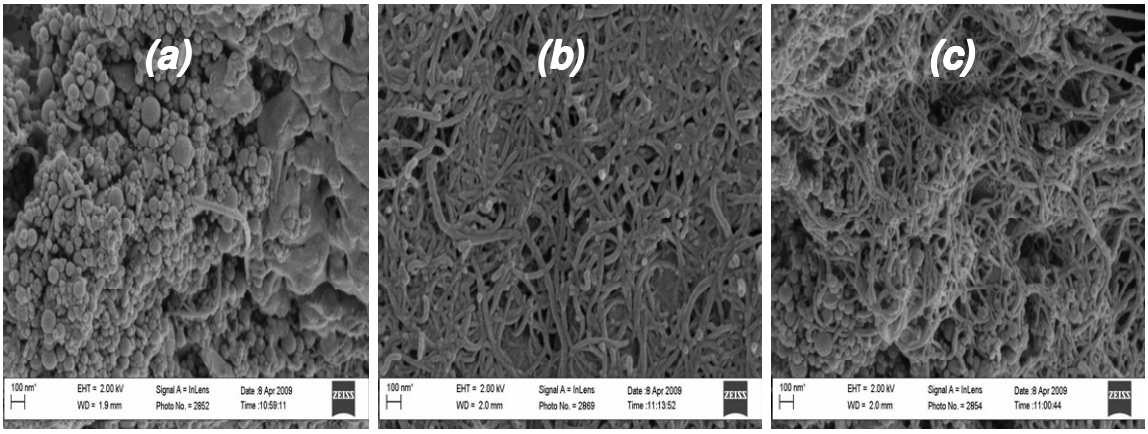


***Figure 5.1:*** *SEM images of MOBSPc (a), MWCNT (b) and MWCNT/MOBSPc*

### 5.1.2. *Characterization using UV-visible Spectrophotometer*

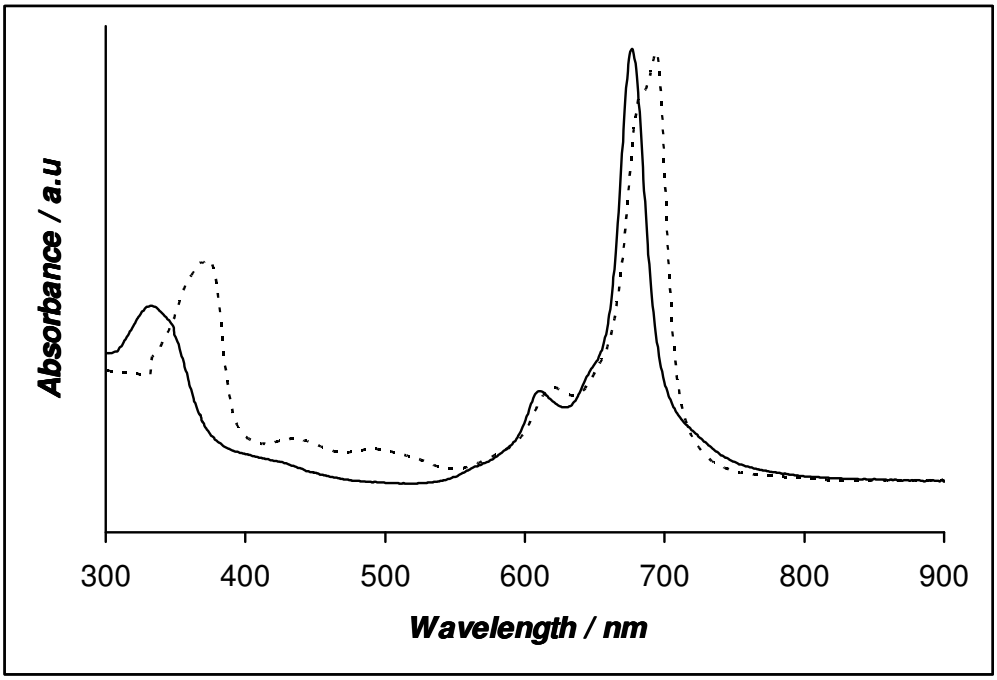


***Figure 5.2:*** *UV-visible spectrum of CoOBSPc (bold lines) and FeOBSPc (dashed lines) in chloroform.*

Figure 5.2 shows the comparative UV – visible spectrum for CoOBSPc and FeOBSPc in chloroform. The observed spectra exhibited the characteristic Q – band typical for monomeric species of metallophthalocyanine complexes. The CoOBSPc complex shows two absorption bands at 343 nm (B – band) and 678 nm (Q – band), while for FeOBSPc, the B – band and the Q – band appears at 360 nm and 696 nm respectively. The two weak bands at 435 nm and 495 nm observed for the FeOBSPc complex is typical of a low-spin six-coordinate $Fe^{II}Pc$ species and is usually associated with $Fe^{II}$ – to - ligand transfer transition.[2] Hence its presence is a good indication that

the central metal ion remain in the +2 oxidation state. Both B and Q bands of the FeOBSPc complex slightly shifted to longer wavelength when compared to the CoOBSPc complex, such a shift is an indication that the energy gap between the highest occupied molecular orbital (HOMO) and the lowest unoccupied molecular orbital (LUMO) of the FeOBSPc are narrower than those of CoOBSPc complex.[3]

## 5.2 Electrochemical Characterisation

### 5.2.1. *Solution Electrochemistry*

Figure 5.3 (a) and (b) shows typical cyclic voltammograms and inset, corresponding square wave voltammograms obtained in DMF containing about 1 mM of FeOBSPc and CoOBSPc in 0.1 M TBAP (second scans). All the redox processes were diffusion-controlled as the plots of $j_p$ vs. $\nu^{1/2}$ (not shown) were linear. The values of the redox potentials are summarized in Table 5.1. From Table 5.1, we can conclude the following. First, the first reduction and oxidation processes of the FeOBSPc and CoOBSPc complexes are attributed to the metal centers ($M^{3+}/M^{2+}$), in comparison with literature.[4] The other reduction processes of the MOBSPc complexes are ascribed to the Pc rings; Peak III' seen at the FeOBSPc species is ascribed to the electrolyte as it was unstable, disappeared at high scan rates or during repetitive scans.

***Table 5.1****: Redox potentials of compounds recorded in DMF containing 0.1 M TBAP.*

| **Compound** | **Potential, $E_{1/2}$ (V vs. Ag/AgCl wire)** | | | | |
|---|---|---|---|---|---|
| | **V** | **IV** | **III** | **I** | **II** |
| FeOBSPc | -1.62 | -1.16 | -0.67 | 0.76 | 1.48 |
| CoOBSPc | -1.61 | -1.06 | -0.58 | 0.32 | 1.63 |

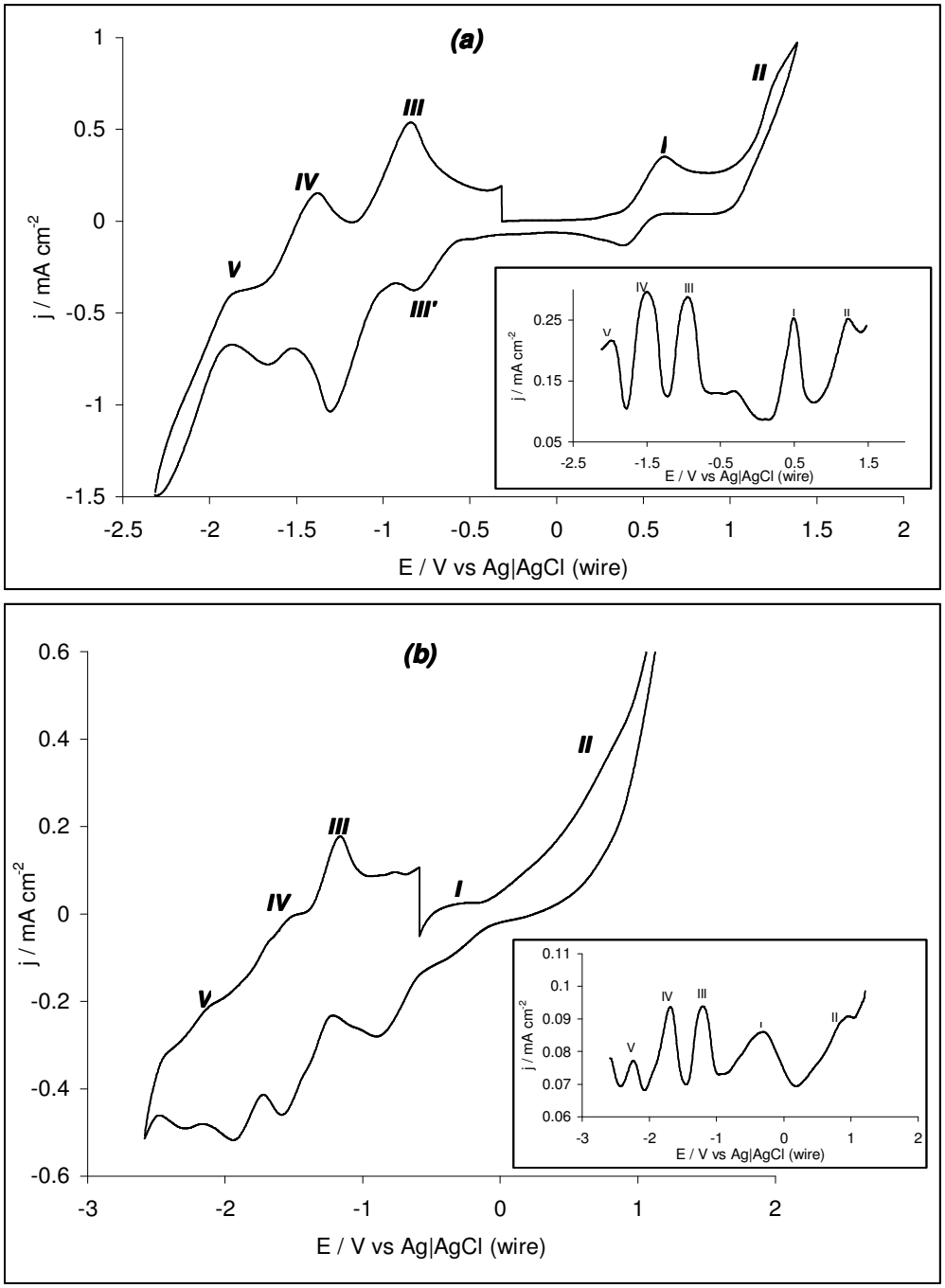


***Figure 5.3:*** *Typical cyclic voltammograms and inset square wave voltammograms for FeOBSPc (a) and CoOBSPc (b) recorded in DMF containing 0.1 M TBAP.*

### 5.2.2. *Electron transfer behaviour: cyclic voltammetry*

Figure 5.4 presents the comparative cyclic voltammograms of the various electrodes studied in a 1.0 M KCl solution containing 0.1 M $[Fe(CN)_6]^{3-}/[Fe(CN)_6]^{4-}$. This experiment is to explore the extent to which the modifying species permit the electron transfer of the $[Fe(CN)_6]^{3-}/[Fe(CN)_6]^{4-}$ to and from the underlying EPPG electrode. Analysis of the potential peak-to-peak separation ($\Delta E_p$) of the various electrodes gave the following values: EPPGE–CoOBSPc (122mV) > EPPGE–FeOBSPc (95mV) > EPPGE–MWCNT–CoOBSPc (92mV) > bare EPPGE(83mV)>EPPGE–MWCNT≈EPPGE–MWCNT–FeOBSPc (56mV).This result shows that EPPGE–MWCNT–FeOBSPc gave the fastest electron transfer, while the EPPGE–CoOBSPc was the worst. In general, the result indicates that the MPc complexes gave the best electron transport in the presence of MWCNTs rather than when alone, suggesting that MWCNT platform acts as efficient electron-conducting nanowires.

Next, the diffusion domain approximation theory as discussed in Chapter 4 was used to interrogate the type of diffusion process that could be occurring at these electrodes. It can be seen in Figure 5.4 that the voltammetric responses by the EPPGE–FeOBSPc and EPPGE–CoOBSPc electrodes are about half the current of the bare EPPGE electrode, suggesting that these electrodes behave as single macro-

blocks where "linear" diffusion plays the active role without any significant depletion in the concentration of the redox couple hence a reduced current response. The increased current response observed for the MWCNT-based electrodes is as discussed in 4.2.1.1.

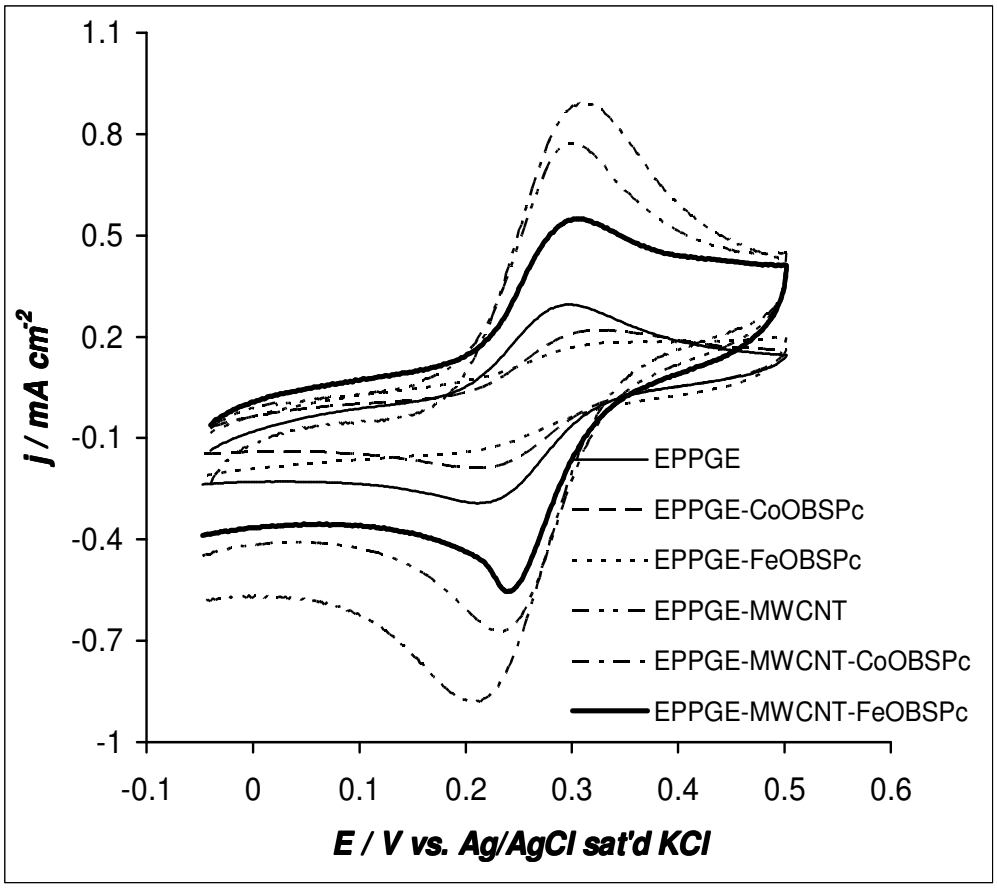


***Figure 5.4:*** *Comparative cyclic voltammograms of the various electrodes in 0.1 M* $[Fe(CN)_6]^{3-}/[Fe(CN)_6]^{4-}$ *in 1.0 M KCl solution.*

The type of diffusion occurring at the electrodes was categorized using the modified Einstein equation for the root mean square displacement of diffusing particles (equation 4.1) From the estimated ΔE values of the electrodes, ~0.15 V for the EPPGE and EPPGE–

MWCNT–FeOBSPc, ~0.17 V for the EPPGE–FeOBSPc and EPPGE–MWCNT–CoOBSPc, and ~0.19 V for the EPPGE–CoOBSPc, an approximate value of 63.5 μm was estimated as the diffusional distance, which corresponds to the type 3 behaviour of the voltammetric responses at spatially heterogeneous electrodes. This type of voltammetric behaviour is associated with an overlap of adjacent diffusion layers resulting from the small size of the inert part of the electrode.

### 5.2.3. *Electron transfer behaviour: impedimetric characterisation*

Figure 5.5(a) presents the Nyquist plots for the various electrodes studied in 1.0 M KCl solution containing 0.1M $[Fe(CN)_6]^{3-}/[Fe(CN)_6]^{4-}$. The impedance spectra of the electrodes were satisfactorily fitted with the proposed modified Randles equivalent electrical circuits (Figure 5.5(d)). The bare EPPGE and EPPGE–CoOBSPc electrodes were fitted with circuit (i), while EPPGE–FeOBSPc and the MWCNT- based electrodes were fitted with circuit (ii).The fitting parameters involve the electrolyte resistance ($R_s$), electron transfer resistance ($R_{ct}$), constant phase element (CPE), double layer capacitance ($C_{dl}$) and Warburg-type impedance ($Z_w$) which is associated with the diffusion of the ions of the redox probe. The apparent heterogeneous electron transfer rate constant ($k_{app}$) values of the electrodes were obtained using equation.

(4.2) The calculated values are shown in Table 5.2, wherein the $k_{app}$ values decreased as: EPPGE–MWCNT ($782\times10^{-3}$ $cms^{-1}$) > EPPGE–MWCNT–FeOBSPc ($372\times10^{-3}$ $cms^{-1}$) > EPPGE–MWCNT–CoOBSPc ($215\times10^{-3}$ $cms^{-1}$) > EPPGE–FeOBSPc ($93\times10^{-3}$ $cms^{-1}$) > EPPGE ($6.1\times10^{-3}$ $cms^{-1}$) > EPPGE–CoOBSPc ($0.2\times10^{-3}$ $cms^{-1}$), indicating that electron transfer processes between the redox probe and the underlying EPPGE surface are much easier at the EPPGE–MWCNT modified electrodes compared to the other electrodes. This result closely agrees with the $\Delta E_p$ trend from the CV data. The impedance of the CPE ($Z_{CPE}$) is defined as in (equation (2.26)). From the Bode plots (Figure 5.5(b) and (c)), the slopes of the log Z vs. log f plot at the mid frequency region are less than the ideal −1.0 for pure capacitive behaviour, which is indicative of pseudocapacitive behaviour. In circuit Figure 5.5(d) (ii), notice that the Warburg impedance in the ideal Randles circuit has been replaced by the $C_{dl}$, which simply describes the porous nature of the concerned electrodes. All attempt to replace the $C_{dl}$ in circuit (ii) with a CPE (which is a more practical situation) led to huge fitting errors. This should not be interpreted to signify that the $C_{dl}$ is a pure double layer capacitance. According to Orazem and Tribollet,[5] frequency dispersion leading to CPE behaviour takes place through the distribution of time constants along either the area of the electrode surface (involving a 2-dimensional aspect of the electrode, which mimics an ideal RC behaviour) or along the axis normal to the

electrode surface (involving a 3-dimensional surface). Thus, one may conclude here that the observed impedimetric behaviour of the modified electrodes is CPE. The data from the Bode plots (i.e.,–phase angle vs. log f) further confirms the absence of ideal capacitive behaviour as the observed phase angles are less than the 90° expected of an ideal capacitive behaviour.

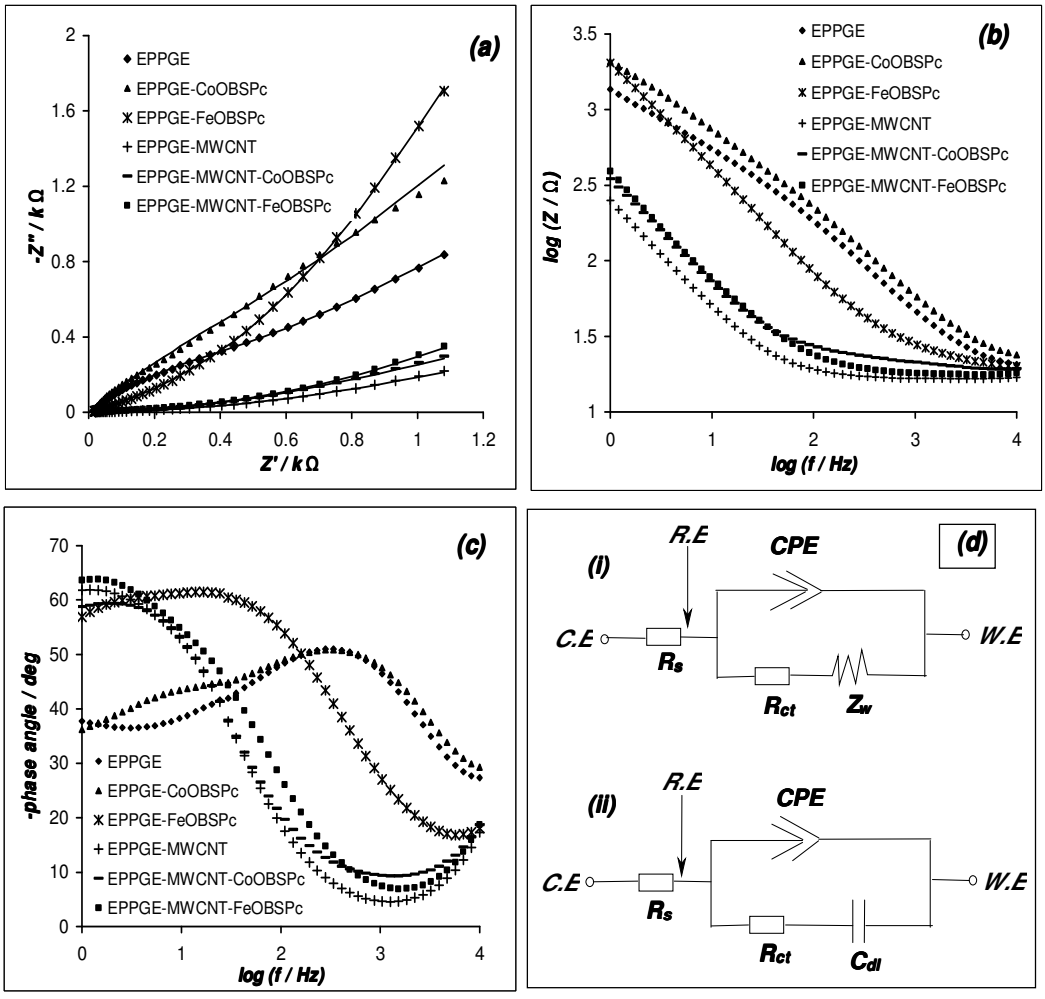


***Figure 5.5:*** *(a) Comparative Nyquist and (b), (c) Bode plots of the various electrodes in 0.1 M $[Fe(CN)_6]^{3-}$/$[Fe(CN)_6]^{4-}$ 1.0 M KCl solution. Proposed equivalent electrical circuits (d)*

***Table 5.2:*** *Impedance parameters and $\Delta E_p$ values obtained for the various electrodes studied in 0.1 M $[Fe(CN)_6]^{3-}$ /$[Fe(CN)_6]^{4-}$ in 1 M KCl solution*

| **EPPGE modifier** | **Electrochemical impedance spectroscopic parameters** | | | | | | |
|---|---|---|---|---|---|---|---|
| | $R_s$ / Ω | $R_{ct}$ / kΩ | CPE / µF | n | $C_{dl}$ /µF | $10^3 k_{app}$ /cm $s^{-1}$ | $\Delta E_p$ / mV |
| EPPGE* | 13.8±0.35 | 0.627±0.004 | 51.9±3.22 | 0.70±0.08 | - | 6.1±0.4 | 83 |
| CoOBSPc* | 13.6±0.53 | 1.438±0.015 | 62.3±4.05 | 0.70±0.08 | - | ~ 0.2 | 122 |
| FeOBSPc | 14.8±0.41 | 0.040±0.003 | 143.9±2.73 | 0.60±0.07 | 652±51.51 | 93.2±7.8 | 95 |
| MWCNT-CoOBSPc | 14.9±0.89 | 0.018±0.001 | 875±50.75 | 0.50±0.03 | 137±10.14 | 214.7±16.5 | 92 |
| MWCNT-FeOBSPc | 16.2±0.49 | 0.010±0.003 | 697.4±35.57 | 0.70±0.03 | 54±1.73 | 371.7±14.6 | 56 |
| MWCNT | 14.7±0.49 | 0.005±0.002 | 1066± (6.1) | 0.60±0.04 | 177±24.25 | 782.3±23.3 | 56 |

*$Z_w$ of EPPGE and CoOBSPc is (319±0.008) x $10^{-6}$ Ω and (186±0.009) x $10^{-6}$ Ω, respectively.

## 5.3 Electrocatalytic Properties

### 5.3.1. *Electrocatalytic reduction of oxygen*

Figure 5.6 shows the comparative CV of the various electrodes studied in oxygen saturated 0.1M NaOH solution. The EPPGE–MWCNT–FeOBSPc electrode showed the best response in terms of current density, peak potential and less onset potential compared to other electrodes. The current density is about three times higher with a peak potential at ~−0.18 V and an onset potential of ~0.0 V compared to the EPPGE–MWCNT–CoOBSPc electrode with an onset potential of ~−0.15 V. Expectedly, both EPPGE–MWCNT and EPPGE–MWCNT–CoOBSPc electrodes showed two peaks at ~−0.2 and −0.5 V, which maybe attributed to the two-step 2-electron reduction of oxygen. This result agrees with literature as it is well known that while the FePc catalysts follow the direct 4-electron pathway,[6,7] CNT-based electrodes[8,9] and CoPc-based electrodes[10] catalyze the ORR via the 2-electron reduction of oxygen to hydrogen peroxide and then the hydrogen peroxide to water in alkaline medium at more negative potentials. The enhanced ORR activity of the EPPGE–MWCNT–FeOBSPc might be due to the structural properties of the carbon nanotube; comprising multiple cylindrical shell of graphite sheets of nanometer diameters, channels in the tubular structure, and the topological defects on the tube surface,

all make the carbon nanotubes provide enough effective reaction sites to increase electron exchange rate and at less negative potentials.[9]

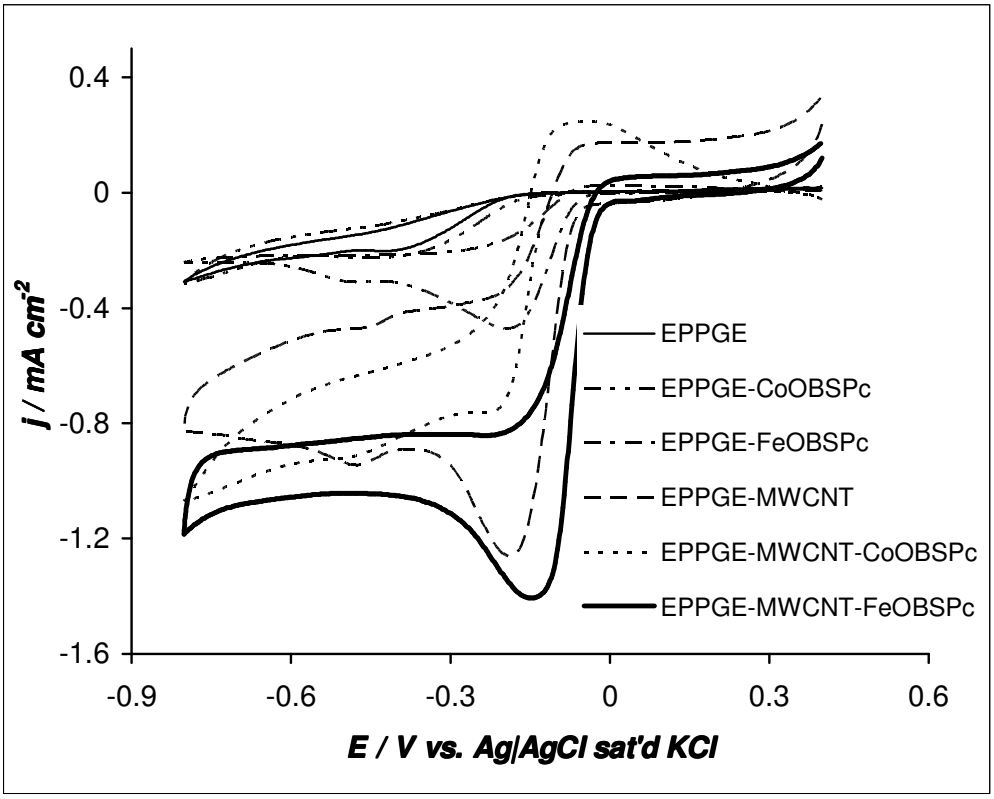


***Figure 5.6:*** *Comparative cyclic voltammograms of the electrodes in 0.1 M NaOH saturated with oxygen. Scan rate: 10 mV* $s^{-1}$

The central Fe of the FePc complexes undergo axial co-ordination with O-donor and N-donor molecules, faster and more stable, than their CoPc counterparts,[11-14] which further explains the higher ORR activity of the FeOBSPc than the CoOBSPc. Indeed, it is exciting to observe here that the onset potential of the oxygen reduction at the EPPGE–MWCNT–FeOBSPc electrode (0.0 V vs. Ag|AgCl) is much better than that recently reported by Gong *et al*.[15] (approximately −0.2 V vs.

Ag|AgCl) for a commercial platinum catalyst supported on carbon, but comparable to the recent work (−0.08 V vs. Ag|AgCl) by Chen and Chen[16] for gold nanoclusters supported on glassy carbon. Because of its best performance, the EPPGE–MWCNT–FeOBSPc electrode was used for subsequent studies.

#### 5.3.1.1. *Effect of scan rates*

Cyclic voltammetry was employed to investigate the effect of varying scan rate on the response of the EPPGE–MWCNT–FeOBSPc electrode in the reduction of molecular oxygen in 0.1M NaOH solution saturated with pure oxygen. Figure 5.7(a) presents the CV evolutions of the EPPGE–MWCNT–FeOBSPc electrode at different scan rates (25–500 $mVs^{-1}$). Inset of Figure 5.7(a) describes the linear relationship between the reduction peak current ($I_p$) and the square root of scan rate ($\nu^{1/2}$), implying that the process is diffusion controlled.

As an irreversible process, it can be observed that the peak potential ($E_p$) shifts to more negative values with increasing scan rate ($\nu$). This process is governed by equation (4.6):[17,18]

$$E_p = \frac{b}{2}\log \nu + \text{constant} \qquad (4.6)$$

$$b = \frac{2.3RT}{\alpha nF} \qquad (4.5)$$

where R is the ideal gas constant, T the absolute temperature, F the Faraday constant, $\alpha$ the charge transfer coefficient and n is the number of electrons involved in the rate-determining step. The plot of peak potential ($E_p$) against logarithm of scan rate (log $\nu$), Figure 5.7(b), gave a straight line with a Tafel slope of approximately 124 mV $dec^{-1}$, with an $\alpha$ value of 0.48.The Tafel slope is close to the theoretical 118 mV $dec^{-1}$ for a 1-electron process involved in the rate-determining step

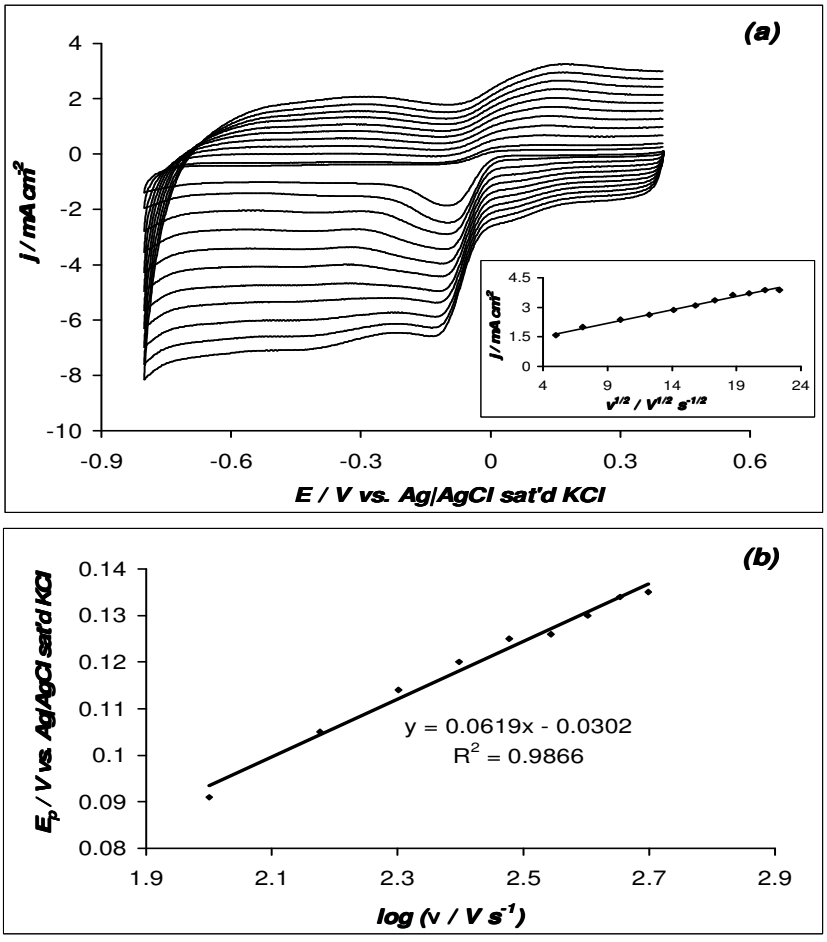


***Figure 5.7:*** *(a) Cyclic voltammetric evolutions of the EPPGE-MWCNT-FeOBSPc electrode at varying scan rates. Inset shows linear relationship between the reduction peak current ($I_p$) and square root of scan rate ($\nu^{1/2}$). (b) Plot of peak potential ($E_p$) against the logarithm of scan rate (log $\nu$).*

### 5.3.1.2. *Chronocoulometric studies*

Figure 5.8 presents the chronocoulometric evolutions of the EPPGE–MWCNT–FeOBSPc electrode in oxygen saturated and nitrogen saturated 0.1M NaOH solution. The charge on the oxygen-saturated electrode is about 3 folds more than the nitrogen-saturated electrode, this is indicative of the electro-active nature of the electrode towards the reduction of oxygen. After subtraction of the background charge, a plot of charge (Q) against square root of time ($t^{1/2}$) was generated from the plot in Figure 5.8(a) for the oxygen-saturated electrode. The plot in Figure 5.8(b) reveals a linear relationship ($R^2$ = 0.9995), characteristic of diffusion-controlled electrode process. According to Cottrell equation,[18] the number of electrons (n) involved in the reduction of oxygen can be estimated from the slope of the plot of Q vs. $t^{1/2}$ using equation (5.1):[18]

$$Q = \frac{2nFAcD^{1/2}t^{1/2}}{\pi^{1/2}} \qquad (5.1)$$

where F is Faraday constant, A is the electroactive area of the EPPGE–MWCNT–FeOBSPc (~0.1cm$^2$), c is the concentration of oxygen in oxygen saturated 0.1 M NaOH ($0.25\times10^{-6}$ mol cm$^{-3}$), D is the diffusion coefficient of oxygen in an aqueous solution ($1.51\times10^{-5}$ cm$^2$ s$^{-1}$)[19] and slope = 30 μCs$^{-1/2}$. The number of electrons involved in the reduction of oxygen was estimated to be ≈4.

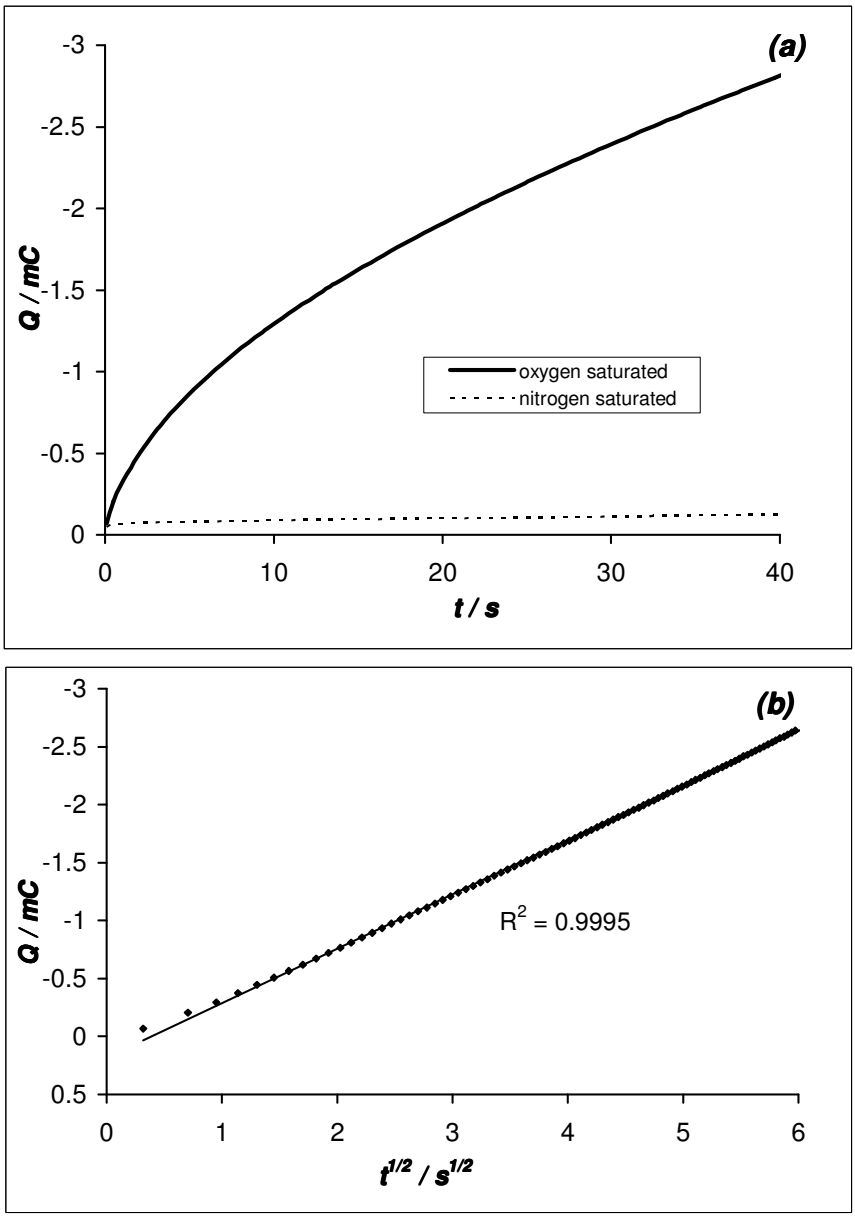


**Figure 5.8:** (a) Chronocoulometry curves of EPPGE-MWCNT-FeOBSPc in 0.1 M NaOH saturated with oxygen (bold line) and saturated with nitrogen (dashed line). (b) Plot of charge (Q) against square root of time ($t^{1/2}$).

### 5.3.1.3. *Hydrodynamic voltammetry investigation*

Hydrodynamic voltammetry was used to carry out further study on the electro-reduction of molecular oxygen on the EPPGE–MWCNT–FeOBSPc

electrode by scanning linearly from 0.4 to −0.8V in oxygen saturated 0.1 M NaOH electrolyte solution (Figure 5.9(a)). The result presented in Figure 5.9(a) clearly shows that as the rotation rate increases there is an enhancement of the limiting current. Figure 5.9(b) presents the Koutecky–Levich plot for the electro-catalytic reduction of molecular oxygen on EPPGE–MWCNT–FeOBSPc electrode in oxygen saturated 0.1 M NaOH generated from Figure 5.9(a), and govern by the Koutecky–Levich equation (2.12). The linearity observed when the inverse of the current density was plotted against the inverse square root of rotation rate implies that the electrode process is diffusion controlled and the reaction is first order. Furthermore, the slope and intercept from the straight line, respectively correspond to $j_{Lev}$ (equation (2.14)) and $j_{kin}$ (equation (2.13)). The number of electrons (n) transferred per oxygen molecule was calculated from equation (2.14) and estimated to be ~4 at −0.15 V. This potential is close to the peak potential observed for EPPGE–MWCNT–FeOBSPc electrode in Figure 5.6. Also, this result supports our finding using chronocoulometry. The dashed lines in Figure 5.9(b) are theoretical lines calculated using equation(2.14) for n = 4 and n = 2.The figure reveals that oxygen reduction at EPPGE–MWCNT–FeOBSPc electrode follows the 4-electron transfer Levich plot, suggesting that oxygen reduction at EPPGE–MWCNT–FeOBSPc electrode proceeds via a single 4-electron transfer.

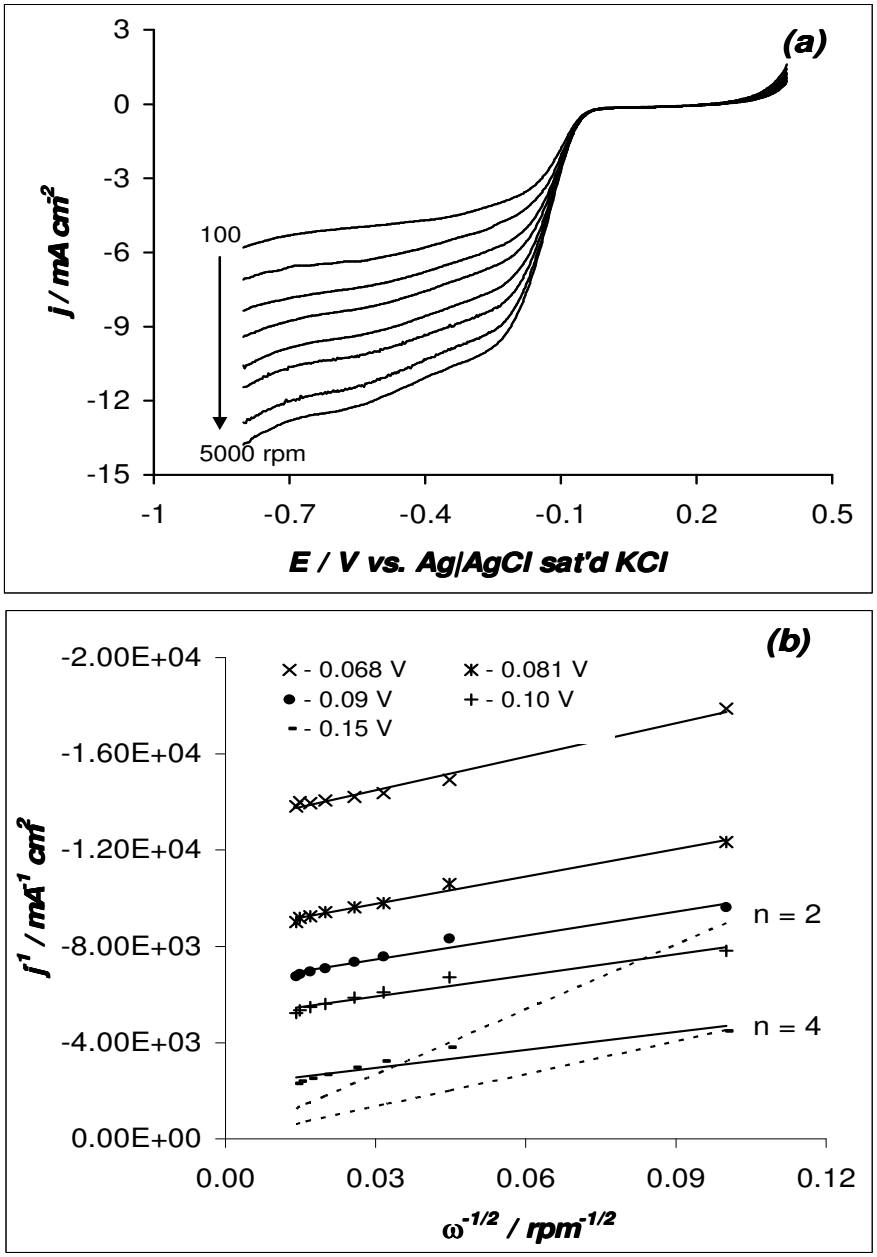


***Figure 5.9:*** *(a) RDE voltammetry for oxygen reduction on an EPPGE-MWCNT- FeOBSPc electrode in oxygen saturated 0.1 M NaOH. Scan rate: 10 mV $s^{-1}$. (b) Koutecky-Levich plots for oxygen reduction on EPPGE-MWCNT-FeOBSPc electrode in oxygen saturated 0.1 M NaOH solution.*

### 5.3.2. *Electrocatalytic oxidation of thiocyanate*

Figure 5.10 presents the comparative cyclic voltammograms of the electrodes studied in 1mM thiocyanate solution (phosphate buffer pH 5). As seen, the EPPGE-MOBSPc electrodes shows no catalytic response towards thiocyanate oxidation, this is probably due to the strong electron-withdrawing effect of the substituents attached to the ring of the phthalocyanine which makes oxidation difficult. However, the EPPGE-MWCNT gave the best catalytic response towards thiocyanate oxidation with oxidation peak at approximately 0.80 V. The catalytic activity of MWCNT has been reported,[20] and was attributed to the edge-plane- like sites nanotube ends where there is a possibility of the presence of oxygenated groups, as in this case, the purification of the MWCNT introduces some oxygenated groups. In comparison, the EPPGE-MWCNT-CoOBSPc and EPPGE-MWCNT-FeOBSPc exhibited irreversible oxidation peaks at approximately 0.90 and 1.0 V respectively, suggesting that the introduction of the MOBSPc shifted the potential to more positive potential hence the slow electron transfer at these electrodes.

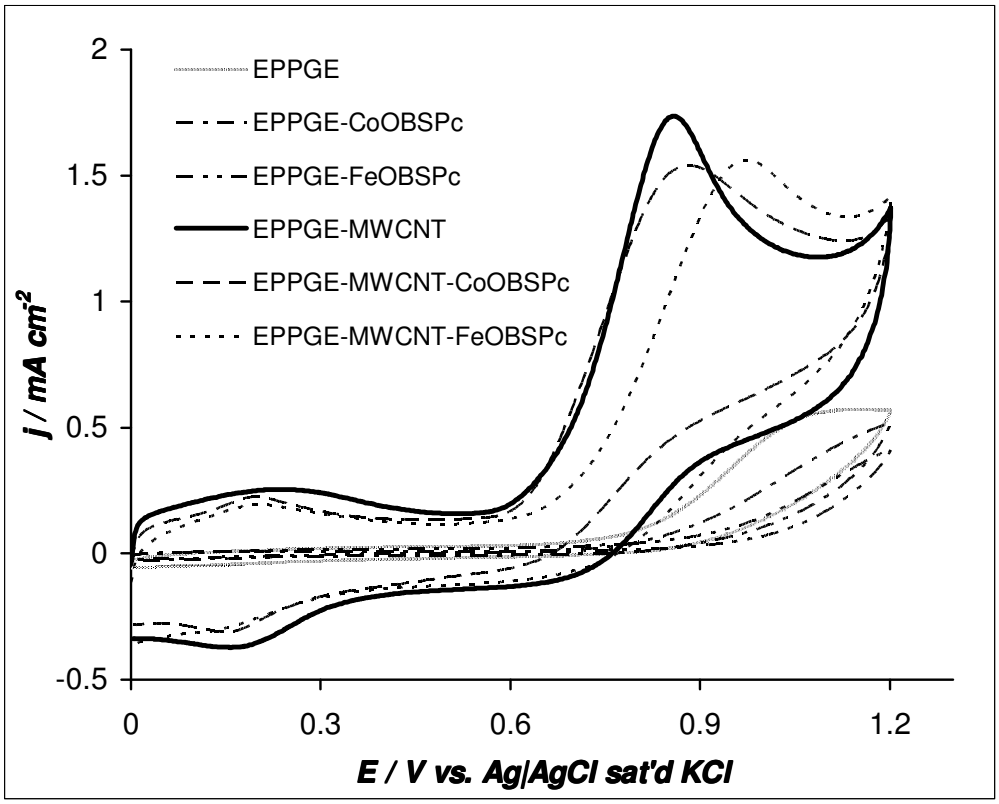


***Figure 5.10:*** *Comparative cyclic voltammograms of the various electrodes in 1mM thiocyanate solution contained in phosphate buffer (pH 5).*

### 5.3.3. Electrocatalytic oxidation of nitrite

Figure 5.11 presents the comparative CV of the various electrodes studied in 1mM nitrite solution (phosphate buffer pH 7.4). As seen, a similar trend as observed for thiocyanate oxidation was noticed. Considering that the aim of the of the study is to establish the electrocatalytic activity of the MOBSPc complexes, no further analysis

was carried on these electrodes because of their poor performance or the MWCNT electrode.

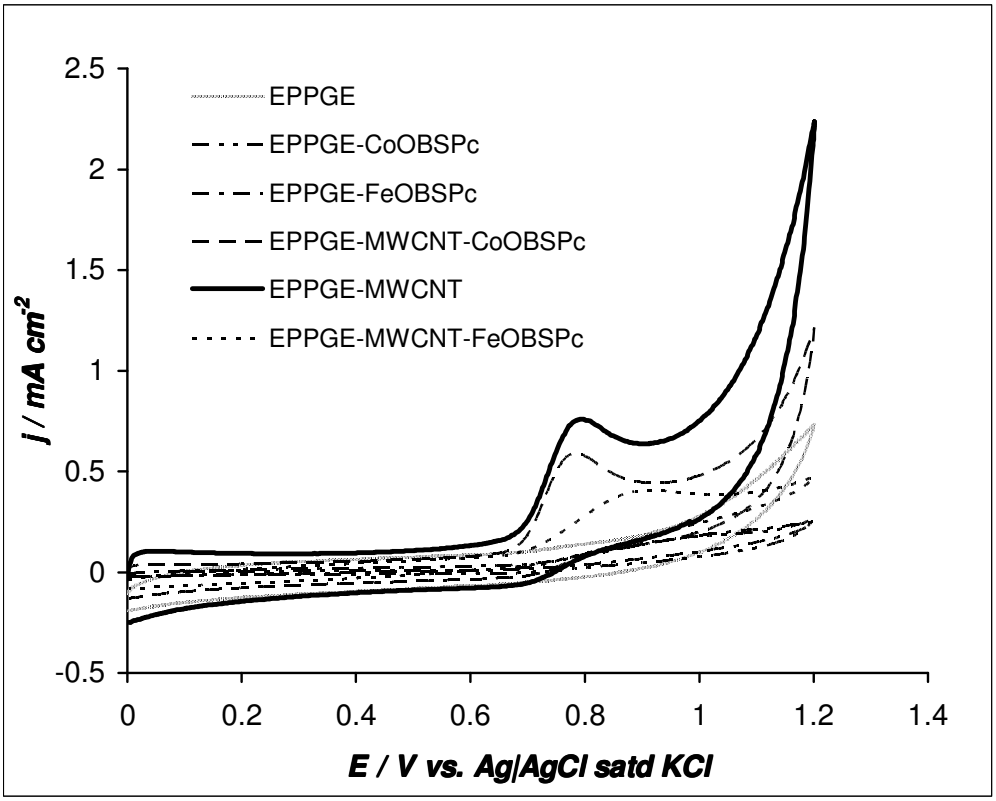


***Figure 5.11:*** *Comparative cyclic voltammograms of the various electrodes in 1mM nitrite solution contained in phosphate buffer (pH 7.4).*

## References

1. I. Streeter, G.G. Wildgoose, L. Shao, R.G. Compton, *Sens. Actuators* B **133** (2008) 462
2. K.I. Ozoemena, T. Nyokong, *Dalton Trans* (2002), 1806
3. M.J. Stillman, T. Nyokong, *Phthalocyanines: Properties and Applications*, eds. C.C. Lenznoff, A.B.P. Lever, VCH, New York, 1989, vol. 1
4. A.B.P. Lever, E.R. Milaeva, G. Spieer, *Phthalocyanines: Properties and Applications*, vol. 3, VCH Publishers, 1993, Chapter 1
5. M. E. Orazem, B. Tribollet, Electrochemical Impedance Spectroscopy, John Wiley & Sons Inc, Hoboken, NJ, 2008
6. N. Kobayashi, P. Janda, A.B.P. Lever, *Inorg. Chem.* **31** (1992) 5172
7. G. Wang, N. Ramesh, A. Hsu, D. Chu, R. Chen, *Mol. Simul.* **34** (2008) 1051
8. A. Sarapuu, K. Vaik, D.J. Schriffin, K. Tammeveski, *J. Electroanal. Chem.* **541** (2003) 23
9. F. Wang, S. Hu, *J. Electroanal. Chem.* **589** (2005) 68
10. J. Zagal, M. Paez, A.A. Tanaka, J.R. dos Santos Jr., C.A. Linkous, *J. Electroanal. Chem.* **339** (1992) 13
11. S. Griveau, J. Pavez, J.H. Zagal, F. Bedoui, *J. Electroanal. Chem*. **497** (2001) 75

12. M.P. Siswana, K.I. Ozoemena, T. Nyokong, *Electrochim. Acta* **52** (2006) 114
13. M. Siswana, K.I. Ozoemena, T. Nyokong, *Talanta* **69** (2006) 1136
14. K.I. Ozoemena, T. Nyokong, P. Westbrooke, *Electroanalysis* **15** (2003) 1762
15. K.P. Gong, F. Du, Z.H. Xia, M. Durstock, L.M. Dai, *Science* **323** (2009) 760
16. W. Chen, S. Chen, *Angew. Chem. Int. Ed*. **48** (2009) 4386
17. J.A. Harrison, Z.A. Khan, *J. Electroanal. Chem.* **28** (1970) 131
18. A.J. Bard, L.R. Faulkner, *Electrochemical Methods: Fundamentals and Applications*, 2nd ed., John Wiley & Sons, Hoboken, NJ, 2001.
19. D.H. Evans, J.J. Lingane, *J. Electroanal. Chem*. **6** (1963) 283
20. C.E. Banks, T.J. Davies, G.G. Wildgoose, R.G. Compton, *Chem. Commun.* (2005) 829

# CHAPTER 6

# Microscopic, Spectroscopic, Electrochemical and Electrocatalytic Properties of Iron(II) tetrakis(diaquaplatinum)octa-carboxy phthalocyanine*

* The following publications resulted from part of the research work presented in this chapter and they are not referenced further in this thesis:

5 S. A. Mamuru, K. I. Ozoemena, T. Fukuda, N. Kobayashi, *Journal of Materials Chemistry*, **20** (2010) 10705.

6 S. A. Mamuru, K. I. Ozoemena, *Electrochemistry Communication*, **12** (2010) 1539.

## 6.1. Microscopic and Spectroscopic Characterisation

Microscopic and spectroscopic information of iron(II) tetrakis (diaquaplatinum)octa-carboxyphthalocyanine, were obtained with transmission electron microscope, scanning electron microscope, UV-visible spectrophotometer, mass spectrophotometer, X-ray diffraction spectrophotometer, and elemental analyser.

### 6.1.1. *UV-visible characterisation*

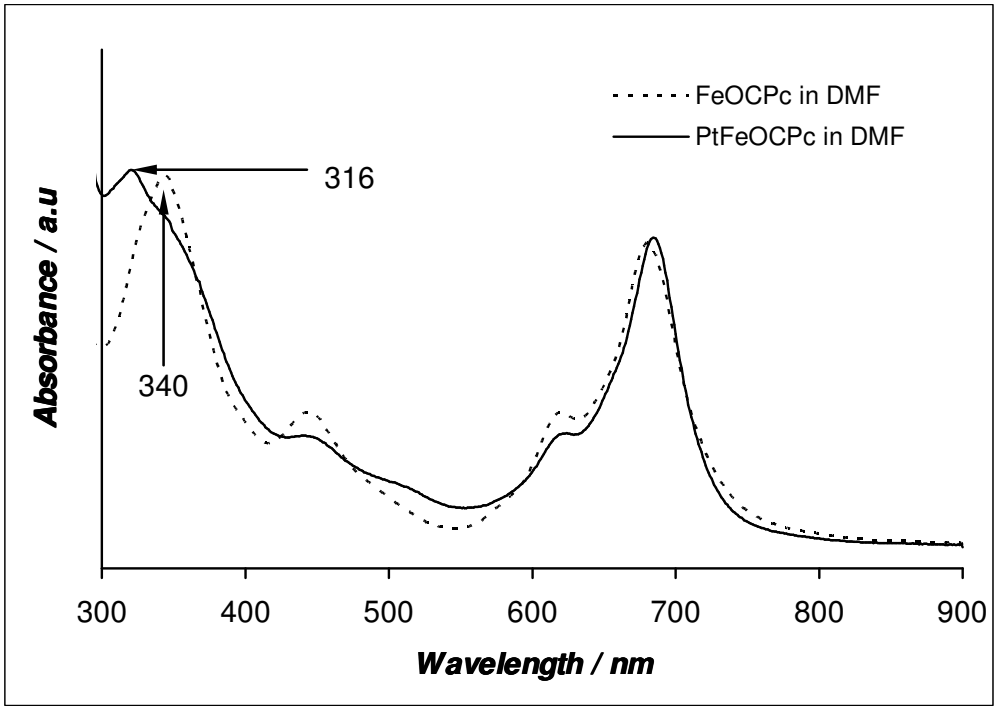


***Figure 6.1:*** *Comparative UV-visible spectrum of FeOCPc and PtFeOCPc in DMF*

Figure 6.1 shows the comparative UV-visible spectrum of FeOCPc and PtFeOCPc in DMF. The Q-bands of the two complexes occur almost at the same wavelength (685 nm), with a slight shift to the red region

(~ 2 nm) by the PtFeOCPc complex. Second, there is a notable change in the spectral pattern of the B-band region (316 – 340 nm range); such change is characteristic of the introduction of the Pt at the periphery of the phthalocyanine ring and can conveniently serve for monitoring the formation of PtFeOCPc complex.[1] Third, notice the peak at ~ 450 nm, which is characteristic of the metal-to-ligand charge transfer band of iron-containing phthalocyanine complexes.

### 6.1.2. *Elemental analysis and mass spectroscopy characterisation*

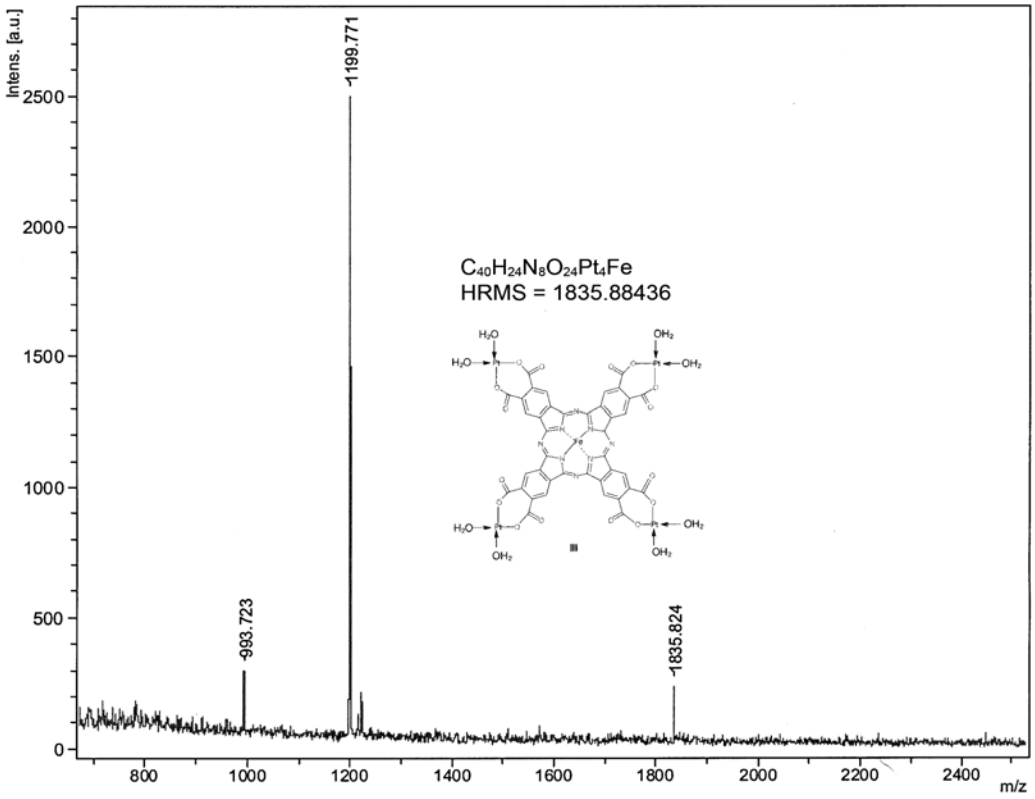


***Figure 6.2:*** *High resolution mass spectra of iron(II) tetrakis (diaquaplatinum)octa-carboxyphthalocyanine ($C_{40}H_{24}N_8FeO_{24}Pt_4$)*

Elemental analysis data (CHN) of the two FePc complexes closely agree with the expected values (as presented in section 3.2.3). The PtFeOCPc was further analysed with mass spectroscopy (Figure 6.2). The peak at $m/z$ 1199.771 is attributed to the $C_{36}H_{18}N_8O_{12}Pt_2Fe$ molecular ion, while that at $m/z$ 993.732 may be related to the $C_{37}H_{10}N_8O_{11}PtFe$ fragment.

### 6.1.3. *XRD and EDX Characterisation*

Figure 6.3(a) presents the x-ray diffraction pattern of FeOCPc and PtFeOCPc. The PtFeOCPc compound exhibited diffraction peaks different from its precursor, FeOCPc, confirming the presence of Pt particles.[2,3] The broad diffraction peak observed at 2θ of 31° is due to C (003) which we associate with the phthalocyanine. This peak is more pronounced at the FeOCPc compound than its PtFeOCPc counterpart. The FeOCPc is amorphous, in agreement with reported results where MPcs were found to be amorphous.[4]

Figure 6.3(b) presents the EDX profile of PtFeOCPc; elemental analysis gave the expected atomic ratio of 1:4 (Fe:Pt).

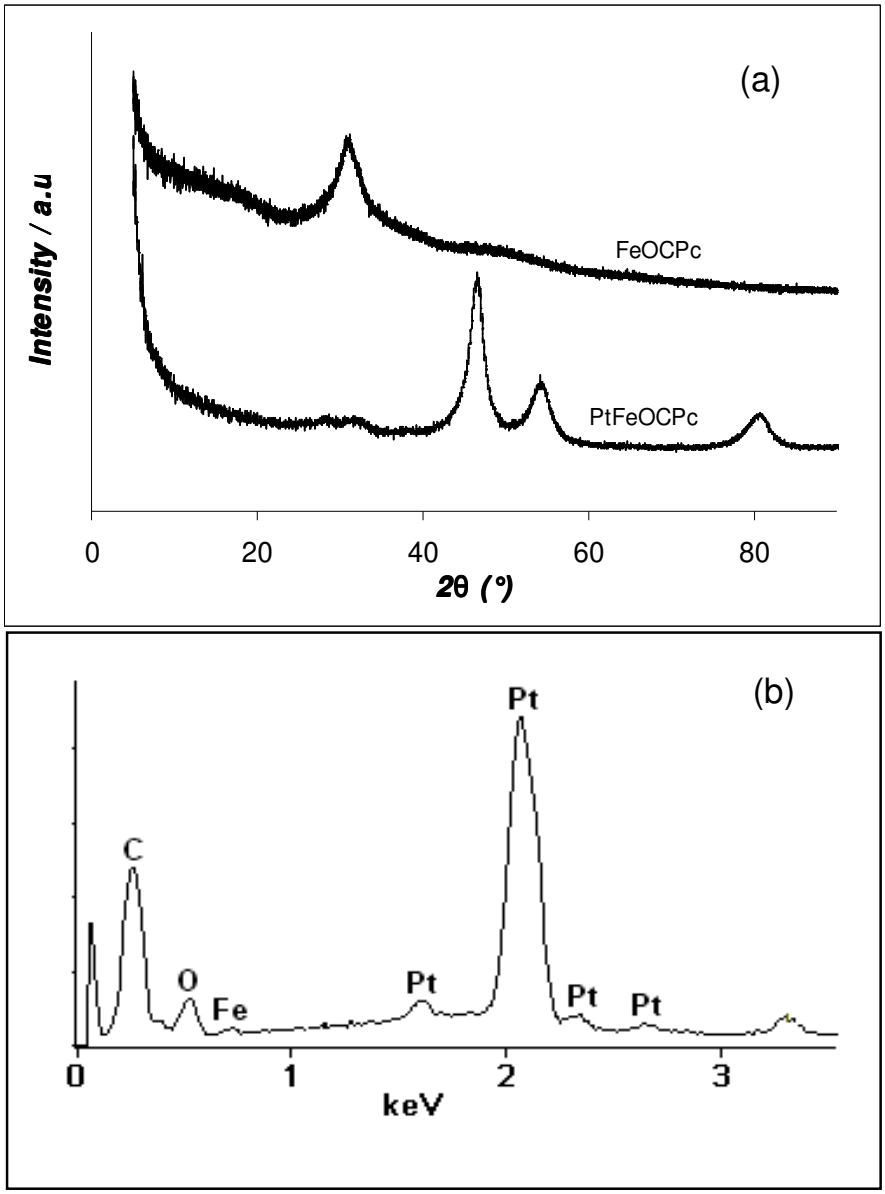


***Figure 6.3:*** *Comparative XRD pattern of FeOCPc and PtFeOCPc (a), EDX spectra of PtFeOCPc (b)*

### 6.1.4. *Comparative SEM and TEM characterisation*

Figure 6.4 (a) and (b) presents the SEM images of MWCNT and MWCNT/PtFeOCPc respectively. The image shows the porosity in the structure of the complex. Figure 6.4 (c) and (d) shows the crystallinity and attachment of the PtFeOCPc to the MWCNTs. In (d) the

entrapment of the PtFeOCPc onto the cylindrical or the nanofibril structures of the MWCNTs might have been enhanced by some electrostatic interactions between the negatively-charged MWCNTs and the positively-charged platinum particles attached to the metallophthalocyanine, the platinum particle can be seen aligned along the MWCNT surface they form clusters and this favours high degree of dispersion and large surface area which increases electrocatalysis.[5]

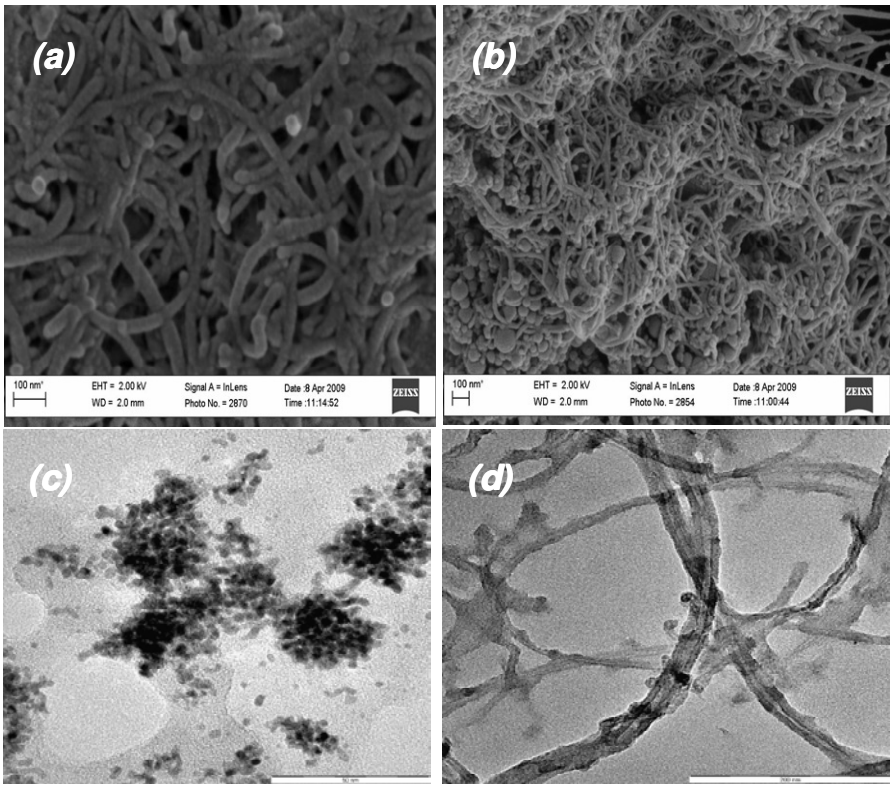


***Figure 6.4:*** *Typical SEM images of MWCNT (a) and MWCNT/PtFeOCPc (b). Typical TEM images of PtFeOCPc (c) and MWCNT /PtFeOCPc (d)*

## 6.2. Electrochemical Properties

### 6.2.1. *Solution electrochemistry*

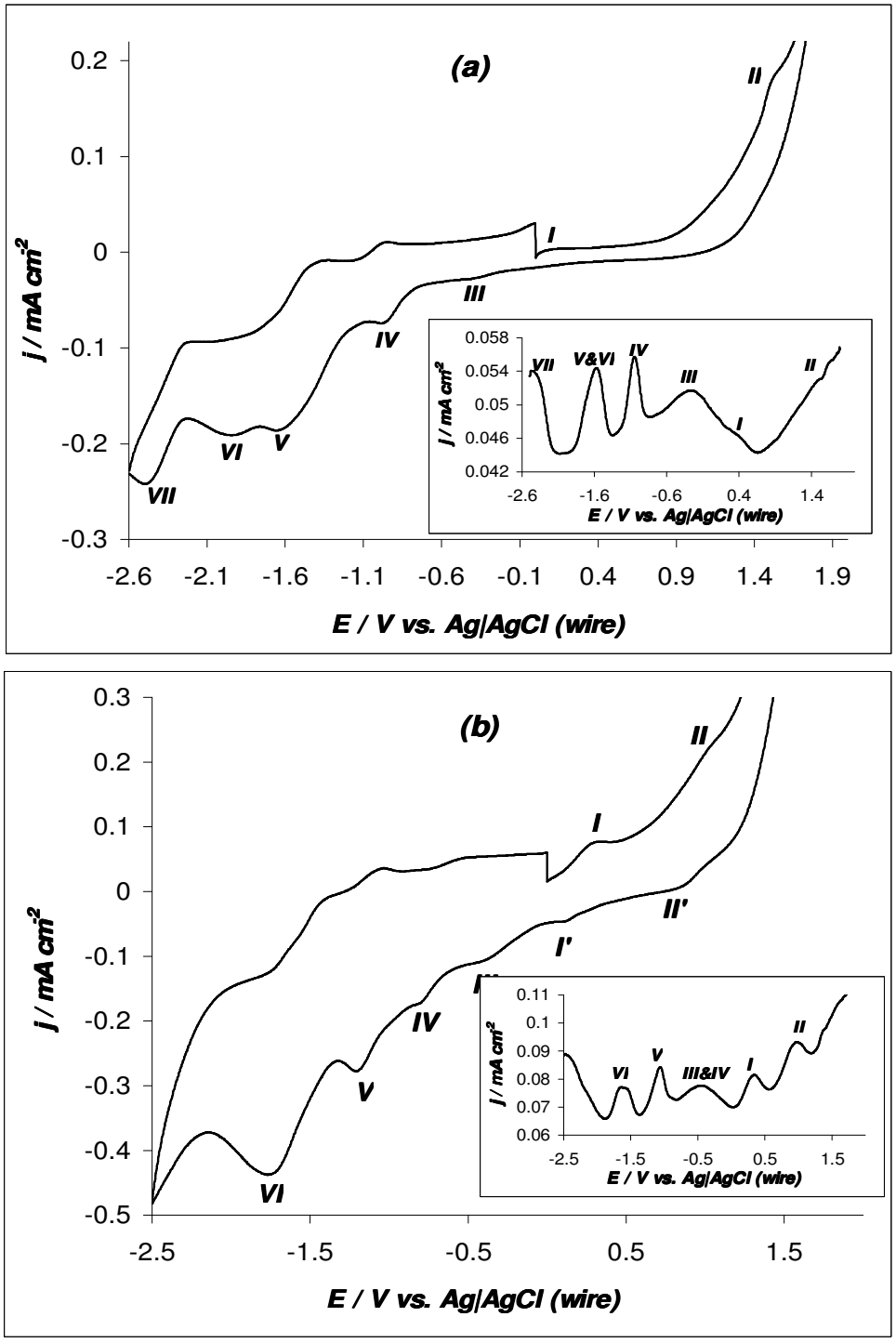


***Figure 6.5:*** *Typical cyclic voltammograms for FeOCPc (a) and PtFeOCPc (b) recorded in DMF containing 0.1 M TBAP. Insets, corresponding square wave voltammograms*

Figure 6.5 shows the typical cyclic voltammograms and inset the corresponding square wave voltammograms obtained in DMF containing about 1 mM FeOCPc (a) and PtFeOCPc (b) in 0.1 M TBAP. The values of the redox potentials are summarised in Table 6.1. From the Table we can deduce that for the PtFeOCPc complex (Figure 6.5(b)), the oxidation and reduction processes denoted as I, I' and II, II' can be attributed to the metal centre ($Fe^{3+}/Fe^{2+}$) and the platinum metal coordinated to the phthalocyanine ring respectively. The other reduction processes are ascribed to the phthalocyanine ring. Peaks III and IV appear as single broad peak in the square wave voltammogram. Each of the two reduction process is considered as one-electron processes each, as the sum of their heights was comparable to the single broad peak. This suggests that the two processes occur close to each other and thus overlap as one peak.

For the FeOCPc complex (Figure 6.5(a)), the first oxidation and reduction process is ascribed to the metal centre while the second oxidation and the other reduction processes are ascribed to the phthalocyanine ring. It can be observed that the reduction processes at the FeOCPc complex occurred at more negative potentials compared to the PtFeOCPc complex; this suggests that the attachment of the platinum on the phthalocyanine ring reduces the electron density on the total conjugated MPc system hence easier reduction and more difficult oxidation, thus leading to the lower reduction potentials recorded for PtFeOCPc complex.

***Table 6.1:*** *Redox potentials of FeOCPc and PtFeOCPc compounds recorded in DMF containing 0.1 M TBAP*

| **Compound** | **Potential, $E_{1/2}$ (V vs. Ag\|AgCl wire)** | | | | | |
|---|---|---|---|---|---|---|
| | **VI** | **V** | **IV** | **III** | **I** | **II** |
| FeOCPc | -2.42 | -1.55 | -1.03 | -0.24 | 0.35 | 1.50 |
| PtFeOCPc | -1.85 | -1.27 | -0.78 | -0.44 | 0.39 | 1.04 |

### 6.2.2. *Electron transfer behaviour*: *cyclic voltammetry*

The surface electrochemistry of these MPc complexes when immobilised on MWCNT-modified EPPGEs was explored, first by examining their cyclic voltammetric evolutions in a solution of an outer-sphere redox probe, $[Fe(CN)_6]^{3-}/[Fe(CN)_6]^{4-}$. Figure 6.6 presents the comparative cyclic voltammograms of the various electrodes studied in 0.1 M $[Fe(CN)_6]^{3-/4-}$ 1.0 M KCl solution. When the same experiment was carried out in 1.0 M KCl alone, no significant redox process was observed compared to when the redox probe was present. This should perhaps not be surprising considering that it is usually very difficult to observe the redox couple ($M^{3+}/M^{2+}$) of surface-confined transition MPc complexes in aqueous solution.

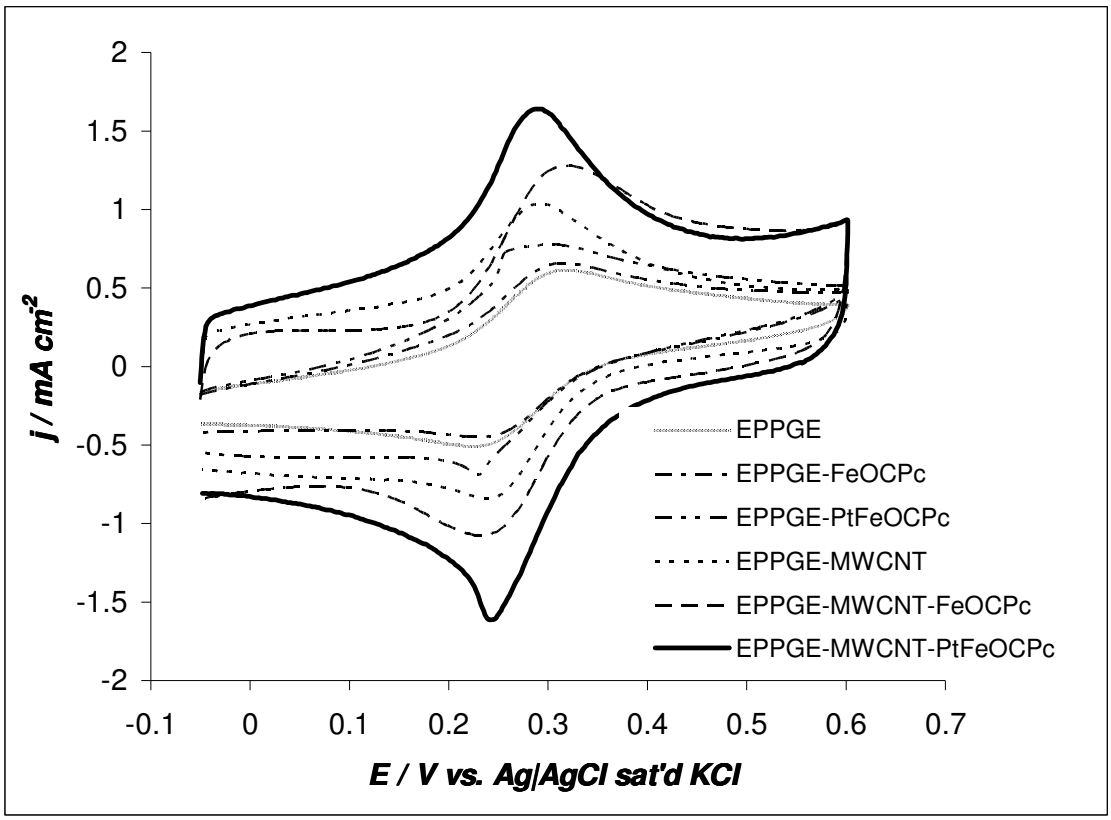


***Figure 6.6:*** *Comparative cyclic voltammograms of the various electrodes in 0.1 M* $[Fe(CN)_6]^{3-/4-}$ *1.0 M KCl solution.*

The heterogeneous electron transfer behaviour was determined by analysis of the potential peak-to-peak separation ($\Delta E_p$): the smaller the value the faster the electron transfer. The $\Delta E_p$ increases as EPPGE-MWCNT-PtFeOCPc (41 mV) < EPPGE-PtFeOCPc (44 mV) < EPPGE-MWCNT (56 mV) < EPPGE-MWCNT-FeOCPc (71 mV) < EPPGE- FeOCPc (78 mV) < EPPGE (90 mV), indicating that EPPGE-MWCNT-PtFeOCPc enhances faster electron transfer compared to other electrodes in the conditions employed. It is seen from the CV that the MWCNT-based electrodes exhibited higher current (Faradaic) response in the 0.2 – 0.35 V region as well as higher capacitive (non-Faradaic) response in

the -0.05 – +0.1 V region. This observation may be related to a change in diffusion regime (i.e., semi-infinite linear diffusion and / or thin layer diffusion processes arising from the redox process of electroactive species/electrolytes ($[Fe(CN)_6]^{3-}/[Fe(CN)_6]^{4-}$) trapped within the porous structure or in pockets in between the high surface area nanotubes) as described by Compton group.[6]

### 6.2.3. *Electron transfer behaviour: Impedimetric characterisation*

Figure 6.7(a) presents the Nyquist plots for the various electrodes studied in $[Fe(CN)_6]^{3-/4-}$ solution. The impedance spectra of the electrodes were satisfactorily fitted with the modified Randles equivalent electrical circuits (Figure 6.7(d)). The bare EPPGE electrode was fitted with circuit (i) while the other electrodes were fitted with circuit (ii) The fitting parameters involve the electrolyte resistance ($R_s$), electron-transfer resistance ($R_{ct}$), constant phase element (CPE), double layer capacitance ($C_{dl}$) and Warburg-type impedance ($Z_w$) which is associated with the diffusion of the ions of the redox probe.

The electron transfer rate constants ($k^o$) may be obtained from the $R_{ct}$ values using the derived equations (6.1-3).[7,8]

$$R_{ct} = \frac{RT}{nFi_o} \qquad (6.1)$$

$$i_o = nFAk^o c_O^\infty c_R^\infty \qquad (6.2)$$

Combining equations (6.2) and (6.3), taking the activity coefficients (∞) equal to unity, and assuming the bulk concentrations of the oxidised and reduced species to be equal ($c_O^\infty = c_R^\infty = c$) such that the equilibrium potential ($E_{1/2}$) equals the formal redox potential ($E_{O/R}^\phi$), then the $k^o$ becomes

$$k^o = k_{app} = \frac{RT}{n^2 F^2 A R_{ct} c} \qquad (6.3)$$

where n is the number of electron transferred (= 1) , *A* is the geometric area of the electrode, *c* is the concentration of the redox probe (in mol $cm^{-3}$, the concentration of $[Fe(CN)_6]^{3-}$ and $[Fe(CN)_6]^{4-}$ are equal), *R* is the ideal gas constant, *T* is the absolute temperature and *F* is the Faraday constant. The calculated values are shown in Table 6.2. The $k^o$ values decreases as: EPPGE-MWCNT-PtFeOCPc (776 x $10^{-3}$ cm $s^{-1}$) > EPPGE-MWCNT (681 x $10^{-3}$ cm $s^{-1}$) > EPPGE-PtFeOCPc (176 x $10^{-3}$ cm $s^{-1}$) > EPPGE-MWCNT-FeOCPc (159 x $10^{-3}$ cm $s^{-1}$) > EPPGE-FeOCPc (151 x $10^{-3}$ cm $s^{-1}$) > EPPGE (20 x $10^{-3}$ cm $s^{-1}$) implying that electron transfer processes between the redox probe and the underlying EPPGE surface is faster at the EPPGE-MWCNT-PtFeOCPc compared to the other electrodes, corroborating the CV data. From the Bode plots, Figures 6.7(b) and (c), the slopes of the log *Z* vs. log *f* plot at the mid frequency region are less than the ideal −1.0 for pure capacitive behaviour, which is indicative of pseudocapacitive behaviour. Also, the EPPGE-MWCNT-PtFeOCPc shows the least impedance value compared to other electrodes. The data from the other Bode plot (i.e.,

–phase angle vs. log *f*) confirms the absence of ideal capacitive behaviour as the observed phase angles are less than the 90° expected of an ideal capacitive behaviour. It is only the bare EPPGE that shows a maximum at ~44°, close to the ideal Warburg value of 45°. This relaxation process is shifted to different phase angles upon modification, indicating that the $[Fe(CN)_6]^{3-/4-}$ redox process now takes place at the surface of the modifying films than directly on the bare EPPGE surface.

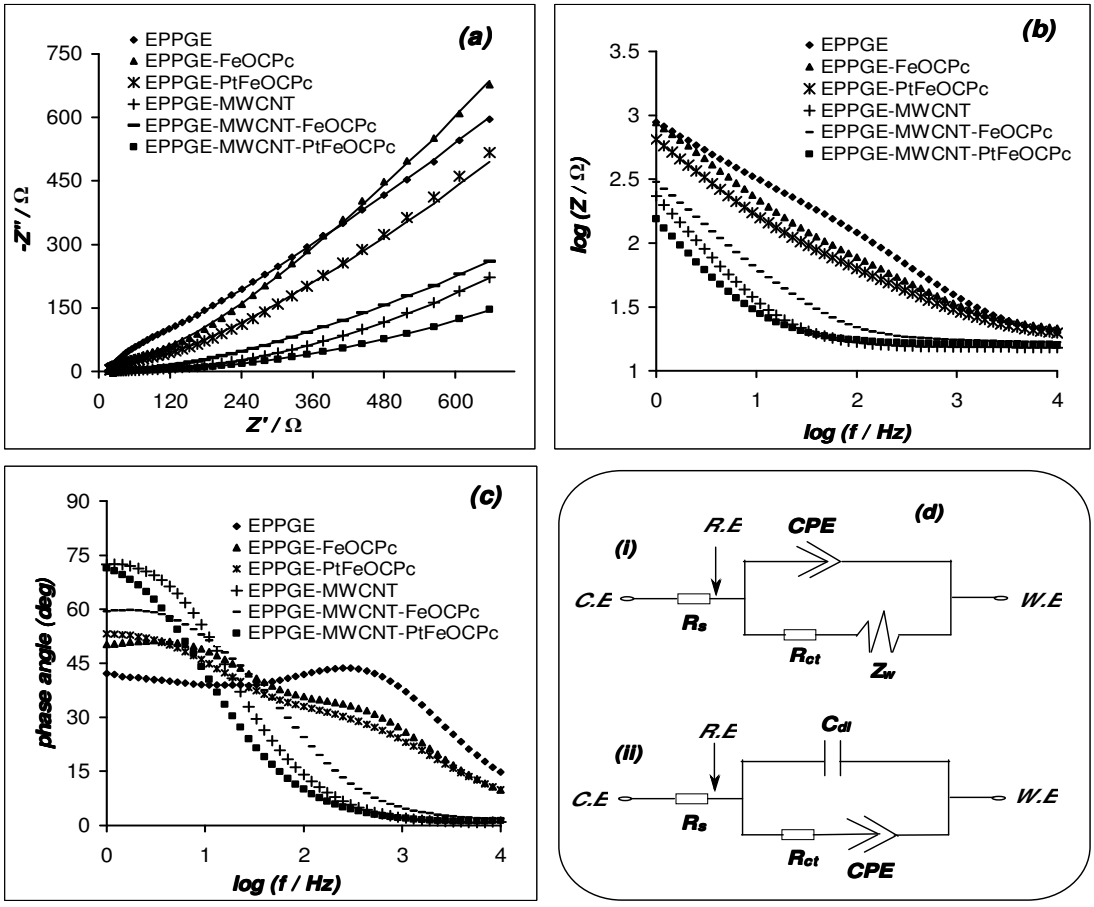


***Figure 6.7:*** *Comparative Nyquist plots (a) and Bode plots: (b) and (c) of the various electrodes in 0.1 M* $[Fe(CN)_6]^{3-/4-}$ *1.0 M KCl solution. Equivalent electrical circuit used for fitting the measured data (d).*

***Table 6.2:*** *Impedance parameters obtained using the electrical equivalent circuit in Figure 6.7 and* $\Delta E_p$ *values for the various electrodes studied in 0.1 M* $[Fe(CN)_6]^{3-/4-}$ *1.0 M KCl solution.*

| **ELECTRODES** | **$R_s$ / Ω** | **$R_{ct}$ / Ω** | **$CPE_1$ /μF** | **n** | **$C_{dl}$/μF** | **$10^3 k^o$/cm $s^{-1}$** | **$\Delta E_p$/mV** |
|---|---|---|---|---|---|---|---|
| EPPGE* | 16.9±0.1 | 195.4±6.0 | 56.8±2.4 | 0.73±0.01 | -- | 19.45±0.01 | 90 |
| EPPGE-FeOCPc | 21.5±0.3 | 25.2±1.6 | 386.9±7.5 | 0.59±0.01 | 6.5±0.3 | 150.63 ±0.01 | 78 |
| EPPGE-PtFeOCPc | 19.8±0.3 | 21.6±1.3 | 535.5±12.1 | 0.60±0.01 | 7.8±0.4 | 175.69 ±0.01 | 44 |
| EPPGE-MWCNT | 15.3±0.1 | 5.6±0.4 | 636.2 ±19.7 | 0.80±0.01 | 279.2±18.9 | 681.00 ±0.04 | 56 |
| EPPGE-MWCNT-FeOCPc | 17.2±0.1 | 23.4±0.9 | 903.3±7.5 | 0.63±0.03 | 45.0±5.2 | 158.48 ±0.01 | 71 |
| EPPGE-MWCNT-PtFeOCPc | 16.1±0.1 | 4.9±0.6 | 10.7±0.2 | 0.82±0.01 | 333.0±18.0 | 775.91±0.09 | 41 |

*$Z_w$ of EPPGE is (433±3.81) x $10^{-6}$ Ω

## 6.3 Electrocatalytic Properties

### 6.3.1. *Electrocatalytic reduction of oxygen*

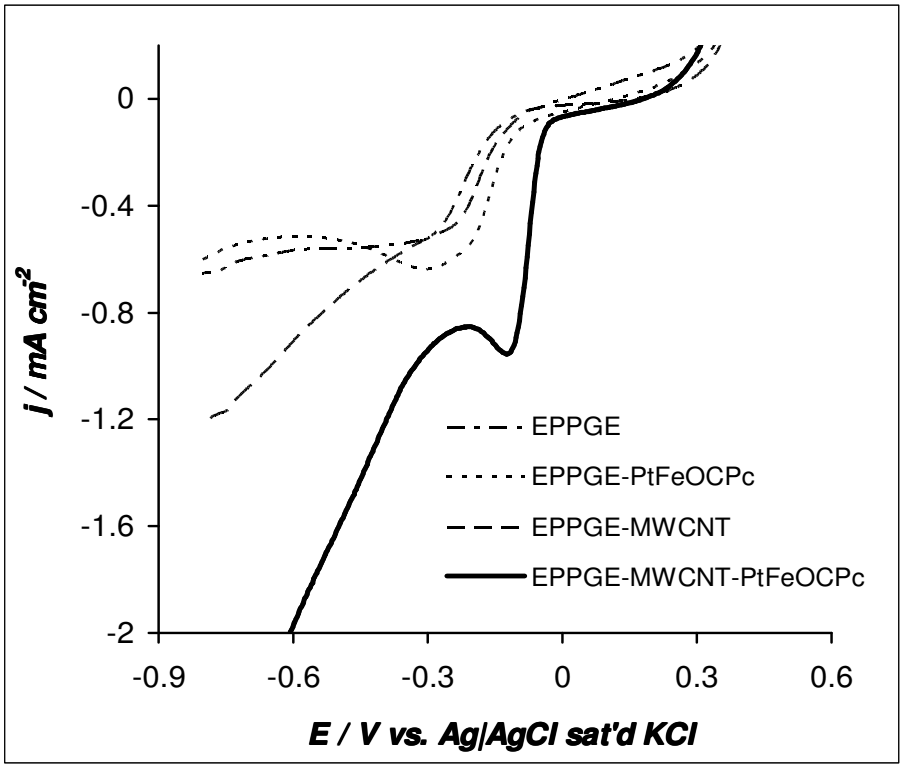


***Figure 6.8:*** *Comparative linear sweep voltammetric curves of the electrodes in oxygen saturated 0.1 M NaOH solution. Scan rate: 10 mV* $s^{-1}$

Figure 6.8 compares the linear sweep voltammetric evolutions of bare EPPGE, EPPGE-PtFeOCPc, EPPGE-MWCNT and EPPGE-MWCNT-PtFeOCPc in oxygen saturated 0.1 M NaOH solution. A change in Gibb's free energy of reaction (ΔG) is related to the electrochemical potential (E) by the relationship;

$$\Delta G = -nFE \qquad (6.4)$$

where n is the number of electron transferred.

As a result, the onset potential for ORR is directly related to the activation energy of the reaction. It is evident from Figure 6.8 that the EPPGE-MWCNT-PtFeOCPc showed the least onset potential (~ 0.0 volt vs. Ag|AgCl saturated KCl) and peak potential (–0.1 V vs. Ag|AgCl saturated KCl) compared to other electrodes that showed onset potential at ~ –0.10 V vs. Ag|AgCl saturated KCl and peak potential at ~ –0.25 V vs. Ag|AgCl saturated KCl. In addition, the current density of the MWCNT-PtFeOCPc electrode (~1.20 mA $cm^{-2}$) is about twice (0.4 – 0.6 mA $cm^{-2}$) of the other electrodes. The higher performance of the MWCNT-PtFeOCPc electrode (in terms of onset potential, reduction peak potential and current density) clearly indicates faster charge transfer kinetics toward ORR compared to other electrodes. This result is remarkable when compared to recent work on gold nanoparticles[9] with onset potential of -0.08 V vs. Ag|AgCl and comparable to $SnO_2$-Au hybrid nanoparticles[10] with onset potential of 0.06 V vs. Ag|AgCl.

The kinetics of the ORR at the MWCNT-PtFeOCPc electrode was explored using the rotating disk electrode (Figure 6.9(a)). The Figure clearly shows that the current density increased as the rotation rate is increased, with a limiting current density of 5.52 mA $cm^{-2}$ at 2,500 rpm. Figure 6.9(b) is the plot of $j^{-1}$ versus $\omega^{-1/2}$ employing the Koutecky-Levich equation:

$$\frac{1}{j} = \frac{1}{J_{\text{Lev}}} + \frac{1}{J_{\text{kin}}} \qquad (2.12)$$

$$J_{kin} = nFkc_O \qquad (2.13)$$

$$J_{Lev} = 0.21nFD^{2/3}\gamma^{-1/6}c_{O_2}\omega^{1/2} \quad (2.14)$$

where $j$ is the measured current density, $j_{Lev}$ and $j_{kin}$ are the limiting current density and the kinetic current density respectively, $\gamma$ is the kinematic viscosity (0.01 $cm^2s^{-1}$),[7] $\omega$ is the angular frequency of rotation, D is the diffusion coefficient of oxygen in an aqueous solution (1.98 x $10^{-5}$ $cm^2s^{-1}$),[11,12] $c_{O2}$ is the concentration of oxygen in solution (1.38 x $10^{-6}$ $molcm^{-3}$),[11,13] $k$ is the kinetic rate constant for the catalyzed oxygen reduction reaction. The linearity of the plot is indicative that the reaction is first order, and controlled by kinetics at the electrode surface as well as mass transport of oxygen species. The number of electrons ($n$) transferred per oxygen molecule was calculated as 3.98±0.24, suggesting that ORR at MWCNT-PtFeOCPc electrode proceeds via a single 4-electron transfer.

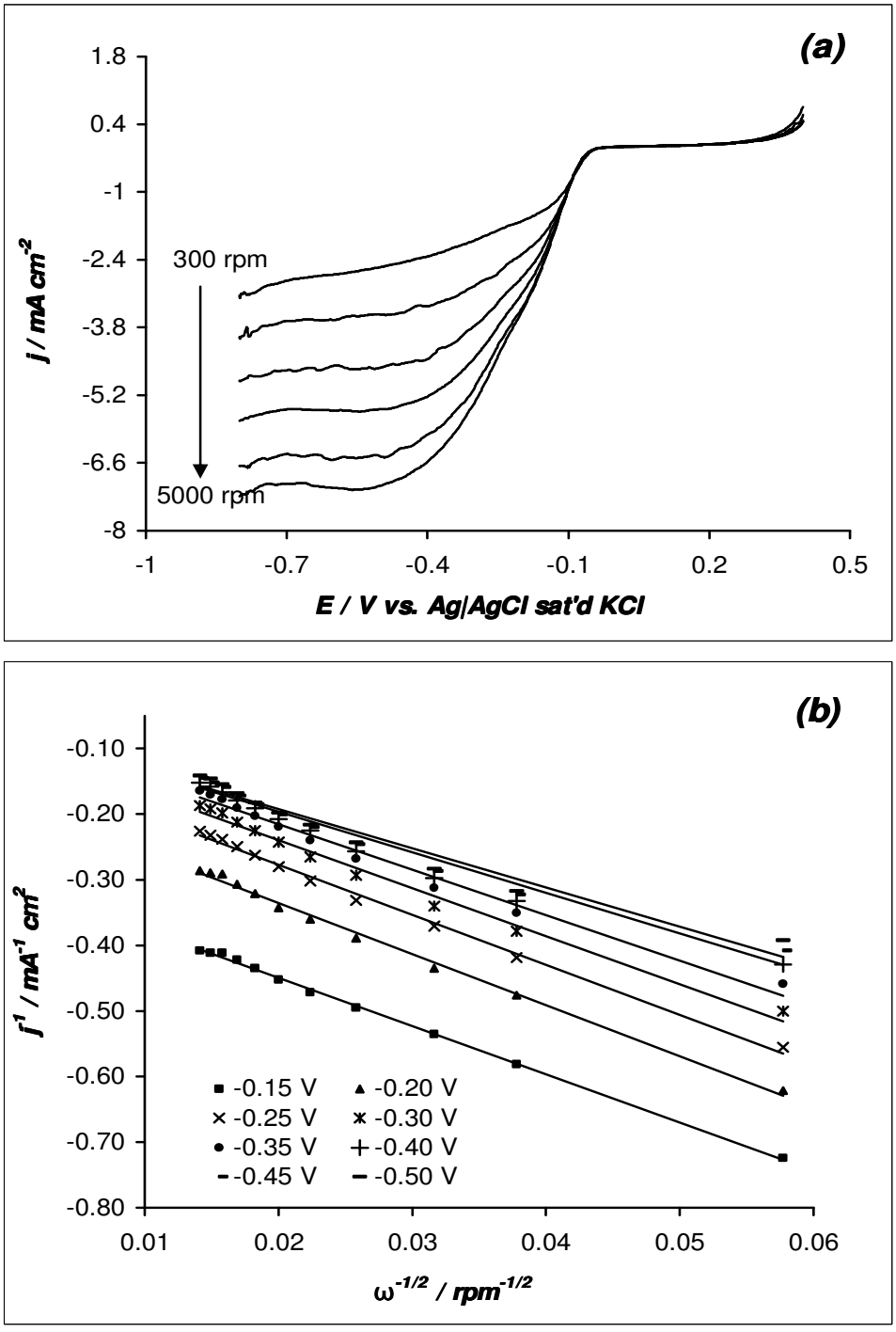


***Figure 6.9:*** *(a) RDE polarization curves at different rotation rates for EPPGE-MWCNT-PtFeOCPc electrode in oxygen saturated 0.1 M NaOH solution scan rate 10 mVs$^{-1}$; (b) Koutecky-Levich plot obtained from RDE data*

$J_{kin}$, obtained from the intercept of the Koutecky-Levich plots, was calculated to be –13.8 mA $cm^{-2}$ at both potentials of –0.45 and –0.50 V. The kinetic rate constant ($k$) was calculated as 2.78 x $10^{-2}$ cm $s^{-1}$. This value is slightly better than the reported 1.4 x $10^{-2}$ – 2.0 x $10^{-2}$ cm $s^{-1}$ range for a glassy carbon modified with anthraquinone,[14] but in the same magnitude (1.96 x $10^{-2}$ – 5.87 x $10^{-2}$ cm $s^{-1}$ range) obtained in alkaline media reported for gold nanoclusters catalyst[9] and tungsten carbide nanocrystals.[15]

Correcting the polarization curve for diffusion effects for first order reaction, one obtains:[16]

$$j_K = \left( \frac{j}{j_L - j} \right) \tag{4.4}$$

The $j_k$ is related to the Tafel equation as Eq. (4.3):[16]

$$E_{app} = E_{eq} - b \log j_k \tag{4.3}$$

$$b = \frac{2.3RT}{\alpha n F} \tag{4.5}$$

where $E_{app}$ is the applied potential, $E_{eq}$ is the equilibrium potential, $j_k$ is the kinetic current density, $j_L$ is the limiting current density (plateau in RDE voltammogram), $j$ is the measured current density at a given potential, $R$, $T$ and $F$ have their usual meaning, $\alpha n$ is the kinetic parameter for the electrode process. The plot of $E_{app}$ versus log $j$k (exemplified in Figure 6.10 for 4000 rpm) yielded a slope of –180±0.04 mV $dec^{-1}$ in the potential region between –0.24 and –0.38 V. The high value of the Tafel slope obtained is characteristic of porous electrode

with high internal surface area leading to high electrocatalytic activities. This value implies that ORR at the MWCNT-PtFeOCPc electrode might be limited by oxygen adsorption, a similar phenomenon also reported for Pt-containing electrodes.[17]

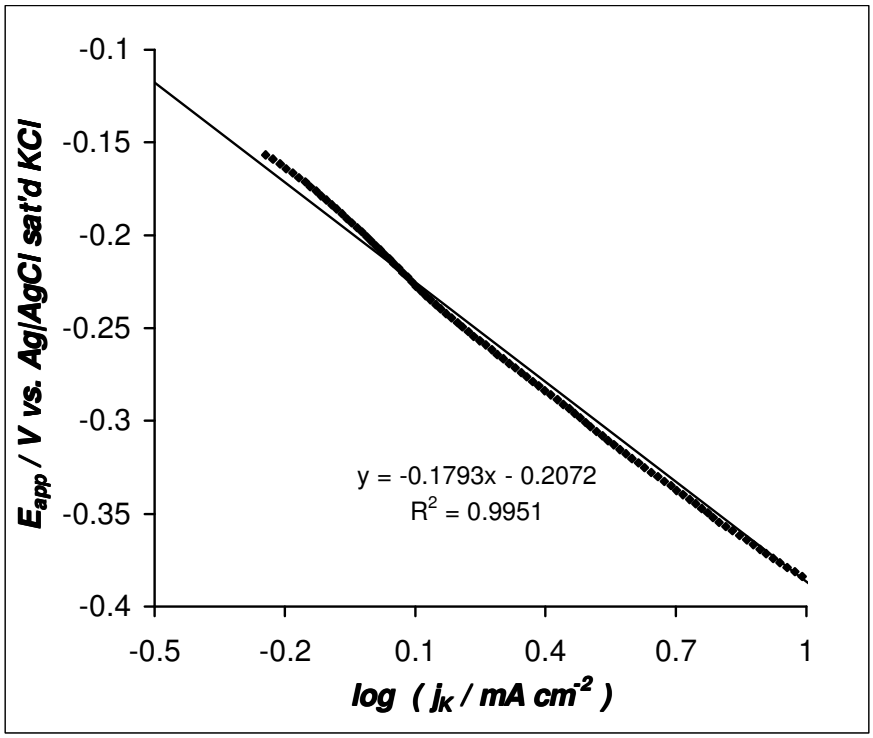


***Figure 6.10:*** *Tafel plot of $E_{app}$ vs. log $j_K$ for oxygen reduction on EPPGE-MWCNT-PtFeOCPc electrode in oxygen saturated 0.1 M NaOH solution.*

### 6.3.2. *Electrocatalytic oxidation of formic acid*

#### 6.3.2.1. *Comparative cyclic voltammetric response*

The electrocatalytic properties of EPPGE-MWCNT-PtFeOCPc for formic acid oxidation were studied in 0.5 M HCOOH + 0.5 M $H_2SO_4$ aqueous solution by cyclic voltammetry. Figure 6.11 presents the cyclic

voltammogramms of the various electrodes. The classical formic acid electro-oxidation peaks were observed only with the EPPGE-PtFeOCPc and EPPGE-MWCNT-PtFeOCPc electrodes, implying that electro-catalytic activity for the oxidation of formic acid takes place in the presence of the platinum containing catalysts. Two distinct oxidation peaks can be observed at ~0.20 and ~0.70 V for the forward scan and a backward oxidation peak at ~0.20 V. The peak at ~0.20 V is attributed to the direct oxidation of formic acid to $CO_2$ via the formation of an active intermediate specie ($-COO^-$)[18] or the "direct pathway", usually used to evaluate the electro-catalytic activity of the catalyst. The peak at ~0.70 V is attributed to the oxidation of adsorbed CO on the surface of the catalyst and formic acid by sites that have been poisoned by the adsorption of CO (poisoning of surface active sites) and the subsequent release of these sites by CO stripping and is usually referred to as the "CO pathway".[19,20,21] The reverse peak at ~ 0.20 V is related to the direct oxidation of formic acid to $CO_2$ after the adsorbed CO has been removed at increased electrode potential with the subsequent recovery of the surface active sites. Notice that unlike the EPPGE-PtFeOCPc, the EPPGE-MWCNT-PtFeOCPc showed a small reverse peak at around 0.8 V. A similar peak was observed recently by Maxakato *et al.*[22] and attributed it to further oxidation of the CO or FA.

It can be seen in Figure 6.11 that the onset for the electro-oxidation of formic acid in the EPPGE-PtFeOCPc and EPPGE-MWCNT-PtFeOCPc electrodes is almost immediate. The current densities of the forward

oxidation peaks are ~2.96 and ~2.55 mA $cm^{-2}$ for the EPPGE-PtFeOCPc electrode; ~3.71 and ~2.51 mA $cm^{-2}$ for the EPPGE-MWCNT-PtFeOCPc electrode. According to Zhou *et al.,*[16] the ratio of the current densities under the first and second forward oxidation is used to determine the pathway for the electro-oxidation of formic acid. A low ratio indicates that formic acid oxidation proceed via the "CO pathway" and a high ratio implies that formic acid oxidation proceed via the direct pathway. The ratios of the current densities calculated for EPPGE-PtFeOCPc and EPPGE-MWCNT-PtFeOCPc is ~1.2 and ~1.5 respectively. These mean that both electrodes favour the direct pathway. According to Chen *et al.,*[18] the ratio of the current densities under the first forward oxidation peak and the reverse oxidation peak essentially reflects the fraction of catalyst surface that is not poisoned by CO adsorption. A low ratio implies a low tolerance to CO poisoning, while a high ratio implies a high tolerance to CO poisoning. The ratios of the current densities calculated for EPPGE-PtFeOCPc and EPPGE-MWCNT-PtFeOCPc is approximately 1, meaning that both electrodes have high tolerance to CO poisoning. For the reverse oxidation, an oxidation peak at almost the same potential is observed, with a current density of ~4 mA $cm^{-2}$ for the EPPGE-PtFeOCPc electrode; and ~5 mA $cm^{-2}$ for the EPPGE-MWCNT-PtFeOCPc electrode. The direct oxidation process observed here is related to the promotional effect of the phthalocyanine as also postulated by Zhou *et al*.[16] for FeTSPc immobilised onto a Pt disc electrode.

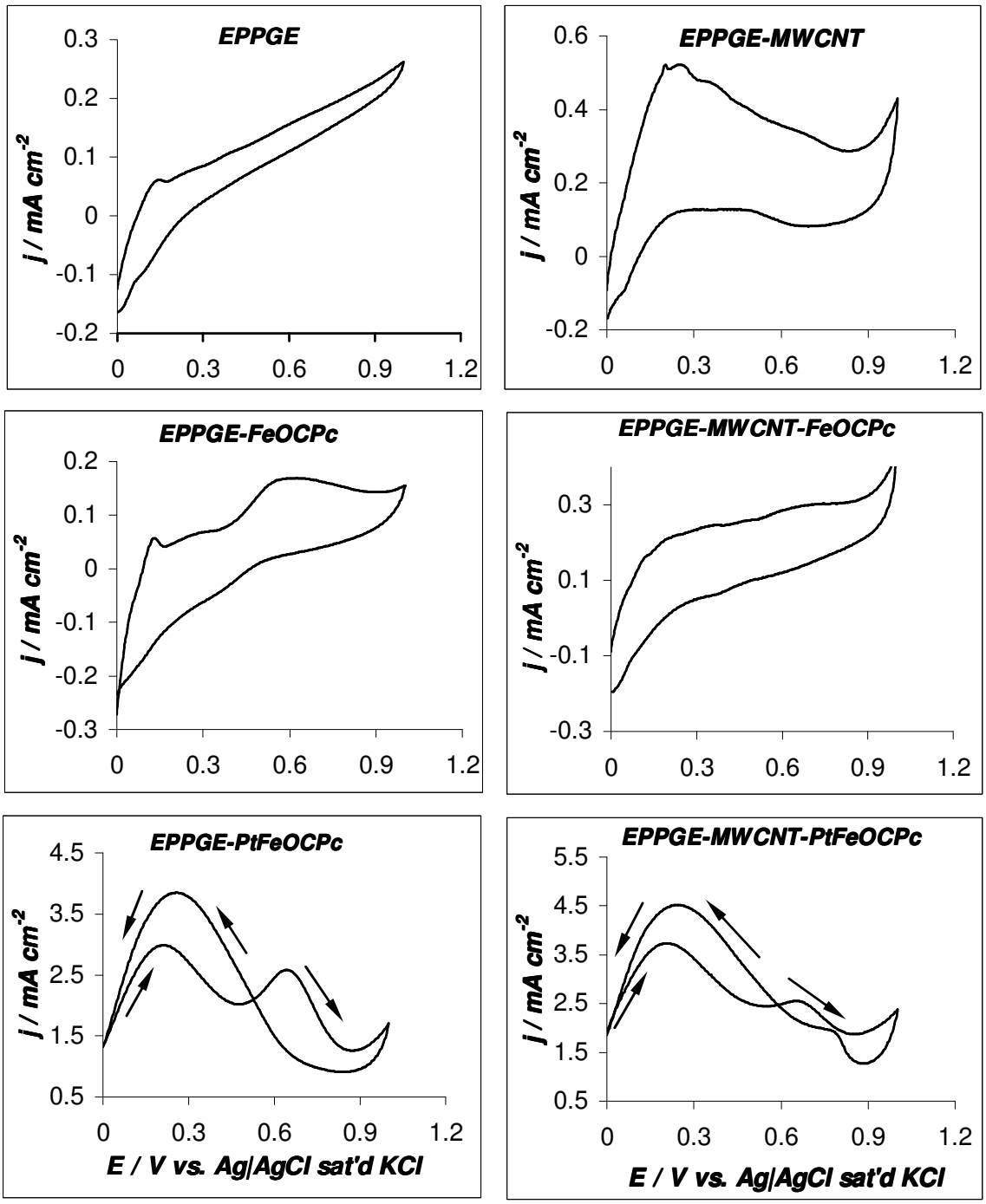


***Figure 6.11:*** *Cyclic voltammograms of the various electrodes in 0.5 M $H_2SO_4$ containing 0.5 M HCOOH solutions*

The reason for this enhanced reaction is not yet fully understood, however, other workers[23,24] have attributed such observation to the enhanced dehydration reaction in the CO pathway that generates the $CO_{ad}$ intermediates. Also, the electronic effect generated by the availability of electrons in the FeOCPc macrocycle could favour the electro-oxidation of formic acid by changing the electron distribution on the platinum surface, hence affecting the reaction pathway. It should be noted here that Pt nanoparticles alone electrodeposited onto MWCNT (MWCNT-Pt) showed poorer current response towards formic acid compared to the MWCNT-PtFeOCPc. This result is in agreement with the result reported by Maxakato *et al*.[22]

### 6.3.2.2. *Chronoamperometry experiment*

Chronoamperometry experiments were performed to provide further insights into the achievable current densities by the electrodes. Figure 6.12 presents the current – time curve of the electrodes studied, showing that the current density first drops to ~0.21 mA $cm^{-2}$ and then to a steady value at ~0.13 mA $cm^{-2}$ after about 2 min. for the EPPGE-PtFeOCPc electrode, while for the EPPGE-MWCNT-PtFeOCPc electrode, the current dropped initially to ~ 0.47 mA $cm^{-2}$ then to a steady value at ~0.27 mA $cm^{-2}$ after about 5 min. The stable current for the EPPGE-MWCNT-PtFeOCPc electrode is much higher than EPPGE-PtFeOCPc. The stability of the EPPGE-MWCNT-PtFeOCPc at high current

signifies better activity towards formic acid oxidation. This confirms our results from cyclic voltammetry.

An insight into the electrocatalytic rate constants ($k_{cat}$) at the two electrodes was obtained by employing the conventional equation below:[7]

$$\frac{j_{cat}}{j_{buff}} = \pi^{1/2}\left(k_{cat}c_o t\right)^{1/2} \qquad (6.5)$$

where $j_{cat}$ and $j_{buff}$ are the current densities in the presence and absence of formic acid, $c$ is the bulk concentration and $t$ is the time. A value of 41.09 $cm^3$ $mol^{-1}$ $s^{-1}$ was obtained for the EPPGE-MWCNT-PtFeOCPc and 10.95 $cm^3$ $mol^{-1}$ $s^{-1}$ for the EPPGE-PtFeOCPc, further confirming the higher electrocatalytic performance of the EPPGE-MWCNT-PtFeOCPc. There is no available literature to adequately compare the $k_{cat}$ values determined in this work. However, the values are smaller than the 2.45 x $10^{-1}$ L $mol^{-1}$ $s^{-1}$ (i.e., 245 $cm^3$ $mol^{-1}$ $s^{-1}$) reported by Blake and Hinshelwood[25] for gaseous formic acid. Considering the higher performance of the EPPGE-MWCNT-PtFeOCPc, all subsequent studies (unless otherwise stated) was devoted to this electrode.

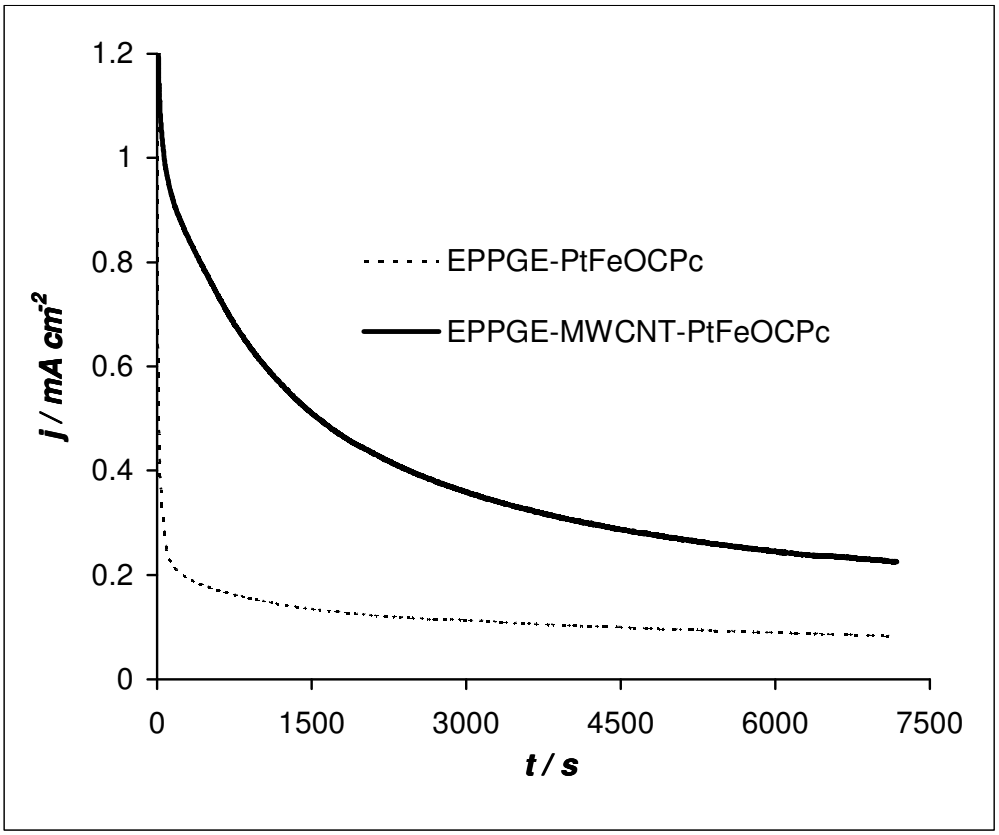


***Figure 6.12:*** *Chronoamperometric curves of EPPGE-PtFeOCPc and EPPGE-MWCNT-PtFeOCPc in 0.5 M $H_2SO_4$ containing 0.5 M HCOOH solutions*

### 6.3.2.3. *Concentration studies: Tafel analysis*

The effect of formic acid concentration on the electrocatalysis was studied at concentrations ranging from 0.10 to 1.20 M formic acid in 0.5 M $H_2SO_4$ solution at EPPGE-MWCNT-PtFeOCPc. Figure 6.13(a) shows that the current density increases as concentration increases and starts to decrease at 0.90 M, meaning that mass transfer resistances and build up of interfacial $CO_2$ formed during the electro-oxidation process or the combination of both might be responsible for this deviation at high concentration.[26] Simply stated, at > 0.75 M the

catalyst becomes easily saturated, meaning that optimum catalysis occur at 0.75 M formic acid.

The electrocatalytic properties was investigated by analyzing the Tafel behaviour, using the conventional relationships for oxidation processes, equations (6.6) and (6.7):[7]

$$\eta = a + b \log j \qquad (6.6)$$

$$b = \frac{2.303\ RT}{(1-\alpha)nF} \qquad (6.7)$$

where $\eta$ is the overpotential (difference between the applied potential and the open circuit potential), $j$ is the current density, $b$ is the Tafel slope, $a$ is the Tafel constant relating to the exchange current density, $\alpha$ is the transfer coefficient, $n$ is the number of electrons involved in the rate determining step, while other symbols retain their usual meaning. From the plots of $\eta$ vs. log j (Figure 6.13(b)), the Tafel slopes were essentially the same (275 – 290 mV $dec^{-1}$ range) at all concentrations, indicating that the same reaction mechanism is probably operating at all the concentrations of the formic acid studied. Assuming a 1-electron transfer process in the rate-limiting step of the overall electrocatalysis, the value of $(1-\alpha) \approx 0.2$, which implies that the transfer coefficient is close to unity.

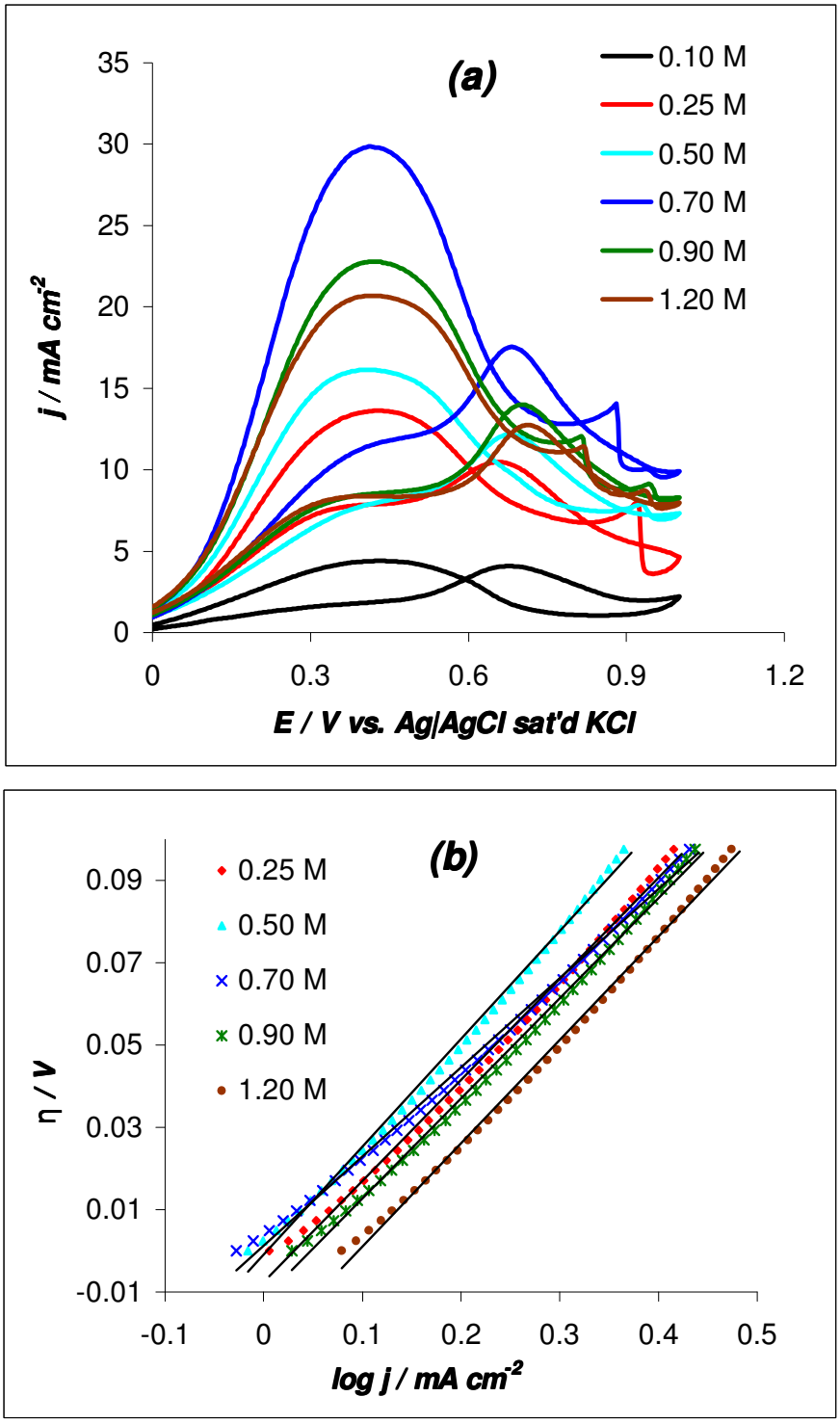


***Figure 6.13:*** *Cyclic voltammetric evolutions following changes in concentration of formic acid (a), Tafel plots of η against log j at different concentration of formic acid (b)*

The proximity of the coefficient to unity is an indication that the probability of product formation is very high. The high value of the Tafel slope obtained is characteristic of porous electrode with high internal surface area leading to high electrocatalytic activities.[26]

#### 6.3.2.4. *Electrochemical impedance spectroscopy experiments*

EIS was employed to further interrogate the electrocatalytic activity of the EPPGE-MWCNT-PtFeOCPc towards formic acid oxidation. Figures 6.14(a) presents the Nyquist plots while Figures 6.14(b) and 6.14(c) were the Bode plots obtained at different potentials measured in 0.5 M HCOOH + 0.5 M $H_2SO_4$ solutions. The Frumkin-Melik-Gaikazyan (FMG)[27] equivalent electrical (Figure 6.14(d)) was used to fit the EIS data. In the circuit the symbols $C_{ad}$ represents the adsorption capacitance arising from the oxidation of carbonaceous species on the electrode surface, while other symbols retain their usual meaning. It can be seen from the figure that all measured spectra are in the same quadrant, the conventional positive Faradaic impedance, at all peak potentials measured, which is indicative of the absence of adsorbed intermediates. This is interesting considering that other workers such as Chen *et al.,*[21,29] Seland *et al.*[18] and Maxakato *et al.*[22] have observed negative Faradaic impedance and attributed such phenomenon to adsorbed intermediates resulting from the formation of chemisorbed

hydroxyl species that compete for surface adsorption sites against the CO. The implication of the data in Table 6.3 resulting from the modelling of this electrode should be emphasised. First, since the FMG electrical equivalent circuit used in fitting our measured data is popularly used for studying adsorbed organic molecules,[30] the presence of adsorbed species cannot be completely ruled out in this work. Second, the values of the $R_s$ and $Z_w$ are approximately the same. Ideally, $R_s$ and $Z_w$ values should not be affected by modification of the electrode surface.[31] Third, considering that electron transfer rate constant is inversely proportional to the $C_{ad}$,[32,33] it suggests that reaction kinetics tends to be faster at higher potentials (≥ 0.90 V). Thus, the low adsorption capacitance at more positive potential suggests some oxidative removal of carbonaceous species present on the electrode surface. The corresponding Bode plots clearly show the phase angles of the electrocatalytic processes as 65° and ≥ 70°, confirming the presence of CPE and the pseudo-capacitive nature of the electrode since the angle is less than the 90° for an ideal capacitive behaviour. The slopes from the plot of log Z vs. log f were ~ -0.68 and -0.05 at mid and high frequency regions respectively, indicative of pseudo-capacitive and resistive behaviour at these frequency regions.

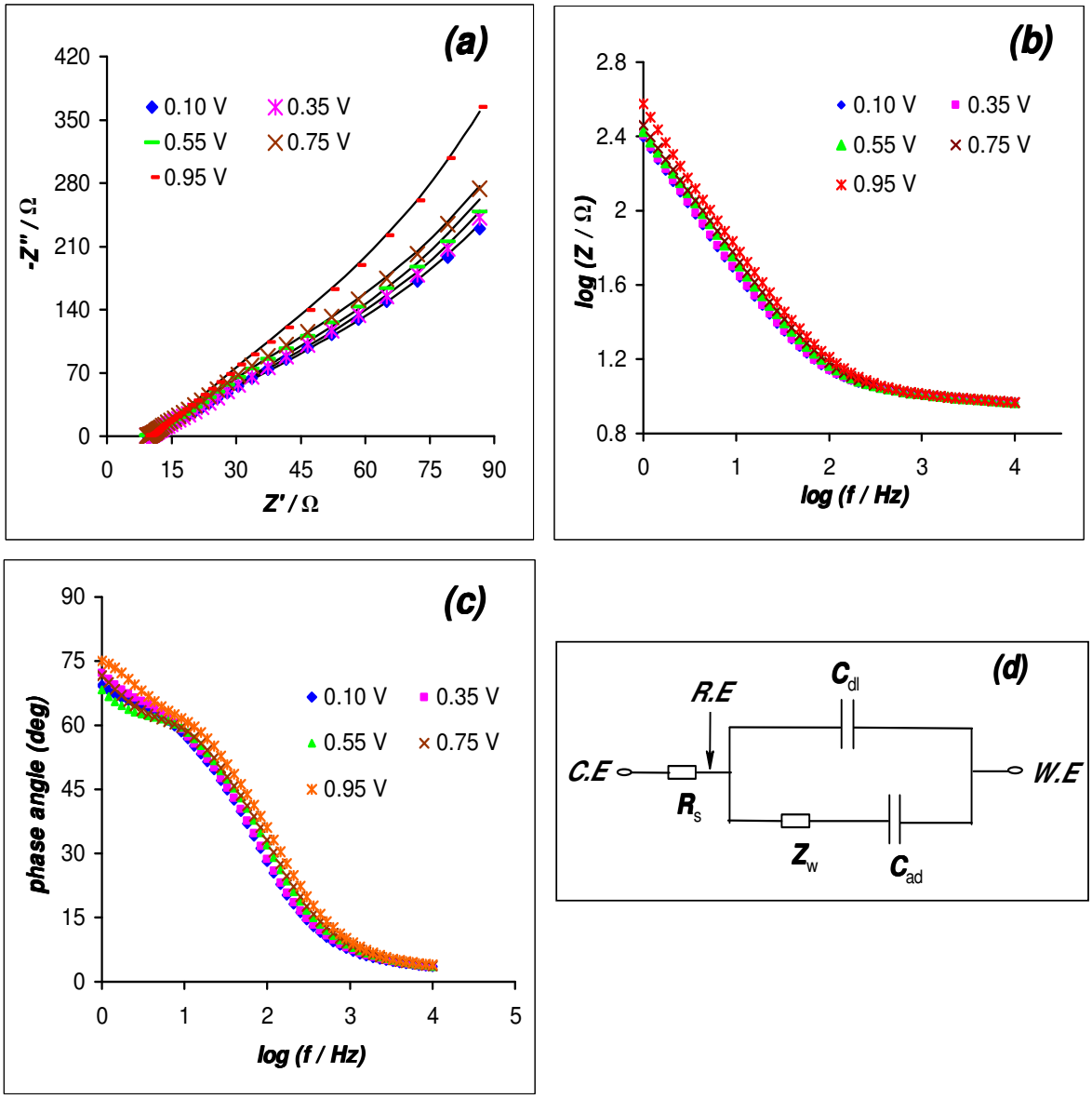


***Figure 6.14:*** *Typical Nyquist(a), Bode (b and c) plots and equivalent circuit (d) used to fit the spectra obtained at different potentials (0.10, 0.35, 0.55, 0.75 and 0.95 V) for EPPGE-MWCNT-PtFeOCPc in 0.5 M $H_2SO_4$ containing 0.5 M HCOOH.*

***Table 6.3:*** *Impedance data obtained for EPPGE-MWCNT-PtFeOCPc electrode studied in 0.5 M $H_2SO_4$ containing 0.5 M HCOOH at different potentials using the electrical equivalent circuit in Figure 6.14.*

| **Bias Potential / V vs. Ag/AgCl sat'd KCl** | **$R_s$ / Ω** | **$C_{dl}$/μF** | **$C_{ad}$/mF** | **$10^3$ $Z_w$ / Ω** |
|---|---|---|---|---|
| 0.10 | 9.82 ±0.10 | 133.70 ±7.42 | 0.88 ±0.04 | 2.72 ±0.14 |
| 0.35 | 9.75 ±0.10 | 121.40 ±6.93 | 0.79 ±0.03 | 2.89 ±0.14 |
| 0.55 | 9.80 ±0.10 | 117.70 ±5.49 | 0.92 ±0.08 | 2.15 ±0.09 |
| 0.75 | 9.73 ±0.08 | 102.00 ±4.63 | 0.78 ±0.03 | 2.26 ±0.09 |
| 0.95 | 9.63 ±0.07 | 80.10 ±3.57 | 0.51 ±0.01 | 2.37 ±0.09 |

### 6.3.2.5. *Tolerance to carbon monoxide poisoning*

Adsorption of CO-like species on the surface of the electrocatalyst is used to evaluate the extent to which an electrocatalyst can tolerates poisoning in a fuel cell system such as direct formic acid fuel cell (DFAFC).[34,35] Thus, we conducted a preliminary experiment to determine the tolerance of the proposed electrocatalyst for formic acid oxidation towards CO. Figure 6.15 shows the comparative CVs of EPPGE-PtFeOCPc (Figure 6.15(a)) and EPPGE-MWCNT-PtFeOCPc (Figure 6.15(b)) in 0.5 M $H_2SO_4$ solution (**I**), 0.5 M $H_2SO_4$ saturated with CO (**II**), and 0.5 M FA containing 0.5 M $H_2SO_4$ saturated with CO (**III**). The MWCNT-PtFeOCPc also shows the unique reverse peak at ~ 0.8 V as in Figure 6.11. The peak potential for CO oxidation at the EPPGE-PtFeOCPc is slightly (~ 40 mV) more positive than at the EPPGE-MWCNT-PtFeOCPc, meaning that the removal of CO from the EPPGE-PtFeOCPc electrode will be slightly difficult.[30] Secondly, from the electrocatalytic waves of (**III**) in both figures, the ratio of the current density of the forward anodic peak to the reverse anodic peak of 2.18 and 1.12 were obtained for EPPGE-PtFeOCPc and EPPGE-MWCNT-PtFeOCPc, respectively, meaning that EPPGE-MWCNT-PtFeOCPc tolerates CO poisoning than its EPPGE-PtFeOCPc counterpart.

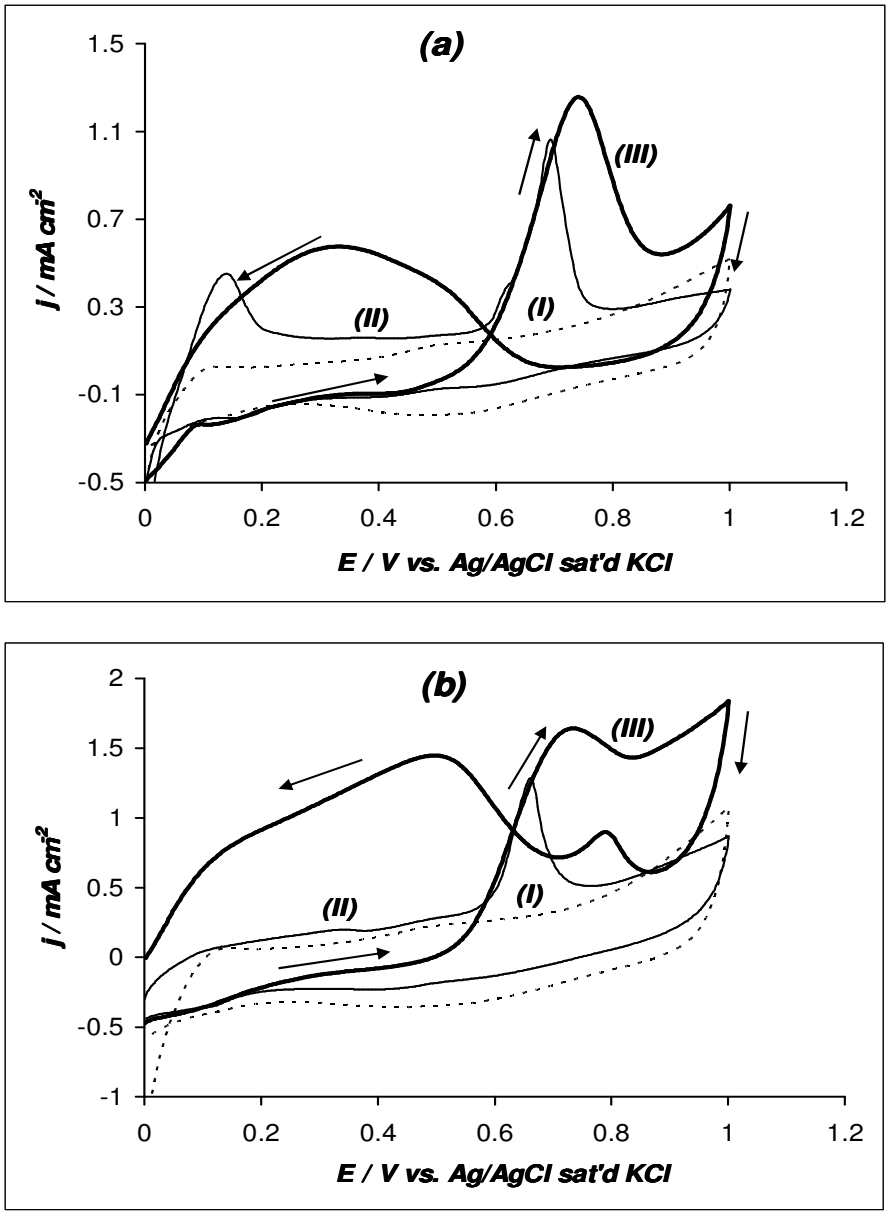


***Figure 6.15:*** *Comparative cyclic voltammograms of EPPGE-PtFeOCPc (a) and EPPGE-MWCNT-PtFeOCPc (b) electrodes studied in 0.5 M $H_2SO_4$ (I), CO saturated in 0.5 M $H_2SO_4$ (II) and CO saturated in 0.5 M $H_2SO_4$ and 0.5 M HCOOH (III)*

## References


1. O.V. Dolotova, O.L. Kaliya, *Russ. J. Coord. Chem*. **33** (2007) 111
2. J. Yang, D. Sung, J. Li, X. Yang, J. Yu, Q. Hao, W. Liu, J. Liu, Z. Zou, J. Gu, *Electrochimica Acta,* **54** (2009), 6300
3. J. Prabhuram, T.S. Zhao, C.W. Wang, J.W. Guo, *J. Power Sources*, **134** (2004), 1
4. J.G. Guan, W. Wang, R.Z. Gong, R.Z. Yuan, L.H Gan, K.C. Tam, *Langmuir,* **18** (2002), 4198
5. Z-Z. Zhu, Z. Wang, H-L. Lin*, Appl. Surf. Sci*., **254** (2008) 2934
6. I. Streeter, G.G. Wildgoose, L. Shao, R.G. Compton, *Sens. Actuat. B,* **133** (2008), 462
7. A.J. Bard, L.R. Faulkner, *Electrochemical Methods: Fundamentals and Applications*, 2nd ed., John Wiley & Sons, Hoboken NJ, 2001
8. H.H. Girault, *Analytical and Physical Electrochemistry*, EPFL Press, Lausanne, Switzerland, 2004, Chapter 7
9. W. Chen, S. Chen, *Angew. Chemie, Int. Ed*., **48** (2009) 4386
10. W. Chen, D. Ny, S. Chen, *J. Power Sources* **195** (2010) 412
11. J. Zagal, P. Bindra, E. Yeager, *J. Electrochem. Soc*. **127** (1980) 1506
12. K. Gubbins, R. Walker, *J. Electrochem. Soc.,* **112** (1965) 469
13. W.G. Wilke, *solubilities of inorganic and metal organic compounds*, Vol 2, 4th ed., American Chemical Society, Washington,D.C. 1965 p.1219
14. K. Vaik, U. Maeorg, F.C. Maschion, G. Maia, D.J. Schiffrin, K.

Tammeveski, *Electrochim. Acta* **50** (2005) 5126

15. H. Meng, P.K. Shen, *Electrochem. Commun*. **8** (2006) 588
16. I. Koc, M. Camur, M. Bulut, A.R. Ozkaya, *Catalysis Lett*. **131** (2009) 370
17. K. Tammeveski, T. Tenno, J. Claret, C. Ferrater, *Electrochim. Acta* **42** (1997) 893
18. F. Seland, R. Tunold, D.A. Harrington, *Electrochim. Acta*, **53** (2008), 6851
19. X. Zhou, C. Liu, J. Liao, T. Lu, W. Xing*, J. Power Sources*, **179** (2008), 481
20. B. Liu, H.Y. Li, L. Die, X.H. Zhang, Z. Fan, J.H. Chen, *J. Power Sources*, **186** (2009), 62
21. W. Chen, J. Kim, S. Sun, S. Chen*, Langmuir*, **23** (2007), 11303
22. N.W. Maxakato, K.I. Ozoemena, C.J. Arendse, *Electroanalysis*, **22** (2010), 519
23. T. Iwasita, X.-H. Xia, E. Herrero, H.-D. Liess, *Langmuir,* **12** (1996) 4260
24. J. Cavalier, S.G. Sun, *J. Electroanal. Chem.,* **199** (1986) 471
25. P.G. Blake, C. Hinshelwood, *Proc. Royal Soc. of London Series A*, *Math. Phys. Sci.,* **255** (1960), 444
26. M. Zhao, C. Rice, R. I. Masel, P. Waszczuk, A. Wieckowski*, J. Electrochem. Soc.,* **151** (2004), A131
27. P.K. Shen, C. Xu, *Electrochem. Commun*., **8** (2006), 184

28. G. Nurk, H. Kasuk, K. Lust, A. Janes, E. Lust, *J. Electroanal. Chem*., **533** (2003), 1

29. W. Chen, J. Kim, L-P. Xu, S. Sun, S. Chen, *J. Phy. Chem. C,* **111** (2007), 13452.

30. F. Ye, S. Chen, X. Dong, W. Lin, *J. Nat. Gas. Chem*., **16** (2007), 162

31. J. Pillay, K.I. Ozoemena, *Electrochem. Commun*., **9** (2007), 1816

32. J. Pillay, K.I. Ozoemena, R.T. Tshikhudo, R.M. Moutloali, *Langmuir*, **26** (2010), 9061

33. S.E. Creager, T.T. Wooster, *Anal. Chem.* **70** (1998), 4257

34. F. Hu, C. Chen, Z. Wang, G. Wei, P.K. Shen, *Electrochim. Acta*, **52** (2006), 1087

35. A. N. Gavrilov, E. R. Savinova, P. A. Simonov, V. I. Zaikovskii, S. V. Cherepanova, G. A. Tsirlina, V. N. Parmon, *Phys. Chem. Chem. Phys.,* **9** (2007), 5476

# Conclusions and Future Perspectives

## CONCLUSIONS

The synthesis of some novel metallophthalocyanine complexes notably; nanostructured iron and cobalt phthalocyanine (nanoMPc), iron and cobalt octabutylsulphonylphthalocyanine (MOBSPc) and iron tetrakis(diaquaplatinum)octa-carboxyphthalocyanine (PtFeOCPc) was described in this work. The microscopic, spectroscopic, electrochemical and electrocatalytic activities of these MPcs were also explored. The fabrication of an electrode by the 'drop-dry' method to produce a stable redox-active MPc complex integrated with multi-walled carbon nanotube on an edge plane pyrolytic graphite electrode surface was developed.

Some findings from this work are remarkable and these include the following: First, the electron transfer dynamics towards an outer-sphere redox probe at MPc/multi-walled carbon nanotubes composite supported on a edge plane pyrolytic electrode (EPPGE-MWCNT-MPc) have been investigated. Employing the Davies-Compton theoretical framework on the "diffusion domain approximation", cyclic voltammetric evolutions showed that the diffusion process occurring at these electrodes correspond to the type 3 behaviour of the voltammetry at spatially heterogeneous electrodes. The electrodes, like that of the MWCNTs alone, generated huge current response, possibly due to the redox chemistry of the redox species that might have been trapped within the porous layers of these high surface areas species.

Comparative electron transfer dynamics, using electrochemical impedance spectroscopy, showed that the electron transfer constants are in the order of $10^{-2}$ cm $s^{-1}$. EPPGE-MWCNT-MPc has demonstrated an outstanding role in facilitating the electron transfer process between the electrode and the electrolyte or redox probe species in solution.

Second, it has also been established that the MWCNT/MPc-based electrodes enhance electrocatalytic activity towards the detection of thiocyanate and nitrite in aqueous solutions compared to the MPc alone.

Third, the oxygen reduction reaction (ORR) in 0.1 M NaOH revealed that the MWCNT-FePc complexes gave the best response compared to the other electrodes, involving a direct 4-electron mechanism, with ORR onset potential that is comparable and even better than reported in literatures.

Fourth, one of the key findings in this work is the PtFeOCPc supported on a MWCNT platform (MWCNT-PtFeOCPc). It exhibited better electrochemical response in terms of catalytic rate constant and tolerance towards CO poisoning during formic acid oxidation. This catalyst is specific only to formic acid oxidation, as other analytes such as ethanol, methanol and ethylene glycol showed no response.Tafel analysis confirmed the porous structure and high electrocatalytic property of the electrode.

The results clearly indicate that the MWCNT/MPc complexes could serve as powerful organometallic functional materials for the development of sensors and electrocatalytic devices.

## FUTURE PERSPECTIVES

Given the high number of existing MPc complexes and new ones constantly reported in the literature, and the importance of ORR and formic acid oxidation in fuel cell development, it is envision that this newest study may likely spark research interests in the electrocatalysis of the ORR and formic acid oxidation by MPc–CNT hybrid electrodes. Possible areas in which further studies can be carried out include:

- The use of the MPc-CNT hybrid in real fuel cell testing employing formic acid and molecular oxygen.
- The use of other nanocarbons such as mesoporous carbon, carbon fiber etc. co-immobilised with MPc
- The use of other functionalised MWCNT such as those containing amine or sulphonated groups
- The use of SWCNTs
- Trying out other transition metal phthalocyanine such as Mn, Pt, Ru-centred phthalocyanine etc.
- The stability and activity of the studied MPc complexes after heat-treatment.

# APPENDIX A

## List of scientific publications

- **S. A. Mamuru**, K. I. Ozoemena, T. Fukuda, N. Kobayashi, Iron(II) tetrakis (diaquaplatinum) octacarboxyphthalocyanine supported on multi-walled carbon nanotubes platform: An efficient functional material for enhancing electron transfer kinetics and electrocatalytic oxidation of formic acid, *Journal of Materials Chemistry*, **20** (2010) 10705.

- **S. A. Mamuru**, K I. Ozoemena, Iron(II) tetrakis (diaquaplatinum) octacarboxy-phthalocyanine supported on multi-walled carbon nanotubes as effective electrocatalyst for oxygen reduction reaction in alkaline medium, *Electrochemistry Communication* **12** (2010) 1539.

- **S. A. Mamuru**, K. I. Ozoemena, T. Fukuda, N. Kobayashi, T. Nyokong, Studies on the heterogeneous electron transport and oxygen reduction reaction at metal (Co, Fe) octabutylsulphonylphthalocyanines supported on multi-walled carbon nanotube modified graphite electrode, *Electrochimica Acta* **55** (2010) 6367

- **S. A. Mamuru**, K. I. Ozoemena, Heterogeneous electron transfer and oxygen reduction reaction at nanostructured iron(II) phthalocyanine and its MWCNTs nanocomposites, *Electroanalysis* **22** (2010) 985

- K. I. Ozoemena, **S. A. Mamuru**, T. Fukuda, N. Kobayashi, T. Nyokong, Metal (Co, Fe) tribenzotetraazachlorin-fullerene conjugates: Impact of direct $\pi$ – bonding on the redox behaviour and oxygen reduction reaction *Electrochemistry Communication* **11** (2009) 1221

- **S. A. Mamuru**, K. I. Ozoemena, Impedimetric and electrocatalytic properties of nanostructured iron(II) phthalocyanine at pyrolytic graphite electrode, *Materials Chemistry and Physics* **114** (2009) 113

# APPENDIX B

## List of scientific conferences

- **Solomon A. Mamuru**, Kenneth I. Ozoemena, "*The electro-catalytic reduction of molecular oxygen at nano-structured iron(II) phthalocyanine and its multi-walled carbon nanotubes composite",* 5th International Conference of African Materials Research Society (A-MRS), Sheraton Hotel and Towers, Abuja, 14th – 18th December, 2009
  (ORAL PRESENTATION BY MAMURU)

- **Solomon A. Mamuru**, Kenneth I. Ozoemena, "*Comparative Oxygen Reduction at Metallophthalocyanines and their $C_{60}$-Conjugates"*, NanoAfrica 2009, 3rd International Conference on Nanoscience and Nanotechnology, CSIR International Convention Centre, Pretoria, South Africa, February 1- 4, 2009
  (ORAL PRESENTATION BY MAMURU)

- **Solomon A. Mamuru**, Kenneth I. Ozoemena, "*Electrochemistry of Nano-scaled Metallophthalocyanine complexes at Pyrolytic Graphite Electrodes*", *ElectrochemSA*, South African Chemical Institute, 1ST International Symposium on Electrochemistry, University of the Western Cape, Bellville, South Africa, July 9 – 11, 2008
  (POSTER PRESENTATION BY MAMURU)

- **Solomon A. Mamuru**, Kenneth I. Ozoemena, "*Electrochemistry of Metallophthalocyanines and their $C_{60}$-Conjugates",* 1st International (SA-UK Research Network) Workshop on

"Electrochemistry for Nanotechnology", CSIR International Convention Center, Pretoria, South Africa, April 9 – 10, 2008
(ORAL PRESENTATION BY MAMURU)

- **Solomon A. Mamuru**, Kenneth I. Ozoemena, "*Electrocatalytic Behavior of Nanostructured Phthalocyaninatoiron(II) complex towards the detection of Thiocyanate*", South Africa Chemical Institute (SACI) Young Spectroscopists' Symposium, University of South Africa (UNISA), October 10, 2007
(ORAL PRESENTATION BY MAMURU)